

**Illuminating reaction pathways in low-temperature  
combustion, pyrolysis & atmospheric oxidation**

by

Mark Jacob Goldman

M. S., Massachusetts Institute of Technology, 2017

B.S., The University of Texas at Austin, 2014

Submitted to the Department of Chemical Engineering  
in partial fulfillment of the requirements for the degree of

Doctor of Philosophy

at the

MASSACHUSETTS INSTITUTE OF TECHNOLOGY

February 2020

© Massachusetts Institute of Technology 2020. All rights reserved.

Author .....  
Department of Chemical Engineering  
Nov 25, 2019

Certified by .....  
Jesse H. Kroll  
Professor of Civil and Environmental Engineering  
Thesis Supervisor

Certified by .....  
William H. Green  
Hoyt C. Hottel Professor of Chemical Engineering  
Thesis Supervisor

Accepted by .....  
Patrick S. Doyle  
Robert T. Haslam (1911) Professor of Chemical Engineering



# Illuminating reaction pathways in low-temperature combustion, pyrolysis & atmospheric oxidation

by

Mark Jacob Goldman

Submitted to the Department of Chemical Engineering  
on Nov 25, 2019, in partial fulfillment of the  
requirements for the degree of  
Doctor of Philosophy

## Abstract

Reaction mechanisms are key to developing many technologies that could aid in addressing climate change. Evaluating how emissions transform in the atmosphere, obtaining more efficient combustion engines, and finding a way to store transient renewable energy all rely on accurate chemical mechanisms. This thesis spans this space by refining basic reaction rate theories, combining information and techniques from various fields to advance knowledge about atmospheric and combustion chemistry, and developing computational tools to model pyrolysis for isotopic analysis.

Having a solid foundation for reaction kinetics is necessary to get accurate kinetic rates. The first chapter corrects a longstanding issue in transition state theory by determining the proper symmetry in reactions with identical reactants and estimating the error from taking incorrect approach. The next chapter then applies transition state theory to develop high pressure limit and pressure-dependent kinetics for peroxy radicals from isobutanol, a potential bio-derived fuel.

To fully understand the behavior of oxygenated bio-based fuels, this thesis utilizes these isobutanol rate coefficients along with other estimated and measured rate coefficients to examine how peroxy radicals react across a range of temperatures, pressures, functional groups, and NO concentrations. This wide perspective elucidates why certain conditions cause pathways in combustion chemistry to start impacting atmospheric systems and vice versa. Peroxy reactions in the condensed phase also matter, so the subsequent chapter addresses this by developing a more accurate framework to simulate oxidation of small particles in the atmosphere. Both of these chapters help improve predictions on how changing emissions impacts the environment.

The final chapter of this thesis describes the creation of a tool to help assess the origin of volatile fuels by applying combustion-based automatic mechanism generation in order to help measure the exact isotopic positions within molecules.

Overall, these projects solve pieces of a larger climate problem which will require, among other things, large-scale technological, political, and social changes.

Thesis Supervisor: Jesse H. Kroll  
Title: Professor of Civil and Environmental Engineering

Thesis Supervisor: William H. Green  
Title: Hoyt C. Hottel Professor of Chemical Engineering

## Acknowledgments

Countless exceptional people have shaped my growth over the past five years. I could not have achieved the expertise and interest in chemical kinetics without outstanding teachers and mentors. Twelve years ago, Diane Aparicio first exposed me to kinetics and with her soft-spoken enthusiasm convinced me that I should start taking extra chemistry exams for fun. Four years later, Dr. Thomas Edison, with an exceptional devotion to student success, showed me how the more advanced math skills can be applied to complex systems with chemical reactions. In grad school, I had the opportunity to learn from Prof. Heather Kulik and Prof. Michael Strano about the techniques applied to kinetic systems in an array of different fields. I then was able to take both of my advisor's kinetics courses which both deepened my knowledge in a specific field, and taught me how to determine the impact that new molecules have on these systems, which I have used throughout this course. A common cultural statement is that the best way to learn something is to teach it, and I got to do this as a teaching assistant under Prof. Heather Kulik. In addition to formal classes, my advisors, Prof. Bill Green and Prof. Jesse Kroll, as well as my thesis committee, Prof. Linda Broadbelt, and Prof. Heather Kulik, provided deep insight into how to tackle the cutting-edge kinetics research discussed in this thesis.

Numerous coworkers have also continued my learning well outside the classroom. Dr. Nathan Wa-Wai Yee mentored me through my first project in graduate school. Dr. Kehang Han, Max Liu, Colin Grambow, Dr. Sarah Khanniche, Dr. Alon Grinberg Dana and Dr. Duminda Ranasinghe helped me learn to use and build upon computational chemistry tools for high-temperature applications. Prof. Anthony Carrasquillo, Dr. Christopher Lim, Prof. Rachel O'Brian, James Rowe and Dr. David Hagan, helped me gain the skills Prof. Marie Camredon, Prof. Bernard Au-mont, Dr. Richard Valorso and Josh Moss worked with me to learn the computational tools used for atmospheric chemistry. Prof. Shuhei Ono motivated and mentored me though learning about prehistoric atmospheric chemistry and its isotopic signatures.

A large part of the journey through graduate school has been deciding what type

of impact do I want to have during my short life and what are the possible ways that can happen. Many people have showed me various avenues to make an impact. Prof. Elsa Olivetti opened my eyes not only to the methods of industrial ecology but also its limitations, showing me that efficiency improvements have not, and likely will not, lead to a long term decreases of resource usage, giving me a more realistic perspective on how we can build a sustainable society. Numerous conversations with various people have helped me understand the opportunities in various fields, including Lynn Eason, Dr. Heather Simon, Prof. Heather Kulik, Dr. Sue Acton, Prof. Rachel O'Brian, Prof. Elizabeth Setren, and my advisors.

I also should acknowledge circumstances at MIT that encouraged me to spend the next few years exploring areas outside of academic institutions, including conversations within the chemical engineering department as well as with President Rafael Reif and Chancellor Cynthia Barnhart.

In a related vein, I could not have done this work without so many people that supported me through this process. My parents, brother, grandma and extended family have continued a steady stream of support for me. Eddie Chua has supported and cared for me daily over the last 4 years, even when he was on the other side of the world. My friends from before MIT who stuck it with me through the time and distance: Yomit Lavi, Vincent Lau, Tasha Gorel, Will Gordon, Kim Do, Klaus Nugraha, Daniar Listyasari, Doris Kisel, Emily Kasman, Madeleine Romeu, and Vivan Yang. My classmates, Sarah Shapiro, Maria Tau, Daniela Espinosa Hoyos, Wentau Dong, Cici Li, Max Liu, Jim Chu, and Fan He, provided me with friendship, support, and, most importantly, solidarity through this process. My weekly Shabbat friends, Elizabeth Setren, Sean Hogan, Morrisa Brenner, Amelie Raz, Issac Oderberg, Sarah Pasternak, Andy Rosenbaum, and Matthew Gurevitch provided me with constant friendship and support.

Participating in student groups and other outside activities also brought some balance to my life. Specifically, the amazing communities within Chinese Student and Scholar Association's dragonboat team, Boston Angklung Ensemble, Association of Indonesian Students, Sangham, Boston Intergenerational Dance Advocates, MIT Hil-

lel, Mechanical Engineering's service outings, the Graduate Climate Conference, the National Association of Graduate and Professional Students Legislative Action Days, the Addir Fellowship Program, Graduate Resident Tutor Committee, Eitz Chayim, and the Title IX student advisory board, helped challenge my ideas, find support, and made my time at MIT enjoyable.

I was blessed to have lived in exceptional communities during my time at MIT. I had a friend and excellent roommate, Emily Kasman, in Porter Square during my first year. This helped me create a network partially outside of MIT, which gave me some much needed distance during my all encompassing courses. I then moved to pika, which had the most wonderful community, with 28-30 students sharing one house, showing what cooperation and caring can accomplish. I then moved into Random Hall as a Graduate Resident Tutor, and saw how undergraduates built a support network for each other and turn their dorm into a home. I joined them on their path through college and into, what they would call, 'real adulthood', helping me to listen to their struggles and work with them navigate the complexities of college and the wider world. These communities, like the organizations and friends I made, will forever shape how I think communities can be built and sustained.

Through these activities and other encounters, I became friends with so many people, that expanded my knowledge about research, society, and life in general. Here are just a few of them: Xiaoyu Wu, Titan Hartono, Mahsa Nami, Jill Katz, Miranda McClellan, Fan He, Alvin Tan, Rose Palmero, Martin Wolf, Danielle Wilson, Jack and Rebecca Reid.

All the fantastic people I have met and opportunities I have gone upon have shaped me to who I am today. Having three clubs run into the ground while an officer, showed me the dangers of over-committing and helped me refocus on what is most important. Living in Boston and Abu Dhabi showed helped be better understand new regions of the world. My friends also exposed me to local housing politics and challenged my views on in various fields. *The Tech* gave me an excellent platform to hone my persuasive writing skills and craft articles that push MIT to be better.

Without the support network I had going into grad school and the hundreds of

people I met while here, my scientific skills, interests, and passions would not have grown into what they are today. This dissertation would not have been possible without all of them.

# Contents

<b>List of Figures</b>	<b>15</b>
<b>List of Tables</b>	<b>19</b>
<b>1 Introduction</b>	<b>21</b>
1.1 Reaction Mechanism Components . . . . .	23
1.1.1 Chemical reactions . . . . .	23
1.1.2 Reaction rates . . . . .	25
1.1.3 Modeling methods . . . . .	26
1.2 Applications . . . . .	26
1.2.1 The atmosphere . . . . .	26
1.2.2 Combustion . . . . .	28
1.2.3 Pyrolysis . . . . .	28
<b>2 Same-reactant symmetry treatment</b>	<b>31</b>
2.1 Summary . . . . .	31
2.2 Introduction . . . . .	32
2.3 Methods . . . . .	33
2.4 Results and Discussion . . . . .	34
2.4.1 Thermodynamic derivation . . . . .	34
2.4.2 Isotopic enrichment . . . . .	36
2.4.3 Enrichment error . . . . .	41
2.4.4 Non-isotopic impacts . . . . .	48

2.5 Conclusion . . . . .	49
<b>3 Pressure-dependent isobutanol kinetics</b>	<b>51</b>
3.1 Summary . . . . .	51
3.2 Introduction . . . . .	52
3.3 Methods . . . . .	55
3.3.1 Quantum calculations . . . . .	55
3.3.2 Thermodynamic and kinetic calculations . . . . .	56
3.3.3 Species and reaction naming . . . . .	57
3.4 Results and Discussion . . . . .	58
3.4.1 $\alpha$ -peroxy network . . . . .	59
3.4.2 $\beta$ -peroxy network . . . . .	62
3.4.3 $\gamma$ -peroxy network . . . . .	71
3.4.4 Pressure-dependent sensitivity analysis . . . . .	75
3.4.5 Comparison with combustion mechanism . . . . .	79
3.5 Conclusion . . . . .	80
<b>4 Stochastic oxidation in ultrafine organic aerosols</b>	<b>83</b>
4.1 Summary . . . . .	83
4.2 Introduction . . . . .	84
4.3 Methodology . . . . .	86
4.3.1 Model development . . . . .	86
4.3.2 Computations . . . . .	90
4.4 Results and Discussion . . . . .	101
4.4.1 Model behavior . . . . .	101
4.4.2 Previous experimental evidence . . . . .	105
4.4.3 Environmental application: night time particle nucleation . .	107
4.5 Conclusion . . . . .	111
<b>5 Fate of RO<sub>2</sub> in the atmosphere and combustion</b>	<b>113</b>
5.1 Summary . . . . .	113

5.2	Introduction . . . . .	114
5.3	Methodology . . . . .	117
5.3.1	N-propyl peroxy model . . . . .	118
5.3.2	$\gamma$ -isobutanol peroxy model . . . . .	118
5.3.3	Simulations . . . . .	119
5.4	Results . . . . .	120
5.4.1	Temperature dependence . . . . .	120
5.4.2	Pressure dependence . . . . .	122
5.4.3	NO dependence . . . . .	125
5.4.4	Structure dependence . . . . .	126
5.4.5	Application: RO <sub>2</sub> + NO impact on engine preignition . . . . .	127
5.4.6	Application: functionalization allows isomerization in atmospheric RO <sub>2</sub> . . . . .	130
5.5	Conclusions . . . . .	134
<b>6</b>	<b>Automated generation of isotope pyrolysis mechanisms</b>	<b>135</b>
6.1	Summary . . . . .	135
6.2	Introduction . . . . .	136
6.3	Calculation . . . . .	138
6.3.1	Mechanism generation . . . . .	139
6.3.2	Symmetry and degeneracy improvements . . . . .	140
6.3.3	Isotope generation . . . . .	144
6.3.4	Isotope mechanism simulations . . . . .	155
6.3.5	Reactor condition calculations . . . . .	158
6.3.6	Code availability . . . . .	164
6.3.7	History of model development . . . . .	166
6.4	Results . . . . .	169
6.4.1	Production of propane models . . . . .	169
6.4.2	Experimental comparison . . . . .	174
6.5	Discussion . . . . .	176

6.5.1	Automatic generation capabilities . . . . .	176
6.5.2	Prediction accuracy . . . . .	178
6.5.3	Applications . . . . .	182
6.6	Conclusion . . . . .	185
<b>7</b>	<b>Conclusion and Future Directions</b>	<b>187</b>
7.1	Main Findings . . . . .	187
7.2	Future Directions . . . . .	188
7.2.1	Obtaining better phenomenological rate coefficients . . . . .	188
7.2.2	Intuitive automation of rate constant determination . . . . .	189
7.2.3	Data requirements for rate constant estimation . . . . .	190
7.2.4	Computer assisted on-line position specific isotope assessment (PSIA) . . . . .	191
7.2.5	Measuring stochastic oxidation in aerosols . . . . .	192
7.3	Path forward . . . . .	192
<b>8</b>	<b>Bibliography</b>	<b>193</b>
<b>A</b>	<b>Atmospheric Aerosol Experiments</b>	<b>229</b>
A.1	Experimental requirements . . . . .	229
A.2	Producing aerosols . . . . .	230
A.2.1	coating method . . . . .	231
A.2.2	atomizing method . . . . .	233
A.3	Aerosol composition . . . . .	234
A.3.1	squalene . . . . .	235
A.3.2	corn oil . . . . .	235
A.3.3	trilinolein . . . . .	238
A.4	Oxidation chamber . . . . .	242
A.5	Oxidation source . . . . .	242
A.5.1	$\text{H}_2\text{O}_2$ photolysis . . . . .	243
A.5.2	OH concentration measurement . . . . .	245

A.6	Measuring aerosols . . . . .	246
A.6.1	size . . . . .	246
A.6.2	composition . . . . .	247
A.6.3	size and composition . . . . .	247
A.7	typical experimental steps . . . . .	249
A.8	AMS pToF analysis methods . . . . .	250
A.9	Conclusions and gaps . . . . .	250



# List of Figures

2-1 Chapter 2 summary . . . . .	31
2-2 Methane concentration in ethane pyrolysis from symmetry differences	49
2-3 Ethane concentration in ethane pyrolysis from symmetry differences .	49
3-1 Reaction pathway overview . . . . .	52
3-2 Isobutanol peroxy radicals . . . . .	53
3-3 Reaction pathways for peroxy radical . . . . .	54
3-4 $\alpha$ -network potential energy surface . . . . .	59
3-5 $\alpha$ -network selected microcanonical rates . . . . .	61
3-6 Pressure dependent branching ratios for $\alpha$ -network . . . . .	63
3-7 $\beta$ -network potential energy surface . . . . .	64
3-8 $\beta$ -network selected microcanonical rates . . . . .	66
3-9 Pressure dependent branching ratios for $\beta$ -network . . . . .	67
3-10 Fraction of excited RO <sub>2</sub> not forming R + O <sub>2</sub> . . . . .	70
3-11 $\gamma$ -network potential energy surface . . . . .	71
3-12 $\gamma$ -network selected microcanonical rates . . . . .	72
3-13 Pressure dependent branching ratios for $\gamma$ -network . . . . .	73
3-14 Sensitivity of branching to reaction barriers . . . . .	76
3-15 Sensitivity of branching to collisional energy transfer . . . . .	77
3-16 Product branching using modified strong collision approximation .	78
3-17 Comparison of rates with detailed mechanism . . . . .	80
4-1 Chapter 4 summary . . . . .	84

4-2	Peroxy pathways . . . . .	88
4-3	Change in oxidation rate with double-radical initiation . . . . .	95
4-4	Average number radicals with HO <sub>2</sub> termination . . . . .	96
4-5	Oxidation rate ratio from having HO <sub>2</sub> termination . . . . .	97
4-6	Average number radicals form HO <sub>2</sub> initiation . . . . .	98
4-7	Ratio oxidation rates from HO <sub>2</sub> initiation . . . . .	98
4-8	Average radical number with alkoxy formation from RO <sub>2</sub> + RO <sub>2</sub> . . . . .	99
4-9	Alkoxy formation from RO <sub>2</sub> + RO <sub>2</sub> at fixed total rate . . . . .	100
4-10	Alkoxy formation from RO <sub>2</sub> + RO <sub>2</sub> with set termination rate . . . . .	100
4-11	Radicals per particle varying [OH] and diameter . . . . .	102
4-12	Radical per particles varying termination rate . . . . .	103
4-13	Oxidation rate varying propagation rate . . . . .	104
4-14	Stochastic effects in experiments . . . . .	105
4-15	Simulated nighttime growth stochastic effects . . . . .	110
5-1	Chapter 5 summary . . . . .	114
5-2	RO <sub>2</sub> pathways . . . . .	115
5-3	Competing pathways . . . . .	118
5-4	n-propyl peroxy radical branching fraction . . . . .	121
5-5	Major products from R· + O <sub>2</sub> . . . . .	123
5-6	Propane branching with temperature . . . . .	125
5-7	Impact of NO <sub>y</sub> on prignition chemistry . . . . .	130
5-8	Evans-Polanyi relationship . . . . .	131
5-9	Fraction KHP formation by C–H bond strength . . . . .	132
5-10	Ring strain and C–H bond variation . . . . .	133
6-1	Allyl radical resonance . . . . .	141
6-2	Symmetry and asymmetric transition state . . . . .	148
6-3	Hydrogen abstraction from methanol transition state . . . . .	149
6-4	Truncation errors from removing highly enriched isotopomers . . . . .	152
6-5	RMG adjacency list . . . . .	164

6-6	Propane pyrolysis reactions . . . . .	171
6-7	Ethene enrichment . . . . .	172
6-8	Ethyl position specific enrichment . . . . .	173
6-9	Product branching ratios . . . . .	175
6-10	Carbon weighted analyte yield . . . . .	175
6-11	Product enrichment . . . . .	176
6-12	Experimental and model slope comparison . . . . .	177
6-13	Product distribution for reduced model . . . . .	179
6-14	Enrichment comparison four models . . . . .	181
6-15	Reaction flux diagram at 750°C . . . . .	183
6-16	Reaction flux diagram at 850°C . . . . .	184
A-1	CMAG size dependence on temperature . . . . .	232
A-2	Experimental AMS time series data . . . . .	234
A-3	Squalene nucleation . . . . .	236
A-4	Oxidation time delay . . . . .	237
A-5	Oxidation trilinolein . . . . .	239
A-6	Experimental variation with trilinolein . . . . .	240
A-7	Impact of double radical initiation on model . . . . .	244
A-8	AMS pToF size calibration . . . . .	248



# List of Tables

3.1	Literature comparison for $\beta$ -network . . . . .	69
3.2	Literature comparison for $\gamma$ -network . . . . .	75
4.1	Reaction rate effect on stochasticity . . . . .	105
4.2	Modeling nighttime growth parameters . . . . .	108
5.1	Removed reactions from propane model . . . . .	120
5.2	Products used to identify pathways . . . . .	121
5.3	Combustion reaction grouping . . . . .	129
6.1	Vibration magnitudes of hydrogen abstraction . . . . .	149
6.2	Model size from reduction . . . . .	152
6.3	$\delta^{13}\text{C}$ sensitivity from initial concentration . . . . .	162
6.4	Branching ratio sensitivity from initial concentration . . . . .	162
6.5	$\delta^{13}\text{C}$ sensitivity from residence time . . . . .	162
6.6	Branching ratio sensitivity from residence time . . . . .	163
6.7	$\delta^{13}\text{C}$ sensitivity from pressure change . . . . .	163
6.8	Branching ratio sensitivity with pressure change . . . . .	163
6.9	Ethyne selectivity with different pressure and wall loss reactions . . . . .	168
6.10	Sizes of the various propane models . . . . .	172
6.11	Variance of model errors on atom filiation . . . . .	177
A.1	Recommended values for seeing stochastic effects . . . . .	229
A.2	Particle generation comparison . . . . .	233

A.3	Experimental decay rates . . . . .	238
A.4	Materials used in experiments . . . . .	242
A.5	GC temperature ramp settings . . . . .	246
A.6	GC valve settings . . . . .	246

# Chapter 1

## Introduction

Humanity stands at crossroads. We are on an earth already 1°C (1.8°F) warmer than fifteen generations before us, accelerating at a rate faster than ever before in our scientific and historical records.[1] Our inertia drives us to continue increasing greenhouse gas emissions as our ability and desire to extract, process, and use resources has typically outpaced any efficiency gains along the way.[2] In order to limit climate change to 1.5°C, the Intergovernmental Panel on Climate Change estimates that our emissions of greenhouse gas will need to be zero in 20 years, which if done properly can reduce droughts, floods, heat waves, sea level rise, forest fires, invasive species, and infectious diseases relative to 2°C warming.[1]

Changing course to a cooler future will require a coordinated effort of policy action, renewable technology adoption, and reduction in consumption.[1, 3] On ensuring technological solutions to emerging problems, chemistry and chemical engineering are essential. During a previous atmospheric crisis, where current refrigerants were depleting the ozone layer, atmospheric chemists identified the critical chemistry of ozone depletion and chemists and chemical engineers worked to develop refrigerants that react and rain out more quickly in the atmosphere. Having adequate alternatives together with international collaboration, regular evaluations, and updated requirements, the average annual ozone concentration in the southern hemisphere reached a minimum in 1995, and has been slowly increasing since.[4, 5]

Climate change has not had as stellar a turnaround as the ozone hole crisis. This

is in part due to it being much more difficult to retrofit our infrastructure to eliminate emissions of greenhouse gases, than it was for refrigeration systems to switch refrigerants.[6] For climate change, we would need to abandon much more of the old infrastructure and start anew. Since consumption is still tied to fossil fuel emissions, increased consumption can offset a shift to renewables, which caused an increase in European greenhouse gas emissions in 2017.[7] Overcoming these issues will require aggressive policy action.[8]

In addition to necessary policy changes, technological improvement will also be critical. Just like how chemistry and chemical engineering helped solve the ozone hole crisis, these fields are also critical in ensuring a transition to a zero-carbon future. We currently have technological gaps in renewable energy storage,[9, 10, 11] carbon capture,[12, 13] and efficient renewable energy production which does not rely on limited metals.[14, 15] Behind each of these new technologies is a chemical mechanism, which must be adequately understood. These mechanisms seek to describe a system's behavior using lists of reactions and their corresponding rates. If built properly, chemical mechanisms can predict behavior at conditions not experimentally tested, can describe phenomena hard to measure experimentally, and can highlight potential side effects that may occur in a process.

This thesis advances knowledge about chemical mechanisms in applications that help us better evaluate a move to a more sustainable future. The results of this thesis improve chemical mechanisms in ways that can help optimize biofuel combustion, investigate whether fuels are biogenic, and more accurately model atmospheric processes. The following sections discuss some necessary parts of reaction mechanisms, which is followed by a section that looks at the major chemistry involved in three interesting systems that impact our climate: the atmosphere, combustion and pyrolysis.

## 1.1 Reaction Mechanism Components

### 1.1.1 Chemical reactions

Obtaining a list of important chemical reactions is a big challenge in chemical kinetics. A large challenge in figuring out that chlorofluorocarbons were depleting the ozone layer was understanding what reactions were causing this effect. There is inherent uncertainty when figuring out what reactions are important. Errors in a mechanism can be grouped into two categories: having the wrong rates in the model (termed parameter estimation error) and missing entire reactions (termed model truncation error). The former error is partially assessed through sensitivity or uncertainty analyses, which modifies one or more parameter values and measures how much another variable changes.[16] These can be done either locally, by looking at the rate of production of an important compound, like OH at a moment in time,[17] or globally, by looking at how a rate change impacts a final system property, like ignition delay time.[18] Since kinetic rates are highly non-linear and these analysis look at first order changes, the information they provide is not always useful if the model deviates significantly from the real system.

Model truncation error is harder to correct for than the parameter estimation error since what is missing from the model is not known. People often generate detailed models, which consist of every imaginable reaction that could exist in the system. These models can be benchmarked against experimental results to check that the model predictions are correct.[19] Then they can be reduced in complexity if necessary for computationally intensive applications, like computational fluid dynamics.[20, 21, 22]

Though detailed models do a good job at reducing model truncation error, they are difficult to create. Traditionally, field experts have written out reactions by hand and combined them with other models. While this is very time consuming, the results are often well-trusted. The most popular models for many applications, such as atmospheric organic chemistry,[23] alkane combustion,[24, 25] and alcohol combustion,[26] are created this way.

Other people have tried to program the information used to generate expert-based detailed mechanisms into software to speed up the model generation process. These automated mechanisms use the computer to decide whether further species or reactions should be included in the model, and exist for a variety of applications, such as atmospheric chemistry,[27] combustion chemistry,[28] and organic synthesis.[29]

One way to get computers to simulate how experts would create mechanisms is to create a list of rules that the experts use when generating mechanisms. The computers follow this list of rules which determine which reactions to add and what rates to give the reactions. This method is simple, fast, and can generate millions of reactions on the order of minutes.[27] A challenge with rule-based mechanism generation is that each system requires different rules, and choosing which rules apply in which cases often requires experts.

Another method of model generation is to use simulation results, rather than rules, to decide which species or reaction to add to the mechanism. The software used in this thesis, Reaction Mechanism Generator (RMG) is of this type.[28] It adds new species to the mechanism based on its formation rate. This allows the model itself, as opposed to hardcoded rules, to determine how to grow the model, which can lead to a smaller model consisting of more important species than obtained through a rule-based approach. The final model using this method is more sensitive to what rates are used, since the wrong rate estimates could cause the model to pick up unimportant species while missing important ones.

Chapter 6 extends RMG to generate isotopic mechanisms and compare the generated mechanism with experimental results. In enumerating all the different isomers that vary in isotopic labeling, termed isotopologues, the model size increases by an order of  $2^n$  where  $n$  is the number of atoms which can contain an isotope. Having a small initial mechanism, like that obtained by RMG's rate-based algorithm is ideal in this situation because it leads to a more condensed mechanisms that can have all the isotopologues enumerated.

Chapter 5 discusses the fate of peroxy radicals, an important atmospheric and combustion intermediate. This mechanism was generated by pulling specific rates

from various sources since accuracy in this case is preferred over speed.

### 1.1.2 Reaction rates

Highly linked with the list of reactions are the rate coefficients that dictate how fast each reaction progresses. Rate coefficients can come from many sources, which vary in accuracy.

The most accurate way to get a rate constant is to measure it experimentally. This, however, can be tricky and time consuming, and is not really feasible when dealing with thousands to millions of reactions contained in detailed mechanisms. For detailed mechanisms, the primary method is to estimate rates using various heuristics. RMG uses a tree-based estimation method that assumes that the unknown reaction has a similar rate to those chemically similar to it, which is determined by distance in the tree. This estimation method is used in Chapter 6 in the thesis.

A middle ground between experiments and heuristics is to perform quantum calculations. These reactions approximate the Schrödinger equation to estimate a molecule's vibrations and electronic energy. Statistical mechanics is then applied to the quantum results to estimate bulk properties of molecules, like heat capacity, entropy and enthalpy.

When using statistical mechanics, other molecular properties are also necessary, like the symmetry of the molecule and whether or not it is chiral. Chapter 2 corrects an error in the current literature about treating the symmetry number of identical molecules that undergo a bimolecular reaction.

To obtain reaction rates from quantum calculations, transition state theory (TST) is often applied,[30] which does a good job at approximating reaction rates when the reactants are in thermal equilibrium, given by a Boltzmann distribution.[31] When this is not the case, which might occur when molecular energy transfer from collisions is slower than the reaction rate, more challenging computations involving discretized energy levels can be used. Reactions in this category are pressure dependent since the rate of reaction depends on the energy transfer rate, which is a function of how frequent collisions occur.[32]

Chapter 3 of this dissertation shows quantum calculations for three important intermediates in isobutanol oxidation, and calculates rates using both TST and pressure-dependent methods. These results are used later in Chapter 5.

### 1.1.3 Modeling methods

The main use of a kinetic mechanism is in simulations, and there are various techniques to simulate mechanisms. The most basic is to model the system as ordinary differential equations (ODEs) using concentrations of various species. Special techniques also exist for dealing with multiphase systems,[33] systems with a wide range of rates (stiff systems),[21] and systems with small numbers of molecules.[34] The last of these, often called stochastic kinetics, is used in Chapter 4 of this thesis.

Stochastic treatment of molecules uses discrete numbers of molecules instead of representing them as a concentration. This is more accurate when only a few molecules exist in a system. This effect has been shown to be important in various fields.[35, 36, 37, 38] Chapter 4 of this thesis develops a model that looks at whether it is necessary to model oxidation in atmospheric aerosols stochastically, and Appendix A described efforts to test that model in experiments.

## 1.2 Applications

Most chapters in this thesis develop a mechanism for a particular application related to dealing with climate change. This section discusses important reactions in these various applications and the potential impact of the mechanisms generated, going in increasing temperature, from the atmosphere (250-350 K), to low-temperature combustion (500-800 K), and then to pyrolysis (900-1300 K).

### 1.2.1 The atmosphere

Atmospheric particles strongly impact human health and earth's climate. A large fraction of these particles come from gas-phase organic compounds that react in

our atmosphere. Understanding these reactions is critical to assessing the impact of emission changes.

Much of the chemistry in the atmosphere deals with reactive radicals. Some of these radicals, like OH, abstract hydrogens from organic molecules leading to an alkyl radical, R. These radicals often add O<sub>2</sub>, to form a peroxy radical, RO<sub>2</sub>. The behavior of peroxy radicals is central to many fields, and a large part of this thesis, specifically chapters 2, 3, 4, and 5, relate to the behavior of peroxy radicals.

In the atmosphere, the different ways peroxy radicals react could lead to the molecule breaking into smaller pieces, which are less likely to condense onto particles, or become more oxygenated, leading to less particle formation. One common cause of fragmentation is when a NO radical converts the peroxy radical to an alkoxy radical, RO and NO<sub>2</sub>. Alkoxy radicals can undergo various pathways, though the one that leads to fragmentation involves a breaking of a C–C bond to form a carbonyl compound, known as  $\beta$ -scission, which is most dominant in tertiary alkoxy radicals.

The peroxy radical reactions that have the most oxygen incorporation, and the most particle formation, involve an intramolecular hydrogen abstraction by RO<sub>2</sub>, leading to an alkyl radical with a hydroperoxide group, which can undergo a second oxygen addition. The incorporation of multiple oxygen molecules with a single initial hydrogen abstraction, leads to extremely low volatility compounds.[39] Given the different fates of RO<sub>2</sub>, understanding their behavior in the atmosphere is critical to understanding the impact of emissions on health and climate.

Multiple chapters in this thesis help reduce the uncertainty on the fate of peroxy radicals. Chapter 2 touches on reaction rate of dimerization of peroxy radicals, which is another volatility-lowering reaction. Chapter 3 discusses the the various unimolecular pathways that an alcohol peroxy undergoes. Chapter 4 evaluates the fate of peroxy radicals in submicron atmospheric particles. Chapter 5 adds bimolecular reactions to the reactions in Chapter 3 to give a more complete accounting of the RO<sub>2</sub> fate in various environments.

Improvements in RO<sub>2</sub> reactions in this thesis could help reduce model uncertainties when simulating climate projections.

### **1.2.2 Combustion**

For internal combustion engines in cars, the time a fuel takes to ignite is important to prevent engine misfiring. This is correlated with the increase in production of reactive OH radicals. The oxygen incorporation reaction pathway discussed in Section 1.2.1, also occurs in fuel engines, and produces as many as three OH radicals for each OH radical that reacts.[40] This fast, chain-branching pathway competes with an alternative pathway that produces a less reactive radical, HO<sub>2</sub>, and a double bonded molecule. The latter pathway, which occurs at higher temperatures, produces less reactive radicals, leading to slower ignition. The trend when ignition timing gets slower as the system gets hotter, called the negative temperature coefficient region, is an important property of fuel, and this is caused by the fate of RO<sub>2</sub> radicals.

Due to the importance of RO<sub>2</sub> reactions in both the atmosphere and combustion, Chapter 5 evaluates the fate of peroxy radicals at conditions spanning both conditions, using data produced in Chapter 3. These advancements can both better constrain isobutanol combustion and help with screening for new potential biofuels.

### **1.2.3 Pyrolysis**

Pyrolysis involves reactions that occur at elevated temperatures in the absence of oxygen. Many reactions in pyrolysis and combustion overlap, but without oxygen, the chemistry is simpler. The alkyl radical, instead of the peroxy radical, is the central intermediate. It can either  $\beta$ -scission, forming smaller radical and a double bond, it can abstract a hydrogen from another compound, or it can terminate by combining with another radical. Pyrolysis is used in a wide range of applications, such as charcoal production, biomass liquification[41], and analytical measurements.[42] One analytical technique, called on-line position specific isotope analysis, uses pyrolysis to measure isotope distributions within molecules.[43] In Chapter 6, a model is created which predicts products in an on-line position specific isotope analysis device, to enable using this device for compounds not previously studied before. This could be applied to evaluating whether a fuel is of biogenic or fossil fuel origin.

The next chapter discusses the proper way to calculate the reaction rate of radical recombination, which can create a significant effect in some pyrolysis simulations.



# Chapter 2

## Same-reactant symmetry treatment

An edited version of this chapter was published by Journal of Physical Chemistry A.[44]

### 2.1 Summary

Confusion over how to account for symmetry numbers when reactants are identical can cause significant errors in isotopic studies. An extraneous factor of two in the reaction symmetry number, as proposed in literature, violates reaction equilibrium and causes huge enrichment errors in isotopic analysis. In actuality, no extra symmetry factor is needed with identical reactants.

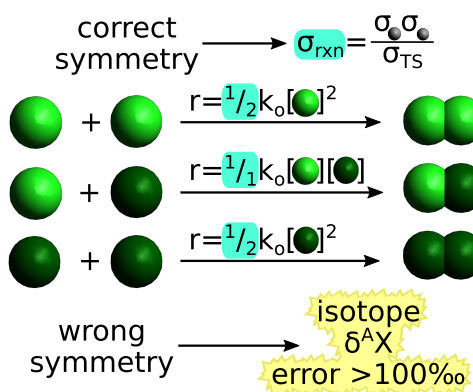


Figure 2-1: Diagram showing the proper reaction symmetry numbers to use when reactions are identical or different

## 2.2 Introduction

The rate of consumption of molecule A,  $r_A$ , in a bimolecular reaction can be calculated with  $r_A = -k[A][B]$ . If the two reactants are identical, a stoichiometric coefficient of two appears in front of the equation for the consumption of A:  $r_A = -2k[A]^2$ . The rate coefficient  $k$  is often computed using transition state theory (TST) at the high pressure limit:[45]

$$k(T) = \kappa \sigma_{rxn} \frac{m_{TS}}{m_A m_B} \frac{k_B T}{h} \frac{q_{TS}^{\ddagger\ddagger}/V}{(q_A^\dagger/V)(q_B^\dagger/V)} e^{\left(\frac{-E_o}{k_B T}\right)} \quad (2.1)$$

where  $\kappa$  is the tunneling factor,  $\sigma_{rxn}$  is the reaction symmetry number,  $m$  is the number of accessible optical, or ‘mirror image’, isomers of a molecule or transition state,  $k_B$  is Boltzmann’s constant,  $h$  is Planck’s constant,  $E_o$  represents the difference in zero point energy between the transition state and reactants,  $q$  represents the partition function of molecule or transition state with  $E = 0$  at its zero point energy,  $\dagger$  indicates removal of the symmetry in the rotational partition function to form  $\sigma_{rxn}$ , and  $\ddagger$  indicates the removal of one degree of freedom corresponding to the reaction coordinate.

This chapter focuses on a discrepancy in defining the reaction symmetry number,  $\sigma_{rxn}$ , when used in TST with two identical reactants. With different reactants,  $\sigma_{rxn}$  is defined according to eq 2.2 with  $\sigma_X$  being the rotational symmetry number of  $X$ .

$$\sigma_{rxn} = \frac{\sigma_B \sigma_A}{\sigma_{TS}} \quad (2.2)$$

Competing theories exist for the correct value of  $\sigma_{rxn}$  when the two reactants are identical. A highly-cited article by Pollak and Pechukas in 1978 argues that  $\sigma_{rxn}$  should be increased by a factor of two when A and B are identical, since the reactants could be translationally interchanged.[46] This assertion conflicted with the previous recommendation by Bishop and Laidler who used an alternative method to correct for reaction symmetry, reaction path degeneracy (RPD).[47] RPD is the number of ways a reaction can proceed with different atoms and is equivalent to the combination of

symmetry and optical isomers terms in eq 2.1. When reactants are identical, the RPD algorithm will interchange the two molecules and count the number of possible pathways twice. To prevent double-counting due to molecule interchangeability, Bishop and Laidler recommend dividing the RPD by two when the reactants are identical.[47] These two competing perspectives on how to deal with identical reactants have persisted in the literature. A widely-cited review[48] recommends multiplying the reactant symmetry numbers by a factor of two, referencing Pollak and Pechukas, though many studies involving identical reactants do not mention, and likely do not include, this factor of two.[49, 50, 51, 52, 53]

Though a factor of two mistake can impact many phenomena, it causes huge errors in isotopic enrichment since the disputed factor of two is much larger than most non-hydrogen kinetic isotope effects.[54]

This paper uses two methods to explain proper symmetry treatment in reaction kinetics. We first show that the factor of two proposed by Pollak and Pechukas causes thermodynamic inconsistencies in the equilibrium constant and then describe how this error creates huge discrepancies in isotopic enrichment, using  $\text{Cl} + \text{Cl} \longrightarrow \text{Cl}_2$  as an example.

## 2.3 Methods

When estimating rate coefficients, we use TST, shown in eq 2.1. Reactions in this paper are analyzed at the high pressure limit, since errors in the reaction symmetry number would impact reaction rates at both the low and high pressure limit. When reactions are barrierless, the transition state structure is defined along the reaction path by variational TST.[55] This approach leads to the same relative rate coefficients for  $\text{O} + \text{O}_2 \longrightarrow \text{O}_3$  as an alternative approach which involved analysis of metastable  $\text{O}_3$ .[56]

To evaluate the correct method for treating symmetry numbers, this work varies the reaction symmetry number, shown in eq 2.2, by either adding or not adding a factor of two. The two different rate coefficients derived from the different treatments

of eq 2.2 are evaluated for thermodynamic equilibrium and for determining isotopic enrichment. To isolate the effect of symmetry numbers, examples are chosen which highlight the variation introduced in reaction symmetry number.

The usage of symmetry numbers in this work leads to the same rates as the full treatment of rotation with nuclear spin degeneracy at the classical limit.[57, 48]

## 2.4 Results and Discussion

### 2.4.1 Thermodynamic derivation

The extra factor of two recommended in Ref. 46 leads to inconsistencies in equilibria. To show this, we plug eq 2.1 into the definition of equilibrium constant for the reaction  $2\text{B} \longrightarrow \text{BB}$  and compare that to the equilibrium constant for this reaction derived from the Gibbs free energy. We can then determine if an extra factor of two appears when evaluating the forward reaction symmetry number,  $\sigma_{f,rxn}$ .

The equilibrium constant,  $K_c$ , is the ratio of forward,  $k_f$ , and reverse,  $k_r$ , rate coefficients. Substituting  $k_f$  and  $k_r$  obtained from eq 2.1 results in

$$K_c = \frac{k_f}{k_r} = \frac{\sigma_{f,rxn}}{\sigma_{r,rxn}} \frac{m_{\text{BB}}}{m_{\text{B}}^2} \frac{q_{\text{BB}}^\dagger/V}{(q_B^\dagger/V)(q_B^\dagger/V)} e^{\left(\frac{-E_{rxn}}{k_B T}\right)} \quad (2.3)$$

where  $\sigma_{f,rxn}$  is the reaction symmetry number in the forward direction,  $\sigma_{r,rxn}$  is the equivalent in the reverse direction, and  $E_{rxn}$  is the difference between the zero point energies of the product and reactants. The tunneling factors and transition state partition function cancel out since neither affects equilibrium.

To determine whether  $\sigma_{f,rxn}$  contains the factor of two recommended by Pollak and Pechukas,[46] we derive the equilibrium constant in a different way based on the definition that at equilibrium the Gibbs free energy,  $G$ , is at a minimum in a constant temperature and pressure system. The change in  $G$  can be represented by a constant temperature and pressure chemical potential,  $\mu$ .

$$dG = -2\mu_{\text{B}} + \mu_{\text{BB}} = 0 \quad (2.4)$$

The chemical potential of a pure species  $j$ ,  $\mu_j$ , can be derived from its partition function,  $Q_j$ . Neglecting intermolecular forces with the ideal gas assumption, the partition function can be put in terms of a single molecule's partition function,  $q_j$ , and the number of those molecules,  $N_j$ . Since the molecules are also indistinguishable, a factor of  $N_j!$  appears, which can be simplified by Stirling's approximation,  $N_j! \approx \left(\frac{N_j}{e}\right)^{N_j}$ , as shown in eq 2.5.[58]

$$Q_j = \frac{q_j^{N_j}}{N_j!} \approx \left(\frac{eq_j}{N_j}\right)^{N_j} \quad (2.5)$$

If species  $j$  represents a mixture with  $m_j$  optical isomers of equal concentration, energy and reactivity, then the partition function ( $Q_j$ ) can be separated into the product of each isomer  $i$ ,  $Q_j = \prod_i^{m_j} Q_{j,i} = (Q_{j,i})^{m_j}$ , which is simplified with Stirling's approximation in eq 2.6.

$$Q_j = \left(\frac{q_j^{N_j/m_j}}{(N_j/m_j)!}\right)^{m_j} \approx \left(\left(\frac{eq_j}{N_j/m_j}\right)^{N_j/m_j}\right)^{m_j} = \left(\frac{m_j eq_j}{N_j}\right)^{N_j} \quad (2.6)$$

Since  $\mu_j$  can equivalently be defined using Gibbs or Helmholtz free energy,[58]  $\mu_j$  can be found using  $Q_j$  and eq 2.6.

$$\mu_j = \left(\frac{\delta A}{\delta N_j}\right)_{T,V,N_i} = -RT \left(\frac{\delta \ln Q_j}{\delta N_j}\right)_{T,V,N_i} \approx -RT \ln \frac{m_j q_j}{N_j} \quad (2.7)$$

Substituting the chemical potentials for B and BB from eq 2.7 into the equilibrium relationship in eq 2.4 results in

$$\frac{N_{BB}}{N_B^2} = \frac{m_{BB} q_{BB}}{m_B^2 q_B^2} \quad (2.8)$$

Since the partition function of an ideal gas molecule is proportional to volume, each term in eq 2.8 can be divided by volume to obtain concentrations,  $C_j = \frac{N_j}{V}$ , and the equilibrium constant,  $K_c$ .[58]

$$\frac{C_{BB}}{C_B^2} = \frac{m_{BB} (q_{BB}/V)}{m_B^2 (q_B/V)^2} = K_c \quad (2.9)$$

There is no special factor of two in eq 2.9 due to translational indistinguishability, and this equation is analogous to the equilibrium constant for a reaction with two different reactants.

We then extract the symmetry and zero point energy from the partition functions,  $q_j = \frac{q_j^\dagger}{\sigma_j} e^{E_{o,j}/k_B T}$ , to get eq 2.9 into the same form to compare with eq 2.3.

$$K_c = \frac{\sigma_B^2 m_{BB}}{\sigma_{BB} m_B^2} \frac{(q_{BB}^\dagger/V)}{\left(q_B^\dagger/V\right)^2} e^{\left(\frac{-E_{rxn}}{k_B T}\right)} \quad (2.10)$$

Equating eq 2.10 with eq 2.3 results in

$$\frac{\sigma_B^2}{\sigma_{BB}} = \frac{\sigma_B^2 / \sigma_{TS}}{\sigma_{BB} / \sigma_{TS}} = \frac{\sigma_{f,rxn}}{\sigma_{r,rxn}} \quad (2.11)$$

By equating these two equilibrium constants, no factor of two appears in the definition of  $\sigma_{f,rxn}$  even if A = B. Ref. 58 includes a derivation for  $K_c$  when A  $\neq$  B, which results in the same conclusion.

Interchange of the identical reactants, postulated by Pollack and Pechukas as the reason for the factor of two,[46] is already accounted for when going from an ensemble partition function to a molecular partition function in eq 2.5. Since the RPD algorithm accounts for the interchange, it must be removed by halving the RPD for reactions with identical reactants, as recommended by Bishop and Laidler.[47]

Due to this thermodynamic inconsistency, kinetic simulators that estimate reverse kinetics using equilibrium and forward kinetics will also incorrectly double the reverse rate of reaction if the factor of two recommended by Pollack and Pechukas is used for the forward reaction.

## 2.4.2 Isotopic enrichment

### **symmetric B + B recombination**

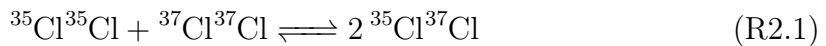
In many fields a factor of two error in a computed rate coefficient can have modest effects, but when studying isotopic enrichment, it dominates any realistic enrichment. Increasing the rate coefficients of reactions with identical reactants by the extra factor

of two proposed in some literature [46, 48] leads to unphysical behavior which is significantly inconsistent with experimental isotopic enrichment values of identical reactant reactions.[59] As a simple example, consider chlorine atom recombination involving  $^{35}\text{Cl}$  and  $^{37}\text{Cl}$  which has three distinct reactions depending on the isotopes involved. By analyzing the rates of these three reactions, we show that adding the factor of two to eq 2.2 creates unrealistic isotopic enrichment.

To isolate the effect of the factor of two, this example makes several simplifying assumptions:

1. The reactions occur at the high pressure limit, so variable lifetimes of excited states, like in atmospheric ozone,[60] would not be expected, and we can use canonical TST (eq 2.1) to estimate the rate coefficients.
2. Mass-dependent kinetic isotope effects for isotopic chlorine are negligible (< 5% change in rate coefficient for non-hydrogen isotopes[54]) when compared to deviations expected by doubling a rate coefficient, so they are omitted from this simple model.
3. Non-symmetry based mass-independent isotope effects, e.g. nuclear field shift and magnetic properties, are also negligible when compared to deviations expected by doubling a rate coefficient,[54] so they are also omitted from this model.

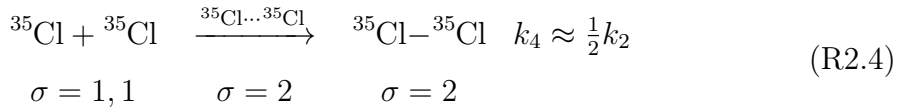
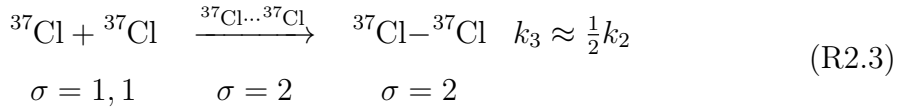
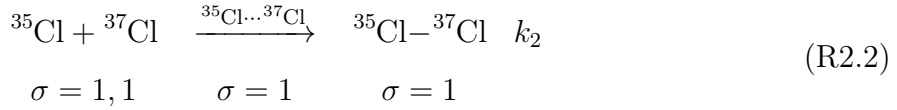
Suppose we start with a system of Cl atoms at a  $^{37}\text{Cl}$  abundance of  $\alpha = \frac{^{37}\text{Cl}}{^{37}\text{Cl} + ^{35}\text{Cl}}$ . When they finish recombining, we expect to have a system full of  $\text{Cl}_2$  molecules. If no kinetic isotope effects occur, the products should be in isotopic equilibrium shown by reaction R2.1 with the equilibrium relationship given in eq 2.12.



$$K_c = \frac{[^{35}\text{Cl}^{37}\text{Cl}]^2}{[^{35}\text{Cl}^{35}\text{Cl}][^{37}\text{Cl}^{37}\text{Cl}]} \approx \frac{\sigma_{3535}\sigma_{3737}}{\sigma_{3537}^2} = 4 \quad (\text{2.12})$$

Solving eq 2.12 for  $\alpha$ , given isotopologue concentrations of  $[^{37}\text{Cl}^{37}\text{Cl}] = c\alpha^2$  and  $[^{35}\text{Cl}^{35}\text{Cl}] = c(1 - \alpha)^2$ , results in isotopologue ratios  $[^{35}\text{Cl}^{35}\text{Cl}] : [^{35}\text{Cl}^{37}\text{Cl}] : [^{37}\text{Cl}^{37}\text{Cl}] \approx (1 - \alpha)^2 : 2\alpha - 2\alpha^2 : \alpha^2$ . Note that this ratio is exactly the same as predicted by combinatorics if one randomly chooses pairs of balls from a population where  $P_{blue} = \alpha$  and  $P_{red} = 1 - \alpha$ .

These values can be compared with the products obtained from a kinetic model using TST rate coefficients to see the impact of adding the extra symmetry factor. Reactions R2.2-R2.4 show three chlorine recombination reactions using different isotopes of chlorine. The symmetry numbers of the reactants, product, and transition state,  $\sigma$ , are used to find the ratio of reaction rate coefficients,  $k_i$ , using eqs 2.1 and 2.2. Here all the  $\sigma = 2$  factors are from rotational symmetry; the extra factor of two proposed by Pollack and Pechukas has not been included.[46]



If we assert that there is an initial system with 50%  $^{35}\text{Cl}$  and 50%  $^{37}\text{Cl}$ , eq 2.12 would predict a product distribution of 25%  $^{37}\text{Cl}-^{37}\text{Cl}$ , 50%  $^{35}\text{Cl}-^{37}\text{Cl}$ , and 25%  $^{35}\text{Cl}-^{35}\text{Cl}$  based on thermodynamics. From a kinetics perspective, this same product ratio occurs when  $k_2$  is twice as large as  $k_3$  and  $k_4$ , which is caused by changes in the rotational partition functions due to molecular symmetry. In this example, the transition states for reactions R2.3 and R2.4 are symmetric ( $\sigma = 2$ ) whereas the one for reaction R2.2 is not ( $\sigma = 1$ ), creating the difference in rate coefficient.

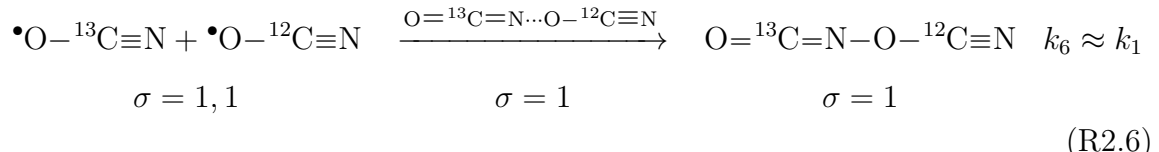
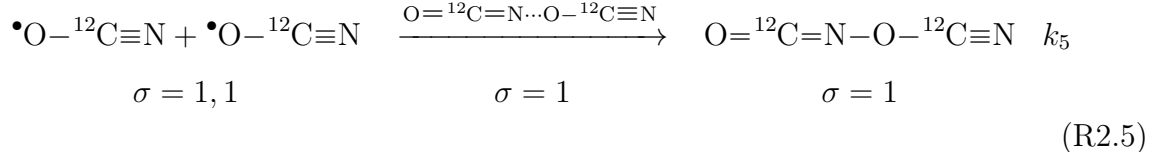
This lack of enrichment caused by molecular symmetry agrees with previous analysis which indicates that the difference in rate coefficients in reactions R2.2-R2.4 just represents relative probabilities of forming symmetric and asymmetric molecules[61]

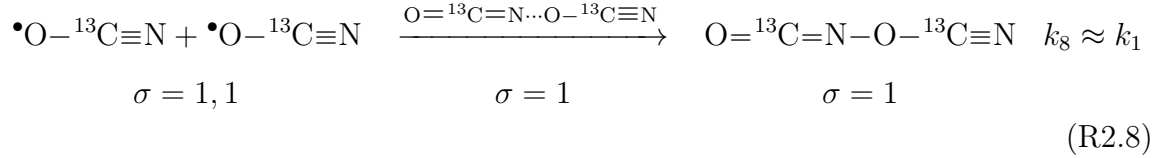
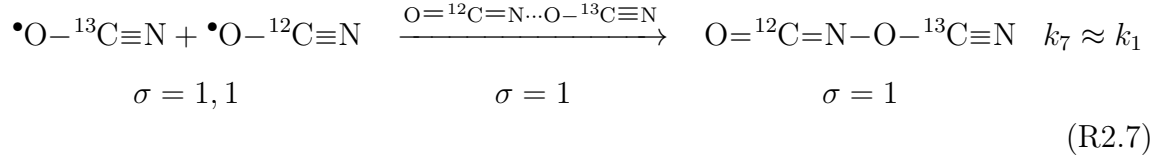
which cancels out in the classical limit when determining fractionation and enrichment factors. Some compounds, like O<sub>3</sub>, do achieve fractionation between symmetric and asymmetric isotopologues. However, these observed enrichments are not caused by the symmetry factor discussed here. Instead the observed small enrichments are likely due to other effects, such as tunneling.[62]

If the method of Ref. 46 is applied to reactions R2.2-R2.4,  $k_3$  and  $k_4$  would be doubled, and all three reactions would have equal rates leading to a 33% accumulation of each Cl<sub>2</sub> isotopologue. This would significantly favor symmetrical products and deviate from isotopic equilibrium in reaction R2.1. Having an asymmetric transition state, described in the next section, provides the same conclusion as for the chlorine recombination system.

### asymmetric B + B reaction

Reactions with an asymmetric transition state have more possible reaction channels than reactions with symmetric ones, which could potentially affect how we treat isotopic reactions. Here we use the asymmetric recombination of NCO radicals, which is analogous to propargyl recombination important in aromatic formation.[52] NCO radicals have two resonance forms,  $\bullet\text{O}-\text{C}\equiv\text{N} \longleftrightarrow \text{O}=\text{C}=\text{N}\bullet$ , which allows a radical recombination reaction to occur with an asymmetric transition state, giving an asymmetrical product, O=C=N-O-C≡N. There are four possibilities for asymmetric radical recombination with two carbon isotopes, <sup>12</sup>C and <sup>13</sup>C, shown below.





The symmetry numbers,  $\sigma$ , are used to find the ratio of reaction rate coefficients,  $k_i$ , using transition state theory (Equations 2.1 and 2.2 in the main text). These  $\sigma$ 's are from the rotational partition functions and do not include the extra factor of 2 proposed in some literature.[46, 48] The four reactions are expected to have approximately identical rates, since the symmetry numbers of reactants and transition states are identical across the reactions. The only difference is in a heavy isotope which is not located at reaction center.

A 50:50 mixture of starting reactants,  $\bullet\text{O}-{}^{12}\text{C}\equiv\text{N}$  and  $\bullet\text{O}-{}^{13}\text{C}\equiv\text{N}$ , would yield the four products with approximately equal concentrations. The two products with exactly one  ${}^{13}\text{C}$ , from Reactions R2.7 and R2.6, together make up 50% of the total products in this system. This would lead to 25% of products with no  ${}^{13}\text{C}$  atoms, 50% of products with one  ${}^{13}\text{C}$  atom, and 25% of products with two  ${}^{13}\text{C}$  atoms, as one would expect from combinatorics.

If a factor of 2 was added to reactant symmetries that had the same labeling, as proposed in literature,[46, 48] the rate coefficients for Reactions R2.5 and R2.8 would be twice as big as those for Reactions R2.7 and R2.6. This would lead to the fraction of products with no  ${}^{13}\text{C}$  atoms, one  ${}^{13}\text{C}$  atom, and two  ${}^{13}\text{C}$  atoms to each be 33%. Like the chlorine recombination case, this leads to much more isotope segregation than would be expected from random collisions or kinetic isotope effects.

### 2.4.3 Enrichment error

Given that substituting non-hydrogen isotopes typically modifies rate coefficients by only a few percent,[54] the introduction of a factor of two to some rate coefficients can lead to significant errors at natural abundance. To quantify this error, we compare the change in enrichment between reactants and products with and without the factor of two proposed by Pollak and Pechukas.[46]

For the chlorine recombination reaction described above whose reactants have an isotopic ratio of  $R_r = \frac{^{37}\text{Cl}}{^{35}\text{Cl}}$ , the rates of reactions R2.2-R2.4 without the factor of two, given by eqs 2.13-2.15, can be used to find product enrichments.

$$r_{R2.4} = k_{R2.4}[^{35}\text{Cl}]^2 \quad (2.13)$$

$$r_{R2.2} = k_{R2.2}[^{35}\text{Cl}][^{37}\text{Cl}] \approx 2R_r k_{R2.4}[^{35}\text{Cl}]^2 = 2R_r r_{R2.4} \quad (2.14)$$

$$r_{R2.3} = k_{R2.3}[^{37}\text{Cl}]^2 \approx R_r^2 k_{R2.4}[^{35}\text{Cl}]^2 = R_r^2 r_{R2.4} \quad (2.15)$$

A factor of two appears in eq 2.14 since the rate coefficient for reaction R2.2 is twice that of reaction R2.4. Using eqs 2.13-2.15, the ratio of the nonstandard to standard isotope in the products is

$$R_p = \frac{^{37}\text{Cl}}{^{35}\text{Cl}} = \frac{r_{R2.2} + 2r_{R2.3}}{2r_{R2.4} + r_{R2.2}} = \frac{2R_r + 2R_r^2}{2 + 2R_r} = R_r \quad (2.16)$$

Since  $R_p$  is equal to  $R_r$ , no enrichment occurs without the factor of two suggested by Pollak and Pechukas.

If the factor of two is applied, the rate coefficients of all three reactions R2.2-R2.4 are equal, leading to the factor of two disappearing in eq 2.14. The subsequent eq 2.16 would become

$$R_p = \frac{^{37}\text{Cl}}{^{35}\text{Cl}} = \frac{r_{R2.2} + 2r_{R2.3}}{2r_{R2.4} + r_{R2.2}} = \frac{R_r + 2R_r^2}{2 + R_r} \quad (2.17)$$

which does not simplify down to  $R_r$  indicating some type of enrichment error is created. Since enrichment is defined as the ratio of sample to standard minus one,

the change in enrichment from including the error would just be a function of the standard enrichment,  $R_{std}$  and the original sample enrichment,  $R_r$ .

$$\delta_{products} - \delta_{reagents} = \frac{1}{R_{std}} \left( \frac{R_r + 2R_r^2}{2 + R_r} \right) - \frac{R_r}{R_{std}} = \frac{R_r^2 - R_r}{(2 + R_r) R_{std}} \quad (2.18)$$

Given a starting enrichment near the standard enrichment,  $R_r \approx R_{std}$ , eq 2.18 reduces to  $(R_{std} - 1) / (2 + R_{std})$ .

Though the example here uses chlorine, this equation can be applied to different atomic recombination reactions by using the corresponding  $R_{std}$ . For  $^{37}\text{Cl}/^{35}\text{Cl}$ ,  $^{13}\text{C}/^{12}\text{C}$ ,  $^{15}\text{N}/^{14}\text{N}$ , and  $^{34}\text{S}/^{32}\text{S}$  with  $R_{std}$  of 0.320, 0.0111,[63] 0.0037[64], and 0.045,[65] the enrichment errors from Pollak and Pechukas's doubling of the symmetry number are 293‰, 491‰, 497‰, and 467‰ respectively. These predicted enrichments are much larger than typically observed experimentally.[54]

This enrichment error is of similar magnitude to the 500‰ enrichments recently computed to occur in  $\text{S}_2 + \text{S}_2 \longrightarrow \text{S}_4$  and  $\text{S}_4 + \text{S}_4 \longrightarrow \text{S}_8$ .[66] This suggests that these very large enrichments[66] associated with the  $\text{X} + \text{X}$  reactions might arise from a factor of two mistake like that identified in this paper (though these reactions are more complicated than the simplistic examples presented here, as described in 2.4.3). We suspect that in reality the isotopic enrichment due to the reactions  $\text{S}_2 + \text{S}_2$  and  $\text{S}_4 + \text{S}_4$  is much smaller than the recently reported value.[66] This insight opens the field to investigate other explanations for the anomalous sulfur enrichment in Archean earth.

In addition to the errors caused by estimating reaction symmetry in Refs. 46 and 66, a similar factor of two error for  $\text{B} + \text{B}$  reactions can arise when doing kinetic Monte Carlo simulations if the conversion from bulk rate coefficients to probabilistic rate coefficients is not done correctly, as described below.

There are two ways to formulate the conversion from bulk kinetic rates to stochastic rates for  $\text{B} + \text{B}$  reactions, and both are internally consistent. However, if one is half implemented, then an erroneous factor of 2 would be created for rate constants.

This section describes the background and difference between the two methods of implementation. We first discuss how the  $A + B$  reaction was originally formulated by Gillespie, then describe how he implemented  $A + A$  reaction, and conclude with a valid alternative representation used in other work.

In the original Gillespie papers,[67, 68] he formulates the rate coefficient,  $c$ , for a stochastic reaction as the average probability that a unique combination will react in a given system per time. The total number of reactions over a given time  $dt$  in a volume  $V$  for a reaction with reactants  $A$  and  $B$  is  $ABcdt/V$ , given  $A$  and  $B$  are the number of reactants  $A$  and  $B$  respectively. For an ensemble of systems, the rate can then be described by the average,  $\langle AB \rangle cdt/V$ . Comparing this with the deterministic rate  $k\langle A \rangle \langle B \rangle dt/V^2$  yields the relationship  $k = Vc\langle AB \rangle / \langle A \rangle \langle B \rangle$ . At the deterministic limit, where  $\langle AB \rangle = \langle A \rangle \langle B \rangle$ ,  $c = k/V$ .[68, 67]

Gillespie discusses this framework for a  $B + B$  reaction. The stochastic description of reaction rate becomes  $(B(B - 1)/2!)cdt/V$ . The factor of 2 prevents the doubling counting of pairs of molecules. When the ensemble of stochastic rates is set equal to the deterministic rate coefficient, we get  $k\langle B \rangle^2/V^2 = \langle B(B - 1) \rangle cdt/2V$ . At the deterministic limit for a Poisson distribution, where  $\langle B \rangle^2 = \langle B(B - 1) \rangle$ , this comes out to  $c = 2k/V$ .[68]

One interesting thing to note about Gillespie's formulation is that the factor of 2 which is used in converting the  $k$  to  $c$  is then eliminated when going from  $c$  to the probability of reaction, with the addition of  $1/2$ . Some people have eliminated both factors entirely,[69] which is also a valid way of implementing kinetic Monte Carlo, though it changes Gillespie's definition of  $c$ .

If one were to only use the factor when determining  $c$  from  $k$  or when going from  $c$  to the reaction rate, the  $B + B$  reactions in that system would be off by a factor of 2, leading to errors similar to those discussed in this paper.

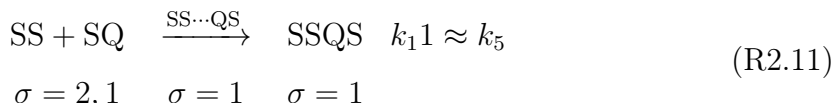
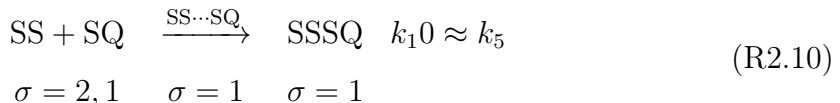
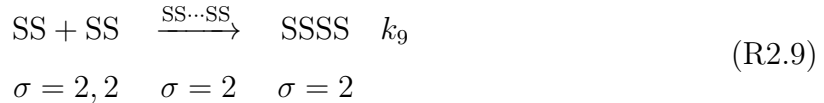
### **symmetry analysis of $S_2$ and $S_4$ self-reactions**

This section is intended for readers interested in more details about the causes of the apparent symmetry effect in a 2017 paper published in Proceedings of the National

Academy of Science,[66] which is referred to as ‘the PNAS paper’ in this section.

Symmetry effects on enrichment were noted in two reactions,  $\text{SS} + \text{SS} \longrightarrow \text{S}_4$  and  $\text{S}_4 + \text{S}_4 \longrightarrow \text{S}_8$ . Here we describe why we think these reactions should not cause nearly as much enrichment as originally proposed. In both of these reactions, we first represent  $\text{S}_4$  as the minimum energy acyclic form (i.e.,  $\text{C}_{2v}$  symmetry with  $\sigma = 2$ ), which is separated from another acyclic form by a small barrier as described in the PNAS paper. We then discuss the case for cyclic  $\text{S}_4$  and for a non-rigid  $\text{S}_4$  which can switch between different structures at room temperatures. We use S to represent the most abundant sulfur isotope and Q to represent any other sulfur isotope. Like the original work, we assume that there is a very low abundance of Q, so reactions between two molecules containing Q can be neglected.

**SS + SS  $\longrightarrow$  S<sub>4</sub>** The PNAS paper analyzes three reactions involving SS self-reaction, shown by Reactions R2.9 to R2.11 with symmetry numbers assigned based on the rigid and linear  $\text{S}_4$ . Here we analyze these three reactions using reaction symmetry described in Equation 2.2 of the main text and then compare with what the PNAS paper suggested.



Since there is a loss of symmetry in both a reactant and the transition state in the labeled Reactions R2.10 and R2.11 relative to Reaction R2.9, all three reactions have a reaction symmetry number of 2. Since heavy-atom kinetic isotope effects are small, the rate coefficients for all three reactions would be approximately equal, and no enrichment would be expected from symmetry, which corresponds to the relative

rates used in previous models, which the PNAS paper discusses.[70, 66]

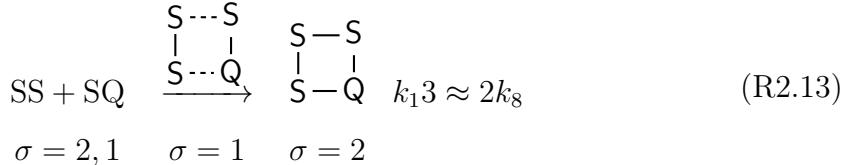
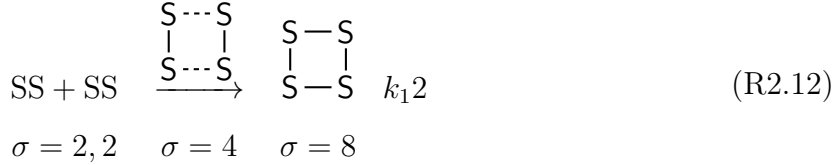
One hypothesis in the PNAS paper states that the rates of Reaction R2.9 should be twice of either Reaction R2.10 or Reaction R2.11 by arguing that metastable S<sub>4</sub> has all the conformational possibilities present in forming SSSQ and SSQS. This leads to counting both indistinguishable reaction pathways that form SSSS.[66] The sulfur system discussed in the PNAS paper is rather complicated and does not use exactly the same methods for estimating rate coefficients as discussed in the main text of this manuscript. However, it appears to us that the PNAS paper made a similar factor of 2 mistake as one would make if one used the Pollak and Pechukas method.[46] Our paper has shown that rearrangements which result in indistinguishable conformations do not lead to an increase in reaction symmetry number or a change in the final reaction rate. Since this rearrangement should not change the kinetics, the rate coefficient for formation of isotopically enriched SSSQ and SSQS should be equal to that of SSSS.

The PNAS paper also notes that S<sub>4</sub>, SSSQ, and SSQS are not rigid molecules, which can make the rigid rotor approximation for finding the symmetry number incorrect. Using this non-rigidity, the PNAS paper arrives at a hypothesis that the partition functions for S<sub>4</sub>, SSSQ, and SSQS are equal, which appears to result from a decrease in the symmetry of S<sub>4</sub>. Looking at this viewpoint from the perspective of reaction symmetry, we do not obtain the same result, and find our result consistent with previously reported rate coefficients.

Contrasting the argument in the PNAS paper, non-rigid molecules can still have symmetry.[57] If there is an effect of non-rigidity on molecular symmetry, it would likely increase the number of symmetry operations, as is the case with many non-rigid compounds like NH<sub>3</sub> and H<sub>2</sub>O<sub>2</sub>,[71] lowering the corresponding molecules' partition function. Using NH<sub>3</sub> as an example, NH<sub>3</sub>'s most stable form is non-planar, but since it can undergo low barrier inversion tunneling, it switches between its two non-planar forms by going through a planar transition. With this inversion tunneling, the symmetry properties of NH<sub>3</sub> become identical to that of the planar BF<sub>3</sub>,[71] increasing the number of symmetry operations. Similarly, S<sub>4</sub>'s most stable conformation is not cyclic, but it can interconvert between two forms through a cyclic transition. Counting

this non-rigid effect would likely give  $S_4$  the same symmetry operations available in its cyclic structure, increasing its symmetry number as well.

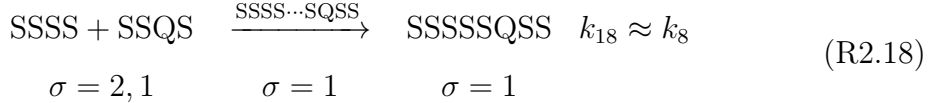
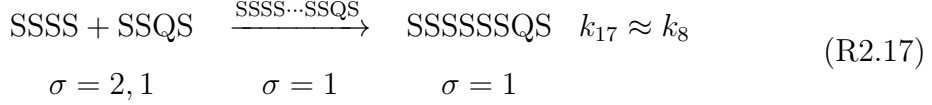
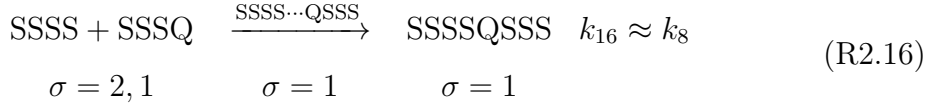
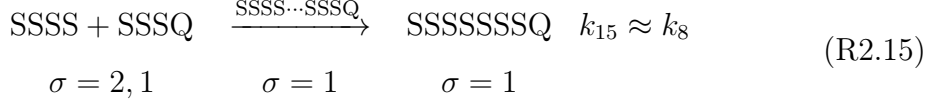
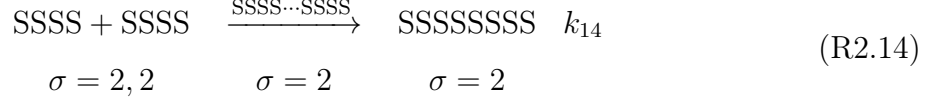
If we analyze  $S_4$  as non-rigid, using the similar analogy to  $NH_3$  (or equivalently analyze the direct cyclic formation, which creates the same effect),  $S_4$  would have a symmetry number of 8, and  $SSQS \longleftrightarrow SSSQ$ , which are no longer distinct species, would have a symmetry number of 2, with their corresponding transition states having symmetry numbers of 4 and 1 respectively. This would give the labeled reaction twice the rate constant of the unlabeled reaction, as shown by Reactions R2.12 and R2.13.



To compare with the rigid analysis, we can count  $SSQS$  and  $SSSQ$  as separate species by halving the combined species's partition function, halving the rate constant of Reaction R2.13, and creating a duplicate reaction forming the other structure, as is done in the PNAS paper. This would lead to three reactions with equal rate constants, which is the same as using the rigid structures in Reactions R2.9 to R2.11. Using this analysis in this instance, the rigid and non-rigid structures lead to the same relative rate constants since the non-rigidity proportionally increases the symmetry numbers of these three isotopologues.

**$S_4 + S_4 \longrightarrow S_8$**  For the set of reactions forming  $S_8$ , the PNAS paper uses three reactions,  $S_4 + S_4$ ,  $S_4 + SSSQ$  and  $S_4 + SSQS$ , and mentions that equal rate coefficients would correspond to no mass-independent fractionation.[66] Looking more deeply at this reaction may indicate more complexity. Instead of three reactions, we represent this system as a set of 5 elementary reactions which form a linear eight sulfur compound. The linear  $S_8$  compound, which has been well-characterized,[72] would

likely form before any ring closure occurs, so this would more accurately represent elementary kinetics. The set of five reactions are shown below.



Based on standard transition state theory used in other parts of this work, which results in no mass-independent fractionation, Reactions R2.14 to R2.18 should have equal rates.

If the set of five reactions is lumped into the three reactions used in the PNAS paper, the two reactions involving a non-abundant isotopes, SSSS + SSSQ and SSSS + SSQS, would have a rate coefficient twice that of the reaction with only  $^{32}\text{S}$  isotopes. Applying this difference in rate coefficients to Equation 14 in the PNAS paper[66] leads to no enrichment.

Overall, this section provides multiple perspectives which indicate that the large enrichments described in the PNAS paper may have been due to some factor of 2 mistake in estimating molecular symmetry leading to similar enrichment errors as found by our analysis of the method by Pollak and Pechukas.[46]

## 2.4.4 Non-isotopic impacts

In addition to isotopic studies, a factor of two error in rate coefficients of B + B reactions obtained from TST can create substantial changes in non-isotopic phenomena. This factor can alter major product concentrations by over 15% in pyrolysis simulations of hydrocarbons (shown in Section 2.4.4 of the Supporting Information). Even in the atmosphere, where many of the reactions have been quantified experimentally, detectable concentrations of large peroxy dimerization products,[73, 74] whose formation rate in models would typically be estimated using TST, indicates that including an extra factor of two could also impact estimation of how much a substance forms lower volatility products, affecting secondary organic aerosol formation.

### impact on ethane pyrolysis

Isotopic systems are not the only systems which could be affected by mistakes in rate coefficients. Large kinetic mechanisms, where many rate coefficients are estimated using symmetry numbers, could also have a substantial impact. To quantify the effect of doubling the rates of B + B reactions, the Reaction Mechanism Generator software package was used to create an ethane pyrolysis model with the specifications of the example ‘minimal’ included in the software package.[28] This model was used to simulate pyrolyzing a mixture of 10mol% ethane in helium at 1273 K and 2 bar for 0.1 seconds.

This model was then compared to one where each reaction involving identical reactants had the rate doubled. The difference in predicted production of methane is shown in Figure 2-2.

The model with the doubled rates produced 19% more methane than the standard model. This is caused by the methyl recombination reaction,  $\text{CH}_3 + \text{CH}_3 \rightleftharpoons \text{C}_2\text{H}_6$ , which had twice the rate of the control in both forward and reverse directions. Despite not having two identical reactants, the rate of reverse reaction ends up doubled since it is estimated from the forward rate and equilibrium constant in common chemical kinetic solvers like Chemkin and Cantera. The methyl radicals formed from ethane

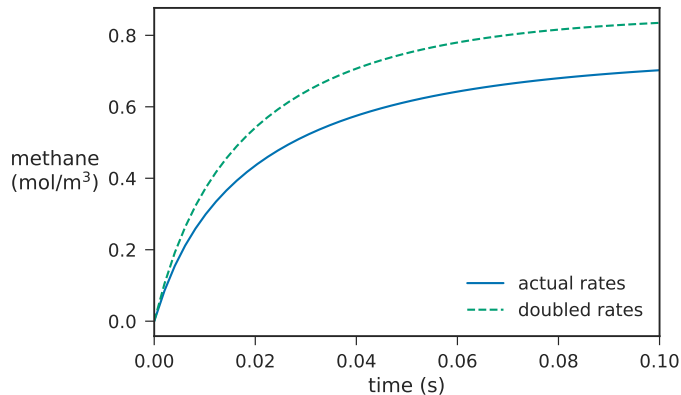


Figure 2-2: The difference in methane concentration between the original model and the one with doubled self-reaction rate coefficients.

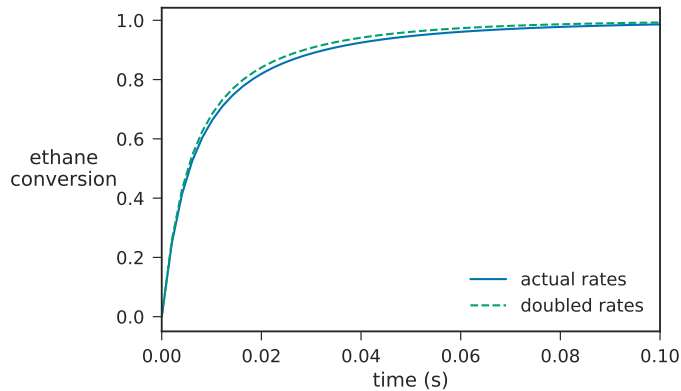


Figure 2-3: The difference in ethane conversion between the original model and the one with doubled self-reaction rate coefficients.

degradation then abstract a hydrogen from other molecules to form methane.

Since the model only had a few reactions involving two identical reactants, the change in other properties, like the overall ethane conversion, shown in Figure 2-3, is very minor.

## 2.5 Conclusion

The interchangeability of identical reactants, which justified doubling the reaction symmetry number in Ref. 46, is already accounted for when determining the reactant

concentrations.

Including a factor of two in reaction symmetry number for identical reactants causes thermodynamic inconsistency when applying transition state theory in both forward and reverse directions. Adding a factor of two in reaction symmetry number for reactions with identical reactants causes unphysical predicted isotopic enrichments well over 100‰ for many elements.

For B + B reactions, the rate calculation method of Ref. 46 is incorrect; the method of Ref 47 is correct.

The correct application of transition state theory, is applied later in Chapter 6. The next chapter continues to use transition state theory applying it to quantum calculations of isobutanol, an emerging biofuel.

# Chapter 3

## Pressure-dependent isobutanol kinetics

### 3.1 Summary

Bio-derived isobutanol has already been approved as a gasoline additive in the U.S., yet low-temperature O<sub>2</sub> dependence is currently incorrectly estimated in state-of-the-art detailed models. Better predicting its chemistry can help more accurately model the performance and environmental impact of using isobutanol fuels in various applications. This work examines 47 molecules and 38 reactions involved in the first oxygen addition to isobutanol's three alkyl radical. Quantum calculations were mostly done at CCSD(T)-F12/cc-pVTZ-F12//B3LYP/CBSB7, with 1-D hindered rotor corrections obtained at B3LYP/6-31g(d). The resulting potential energy surfaces are the most comprehensive isobutanol peroxy networks published to date. Canonical transition state theory and a 1-D microcanonical master equation are used to derive high pressure and pressure dependent rate coefficients, respectively. At all conditions studied,  $\alpha$ R + O<sub>2</sub> forms HO<sub>2</sub> and isobutaldehyde. The  $\gamma$ R + O<sub>2</sub> forms a stabilized hydroperoxy alkyl radical below 400 K and water and an alkoxy radical at higher temperatures, with HO<sub>2</sub> and alkene predicted above 1200 K. The  $\beta$ R + O<sub>2</sub> reaction results in a mixture of products between 700-1100 K, mostly undergoing the Waddington pathway (to form acetone, formaldehyde and OH) at lower temperatures

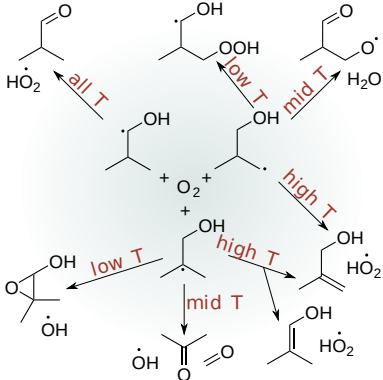


Figure 3-1: Main pathways found in this work of isobutanol radicals reacting with  $O_2$

and forming  $HO_2$  and alkenes at higher temperatures. The barrier heights, high pressure rates, and pressure dependent kinetics generally agree with previous quantum chemistry calculations. Larger differences exist when comparing to estimates derived from structure activity relationships in a detailed combustion mechanism, indicating a potential for the rates in this work to help improve detailed isobutanol combustion models.

## 3.2 Introduction

In June 2018, the U. S. Environmental Protection Agency approved the large scale blending of bio-derived isobutanol into gasoline at concentrations up to 16%,[75, 76] which multiple advantages over ethanol, such as lower volatility,[77] lower hydroscopicity,[78] and higher energy density,[77] and similar knock resistance.[79] Relative to larger alcohol additives, isobutanol shows longer ignition delay times with lower CO and  $NO_x$  emissions.[80] With this approval, isobutanol could become a major component of transportation fuel in the United States.

While extensive experimental testing was necessary prior to the approval,[78] detailed isobutanol combustion models are still inaccurate at engine-relevant conditions, indicating a gap in our understanding of isobutanol combustion. Detailed isobutanol mechanisms typically deviate more from experiments than do models of *n*-butanol, *tert*-butanol and *sec*-butanol.[81, 82] Multiple intermodel comparisons using detailed

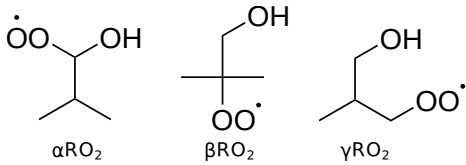


Figure 3-2: The three peroxy isomers derived from isobutanol correspond to the three sites for hydrogen abstraction from isobutanol.

isobutanol models have showed that at lean, low-temperature conditions the models had a wide range of ignition timing that deviated from experiments for both homogeneous charge compression ignition[83] and shock tube setups.[84] One mechanism by Merchant et al. deviates the most from experiments below 850 K and at fuel lean conditions, showing that the dependence on O<sub>2</sub> might be incorrectly accounted for.[19]

The inaccuracies in models all indicate a need for an improved understanding of isobutanol combustion in regions where peroxy radical chemistry is often important.[40] The dominant degradation pathway of peroxy radicals at various temperatures and pressures impacts overall ignition properties like the negative temperature coefficient region, where ignition slows with increasing temperature.

While several aspects of combustion chemistry have been studied in detail, such as the initial hydrogen abstraction by OH[85] and single carbon oxidation,[86] accurate pressure dependent kinetics of peroxy radicals formed in isobutanol combustion has not been fully developed nor incorporated into detailed models. This is in spite of some isobutanol studies showing that ignition delay is sensitive to peroxy radical reactions.[84, 82] Given the sensitivity of this fuel to equivalence ratio and pressure,[79] the formation and fate of peroxy radicals can significantly impact ignition timing and multi-stage heat release[40, 87]

Figure 3-2 shows the peroxy radicals studied in this work, which correspond to the three distinct hydrogen abstractions that isobutanol can undergo. For each of these isomers, various unimolecular reactions can occur, shown in Figure 3-3. The peroxy radicals (RO<sub>2</sub>) can isomerize through an intramolecular hydrogen abstraction with any hydrogen to form various alkyl hydroperoxide radicals (QOOH) or can unimolec-

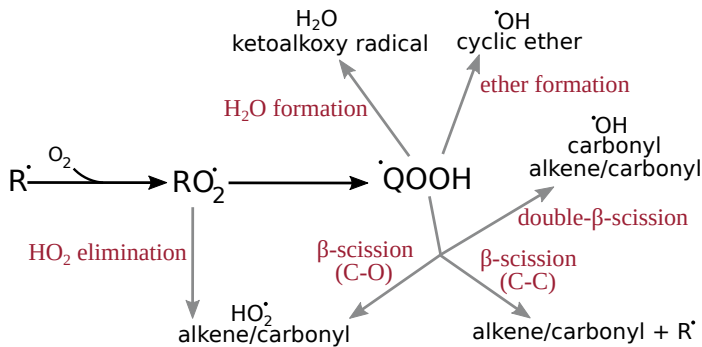


Figure 3-3: Unimolecular reaction pathways available for alcohol-based peroxy radicals.

ularly decompose to form  $\text{HO}_2$  and a double bond.  $\text{QOOH}$  can then decompose in multiple pathways, forming  $\text{H}_2\text{O}$  and an ketoalkoxy radical[88] or a cyclic ether and  $\text{OH}$ .  $\beta$ -scission reactions can occur, forming the same products as  $\text{HO}_2$  elimination (if a C-O bond breaks), an alkyl radical and double bond (if a C-C bond breaks), or an OH, carbonyl, and alkene/carbonyl (if both a C-O and C-C is broken).[89]

Previous quantum calculations of these important radicals have mostly focused on  $\beta\text{RO}_2$ , since it forms during OH initiated oxidation of isobutene. Sun et al. and Lizardo-Huerta et al. report high pressure rates obtained from CBSQ//B3LYP/6-31G(d,p) and CBS-QB3, respectively.[90, 91]

Similar work has not been conducted for the other two isomers,  $\alpha\text{RO}_2$  and  $\gamma\text{RO}_2$ , but relevant literature still exists. Zádor et al. have studied the fate of the  $\alpha$ -peroxy radical derived from ethanol, though the full surface of  $\alpha\text{RO}_2$  derived from isobutanol has not, to our knowledge, been evaluated.[92] Welz et al. calculated a potential energy surface for the  $\gamma\text{RO}_2$  isomer, but does not include reactions of all isomers nor reports reaction rates.

Given the errors for isobutanol models at low temperature and the lack of quantum calculations for the peroxy intermediate, we present thermodynamic and kinetic parameters for isomers, reactants, and products on the  $\alpha$ -,  $\beta$ -, and  $\gamma$ -isobutanol peroxy surfaces. Since there is potential for pressure-dependent kinetics to occur during isobutanol combustion,[93] both pressure-dependent and high pressure rate coefficients are reported. Comparison to other work and sensitivity analysis are conducted

to determine the robustness of the rates.

### 3.3 Methods

To quantify the rates of reaction of isobutanol peroxy radicals, we conducted quantum calculations of the lowest energy stable conformers and transition states and used those calculations in deriving rate coefficients with both transition state theory (TST) and the 1-D master equation.

#### 3.3.1 Quantum calculations

To efficiently obtain accurate rate coefficients necessary for our analysis, we conducted geometry optimization, hindered rotor scans, and frequency calculations with B3LYP/CBSB7 or BMK/6-31g(d) on Gaussian 03[94]. Energy was calculated with CCSD(T)-F12/cc-pVTZ-F12 using either Molpro 2012.1.21 or Molpro 2015.1.37, including scaling the triples energy to the ratio of correlation energies from F12 and MP2.[95] For each molecule and transition state, we first conducted a geometry optimization of an initial guess. Transition states were verified to have one imaginary frequency. Internal Reaction Coordinate (IRC) calculations were conducted at B3LYP/CBSB7 level theory and visualized to ensure the transition states correspond with the correct reactants and products (see SI for trajectories of each IRC calculation). For each rotatable dihedral, we calculated relaxed hindered rotor scans using 10 degree increments. In some cases where hindered rotor scans resulted in an unexpected reaction, hindered rotor scans were rerun with the fixed dihedral angles and bond lengths to prevent an undesired reaction from occurring. While most geometry, hindered rotor and frequency calculations used the B3LYP method, calculations for compounds with a hydroperoxy attached to the  $\alpha$  carbon used BMK because B3LYP had difficulty with these structures.

Energy calculations were done with the optimized geometry at CCSD(T)-F12/cc-pVTZ-F12, using the F12a corrected energy. Quantum outputs necessary to run thermodynamic and kinetic calculations are available in the supporting information

(SI).

Of the 85 calculations performed, three have a  $T_1$  diagnostic above 0.05, which corresponded to the three transition states involving isomerization from RO<sub>2</sub> to an alkoxy radical, and over a third had  $T_1$  diagnostic above 0.02, indicating that many of these structures likely have multireference character.[96] The  $D_1$  values alter a third of structures having a value greater than 0.1. The multireference potential in this work increase the uncertainties the final energies for structures with multireference potential to approximately 21 kJmol.[92]

### 3.3.2 Thermodynamic and kinetic calculations

For thermodynamic and kinetic parameters, this work used Arkane, which is freely available as part of the Reaction Mechanism Generator software suite.[28] Arkane calculated the partition function for each molecule and transition state using the rigid-rotor harmonic oscillator approximation with independent 1-D hindered rotor corrections. The data from the scans were fit using a Fourier series and separated from vibrations following Goldsmith et al.[97] In a few cases where relaxed scans broke hydrogen bonds but did not reform them during the scan and in which rigid scans were not accurate, the resulting Fourier fits gave unrealistic negative energies, so a cosine fit was used instead. Moments of inertia for each rotation was estimated using the lowest energy conformer geometry. Remaining vibrations were treated harmonically, and their frequencies were scaled by the recommended value of 0.975 for CCSD(T)/cc-pVTZ.[98] When applied for zero point energy corrections, the frequencies were divided by 1.014.[99]

Standard enthalpies, entropies and heat capacity were obtained from the partition function, with energy adjustments based on atoms, bonds, and zero point energies. These were fit over the range 10 to 3000 K using two NASA polynomials in the standard CHEMKIN II format.[233]

High pressure limit kinetics used canonical transition state theory with 1-D Eckart tunneling corrections. Twenty data points from 180 to 1500 K were fit to the modified Arrhenius form ( $k = AT^n \exp(-E_a/RT)$ ).

Pressure-dependent networks were constructed for  $\alpha$ ,  $\beta$ , and  $\gamma$  isobutanol radicals. Pressure-dependent rate coefficients for each network were obtained from a master equation solver at 20 temperatures from 180 K to 1500 K and 20 pressures from 0.01 bar to 100 bar. To get phenomenological rate coefficients, a method using reservoir state and pseudo-steady state approximations was applied due to its accuracy and robustness.[32, 100] Since Eckart tunneling was used in this work, the cutoff for the Boltzmann-distributed reservoir was taken when the transition state with the lowest barrier had a reaction rate that was 1% of the rate given at the transition states's energy with zero point corrections. This allows the barrier depth to be dependent on the amount of tunneling. The maximum energy separation was 2 kJ/mol with at least 200 grains. Lennard-Jones diffusivity parameters of  $\sigma = 4.64 \text{ \AA}$  and  $\epsilon = 318 \text{ cm}^{-1}$  were calculated using the 1-D minimization method with  $\gamma\text{RO}_2$  and  $\text{N}_2$  as a bath gas.[101] Collisional energy transfer parameters of  $\langle \Delta E_{down} \rangle = 250 \times (T/300 \text{ K})^{0.85} \text{ cm}^{-1}$  which has been used for a similar system of 2-butanol radicals in helium.[102]

For the three barrierless entrance channels of  $\text{R} + \text{O}_2$ , inverse Laplace transfer (ILT) of analagous reaction rates was used to obtain  $k(E)$  from  $k(T)$ .[32] For  $\alpha\text{R} + \text{O}_2$ , we used the high pressure rate of the analogous ethanol reaction,  $\text{CH}_3\text{CHOH} + \text{O}_2$ , from Zádor et al.[92] Rates for oxygen addition to  $\beta\text{R}$  and  $\gamma\text{R}$  came from the rate rules developed by Miyoshi for tertiary and primary additions, respectively.[103]

Arkane fit the rates at each temperature and pressure to Chebushev polynomials. Thermodynamic parameters, pressure dependent and high pressure limit rate coefficients are available in CHEMKIN II format in the SI.

### 3.3.3 Species and reaction naming

In total, this study involves 43 species and 42 reactions, so there is a need to develop a succinct and descriptive nomenclature. To ease discussion,  $\alpha$ ,  $\beta$ , and  $\gamma$  always refer to the carbon location relative to the alcohol group, even if multiple functional groups are present.

To this end, species can be grouped into three categories: common molecules, cyclic products, and path-specific molecules. Common molecules include products

which have easily recognizable names or formulas (such as acetone and H<sub>2</sub>O) or short functional group descriptors (such as *ibutaldehyde* and *npropen3ol*). Cyclic ethers are described by the number of substituents off of the ring, like *trisub\_epoxy* or *monosub\_c4ether*. The remaining compounds are typically network-specific isomers or multifunctional products, and are described with the Greek network letter, followed by a descriptor of the major functional groups, like  $\alpha R$  for the  $\alpha$ -alkyl radical,  $\beta RO_2$  for the  $\beta$ -peroxy radical, and  $\gamma QOOH\alpha$  for the compound with a hydroperoxide group located on one of the  $\gamma$  carbons and a radical site on the  $\alpha$  carbon. All compound names are listed next to their corresponding structure on the three networks in Figures 3-4, 3-7, and 3-11. Stable compound names are italicized throughout the text.

In contrast, reaction names are bolded. Each reaction starts with the Greek letter of the network to which it belongs. The next part describes either the type of reaction undergone (such as  **$\alpha QOOHIsom$**  for abstraction of an alpha hydrogen by the peroxy radical or **HO2Elim** for the formation of HO<sub>2</sub> as a product). If ambiguity exists in the reactant undergoing the reaction, the name will specify the reactant at the end of the name using the keyword ‘From’ (such as **FromRO2** to indicate the reactant is the peroxy radical or **From $\alpha$**  to indicate the reactant is the QOOH with a radical on the  $\alpha$ -carbon). One of the more complicated examples involves HO<sub>2</sub> elimination, four of which occur in the  $\beta$ -network alone.  **$\beta-\gamma HO2elimFromRO2$**  describes the HO<sub>2</sub> elimination from the  $\beta$ -peroxy radical which obtains the hydrogen from a  $\gamma$ -carbon (instead of from the  $\alpha$ -carbon, which is a separate reaction). All reaction names are listed on the potential energy surfaces in Figures 3-4, 3-7, and 3-11.

### 3.4 Results and Discussion

For each peroxy radical in Figure 3-2, reactions shown in Figure 3-3 were found. A QOOH was found for each unique abstractable hydrogen, and for each of these intermediates, the lowest energy  $\beta$ -scission reaction, cyclic ether formation, and, if available, water formation pathways were found. In total 38 transition states were obtained.

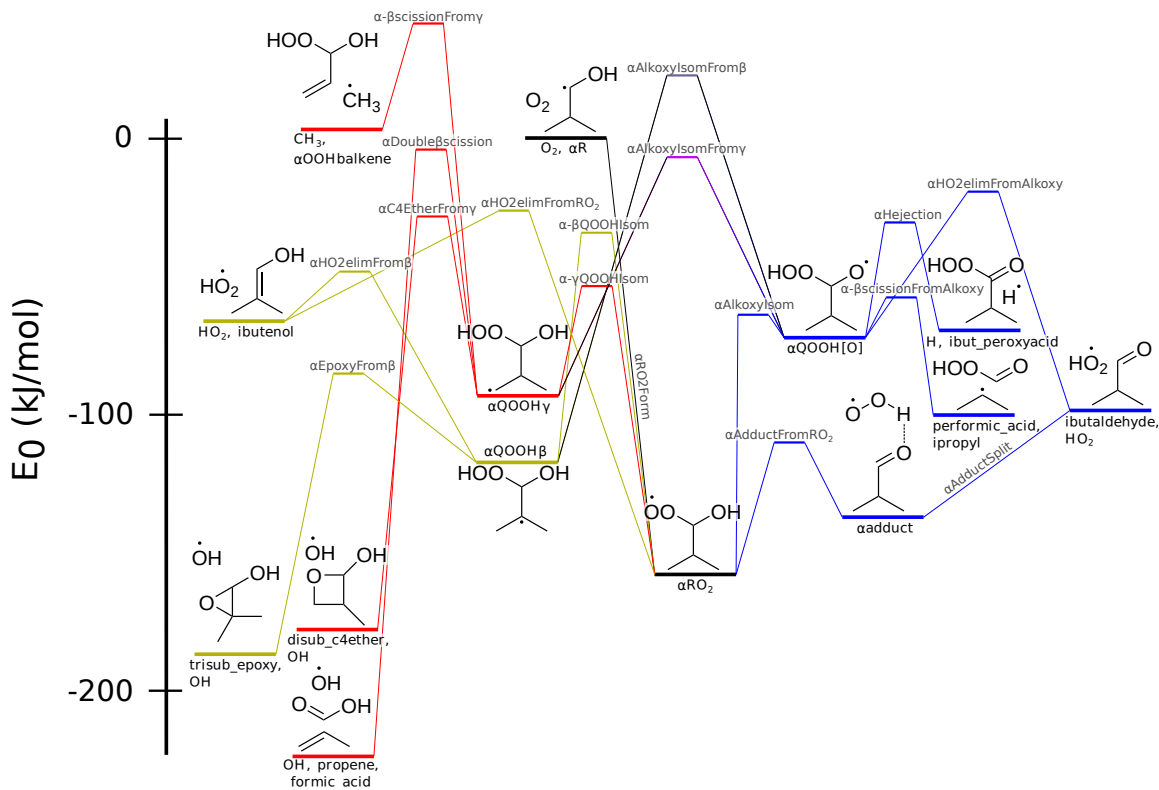


Figure 3-4: The potential energy surface for  $\alpha$ -peroxy radical, showing pathways involving  $\alpha\text{QOOH}\gamma$  (red),  $\alpha\text{QOOH}\beta$  (yellow) and  $\alpha\text{QOOH}[O]$  (blue). Energy includes zero point energy and atom corrections.

In the following sections we describe major results from each peroxy individually, showing potential energy surfaces, microcanonical rates, pressure dependent branching ratios, and comparisons to other quantum calculations. We then discuss the sensitivities of our results and compare the rates to detailed mechanisms.

### 3.4.1 $\alpha$ -peroxy network

The  $\alpha$ -peroxy network, shown in Figure 3-4, includes three intramolecular hydrogen abstraction reactions from the peroxy radical to form alkyl or alkoxy radicals. The lowest direct hydrogen abstraction involves the formation of the alkoxy product,  $\alpha\text{QOOH}[O]$ . Unlike the formation of  $\alpha\text{QOOH}\beta$  and  $\alpha\text{QOOH}\gamma$ , this does not require the breaking of a hydrogen bond, allowing for a lower barrier despite a higher ring strain and larger bond dissociation energy.[104] For the other hydrogen abstraction reactions, the six-membered transition to  $\alpha\text{QOOH}\gamma$  has a lower barrier than the five

member transition to  $\alpha QOOH\beta$ , due differences in ring strain.

This network also includes subsequent isomerization reactions,  **$\alpha AlkoxyIsomFrom\beta$**  and  **$\alpha AlkoxyIsomFrom\gamma$** , forming  $\alpha QOOH/O]$ . These subsequent isomerization reactions have even higher barriers than both the direct isomerization from  $\alpha RO_2$  ( **$\alpha AlkoxyIsom$** ) and the lowest energy decomposition pathways ( **$\alpha EpoxyFrom\beta$**  and  **$\alpha C4EtherFrom\gamma$** ). Due to the high barriers of these alkyl-based isomerizations, they were not calculated for the  $\beta$ - and  $\gamma$ -networks.

The products formed from the isomerizations,  $\alpha QOOH\beta$ ,  $\alpha QOOH\gamma$ , and  $\alpha QOOH/O]$ , each have a number of decomposition pathways. The alkoxy pathway has three  $\beta$ -scission reactions that break a bond connected to the  $\alpha$ -carbon. The  $\alpha QOOH\beta$  behaves similar to peroxy radicals from non-oxygenated fuels, with the formation of an epoxide (in this case *trisub\_epoxy*) and OH or an alkene (*ibutanol*) and  $HO_2$  as the main channels. The  $\alpha QOOH\gamma$  decomposition can undergo reactions  **$\alpha Double\beta\text{-scission}$** ,  **$\alpha C4EtherFrom\gamma$** , and  **$\alpha\beta\text{scissionFrom}\gamma$** . The last of these reactions has the highest barrier and forms a methyl radical and alkene. Since this reaction is unlikely to dominate at any realistic condition, reactions that form both alkenes and methyl radicals were excluded for the other peroxy networks. The other  $\beta$ -scission reaction involves the simultaneous breaking of two bonds, similar to the Waddington mechanism described for  $\beta$ -peroxy radicals,[89] but with a higher barrier.  **$\alpha C4EtherFrom\gamma$**  has the lowest decomposition barrier for  $\alpha QOOH\gamma$ , but it is still significantly higher than the decomposition reactions of  $\alpha QOOH\beta$  and  $\alpha QOOH/O]$ .

The lowest energy pathway in this network is not through the intramolecular H-abstraction paths discussed above. It comes from direct  $HO_2$  elimination of the peroxy. Since this forms a hydrogen bonded complex (*aadduct*) with an activation energy lower in energy than the separated products, the reaction is called  **$\alpha AdductFromRO2$** . The breaking of this hydrogen bond ( **$\alpha AdductSplit$** ) to form *ibutaldehyde* and  $HO_2$  was included in the master equation by using an inverse Laplace transform of the collision limit of the products  $HO_2$  and *ibutaldehyde*.[105, 32]

From the quantum calculations, we derived density of states and microcanonical rates, with selected microcanonical rates shown in Figure 3-5. The fastest isomeriza-

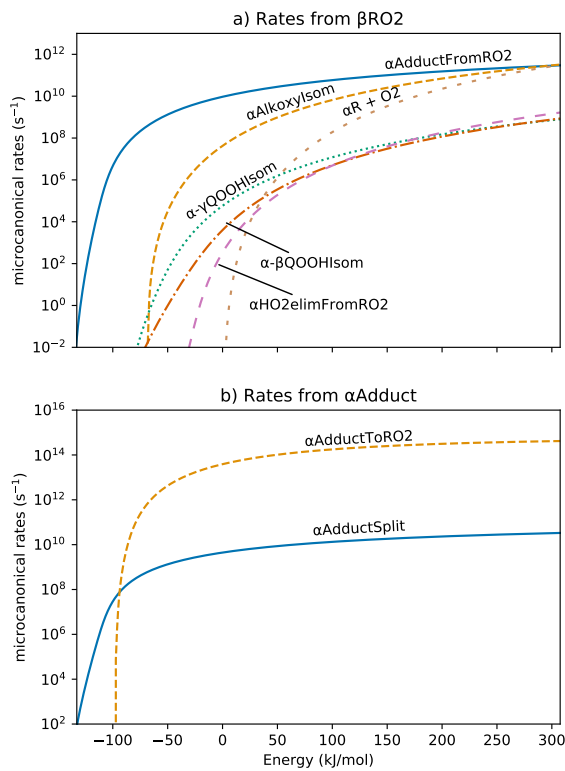


Figure 3-5: Microcanonical rates for all the reaction channels coming from (a)  $\alpha\text{RO}_2$  (b) and  $\alpha\text{Adduct}$ . The reaction names correspond to those in Figure 3-4, with  $\alpha\text{R} + \text{O}_2$  being the reverse of  $\alpha\text{RO2Form}$ , and  $\alpha\text{RO2Isom}$  being the reverse of  $\alpha\text{AdductForm}$ .

tion or product formation pathway for  $\alpha RO_2$ , shown in Figure 3-5a, is the formation of  $\alpha Adduct$  by at least an order of magnitude at all energy levels. For  $\alpha Adduct$ , shown in Figure 3-5b, most energies result in the decomposition breaking of the hydrogen bond to form  $HO_2$  and *ibutaldehyde*. Since this rate is based largely on the inverse Laplace transform for forming  $\alpha Adduct$  from  $HO_2$  and *ibutaldehyde* through micro-canonical equilibrium, the exact rate is highly uncertain. However, given the wide gap in Figure 3-5b, one or two orders of magnitude change in the  **$\alpha AdductSplit$**  rate will not shift the major product.

Figure 3-6a shows the major products from phenomenological rate coefficients. Under practically all conditions studied,  $\alpha R + O_2$  goes through well-skipping reaction to form  $HO_2$  and *ibutaldehyde*. Even the stabilized  $\alpha RO_2$  formed at low temperature and high pressure forms the same product or the hydrogen bonded adduct, as shown in Figure 3-6b. This result is consistent with isobutanol oxidation experiments between 500-700 K, which show *ibutaldehyde* as a major product.[106]

The main products,  $HO_2$  and *ibutaldehyde*, could also form by direct hydrogen abstraction of  $\alpha R$  by  $O_2$ , which was not studied in this work. However, based on the work of an analogous ethanol network by Zádor et al., this channel is unlikely to be important even at temperatures as high as 1000 K.[92]

The lack of intramolecular H-abstraction and second  $O_2$  addition prevents the chain branching pathway that accelerates low-temperature combustion. Since the  $\alpha R$  is predicted to be the dominant radical from isobutanol combustion,[19, 87, 85] a large negative temperature coefficient effect is not expected, which agrees with previous experiments that did not find a negative temperature coefficient region in isobutanol combustion.[82, 79]

### 3.4.2 $\beta$ -peroxy network

Figure 3-7 shows three isomerization reactions of  $\beta RO_2$  forming  $\beta QOOHa$ ,  $\beta QOOH\gamma$ , and  $\beta QOOH/O$ .  $\beta QOOH\gamma$  can undergo  $\beta$ -scission and cyclic ether formation.  $\beta QOOHa$  can undergo both of those pathways as well as a water formation path. The  $\beta$ -scission of the alkoxy radical,  $\beta QOOH/O$ , commonly referred to as the Waddington

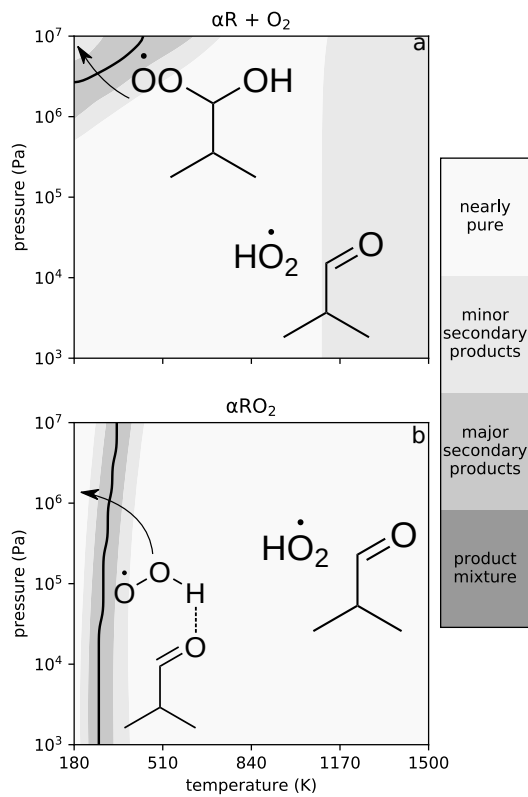


Figure 3-6: Major stabilized products for the reactions of  $\alpha R + O_2$  (a) and  $\alpha RO_2$  at various temperatures and pressures. Shading indicates the fraction going to the major pathway indicated, with cutoffs at 90%, 75%, and 40%.

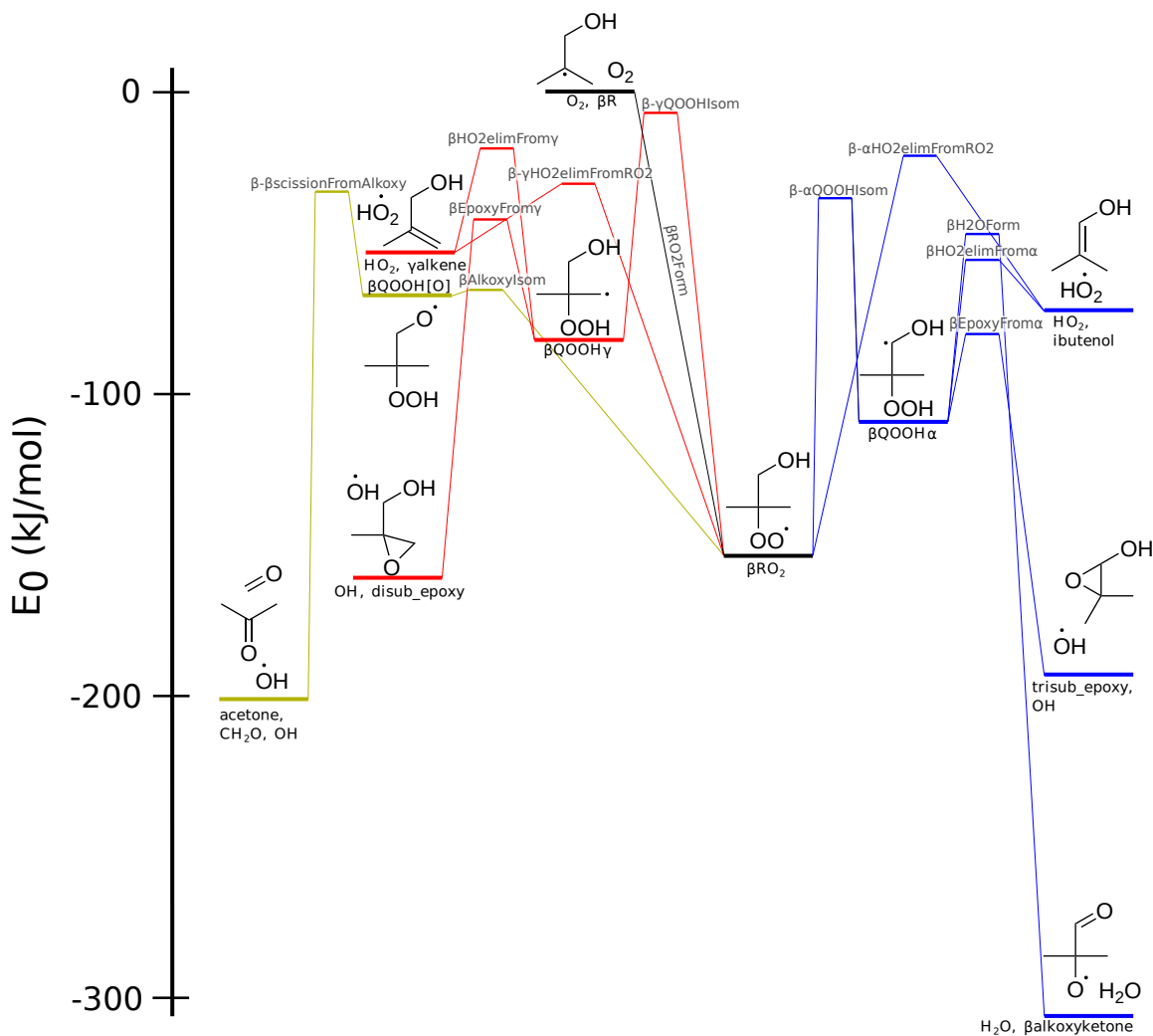


Figure 3-7: The potential energy surface for  $\beta$ -peroxy radical, showing pathways involving  $\beta\text{QOOH}\gamma$  (red),  $\beta\text{QOOH}\alpha$  (blue) and  $\beta\text{QOOH}[\text{O}]$  (yellow). Energy includes zero point energy and atom corrections.

mechanism,[89] is often the major sink of  $\beta RO_2$  radicals.[106, 90]

The microcanonical rates of the major intermediate are shown in Figure 3-8. Of all the pathways available to  $\beta RO_2$ , three pathways dominate at different energies. At the lowest energies (less than 65 kJ/mol),  **$\beta$ - $\alpha$ QOOHIsom** is the fastest reaction. After forming  $\beta QOOHa$  at this low energy, it will likely form *trisub\_epoxy* + *OH* through  **$\beta$ EpoxyFrom $\alpha$** , as shown in Figure 3-8c.

At moderate energies, the fastest rate for  $\beta RO_2$  is  **$\beta$ AlkoxyForm**. The rates of the alkoxy intermediate are given in Figure 3-8b. The reverse reaction for  $\beta QOOH/O$  reforming  $\beta RO_2$  is favored at most energies and the  **$\beta$ - $\beta$ FromAlkoxy** is favored only at high energies. The strong reversibility of the alkoxy isomerization allows for other secondary pathways to also form products.

The reverse reaction rate forming  $\beta RO_2$  in Figure 3-8b is nonmonotonic, decreasing at higher energies. This is because the zero point corrected energies of  $\beta QOOH/O$  and  **$\beta$ RO2Isom** are similar (differing by only 2 kJ/mol) and because  $\beta QOOH/O$  has more freedom of motion than  **$\beta$ RO2Isom**. This causes the ratio of density of states between transition state and reactant to reach a peak around -60 kJ/mol and then decrease.

At high energies, the direct formation of various alkenes and  $HO_2$  is predicted to dominate through both  **$\beta$ - $\alpha$ HO2ElimFromRO2** and  **$\beta$ - $\gamma$ HO2ElimFromRO2**. At these high-energy conditions, the reverse reaction is strongly favored.

The pressure-dependent products of  $\beta R + O_2$  in Figure 3-9a show that the two  $HO_2$  pathways become dominant at higher temperatures, with the Waddington pathway occurring at moderate temperatures and low pressures, though it is a substantial minor path at higher pressures. Stabilized  $\beta RO_2$  forms at the moderate and lower temperatures.

The products of a stabilized  $\beta RO_2$ , shown in Figure 3-9b look quite different than for the entrance channel due to lower available energy. For one, the formation of epoxides, which Figure 3-8 shows require low energies, only forms in substantial amounts from stabilized  $\beta RO_2$  and at low temperatures. While epoxides have not been observed in isobutanol oxidation,[106] most studies have focused mostly on temperatures

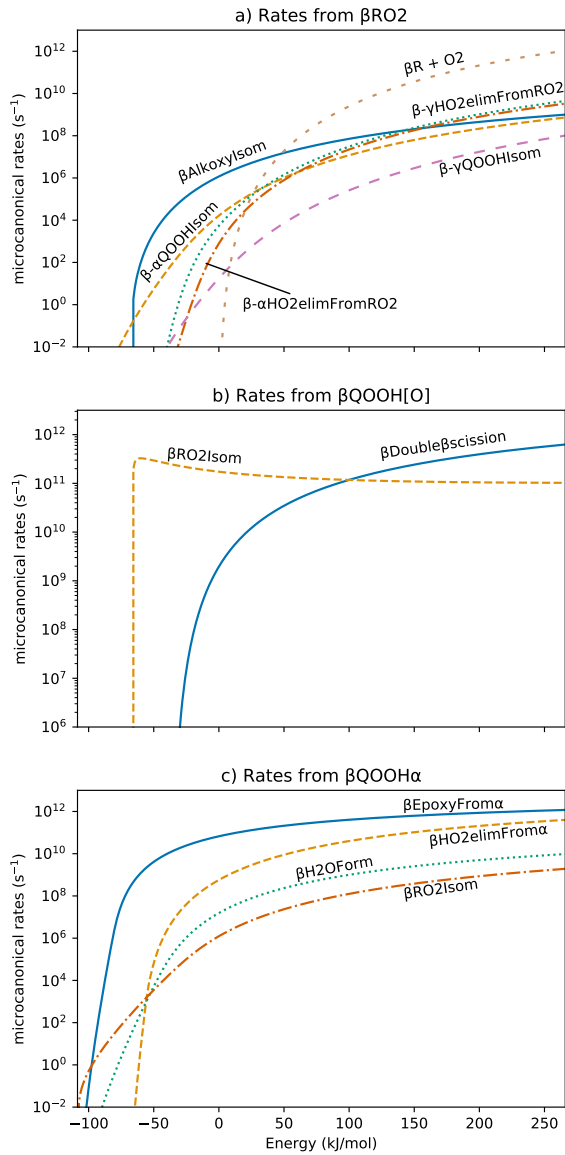


Figure 3-8: Microcanonical rates for all the reaction channels coming from (a)  $\beta RO_2$ , (b)  $\beta QOOH[O]$ , and (c)  $\beta QOOH\alpha$ . The reaction names correspond to those in Figure 3-7, with  $\beta R + O_2$  being the reverse of  $\beta RO_2 Form$ , and  $\beta RO_2 Isom$  being the reverse of  $\beta AlkoxyIsom$  (for subplot b) and  $\beta-\alpha QOOHIsom$  (for subplot c).

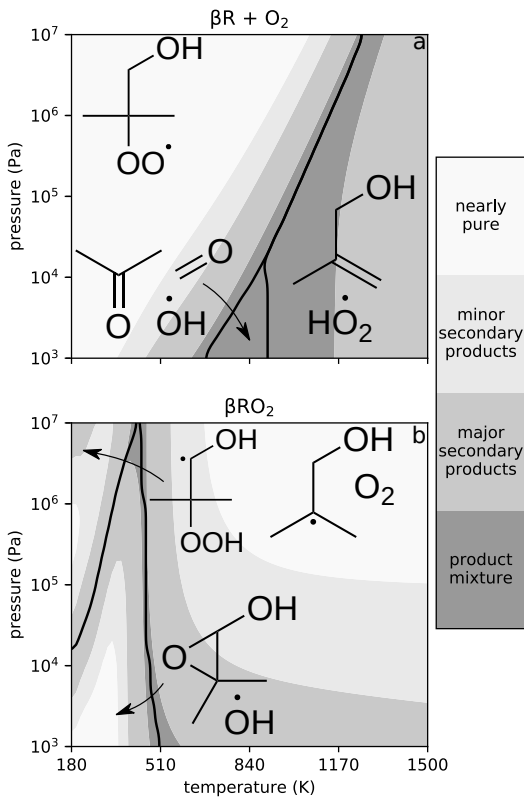


Figure 3-9: Major stabilized products for the reactions of  $\beta R + O_2$  (a) and  $\beta RO_2$  at various temperatures and pressures. Shading indicates the fraction going to the major pathway indicated, with cutoffs at 90%, 75%, and 40%.

higher than 500 K.

Though stabilized  $\beta RO_2$  is unlikely to form at higher temperatures (so the right side of Figure 3-9b is unlikely to occur in nature), the breakdown of major products provides insight into pressure-dependent effects. At high temperatures and pressures, where the high end of the Boltzmann energy distribution can be replenished quickly, the higher-barrier formation of  $\beta R + O_2$  dominates. At lower pressures, with slower energy transfer, lower-energy pathways start to matter, with the Waddington pathway occurring at intermediate pressures and the well-skipping reactions  $\beta\text{-}\alpha QOOH\text{Isom}$  followed by  $\beta\text{EpoxyFrom}\alpha$ . Since lower temperatures also reduce the higher end of the Boltzmann distribution, we also see lower temperatures giving way to lower energy pathways, with the stabilized  $\beta QOOH\alpha$  forming at sub-atmospheric temperatures. The lack of QOOH radicals at atmospheric or combustion relevant temperatures, also prevents the  $\beta$ -network from contributing to two stage ignition.

### Comparison with previous results

More extensive calculations have been conducted for the  $\beta RO_2$  surface than for the other two isomers because  $\beta R$  can also form from OH addition to isobutene.[90, 91] Two quantum studies compared with this work include all the same reactions except they for  $\beta\text{H2OForm}$ .[88]

The barrier heights in this work generally agree with those previously published with a few slight differences, shown in Table 3.1.[90, 91] For  $\beta\text{EpoxyFrom}\gamma$ , the reaction barrier was 5 kJ/mol and 15 kJ/mol lower than the barriers in Lizardo-Huerta et al. and Sun et al., respectively. This may be due to the presence of hydrogen bonding in the conformers in this work and that of Lizardo-Huerta et al. but not in Sun et al.[90, 91] For  $\beta\text{-}\gamma HO2\text{elimFrom}RO2$ , the barrier in this work is 10 kJ/mol lower than the rate by Sun et al., but only 3 kJ/mol off from the barrier in Lizardo-Huerta et al. The barrier for  $\beta HO2\text{elimFrom}\alpha$  fell between the two studies' barrier heights. The calculated barriers for the rest of the reactions fell within 8 kJ/mol of those in other studies.

The high-pressure rates in this network can be compared to those presented in

Table 3.1: Reaction barriers at 0 K of reactions in the  $\beta$ -network (kJ/mol) in this work and other published works.

reaction	this work	Sun et al.[90]	Lizardo-Huerta et al.[91]
$\beta\text{-}\gamma\text{QOOHIsom}$	147	149	149
$\beta\text{EpoxyFrom}\alpha$	29	21	35
$\beta\text{EpoxyFrom}\gamma$	40	55	45
$\beta\text{HO2elimFrom}\gamma$	64	63	62
$\beta\text{-}\gamma\text{HO2elimFromRO2}$	124	134	127
$\beta\text{-}\alpha\text{HO2elimFromRO2}$	133	134	136
$\beta\text{HO2elimFrom}\alpha$	54	49	66
$\beta\text{-}\alpha\text{QOOHIsom}$	119	120	116
$\beta\text{AlkoxyIsom}$	89	92	94
$\beta\text{-}\beta\text{scissionFromAlkoxy}$	35	38	28

Sun et al. and Lizardo-Huerta et al.[90, 91] Nine out of the ten rates in Lizardo-Huerta et al. come within one order of magnitude with the rates in this work over the temperature range 500-1000 K, indicating good agreement. For the rate coefficients by Sun et al. over the same temperature range, the rates were shifted slower, with our results being approximately 25 times faster than those in Sun et al.

The major pressure-dependent pathways, shown in Figure 3-9, show general agreement with the conclusions drawn in Sun et al., though show more alkene formation. The products from  $\beta R + O_2$ , both show stabilized  $\beta RO_2$  forming at higher pressures and temperatures, with the switching of major pathway at around the same pressure at 1000 K. With lower pressures at 1000 K, we predict forming alkenes will occur faster than Waddington reaction, whereas Sun et al. finds the Waddington pathway more dominant than alkene formation. Other major products in this work include *ibutanol* and *trisub\_epoxy*, which Sun et al. also found as large secondary pathways.[90]

For the reactions of stabilized  $\beta RO_2$ , this work and that of Sun et al. find the reaction forming  $\beta R + O_2$  to dominate for all pressures at 800 K. For lower pressures at 800 K, this work and that of Sun et al. predict the main secondary channel to be the Waddington pathway.[90] Though at high pressures, Sun et al. found  $\beta QOOH/O$  formation to be the main secondary channel where this work found it to be one of the slower pathways. This difference could have arisen from the approximations to get

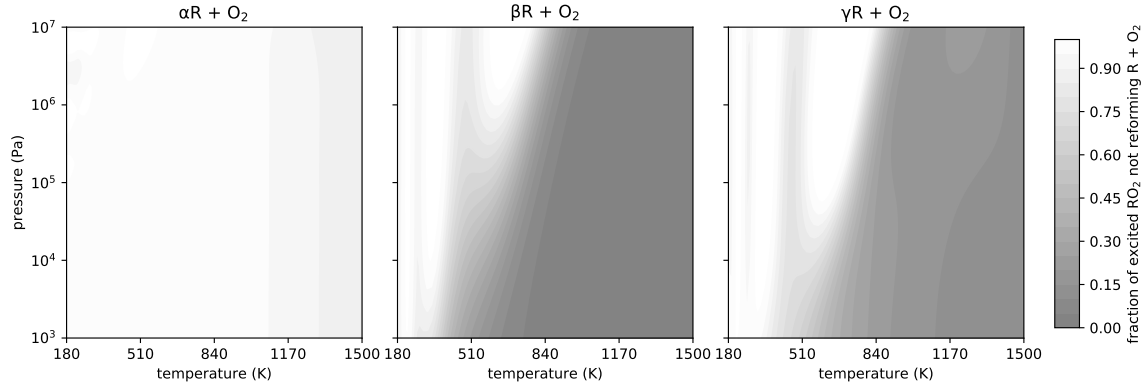


Figure 3-10: The fraction of excited  $\text{RO}_2$  that go back to form  $\text{R} + \text{O}_2$  for the three surfaces at various temperatures and pressures. Periodic behavior at lower temperatures and high fractions of reaction are likely artifacts created from the sum of all the fitted pressure-dependent rates not perfectly fitting to the high pressure Arrhenius rate.

phenomenological rates. Using modified strong collision in this work, see Figure 3-16 in the SI, predicts more formation of  $\beta\text{QOOH}/\text{O}_2$ , than the reservoir state method in Figure 3-9.

The reactions shown in Figure 3-9 do not explicitly include the non-reaction path, in which excited  $\beta\text{RO}_2$  reforms  $\beta\text{R}$  and  $\text{O}_2$  (though this is taken into account implicitly by an overall decrease in reaction rate). This non-reaction can be important when determining how much of  $\beta\text{R}$  will  $\beta$ -scission to form *isobutene* instead of adding  $\text{O}_2$ , which the model by Merchant et al. had trouble accurately predicting.[19] Figure 3-10 in the SI shows the fraction of excited  $\beta\text{RO}_2$  which reverses back to the  $\beta\text{R}$ . For the  $\beta$ -network at high temperatures, over 95% of excited  $\beta\text{RO}_2$  reforms  $\beta\text{R} + \text{O}_2$ , which agrees with the results in Sun et al.[90]

Given the small region showing the formation of *acetone*,  $\text{CH}_2\text{O}$ , and  $\text{OH}$  in Figure 3-9a, it may seem like this work does not predict the Waddington pathway as much as seen in experiments.[107, 106] This is due to sensitivity in the kinetic rates and the masking of secondary products in the figure. The fraction going to this path is highly dependent on the barrier heights. A sensitivity study raising the barrier of  $\beta\text{-}\gamma\text{HO2FromRO2}$  by 10 kJ/mol, to correspond to that of Sun et al., dramatically increased where the Waddington pathway was the most dominant pathway, shown in

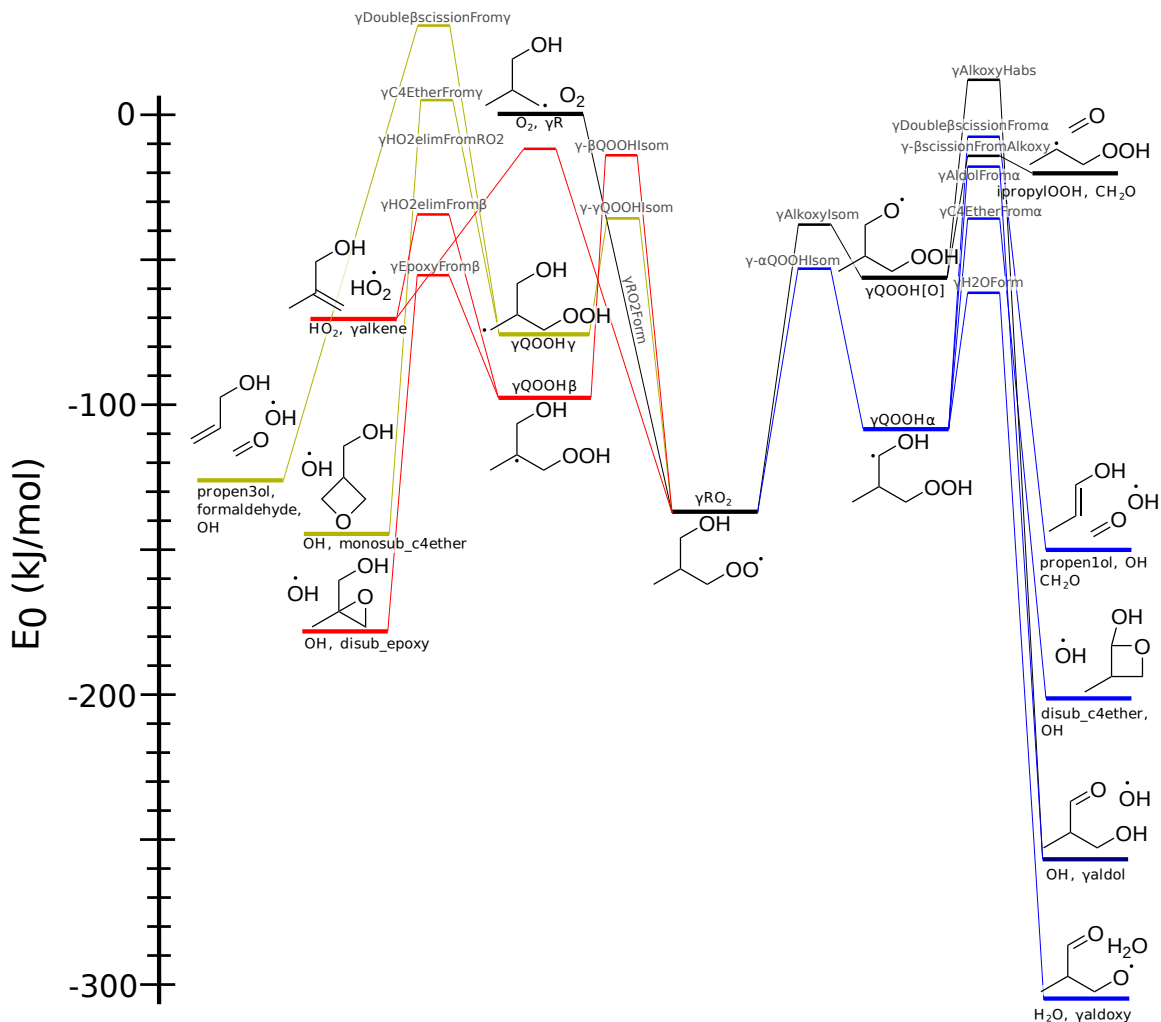


Figure 3-11: The potential energy surface for the  $\gamma$ -peroxy radical. Energy includes zero point energy and atom corrections. Species name and structures appear in black near the structure energy level. Reaction names appear in gray above the transition state energy.

Figure 3-14. In addition, in the region around 800 K and 50 bar, where  $\beta R + O_2$  and stabilized  $\beta RO_2$  are essentially reversible, the major secondary pathway is the Waddington path.

### 3.4.3 $\gamma$ -peroxy network

As shown in Figure 3-11,  $\gamma RO_2$  has four isomerization reactions and a direct path to form  $HO_2$ . The lowest energy isomerization involves a 6-member transition state to form  $\gamma QOOHa$ , which can decompose via a number of pathways:  **$\gamma$ Double $\beta$ scissionFrom $\alpha$** ,

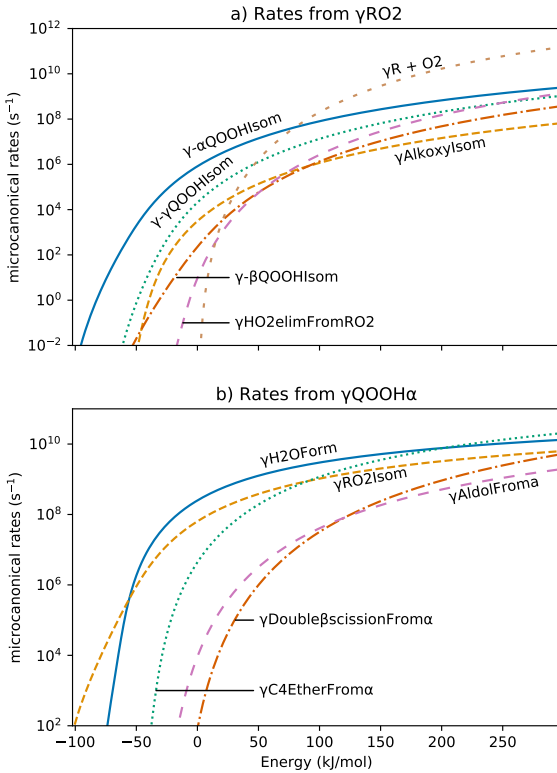


Figure 3-12: Microcanonical rates for all the reaction channels coming from (a)  $\gamma RO_2$  and (b)  $\gamma QOOH\alpha$ . The reaction names correspond to those in Figure 3-7, with  $\gamma R + O_2$  being the reverse of  $\gamma RO2Form$ , and  $\gamma RO2Isom$  being the reverse of  $\gamma\text{-}\alpha QOOHIsom$ .

### $\gamma AldolFrom\alpha$ , $\gamma C4EtherFrom\alpha$ , and $\gamma H2OForm$ .

The other isomerizations are less important. Despite only slightly higher energy requirements to form,  $\gamma QOOH\alpha$  and  $\gamma QOOH/O$ 's decomposition pathways all have high barriers, making them unlikely to be important at many conditions. The isomerization with the highest barrier,  $\gamma\text{-}\beta QOOHIsom$ , it has lower energy decomposition paths forming either an alkene or a cyclic ether. The direct HO<sub>2</sub> elimination pathway from  $\gamma RO_2$  has a similar barrier to  $\gamma\text{-}\beta QOOHIsom$ .

Figure 3-12 shows the microcanonical rates for relevant intermediates. For  $\gamma RO_2$ , the  $\gamma\text{-}\alpha QOOHIsom$  pathway is dominant at the lower energies and is only taken over by the rate to reform  $\gamma R + O_2$  at higher energies. At high energies other product channels such as  $\gamma\text{-}\gamma QOOHIsom$  and  $\gamma HO_2\text{ElimFromRO2}$  also have significant rates.

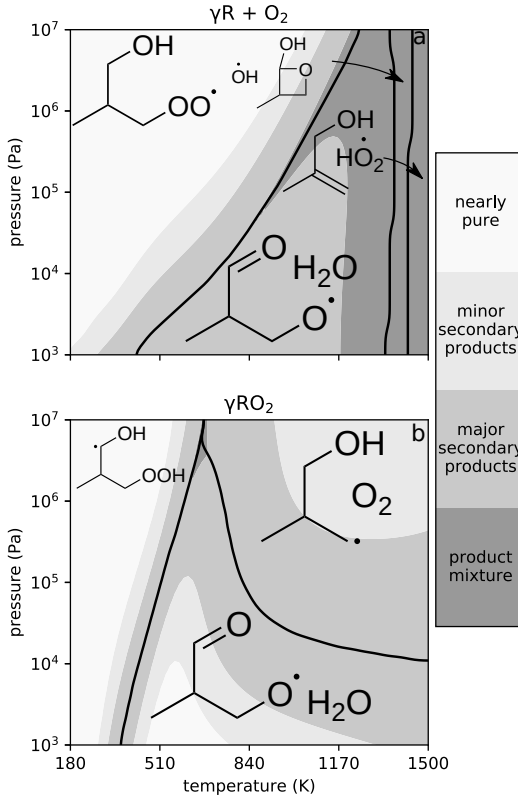


Figure 3-13: Major stabilized products for the reactions of  $\gamma R + O_2$  (a) and  $\gamma RO_2$  (b) at various temperatures and pressures. Shading indicates the fraction going to the major pathway indicated, with cutoffs at 90%, 75%, and 40%.

At the lowest energies shown in Figure 3-12b,  $\gamma QOOHa$  will reform  $\gamma RO_2$ , though this is taken over at slightly higher energies by  **$\gamma H2OForm$** . At the highest energies, many reactions can effectively compete, as was the case for the microcanonical rates of  $\gamma RO_2$ .

The large number of potential pathways at high energies can be seen in Figure 3-13a, with a mixture of  $HO_2 + \gamma alkene$ ,  $CH_2O + OH + propene1ol$ , and  $OH + disub\_c4ether$  at higher temperature. Between 800-1100 K, the dominant product is  $H_2O + \gamma aldoxy$ , which agrees with Welz et al.[88] Below 600 K, the major product is stabilized  $\gamma RO_2$ .

Stabilized  $\gamma RO_2$  starts with much lower internal energy, which prohibits the higher energy reactions that occur for the entrance channel  $\gamma R + O_2$ . At the lowest temperatures simulated stabilized  $\gamma QOOHa$  radical is formed. Above 400 K, well-skipping water formation is the major pathway. At high temperatures and pressures,  $\gamma R +$

$O_2$  is the dominant pathway.

Relative to the other two networks, the  $\gamma$ -network is most likely to produce a stabilized QOOH radical. Reaction rate comparisons using the unimolecular high pressure reaction rates of  $\gamma QOOHa$  in this work and bimolecular oxygen addition and H-abstraction by oxygen taken from Sarathy et al.[87] found that  $\gamma QOOHa$  reacts almost entirely through bimolecular H-abstraction channel in air, forming  $HO_2$  and a ketohydroperoxide, over the range of conditions in this study. If the subsequent peroxide bond breaks, following reactions similar to alkane-derived ketohydroperoxides,[40] it is possible to get one  $HO_2$  and two OH radicals from a single initiation, which could create a negative temperature coefficient region. However, since  $\gamma QOOHa$  forms only below 500 K, it is unlikely to impact combustion significantly.

## Literature comparison

With regards to which reactions are included, this work included almost all the reactions of Welz et al. and added on decomposition pathways for the other isomers:  $\gamma QOOH[O]$ ,  $\gamma QOOH\gamma$ , and  $\gamma QOOH\beta$ .[88] Instead of a direct path from  $\gamma RO_2$  to  $\gamma aldol + OH$  in Welz et al., we found a transition state from  $\gamma QOOH[O]$  to form  $\gamma aldol$  and  $OH$ . This reaction, named  **$\gamma$ AldolForm**, involves a hydrogen abstraction of the  $\alpha$ -hydrogen with a simultaneous breaking of the O-O bond.

Table 3.2 shows the barrier height differences between this work and that of Welz et al. Decent agreement, within 8 kJ/mol, occurs for all but three reactions. We report barrier heights for  **$\gamma$ AlkoxyIsom** to be 20 kJ/mol lower and that of  **$\gamma$ AldolFrom $\alpha$**  to be 20 kJ/mol higher than those in Welz et al. The barrier for  **$\gamma$ C4EtherFrom $\alpha$**  was calculated to be 12 kJ/mol higher than Welz et al. A smaller difference of 6 kJ/mol occurs for  **$\gamma$ H2OForm**, the dominant pathway at most conditions. These differences may be due to different level of theories, possibly amplified by multireference effects. Using the barriers given by Welz for the  **$\gamma$ H2OForm** reactions does not lead to significant shifts in product distribution (see Figure 3-14 in the SI).

Table 3.2: Reaction barriers at 0 K of reactions in the  $\gamma\text{RO}_2$  network (kJ/mol), compared to CBS-QB3 calculations by Welz et al.[88]

reaction	this work	Welz et al.[106]
$\gamma\text{AlkoxyIsom}$	99	123
$\gamma\text{-}\alpha\text{QOOHIsom}$	84	85
$\gamma\text{-}\gamma\text{QOOHIsom}$	102	99
$\gamma\text{-}\beta\text{QOOHIsom}$	124	127
$\gamma\text{HO}_2\text{elimFromRO2}$	126	133
$\gamma\text{H2OForm}$	47	41
$\gamma\text{C4EtherFrom}\alpha$	73	61
$\gamma\text{Double}\beta\text{scissionFrom}\alpha$	102	94
$\gamma\text{AldolFrom}\alpha$	91	69

### 3.4.4 Pressure-dependent sensitivity analysis

To test the robustness of the pressure-dependent results, various sensitivity studies were conducted. To investigate sensitivity to barrier heights, one important barrier in each network was adjusted, shown in Figure 3-14 in the SI. With the  **$\alpha\text{AdductFromRO2}$**  barrier height increased 13 kJ/mol, the  $\alpha$ -network still forms entirely  $\text{HO}_2$  and *ibut-aldehyde*. With a 10 kJ/mol barrier increase to  **$\beta\text{-}\gamma\text{HO}_2\text{elimFromRO2}$**  corresponding to that of Sun et al., the branching ratio of the Waddington pathway increased noticeably. At higher temperatures, the other  $\text{HO}_2$  elimination pathway, forming ibutenol, becomes the major product. Decreasing the barrier height of  **$\gamma\text{H2OForm}$**  by 6 kJ/mol to that given by Welz et al. shifts the system to form more of that product, but this is much less significant than the changes in the  $\beta$ -network. Overall, while some changes resulted from changing barrier heights, there were no significant shifts in product distributions, indicating that the differences in barriers in this work and that of others might not significantly change product distributions.

Sensitivity to the collisional energy transfer was tested by decreasing the average energy transferred by collision by a factor of two, shown in Figure 3-15. Very little differences resulted from this change, leaving Figure 3-15 to look very much like data in Figures 3-6, 3-9, and 3-13, indicating the system is not very sensitive to this parameter.

To see if there is any dependence on the approximations used for obtaining phe-

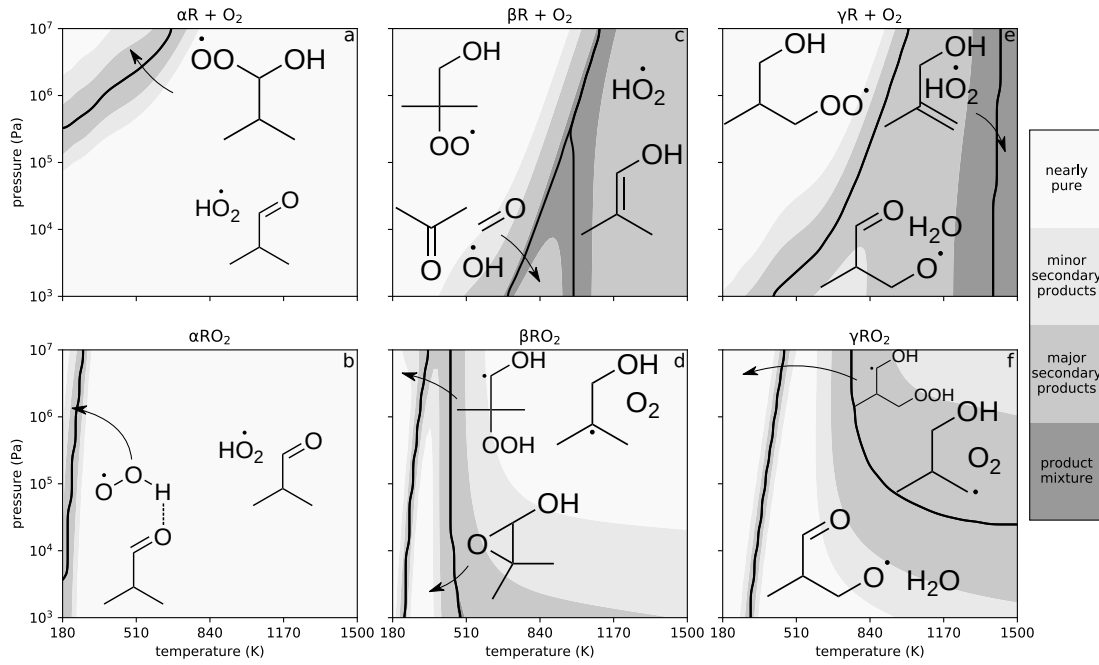


Figure 3-14: To observe sensitivity to barrier heights,  $\alpha$ **AdductFromRO2** was increased by 13 kJ/mol,  $\beta$ - $\gamma$ **HO2elimFromRO2** was increased by 10 kJ/mol (corresponding to the barrier height in Sun et al.), and  $\gamma$ **H2OForm** was decreased by 6 kJ/mol (corresponding to the barrier height in Welz et al.).[88] The major products formed and branching ratio of alkyl + O<sub>2</sub> reactions and peroxy reactions for the  $\alpha$ ,  $\beta$ , and  $\gamma$  networks at various temperatures and pressures. The structures indicate the major product from the reaction. Shading indicates the fraction going to the major pathway indicated, with cutoffs at 90%, 75%, and 40%. Text gives a qualitative description to the different colors.

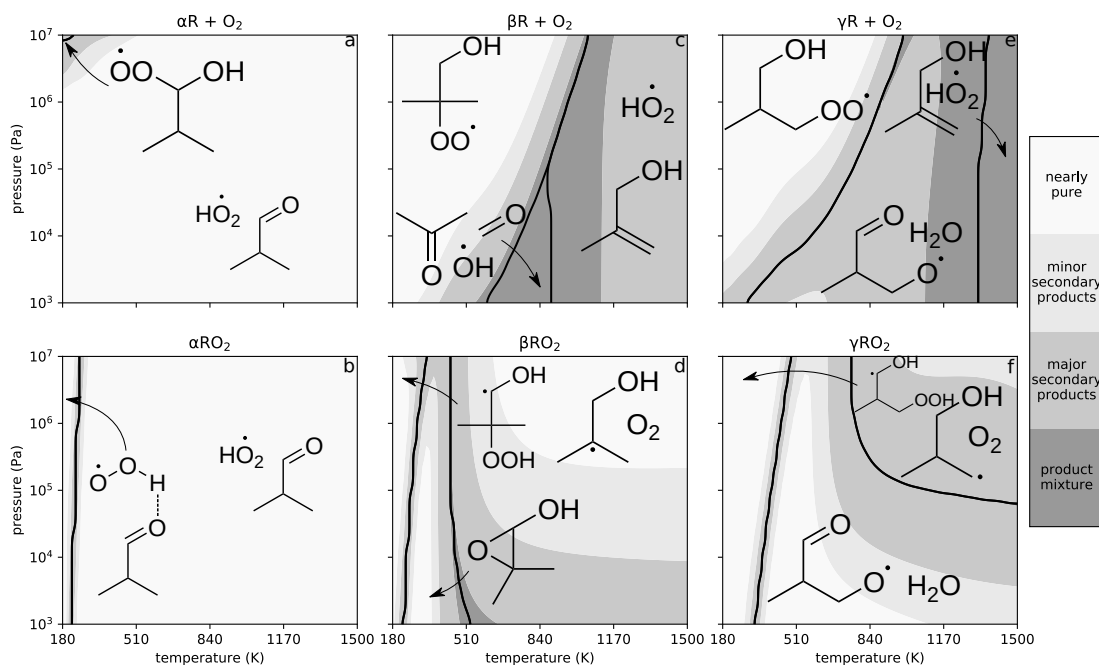


Figure 3-15: To observe sensitivity to the collisional energy, the collisional energy transfer of all isomers was decreased by a factor of two. The major products formed and branching ratio of alkyl +  $O_2$  reactions and peroxy reactions for the  $\alpha$ ,  $\beta$ , and  $\gamma$  networks at various temperatures and pressures. The structures indicate the major product from the reaction. Shading indicates the fraction going to the major pathway indicated, with cutoffs at 90%, 75%, and 40%. Text gives a qualitative description to the different colors.

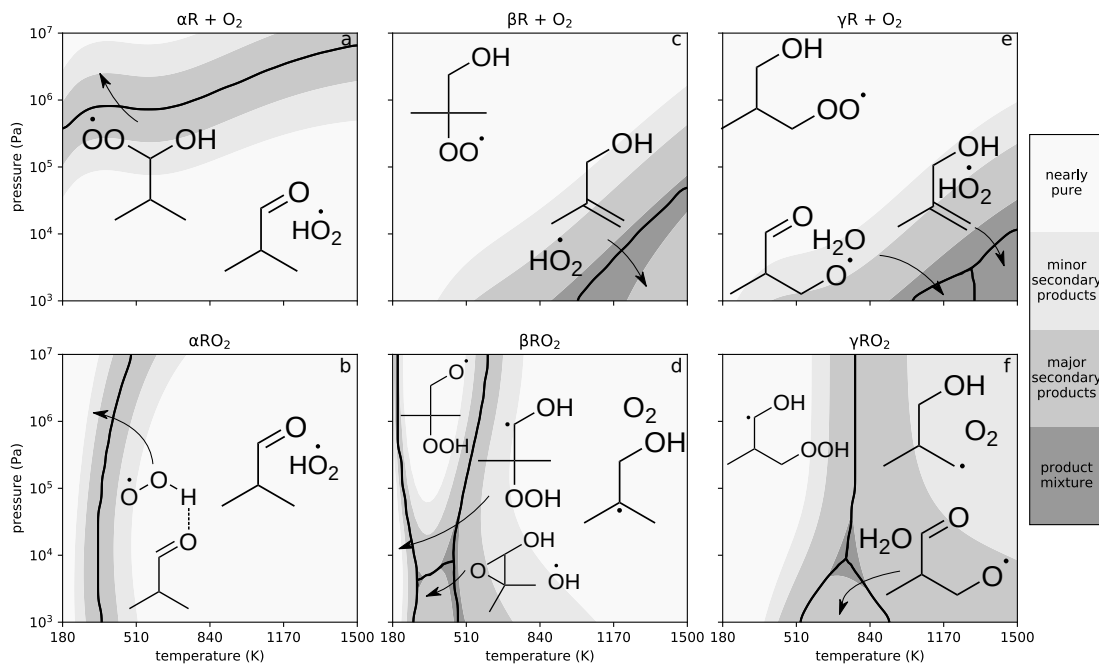


Figure 3-16: To observe sensitivity to the method used, modified strong collision approximation was used instead of reservoir state approximation.[32] The major products formed and branching ratio of alkyl + O<sub>2</sub> reactions and peroxy reactions for the  $\alpha$ ,  $\beta$ , and  $\gamma$  networks at various temperatures and pressures. The structures indicate the major product from the reaction. Shading indicates the fraction going to the major pathway indicated, with cutoffs at 90%, 75%, and 40%. Text gives a qualitative description to the different colors.

nomenological rate coefficients, the pressure dependent network was also solved with modified strong collision assumptions, shown in Figure 3-16. In this work, the modified strong collision predicts significantly more stabilization of RO<sub>2</sub> than the reservoir state approximations. For stabilized RO<sub>2</sub> radicals, more stabilized intermediates were formed in all three networks, and at high temperatures, both the  $\beta$ - and  $\gamma$ -networks show more reforming of R + O<sub>2</sub>. Both the rates for R + O<sub>2</sub> and RO<sub>2</sub> indicate a faster energy transfer rate, which might be due to how the collision efficiency is approximated in the modified strong collision method, which has led to inaccuracies in highly activated systems before.[32]

### 3.4.5 Comparison with combustion mechanism

The reaction rates from these calculations can be compared to estimates in one of the most frequently used detailed isobutanol mechanisms by Sarathy et al.[87] Two other isobutanol mechanisms, published by Hui et al.[81] and Merchant et al.[19], do not include explicit representation of peroxy radicals, so these cannot be effectively compared with the calculations here.

The Sarathy mechanism uses pressure-independent rate coefficients, which we compare to our high-pressure rate coefficients. Of our 38 reactions, only 25 correspond directly to reactions in the Sarathy mechanism. The Waddington mechanism, which the Sarathy mechanism represents as one step, was also added and is compared to the  $\beta$ AlkoxyIsom reaction in this work. These reactions were compared at 50 temperatures between 500 and 1000 K by taking the mean of the ratio of rates from this work to rates in the Sarathy mechanism. Figure 3-17 shows these ratios as a histogram, with color coding indicating different types of reactions.

Given that the rates in Sarathy et al. consist of estimates, obtaining a rate within two order of magnitude is reasonable. Good agreement are obtained for HO<sub>2</sub> elimination reactions from RO<sub>2</sub> and most of the isomerization reactions. Other reaction types deviate more, with Sarathy et al. estimating epoxy formation around a million times slower than this work suggests. In the Sarathy mechanism, these rates originate from rate rules based on alkane fuels, with an activation energy of 92 kJ/mol,[108]

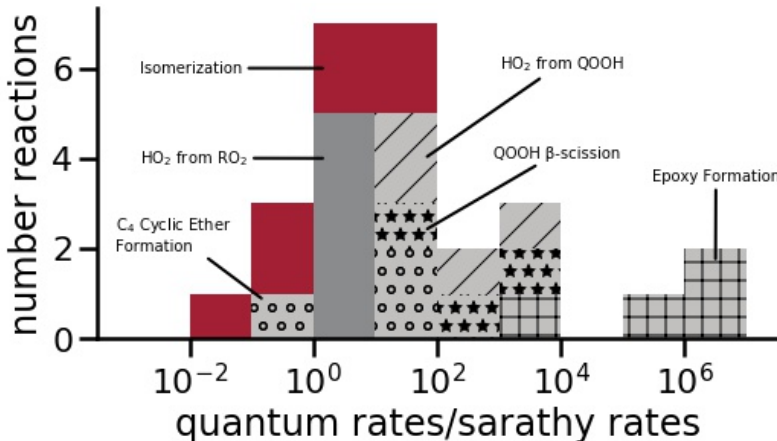


Figure 3-17: Average ratio of rates calculated in this work and estimated in Sarathy mechanism[87] between 500-1000 K, divided into groups based on reaction type.

which is substantially higher than activation energies given from quantum calculations for ethane oxidation, between 50-70 kJ/mol.[109] The rate itself is 2-3 orders of magnitude slower than more recent calculations of epoxidation of alkanes.[110] The barrier heights for this reaction in isobutanol in this and other work[90, 91] is also 21 kJ/mol lower than those reported for alkane and ethanol oxidation.[92, 109, 110] The large deviation between the estimates in Sarathy et al. and in this work can be attributed to the use of older structure activity relationships based only on alkane fuels and possibly differences in chemistry between the alkane compounds which the rate rule is based and isobutanol.

The two decomposition types for QOOH shown in Figure 3-17, ‘QOOH  $\beta$ -scission’ and ‘HO<sub>2</sub> from QOOH’, are also predicted by Sarathy et al. to be 10-10<sup>4</sup> times slower than in this work. The slower decomposition of QOOH would increase the amount of QOOH which could add another O<sub>2</sub>, leading to a faster simulated ignition than what would be predicted based on in this work.

### 3.5 Conclusion

The calculations in this work update the chemistry of isobutanol peroxy radicals, with pressure dependent rates for all three isomer networks. We obtain general agreement

with the potential energy surface proposed by Zador et al. for  $\alpha RO_2$ , the works of Sun et al. and Lizardo-Huerta et al. for  $\beta RO_2$ , and the work of Welz et al. for  $\gamma RO_2$ .

The high-pressure rate coefficients between this work and previous works shows good agreement with Lizardo-Huerta et al. and a slight deviation of around a factor of 25 for Sun et al.[90, 91]. When compared to rate estimates contained in combustion mechanisms, deviations dependent on reaction type up to  $10^6$  occurred.[87] The pressure dependent rates reported in Sun et al. show more stabilization and less competition between multiple pathways than in this work.[90]

The three isomers in this work react through different channels. The fate of  $\alpha R O_2$  almost entirely results in  $HO_2 + ibutaldehyde$ , which agrees with the results of Zador et al.[92] The reaction of  $\gamma R + O_2$  almost entirely forms  $H_2O$  and  $\gamma aldoxy$  at lower temperatures, as suggested by Welz et al., with a mixture of products at higher temperatures. The  $\beta$ -network predominately goes down the Waddington pathway at lower temperatures, though there is much more competition with other pathways at higher temperatures than indicated in other literature. The rates from this work can explain the lack of two-stage ignition from isobutanol combustion.

This work builds upon other kinetic studies to provide rate coefficients for isobutanol-derived peroxy radicals. Given the potential usage of isobutanol as a biofuel, these rates can be integrated into detailed kinetic mechanisms to try to improve the accuracy of models at low temperatures.

Chapter 5 uses these kinetics to understand the fate of  $RO_2$  across various environments and functional groups. The next chapter looks at condensed phase  $RO_2$ , evaluating the error caused by incorrectly modeling the chemistry.



# Chapter 4

## Stochastic oxidation in ultrafine organic aerosols

### 4.1 Summary

Ultrafine organic aerosols impact critical atmospheric processes and human health, and there are still many unknowns about their formation, growth, and atmospheric oxidation. By looking at inorganic aerosol reactions, previous work has suggested that the traditional, concentration-based approach to reactions within particles is sufficient to model aerosol chemistry. This work shows that this concentration-based approach fails to capture the oxidation rate of ultrafine liquid aerosols with fast radical propagation reactions, since it inaccurately calculates the radical termination reaction rate in confined systems with fewer than three radicals. A simplified stochastic model of radical chain propagation developed in this work indicates that low termination reaction rate, small particle diameter, and low gas-phase oxidant concentrations lead to higher, and more accurate, peroxy radical concentrations than predicted by traditional kinetics. In combination with propagation chemistry, this leads stochastic kinetics to predict a faster oxidation rate. To test this under atmospheric conditions, we simulate a rural nighttime particle nucleation and growth event which showed that stochastic chemistry more than doubled the fraction of molecules in 80 nm particles that underwent condensed phase radical reactions relative to the amount predicted by

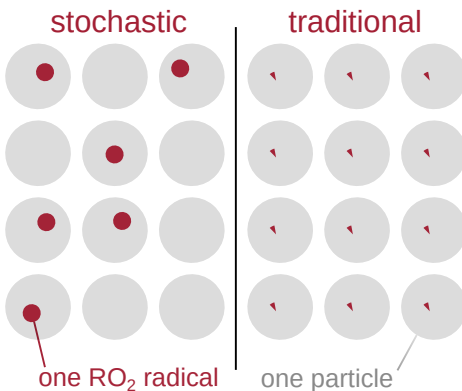


Figure 4-1: Diagram showing the difference between using stochastic and deterministic kinetics on the number of radicals per particle.

traditional chemistry. This suggests that stochastic kinetics could measurably impact atmospheric aerosol properties. We also show that previously published OH heterogeneous oxidation experiments are typically outside region where stochastic chemistry is important. This is likely due to, among other things, difficulties in measuring oxidation in these conditions. A full understanding of the role of stochastic kinetics in organic aerosol aging will require an improved understanding of diffusion limited radical termination rates and radical propagation rates.

## 4.2 Introduction

Fine atmospheric aerosols (defined here as  $\leq 1 \mu\text{m}$  in diameter) can impact human health and earth's climate.[111, 112] These particles typically have a lifecycle that starts with nucleation of gas phase molecules, followed by growth by molecular condensation, and ending with growing larger in size, being deposited on surfaces, or washing out during precipitation. Throughout their lifetime, they are subject to oxidation by atmospheric oxidants, like  $\text{O}_3$ ,  $\text{NO}_x$  and  $\text{OH}$ , which change the chemical and physical properties of these materials, with subsequent effects on humans and the environment.

For many chemical systems, a concentration-based approach to kinetics, in which reaction rates are functions of molecules' concentration, can adequately represent the system's chemistry. This approach works well for systems where there are many

molecules of any particular reactant since it can be derived from statistics of systems with large numbers of reactants. However, for systems where there may be just one or two molecules of a particular reactant, concentrations cease to adequately describe the chemistry. In this situation, a quantized system that explicitly represents the number of each reactant is needed. Stochastic kinetics meets this requirement by replacing concentrations with probability distributions of the number of molecules in a system and replacing reaction rates with probabilities that a reaction will occur in a specified time interval.[67] This approach results in improved accuracy, relative to traditional concentration-based kinetics, for various areas: lipid micelles,[35] systems biology,[36] enzymes[37], emulsion polymerization,[113] antioxidant properties,[38] and metallic nanoparticles[114].

Mozurkewich suggested that stochastic kinetics may also be important for atmospheric aerosols. He found that in small particles with neutral pH, changes in pH would be more dramatic than predicted by traditional kinetics, which could decrease the uptake of HO<sub>2</sub>.[115] He also found that stochastic kinetics would predict higher concentrations of non-volatile radicals than traditional kinetics,[115] resulting from fundamental differences between stochastic and traditional kinetics. If there is one radical in a system, traditional kinetics return a non-zero rate for radical-radical termination. This is unphysical, since radical recombination cannot occur with just one radical. Stochastic kinetics, however, requires that at least two reactant molecules be present in the system in order to react, so no radical-radical termination can occur with only one radical. This more accurate representation of termination with stochastic chemistry leads to less termination and a higher steady state radical concentration than with traditional kinetics. In another study looking at stochastic effects for condensed-phase chemistry, rate changes by only a few percent were predicted between stochastic and traditional kinetics.[116] Subsequent work has mostly used traditional kinetics.[117, 118, 119] Some modeling efforts used stochastic kinetics,[120, 121, 122, 123] though the effect of stochastic kinetics relative to tradition kinetics was not investigated.

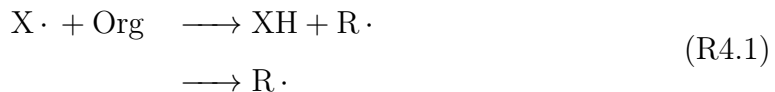
Previous work on the effect of stochastic kinetics in atmospheric aerosols had

focused on inorganic aerosol chemistry,[115, 116] which often lack significant propagation reactions. Subsequent work on organic aerosols has shown that successive radical-based propagation steps might be important.[124, 125, 126, 127, 128] Since the presence of propagation chemistry is known to impact the importance of stochastic chemistry in lipid micelles,[38] these new findings suggest that stochastic treatment might also affect the heterogeneous oxidation of organic aerosols. In this work, we describe a general model for heterogeneous oxidation with propagation chemistry, evaluated how it depends on various environmental factors, discuss whether previous laboratory experiments can show this effect, and evaluate potential impact on atmospheric aerosol systems.

## 4.3 Methodology

### 4.3.1 Model development

The radical-initiated aging of organic aerosol proceeds via chain oxidation, which is summarized in Figure 4-2. This involves the generation of radicals, propagation of radicals through an RO<sub>2</sub> intermediate, and termination through radical recombination. For atmospheric aerosols, radical initiation can come from within the particle, through photolysis or thermal degradation, or from outside the particle, from reactive gas phase species like OH, O<sub>3</sub>, NO<sub>3</sub>, or HO<sub>2</sub>. This work only includes initiation from external radicals, shown in Reaction R4.1, where a gas phase radical, X, encounters a particle and reacts with one of its organic molecules, Org, which forms an alkyl radical, R either by hydrogen abstraction or addition to a double bond.



The carbon-centered organic radical can undergo a number of reactions including β-scission, hydrogen abstraction, or radical recombination. The most prominent reaction of carbon-centered radicals in our atmosphere is recombination with O<sub>2</sub>, Reaction

R4.2.



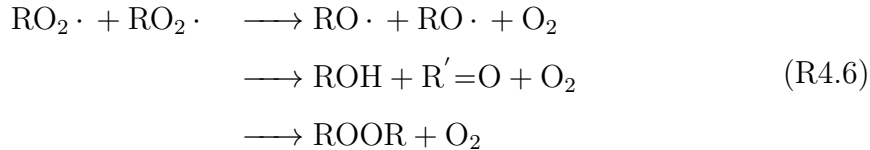
This  $RO_2$  radical can then either dissociate back into  $R \cdot + O_2$ , react with other long-lived atmospheric radicals, such as  $HO_2$ ,  $NO$ , or  $RO_2$ , react with another organic molecule, or undergo unimolecular isomerization reactions. In the framework of radical mechanisms, the hydrogen abstraction and double bond addition reactions are both considered a propagation step, though the products formed are different.



Unimolecular hydrogen abstractions and addition reactions can also occur, forming hydroperoxy alkyl and alkyl peroxy alkyl radicals, shown by Reaction R4.5. Whether or not unimolecular reactions can occur, and which pathway they undergo, is highly structure dependent.



When two organic peroxy radicals react, they will either form two alkoxy radicals,  $RO$ , (a propagation reaction), form an carbonyl and alcohol, or form an alkyl peroxide,  $ROOR$  (both termination reactions). The branching between these pathways is highly structure dependent, with two tertiary  $RO_2$  radicals predominantly forming alkoxy radicals and two secondary  $RO_2$  predominantly forming an alcohol and ketone.[120]



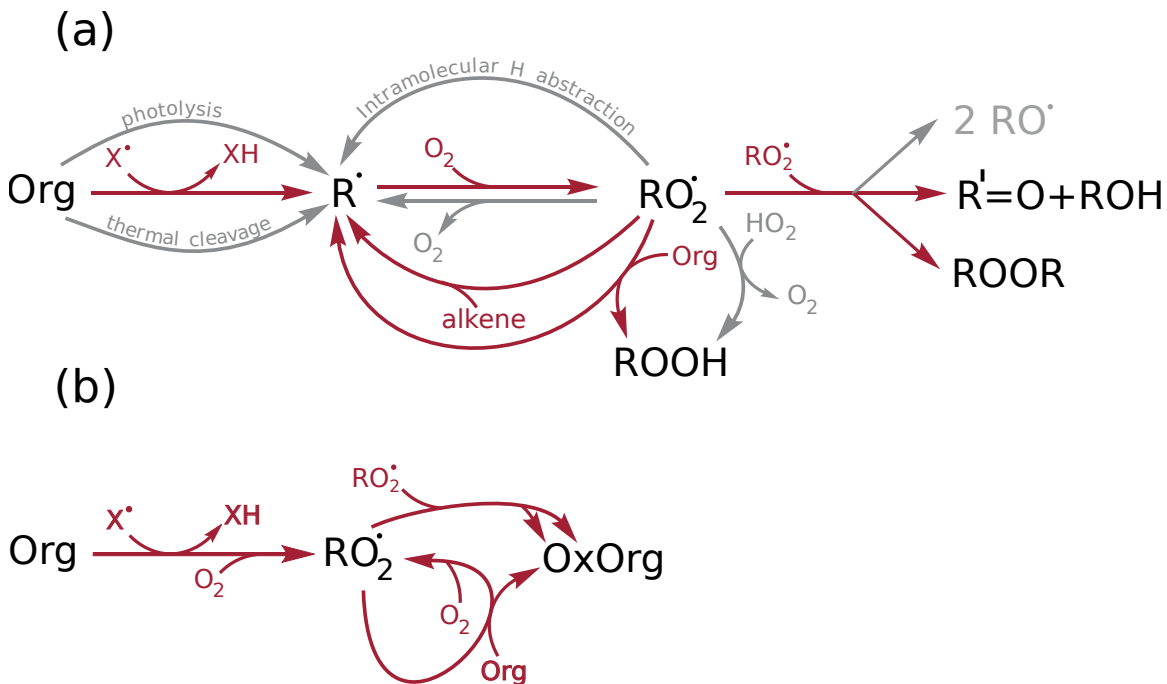
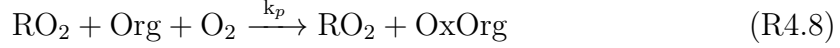


Figure 4-2: (a) common pathways involved in chain oxidation of atmospheric organic aerosols. Red pathways were included in the simplified model and light grey pathways were not included. (b) simplified kinetics used in this work, which combined  $R\cdot$  and  $RO_2\cdot$  and lumped together  $ROOH$ ,  $ROOR$ ,  $R'=O$ , and  $ROH$ .

Organic peroxy radicals can also react with volatile small compounds, such as NO and  $HO_2$ . The reaction with  $HO_2$  primarily leads to termination. The impact of this pathway on the importance of stochastic kinetics is discussed in Section 4.3.2. The reaction with NO could result in a nitrate, which would terminate the radical, or in an alkoxy radical, which would have faster propagation.

In this work, our objective is to show the impact of stochasticity in a wide variety of situations where exact chemistry may not be known. To simplify the model, we removed some of the more minor pathways, shown in light grey in Figure 4-2a, assumed  $R\cdot$  rapidly adds oxygen to form  $RO_2\cdot$ , and lumped all oxidized species together as  $OxOrg$ . The simplified model is shown in Figure 4-2b, which consists of Reactions R4.7-R4.9.





These reactions are the minimum necessary to model chain oxidation. As discussed above, for complex mixtures characteristic of the atmosphere, the reactions are almost certainly more complicated. However, when fitting to experimental data, these reactions are useful in that they can represent a wide variety of scenarios.

In this mechanism,  $r_i$  is the initiation rate,  $r_p$  is the propagation rate given by  $r_p = k_p[\text{Org}][\text{RO}_2]$  using traditional kinetics, and  $r_t$  is the termination rate given by  $r_t = k_t[\text{RO}_2]^2$ .

The initiation rate,  $r_i$  can be found with decent accuracy by applying collision theory between the gas-phase radical and a spherical particle and by including an uptake coefficient,  $\gamma$ , that describes the fraction of collisions that result in a reaction. For spherical particles of diameter  $D_s$ , whose velocity is much slower than that of the gas phase radical, the collision theory simplifies to

$$r_i = \frac{3\gamma\bar{c}_X[X]}{2D_s} \quad (4.1)$$

in which  $[X]$  is the concentration of a gas phase radical oxidant with a mean velocity of  $\bar{c}_X$ .[129] Section 4.3.2 shows that negligible differences result if initiators that produce a pair of radicals are treated as producing single radicals in Reaction R4.1.

The propagation rate constant  $k_p$  depends on the chemical composition of the aerosol. The termination rate constant  $k_t$  typically has a lower activation energy than  $k_p$ , but it can still vary based on sterics and, due to its fast rate, can be diffusion-limited in viscous aerosol systems.

### 4.3.2 Computations

This work applies Reactions R4.7-R4.9 in two frameworks: traditional kinetics and stochastic kinetics. In all cases, pseudo-steady state values for RO<sub>2</sub>, with oxidized concentration given at the start of the simulation were used, so that  $d[\text{RO}_2]/dt = 0$  and  $[\text{Org}] = [\text{Org}]_{\text{initial}}$ .

Traditional kinetics involves differential equations for each molecule in the system, which simplifies to an algebraic expression with the steady state assumption. Solving this for peroxy radical leads to[130]

$$[\text{RO}_2] = \sqrt{r_i/2k_t}. \quad (4.2)$$

The rate of formation of oxidized molecular products for this system is just the sum of initiation and propagation rates,  $d[\text{OxOrg}]/dt = r_i + r_p$ , which at steady state is equivalent to  $r_t + r_p$ .

For stochastic kinetics, the rate expressions themselves shift from using from concentrations of molecules to number of molecules, with propagation given as  $r_p = k_p N_{\text{Org}} N_{\text{RO}_2}$  and termination given as  $r_t = k_t N_{\text{RO}_2} (N_{\text{RO}_2} - 1)$ , where  $N_{\text{RO}_2}$  is the number of RO<sub>2</sub> radicals in the particle, and  $N_{\text{Org}}$  are the number of reactive organic molecules in the particle at the start of oxidation.

When converting traditional rate coefficients (whose dimensions depend on reaction order) to stochastic rate coefficients (which all have dimensions of inverse time), modifications were made using particle volume. In this work  $r_i$  in traditional kinetics was multiplied by the reactor volume to get the stochastic rate. Propagation and termination coefficients,  $k_p$  and  $k_t$ , both had their values divided by the volume to get the stochastic coefficients.[68] The rate was not modified due to identical reactants, which is still kinetically consistent.[44]

The steady state solution to the stochastic system is solved with a one dimensional master equation, which is a set of differential equations that describe the probability,  $p_n$  that the system will contain a certain number of RO<sub>2</sub>,  $n$ , for various values of  $n$ ,[131] which for Reactions R4.7 and R4.9 is shown by Equation 4.3.

$$\frac{dp_n}{dt} = r_i p_{n-1} - r_i p_n + k_t p_{n+2}(n+2)(n+1) - k_t p_n(n)(n-1) = 0. \quad (4.3)$$

For a master equation that goes up to  $n_{max}$ , Equation 4.3 is repeated for values 0 till  $n_{max} - 1$ . The last equation necessary to solve the system of equations if that the sum of probabilities equals one.

Section 4.3.2 describes the development of the master equation in more detail. Each number of RO<sub>2</sub> radicals has its own differential equation, shown in Equation 4.3. Since this analysis involves the steady state solution, each of these equations is set to zero. The system of equations is then solved by linear algebra.

These steady state yield aggregate properties. The average number of RO<sub>2</sub> among an ensemble of identical particles, which is similar to the RO<sub>2</sub> concentration in traditional kinetics, can be found by taking a weighted sum:  $\sum_{n=1}^{\infty} N_{Org} p_n$ .

Likewise, the average rates of propagation and termination reactions can be found with weighted sums:  $r_p = k_p N_{Org} \sum_{n=1}^{\infty} n p_n$  and  $r_t = k_t \sum_{n=1}^{\infty} n(n-1) p_n$ , respectively. Like traditional kinetics, the overall oxidation rate is just the sum of  $r_p$  and  $r_t$ .

Another concept commonly used in studying autoxidation is chain length, which is defined as the number of oxidations that occur per initiation. This gives a general idea of how important propagation is in the system. In both stochastic and traditional models, it can be calculated as  $r_p/r_t + 1$ . Chain length is highly related to effective uptake coefficient,  $\gamma_{eff}$ , reported in aerosol heterogeneous oxidation experiments. Where  $\gamma_{eff}$  describes at the number of oxidations per collision, chain length is the number of oxidations per *reactive* collision. Mathematically, chain length is  $\gamma_{eff}$  divided by the fraction of collisions that result in a reaction, referred to as the update coefficient,  $\gamma$ .

As particle diameters get smaller, at some point the master equation will no longer be valid, which will occur if the particles are no longer well mixed.[132] If there is diffusion limited kinetics, it is possible that the molecules do not have time to disperse between reaction events.[121] Gillespie et al. indicates that for diffusion-limited reactions inside systems which are dilute with respect to the reactants, the

reactants' diameters need to be less than an order of magnitude the diameter of the particle for the master equation to be valid.[132] Since the termination reaction in this work is often diffusion-limited in viscous secondary organic aerosol (SOA), the well-mixed assumption used in stochastic kinetics will likely not be valid for particles smaller than a certain threshold. Since the particles are almost entirely composed of abstractable hydrogens, the system is not dilute with respect to propagation, so if this reaction becomes diffusion limited due to high viscosity, the models and calculations presented in this work will not be valid. Fortunately if that becomes the case, the termination rate is already so slow that stochastic calculations would not be necessary.

### Master equation solution

Many methods exist for solving stochastic kinetic systems. Analytical approaches are often based on solving a master equation that gives probabilities of different states. Numerical approaches step through time choosing a reaction based on a probability of all the different reactions.[67]

To compare traditional kinetics with stochastic kinetics, this chapter uses a master equation based approach for stochastic kinetics.

A  $m$ -dimensional master equation tracks the probability that a system will have a certain number of  $m$  particular molecules. This method scales poorly for higher dimensional systems, which is when time-step approaches become more feasible. Since this work looks at the pseudo steady state at the start of the simulation, the only major compound that needs tracking is RO<sub>2</sub>, so a 1-dimensional master equation is ideal. The system of choice is one particle of a specified size.

A 1-dimensional master equation involves indicating what happens to the probability,  $p_n$ , that a system will have  $n$  tracked molecules when a set of systems with various tracked molecules and corresponding probabilities undergo the set of reactions. For each reaction and initial system that either moves the system to have  $n$  tracked molecules or away from having  $n$  tracked molecules, the corresponding reaction rate and the probability of the initial system existing are placed in the master equation. For example, when the system with  $n - 1$  radicals undergoes initiation, it

forms a system with  $n$  radicals, so the master equation should have a positive rate of reaction of the form  $p_{n-1}r_{i,n-1}$  where  $r_{i,n-1}$  is the rate of initiation for a system with  $n - 1$  radicals. Terms in the system of equations are removed when they are outside the range of radical numbers specified, which is shown in the example below.

Since the propagation reaction, Reaction R4.8, in the main text does not change the number of RO<sub>2</sub>, it is not included in this master equation formulation. The only reactions needed in this analysis are initiation and termination. Once this is done for the set of systems, the following master equation results

$$\frac{dp_n}{dt} = r_i p_{n-1} - r_i p_n + r_t p_{n+2} - r_t p_n \quad (4.4)$$

Substituting the expression for  $r_t$  gives Equation 4.3 in the main publication (also copied below):

$$\frac{dp_n}{dt} = r_i p_{n-1} - r_i p_n + k_t p_{n+2}(n+2)(n+1) - k_t p_n n(n-1) \quad (4.5)$$

Equation 4.5 is then enumerated for a set of values  $n$ . Here is an example showing only radical numbers 0-2.

$$\begin{aligned} \frac{dp_0}{dt} &= -r_i p_0 & +2k_t p_2 \\ \frac{dp_1}{dt} &= r_i p_0 & -r_i p_1 & +6k_t p_3 \\ \frac{dp_2}{dt} &= -r_i p_1 & -(r_i + 2k_t)p_2 & +12k_t p_4 \end{aligned} \quad (4.6)$$

The time derivatives are set to zero to find the steady state solution. There are now five variables,  $p_0-p_4$ , and three equations. Adding a restriction that  $\sum p_x = 1$  and removing the highest order term,  $12k_t p_4$ , allows for the system of equation to be solved. The corresponding solvable equation is below.

$$\begin{bmatrix} 0 \\ 0 \\ 0 \\ 1 \end{bmatrix} = \begin{bmatrix} -r_i & 0 & 2k_t & 0 \\ r_i & -r_i & 0 & 6k_t \\ 0 & r_i & -(r_i + 2k_t) & 0 \\ 1 & 1 & 1 & 1 \end{bmatrix} \begin{bmatrix} p_0 \\ p_1 \\ p_2 \\ p_3 \end{bmatrix} \quad (4.7)$$

This matrix can be solved analytically or numerically. In the main part of this work, numerical solutions were used. Since this is a small system, the analytical solution is shown below.

$$p_0 = \frac{12k_t^2}{k_i^2 + 12k_i k_t + 24k_t^2} \quad (4.8)$$

$$p_1 = \frac{6k_t(k_i + 2k_t)}{k_i^2 + 12k_i k_t + 24k_t^2} \quad (4.9)$$

$$p_2 = \frac{6k_i k_t}{k_i^2 + 12k_i k_t + 24k_t^2} \quad (4.10)$$

$$p_3 = \frac{k_i^2}{k_i^2 + 12k_i k_t + 24k_t^2} \quad (4.11)$$

The calculations in the main body of this work were solved numerically with at least  $n_{max} \geq 100$ . If not enough terms are used in the master equation matrix, the system is no longer accurate, which can happen in our system with high initiation and low termination rates. When this happens, the probability the system is in its highest number of radicals is large. To check if there are too few terms in a calculation,  $n_{max}$  is increased if the probability of the most radicals solved for exceeds 0.1%, up to  $n_{max} = 300$ . Beyond that, stochastic chemistry is not important and the traditional approach should suffice.

This framework for finding steady state radical concentrations was applied to the different chemical networks discussed in the next section.

## Model simplifications

This section tests some of the assumptions behind the simplified chemistry in Reactions R4.7-R4.9, and compares the impact from stochastic chemistry on oxidation

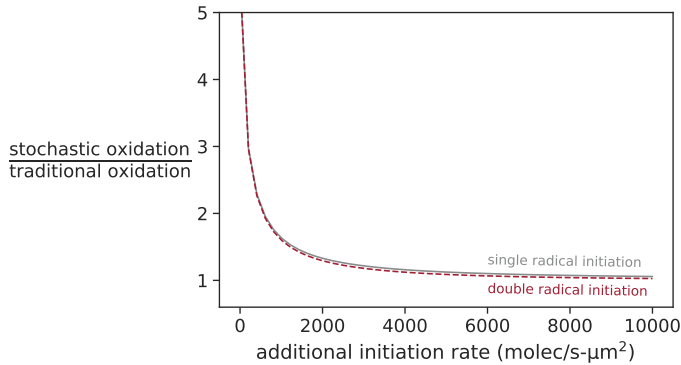


Figure 4-3: Difference in relative oxidation rates for stochastic and traditional kinetics using a model with paired initiation (red, dashed) and a model with only single initiation (grey, solid). The x-axis presents the oxidation rate in addition to single-radical initiation rate of 100 molec/s- $\mu\text{m}^2$

rate and/or radical numbers.

Unless otherwise stated, all calculations in this section apply to a 40 nm particle, a propagation rate of  $10^{-20}$  cm<sup>3</sup>/molec-s, a termination rate of  $1.61 \times 10^{-15}$  cm<sup>3</sup>/molec-s,[121] and a surface area dependent initiation rate of 100 molec/s- $\mu\text{m}^2$ .

**Paired initiation** The simplified model assumes that radicals don't enter the system in pairs, but this is not always true. Ozone reactions can lead to two radicals and so can condensed phase photolysis.

To evaluate the impact of paired initiation, calculations were run with a base single-radical initiation rate of 100 molec/s- $\mu\text{m}^2$  and various amounts of additional initiation from either single or double radicals, up to where 99% of oxidation was occurring due to double radical initiation. Figure 4-3 shows the results of this calculation.

In Figure 4-3, the difference between the two lines never surpasses 4%. This figure suggests pair radical initiation can be represented by single-radical initiation with negligible error. Simulating with different base initiation rates (not shown), does not change this conclusion.

This analysis only looked at the pseudo-steady state values, and not the time it takes to reach pseudo-steady state, which will likely take longer if single-radical initiation is slow. Though given concentrations in our atmosphere, the time till pseudo

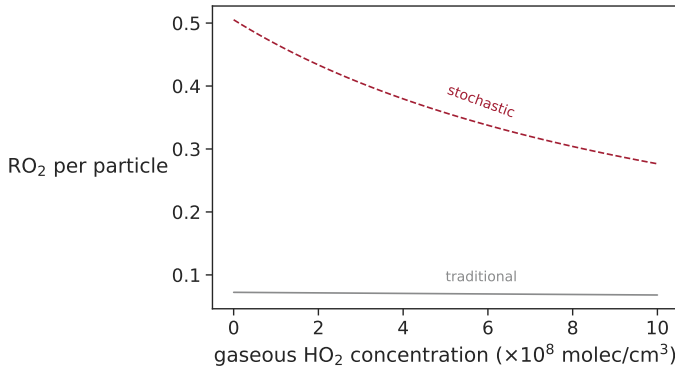


Figure 4-4: Average number of radicals per particle over various concentrations of HO<sub>2</sub> using a model including HO<sub>2</sub> + RO<sub>2</sub> termination reactions with a rate constant of  $5 \times 10^{-13}$  cm<sup>3</sup>/molec-s. The red dashed line shows the results of the stochastic master equation and the grey solid line shows the traditional solution.

steady state is likely to be much shorter than the time scales of oxidation.

**Termination with HO<sub>2</sub>** In addition to the RO<sub>2</sub> + RO<sub>2</sub> reaction discussed in the main text, peroxy termination reactions can also involve HO<sub>2</sub>, which can dissolve into the particle. This section evaluates the impact of including the HO<sub>2</sub> + RO<sub>2</sub> termination reaction in the system. We assumed the HO<sub>2</sub> is in equilibrium in the particle and gas phase, applying a Henry's law constant of 70 mol/L-atm, which has been applied to fatty acid aerosols,[124] but still has large uncertainties. This equilibrium-based approach likely overestimates the impact of HO<sub>2</sub>, which should lead to a conservative estimate of when this complication can be ignored.

For the rate constant of HO<sub>2</sub> + RO<sub>2</sub>, a value of  $5 \times 10^{-13}$  cm<sup>3</sup>/molec-s is used, which is in between values of HO<sub>2</sub> + HO<sub>2</sub> and RO<sub>2</sub> + RO<sub>2</sub> compiled by Denisov and Afanas'ev[130]

Figure 4-4 shows how the average radical number changes with increasing HO<sub>2</sub> concentration. In this simulation, the HO<sub>2</sub> drops the RO<sub>2</sub> concentration of the stochastic simulation by 45%, well below the 0.5 asymptote seen in the main text. Over the same concentration range, the traditional solution only decreased 6%. The lessening of the gap with HO<sub>2</sub> directly translates to decreases in the impact of stochastic chemistry, shown in Figure 4-5, which shows a decrease in the stochastic effect by 40%.

In places where HO<sub>2</sub> concentrations are lower, around  $10^8$  molec/cm<sup>3</sup>, the simplifi-

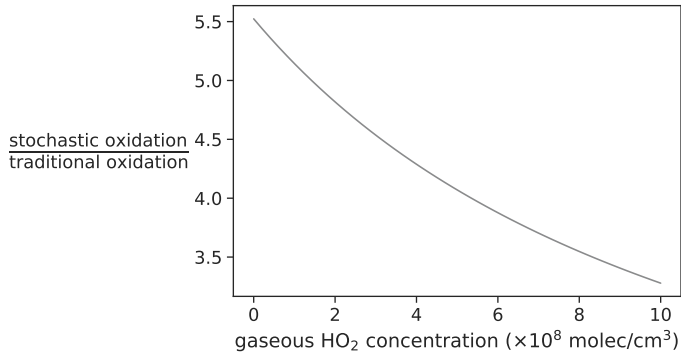


Figure 4-5: Ratio of oxidation rates from the stochastic and traditional solutions using a model including  $\text{HO}_2 + \text{RO}_2$  termination reactions with a rate constant of  $5 \times 10^{-13} \text{ cm}^3/\text{molec-s}$ .

fied model deviates less than 10%, leaving the  $\text{HO}_2 + \text{RO}_2$  reaction to be negligible relative to other uncertainties in other rate constants. Better constraints on the Henry's Law coefficients and reaction rate could better help constrain the impact of termination with  $\text{HO}_2$ . In high  $\text{HO}_2$  environments, this effect should not be ignored.

**Initiation with  $\text{HO}_2$**  For some aerosols, like those with alkenes or exceptionally weak C-H bonds,  $\text{HO}_2$  can act as an initiator of radicals. The impact of  $\text{HO}_2$  initiation is estimated by assuming the  $\text{HO}_2$  is in equilibrium with the gas phase and that the reaction rate is  $2 \times 10^{-18} \text{ cm}^3/\text{molec-s}$ , which corresponds to the hydrogen abstraction reaction of  $\text{RO}_2$  and linoleic acid, which has two particularly weak hydrogens.[133]

Figure 4-6 shows the change in radical concentrations with different gaseous concentrations of  $\text{HO}_2$ . The change is much less pronounced than in Figure 4-4, with a 20% increase in the traditional radical concentration and less than a 1% change in the concentration given by the stochastic master equation.

The change in oxidation rate in Figure 4-7 is larger than expected given the small change in radical concentrations. This shift is due to a general increase in the amount of initiation that occurs, which reduces the impact of stochasticity. Incorporating the  $\text{HO}_2$  initiation rate into the initiation rate constant in the simplified model can adequately capture this effect.

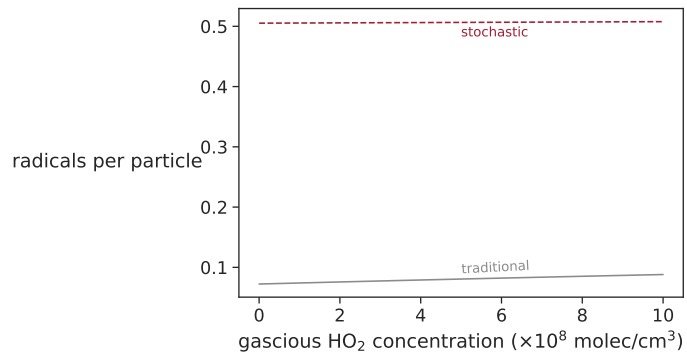


Figure 4-6: Average number of radicals per particle over various concentrations of  $\text{HO}_2$  using a model including a  $\text{HO}_2 + \text{RH}$  initiation reaction with a rate constant of  $2 \times 10^{-18} \text{ cm}^3/\text{molec-s}$ .[133] The red dashed line shows the results of the stochastic master equation and the grey solid line shows the traditional solution.

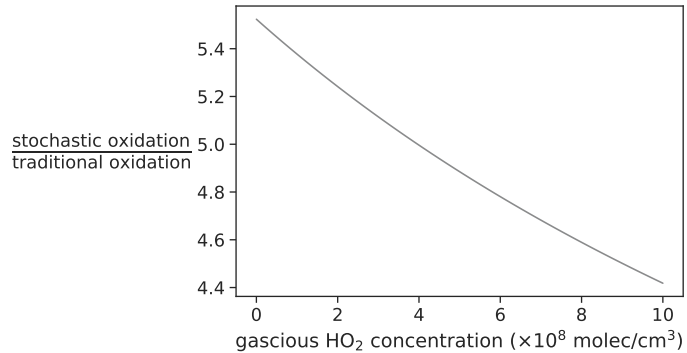


Figure 4-7: Ratio of oxidation rates from the stochastic and traditional solutions using a model including a  $\text{HO}_2 + \text{RH}$  initiation reaction with a rate constant of  $2 \times 10^{-18} \text{ cm}^3/\text{molec-s}$ .[133]

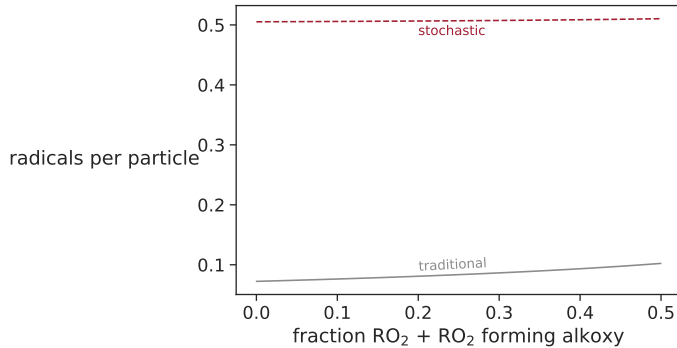
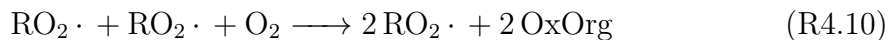


Figure 4-8: Average number of radicals per particle over various branching ratios of  $\text{RO}_2 + \text{RO}_2$  reactions with a fixed total rate of  $1.61 \times 10^{-15} \text{ cm}^3/\text{molec-s}$  using a model including alkoxy formation from  $\text{RO}_2$  recombination. The red dashed line shows the results of the stochastic master equation and the grey solid line shows the traditional solution.

**Alkoxy formation from  $\text{RO}_2 + \text{RO}_2$**  In addition to peroxy radicals reacting together to terminate the radical chain, they can also react to form two alkoxy radicals. These alkoxy radicals can either  $\beta$ -scission or abstract a hydrogen, both of which will likely reform a peroxy radical. Since the alkoxy reaction is faster than the subsequent peroxy radicals, the alkoxy reactions can be simplified into



This propagation is distinct from the propagation used in the simplified model because this propagation rate is second order in  $\text{RO}_2$  concentration.

To evaluate this effect, two simulations were run. The first one sets the total reaction rate of  $\text{RO}_2 + \text{RO}_2$  as a constant and varies the fraction of termination resulting in alkoxy radicals, shown in Figures 4-8 and 4-9. The 40% increase in radicals in the traditional model due to a slower termination rate (Figure 4-8) explains the large shift in the ratio of stochastic to traditional oxidation rates (Figure 4-9). This shows that taking the overall  $\text{RO}_2$  self-reaction and assuming it is all termination could lead to some error. But what happens when the correct reaction rate for termination is used but the alkoxy pathway is ignored?

The second simulation addresses this point by leaving the termination reaction

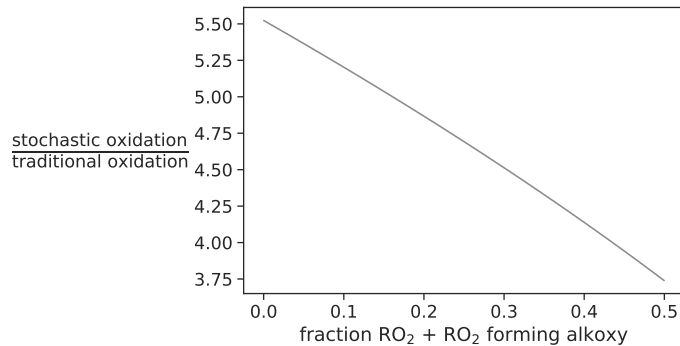


Figure 4-9: Ratio of oxidation rates from the stochastic and traditional solutions over various branching ratios of  $\text{RO}_2 + \text{RO}_2$  reactions with a fixed total rate of  $1.61 \times 10^{-15} \text{ cm}^3/\text{molec-s}$  using a model including alkoxy formation from  $\text{RO}_2$  recombination.

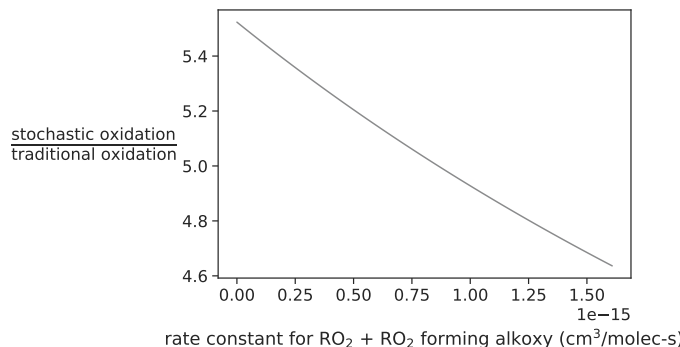


Figure 4-10: Ratio of oxidation rates from the stochastic and traditional solutions while varying the rate of  $\text{RO}_2 + \text{RO}_2 \rightarrow 2\text{RO} + \text{O}_2$ , with a termination rate constant fixed at  $1.61 \times 10^{-15} \text{ cm}^3/\text{molec-s}$ .

rate fixed while varying the alkoxy formation pathway, shown in Figure 4-10. The effect in this circumstance is more minimal, indicating that if a simulation is within the stochastic regime and the rate of alkoxy formation is approximately the rate of termination, it is acceptable to ignore the alkoxy formation reaction, as long as the termination reaction does not mistakenly incorporate the alkoxy pathway. Outside the stochastic regime, however, the alkoxy formation would be more significant.

## 4.4 Results and Discussion

### 4.4.1 Model behavior

Stochastic kinetics impacts macroscopic quantities like aerosol oxidation rate in two parts. The first is by more accurately representing an intermediate quantity, which in this system is the average number of radicals per particle. The change in concentration does not necessarily lead to a difference in oxidation rate, since the radicals could just exist for longer before terminating. The second critical piece is how much oxidation is coming from propagation reactions as opposed to radical initiation. This section starts by discussing the impact of stochastic kinetics on radical concentration and then moves into describing the effect on the overall oxidation rate.

In the stochastic model if there is only one RO<sub>2</sub> radical in the particle, no termination reaction can occur. The traditional treatment, which described reaction rates in terms of concentrations, will still predict termination even if the concentration indicates fewer than one radical per particle. The latter would be accurate if radicals were able to rapidly move between particles in the atmosphere,[38] but given that peroxy radicals formed from heterogeneous oxidation likely have an even lower vapor pressure than their condensed phase precursor, rapid movement of peroxy radicals between particles is highly unlikely. This restriction of radical movement causes a slower termination rate which is captured by stochastic kinetics.

The lower stochastic termination rate manifests itself in a higher RO<sub>2</sub> concentration, which can be seen in Figure 4-11. The dependent axis shows the initiation rate, given by equation 4.1, which could come from initiation by OH, NO<sub>3</sub> or other radicals. As a reference, the range in Figure 4-11 corresponds to OH concentrations between 10<sup>4</sup> to 10<sup>9</sup> molec/cm<sup>3</sup>-s, with a  $\gamma = 1$  at 300 K. At low initiation rates, the stochastic model approaches 0.5 radicals per particle, and the traditional model has much lower values, consistent with results by Mozurkewich.[115]

As the initiation rate increases, the stochastic model's slope increases until both models converge, which occurs around 3 radicals per particle. This observation allows for a general rule that for stochastic kinetics to have an impact, there should be fewer

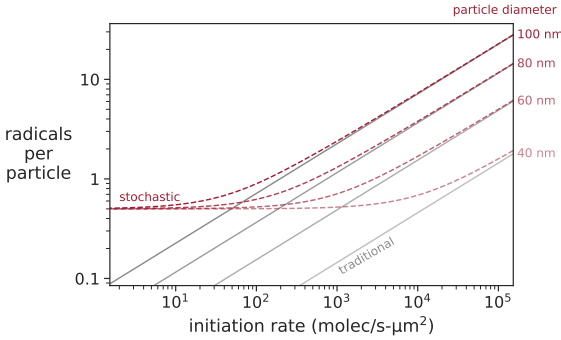


Figure 4-11: Average number of radicals per particle predicted by stochastic (red, dashed) and traditional (grey, solid) kinetics over various sized particles with a termination rate of  $1.61 \times 10^{-15} \text{ cm}^3/\text{molec-s}$ .[120]

than three radicals per particle on average.

Another important variable for determining impact of stochasticity for a given system is particle size. As size increases, the number of radicals per particle also increases, shown in Figure 4-11. For a daytime OH concentration of 0.4 ppt (with an innitiation rate of approximately  $10^3 \text{ molec/s-}\mu\text{m}^2$ ), there is almost no difference between stochastic and traditional effects for the 100 nm particle, but for a 40 nm particle, stochastic kinetics predicts triple the radical concentration of traditional kinetics.

In addition to the initiation rate and particle diameter, the termination rate also strongly impacts the radical concentration in the particle.  $\text{RO}_2 + \text{RO}_2$  reaction products vary due to chemical structure, with tertiary peroxy radical recombination forming only two alkoxy radicals, propagating the reaction instead of terminating it. The recombination reaction rates are also structure dependent, with tertiary peroxy radical recombination being about four orders of magnitude slower than primary peroxy radical recombination.[134] Any of these rates can further be decreased due to diffusion limited kinetics in viscous atmospheric aerosols. Figure 4-12 shows how the termination rate changes the radical concentration in stochastic and traditional kinetic simulations. Slower termination rates increase the concentration of radicals, decreasing the stochastic effect. As a reference, the slowest reaction in Figure 4-12 could be caused by a viscosity of 2000 Pa-s, which approximately corresponds to the

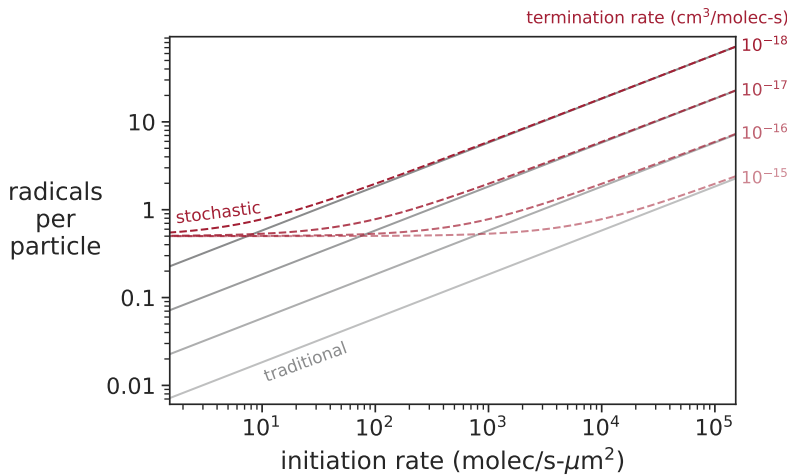


Figure 4-12: Average number of radicals per particle predicted by stochastic (red, dashed) and traditional (grey, solid) kinetics over various termination rate constants for particles with a diameter of 40 nm.

value of  $\alpha$ -pinene ozonolysis SOA at around 60-70% relative humidity.[135]

Just because the concentration of radicals is different between stochastic and traditional methods, does not mean that these two reactions will necessarily have different oxidation rates. In addition to a difference in radical concentration, a large propagation rate constant is also necessary. Figure 4-13 shows the ratio of oxidation rates from stochastic kinetics to that of traditional kinetics for a range of propagation rates. There is an upper limit in which increasing the propagation rate does not significantly alter the impact of stochastic chemistry on oxidation, which is shown by ‘ $\infty$ ’ in Figure 4-13. As the propagation rate decreases, the impact on oxidation rate also decreases.

Functional groups have a large impact on the propagation rate, with C=C bonds allowing for addition reactions and weaker C–H bonds allowing for faster H-abstraction rates. For reference, the propagation rate of 2-butanone in decane, for example, has a propagation rate coefficient around  $10^{-20}$  cm<sup>3</sup>/molec-s, and decanal in decane has a rate coefficient of approximately  $10^{-18}$  cm<sup>3</sup>/molec-s. The abstraction of unoxygenated groups is often slower with rate coefficients typically at or lower than  $10^{-22}$  cm<sup>3</sup>/molec-s.[130]

Since hydrogen abstraction has a high activation barrier, temperature can have a substantial impact on stochasticity. Changing the temperature from 0°C to 30°C

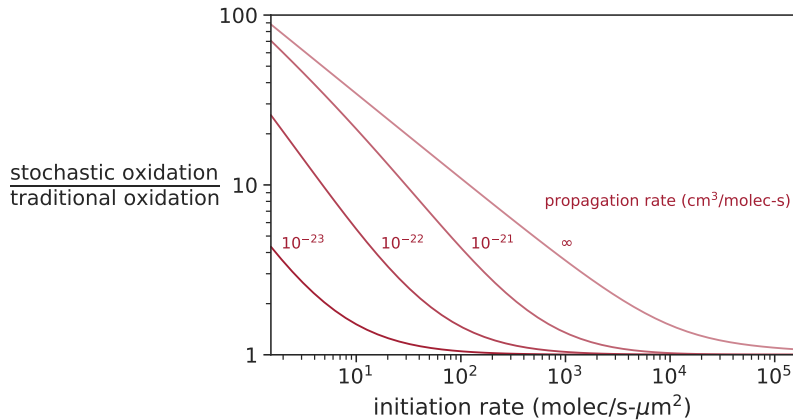


Figure 4-13: Relative difference in the oxidation rates for stochastic and traditional simulations over various initiation and propagation rates. The simulation uses 40 nm particles, with a termination rate of  $1.61 \times 10^{-15} \text{ cm}^3/\text{molec-s}$ , and a density of 0.04 mol/cm<sup>3</sup>.

can increase the propagation rate by a factor of 10 when the activation energy is around 50 kJ/mol, which is typical for hydrogen abstraction from alkanes. Since a factor of 10 can lead to a large difference in impact of stochasticity in Figure 4-13, this temperature effect could exacerbate seasonal differences in aerosols, with more impact in the summer than in the winter.

Figures 4-11, 4-12, and 4-13 show that the difference between stochastic and traditional oxidation rate is based on the rates of the three reactions. The stochastic rate coefficients, which all have units of 1/s and can be interpreted as a type of reaction frequency. Physically the initiation rate,  $r_i$ , represents the average number of times per second a radical is introduced to the particle. The propagation rate coefficient,  $k_p$ , represents how many propagation reactions on average one RO<sub>2</sub> undergoes in the particle. The termination rate coefficient,  $k_t$ , is half of the termination rate when the particle has two RO<sub>2</sub> radicals in the system, which is the minimum number necessary for termination and the most common number for which termination occurs under stochastic conditions. How combinations of these parameters impact stochastic oxidation is shown in Table 4.1. When initiation rate coefficient is faster than the termination or propagation rate, stochastic chemistry is not significant. On the flip side, where initiation is the slowest, stochastic chemistry is likely to be important.

Table 4.1: Impact of stochastic rate coefficients on stochasticity.

rate coefficient comparison	significant stochastic effect	reason
$r_i > k_t$	no	too many radicals per particle
$r_i > k_p$	no	little dependence of RO <sub>2</sub> number
$r_i < k_t$ and $r_i < k_p$	yes	few radicals and dependent on RO <sub>2</sub>

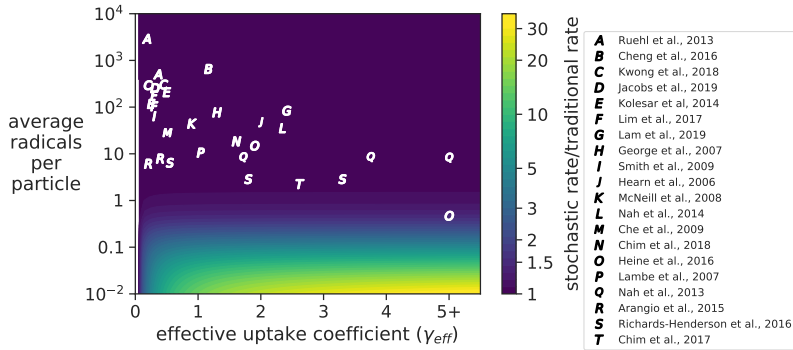


Figure 4-14: Experimental uptake coefficients[129, 136, 137, 138, 139, 140, 126, 127, 128, 125, 124, 141, 142, 143, 144, 145, 146, 147, 148, 149] and the estimated radical number compared to the relative difference in the oxidation rate given by stochastic and traditional simulations. In all calculations, a termination rate of  $1.61 \times 10^{-15}$  cm<sup>3</sup>/molec-s was used. For the shading, simulations were run with 5% of particle-OH collisions resulting in reaction ( $\gamma = 0.05$ ), and initiation from 1 ppp OH while varying diameter and propagation rate constant.

#### 4.4.2 Previous experimental evidence

As shown in Figures 4-12 and 4-13, uncertainties in the model parameters make it difficult to determine exactly where stochastic kinetics is important. To constrain parameters, previous heterogeneous oxidation experiments may offer some insight.

Figure 4-14 shows results from research that report  $\gamma_{eff}$ , the average number of reactions per radical-particle collisions, for OH reaction with various liquid particles and their estimated radical concentration, obtained from Equations 4.1 and 4.2. Approximations made to include research that does not report values necessary to estimate radical concentration, such as average OH concentration. The background color shows the expected impact of stochasticity on oxidation rates determined from our model.

The bulk of measurements in Figure 4-14 occurs at higher radical numbers than are

necessary for stochasticity to be important. One experiment by Heine and Wilson does indicate stochastic behavior, but the simulations show only an increase of 50% from stochastic oxidation. The lack of measurements in the stochastic range originate from experimental difficulties. Many experiments use high oxidant concentrations to get faster oxidation, which can improve signal to noise ratio, reduce the loss of particles to walls, decrease agglomeration, and speed up data collection; however the high initiation rate from high oxidant concentrations increase the number of radicals per particle, inhibiting stochastic effects. Most of these experiments also used particles on the order of 200 nm which are easier to form and are more stable than smaller particles at a similar mass loading but are typically outside the range where stochastic kinetics can have an impact. Many experiments also run for a few minutes in a flow reactor, which requires smaller equipment, reduces particle loss, and results in more rapid data generation but preclude slow enough oxidation. For many scientific questions, these experimental setups are optimal. However, the high oxidant rates and relatively large particles prevent seeing any stochastic effects.

To get measurements where stochastic kinetics dominates, smaller particles must be generated at a high enough mass loading, these particles need to be stable on the order of hours without significant particle agglomeration or wall loss, and they should be oxidized more slowly than current experiments. Then there is also a challenge measuring the chemical properties of the particles. Most techniques for the real-time measurement of the chemical composition of submicron aerosols are not designed and in some cases not able to measure 50 nm particles. For example, the Aerodyne Aerosol Mass Spectrometer has lower collection efficiency when particles get smaller than 70 nm.[150] Literature on optically levitated traps has not been reported for particles below 100 nm.[151] Further development of experimental techniques should be useful in showing whether or not stochastic kinetics occurs in particular systems.

#### 4.4.3 Environmental application: night time particle nucleation

Since measuring oxidation of small particles is limited in part by equipment, it might be useful to determine whether any atmospheric conditions might show stochastic oxidation rates faster than the predicted traditional rate. To exemplify this effect, we chose a type of atmospheric event that has properties which enhance stochastic behavior.

Nighttime particle nucleation, which has been documented across the globe,[152, 153, 154, 155, 156, 157, 158] involves small particles, low oxidant concentrations, and higher diffusivity (due to high humidity), and thus could fall within the stochastic bounds presented above. Heterogeneous oxidation during a monoterpene-dominated nighttime particle nucleation event, where ozone is nearly completely consumed and oxidation is driven by  $\text{NO}_3$  and/or OH, is ideal for this behavior. The simulation involves the first 5 hours after ozone depletion, with a particle growth rate of 10 nm/hr and an initial diameter of 30 nm. In these types of events, nucleation starts at sunset and particles grow at a fast rate, consuming the ozone. After ozone is consumed, the particle growth rate decreases.

Many variables like the temperature, humidity, growth rate, and concentration of  $\text{NO}_x$  and  $\text{O}_3$  come directly from Kammer et al.[159] The  $\text{NO}_3$  concentration is considered similar to other forested nighttime measurements at 6 ppt.[160], with an uptake coefficient of  $2.3 \times 10^{-3}$  taken from  $\text{NO}_3$  uptake on abietic acid.[161] OH may also be important, and is included in the model. Since other rural nighttime environments with low  $\text{NO}_x$  and low  $\text{O}_3$  measure an OH concentration below the detection limit of 0.01 ppt,[160, 162] the [OH] is approximated to be half of that detection limit.[163] The uptake coefficient for OH is taken as 0.79, which was obtained from OH refraction off of a squalene surface.[164] The total initiation rate from OH and  $\text{NO}_3$  was approximated as 43 molec/ $\text{s}\cdot\mu\text{m}^2$ .  $\text{NO}_3$  only contributes twice as much OH to initiation in this system, despite being three orders of magnitude higher in concentration due to a lower uptake coefficient and lower velocity. Table 4.2 lists the conditions used in this

Table 4.2: Parameters used in modeling the nighttime particle growth event.

condition	value	units	source
temperature	15	C	159
relative humidity	>90	%	159
[O <sub>3</sub> ]	<1	ppb	159
growth rate	10	nm/hr	159
density	1.19	g/cm <sup>3</sup>	165
viscosity	6.25	Pa-s	135
[OH]	<0.01	ppt	162
[NO <sub>3</sub> ]	6	ppt	160
$\gamma_{\text{OH}}$	0.79		164
$\gamma_{\text{NO}_3}$	$2.3 \times 10^{-3}$		161
[NO <sub>2</sub> ]	1	ppb	162
$k_t$	$4.4 \times 10^{-16}$	cm <sup>3</sup> /molec-s	see text
$k_p$	$0.5 - 2 \times 10^{-21}$	cm <sup>3</sup> /molec-s	see text
molecular weight	156	g/mol	see text

section.

The density was estimated based on that of  $\alpha$ -pinene ozonolysis SOA[165]. The molecular weight comes from a moderately oxidized monoterpene with formula of C<sub>10</sub>O<sub>4</sub>H<sub>16</sub>. The viscosity was obtained from  $\alpha$ -pinene ozonolysis SOA at 90% relative humidity.[135] The termination rate constant is diffusion limited under these conditions, with a rate constant of  $4.4 \times 10^{-16}$  cm<sup>3</sup>/molec-s found by assuming the reactants are spherical with diffusivities obtained by the Stokes-Einstein equation.[166] This is highly dependent on the viscosity and by extension the humidity. If the humidity had been around 70%, the estimated termination rate constant for  $\alpha$ -pinene ozonolysis SOA would drop over two orders of magnitude to  $3 \times 10^{-18}$  cm<sup>3</sup>/molec-s.[135]

Due to the complex mixture of SOA and the large dependence of  $k_p$  on structure, the propagation rate is one of the most uncertain parameters. This work uses a rate of  $10^{-21}$  cm<sup>3</sup>/molec-s, which is characteristic of hydrogen abstractions from oxygenated compounds by RO<sub>2</sub>.[167] Given the large uncertainty in  $k_p$ , sensitivity analysis was conducted for this value.

Figure 4-15 shows four characteristics of the system from midnight until 5:00 in the morning, shown on the lower x-axis. The corresponding particle sizes are shown on the top x-axis. Shading in the figures corresponds to a factor of two change

in the propagation rate. Figure 4-15a shows the radical concentrations predicted by stochastic and traditional kinetics. As time progresses, both models predict an increase in the number of radicals per particle. The traditional model starts at one tenth the value of the stochastic model and increases faster as well, decreasing the gap between the two models, so that at hour five, the stochastic model is less than 50% greater than the traditional model. This huge difference in radical concentrations drives the differences in chemistry.

Figure 4-15b shows the change in the chain length, which is the number of reacted molecules per initiation. For both the stochastic and traditional cases, a lower initiation rate increases the radical lifetime allowing for more propagation and a longer chain length. In stochastic kinetics, the lowest initiation rate per particle occurs at the smallest sizes. As the initiation rate per particle increases, the radicals terminate more quickly decreasing the chain length. For the traditional model, the opposite trend occurs because the chain length is determined by the initiation rate *per volume* as opposed to per particle. In this case, since the volume increases faster than surface area during particle growth, there is *less* initiation per volume in larger particles, so the radicals can exist for longer, increasing the chain length over the course of the simulation. The two models rapidly converge with time, in part because the chain length decreases with size for the stochastic model and increases with size for the traditional model.

Figure 4-15c shows rate of oxidation within the particle over time. Given the large chain lengths in Figure 4-15b, most of this oxidation comes from propagation for both the stochastic and traditional simulations. Since propagation is largely determined by RO<sub>2</sub> concentration, this leads Figure 4-15c to look very similar to Figure 4-15a (other than the shaded areas that denote the sensitivity of the oxidation rate to the propagation rate coefficient).

Figure 4-15d shows the fraction of molecules within the particle that have undergone heterogeneous or condensed phase reaction. This value is determined by the history of oxidation rate over time, divided by the total number of molecules, shown by Equation 4.12. To allow for proper spinup, the integral starts two hours before

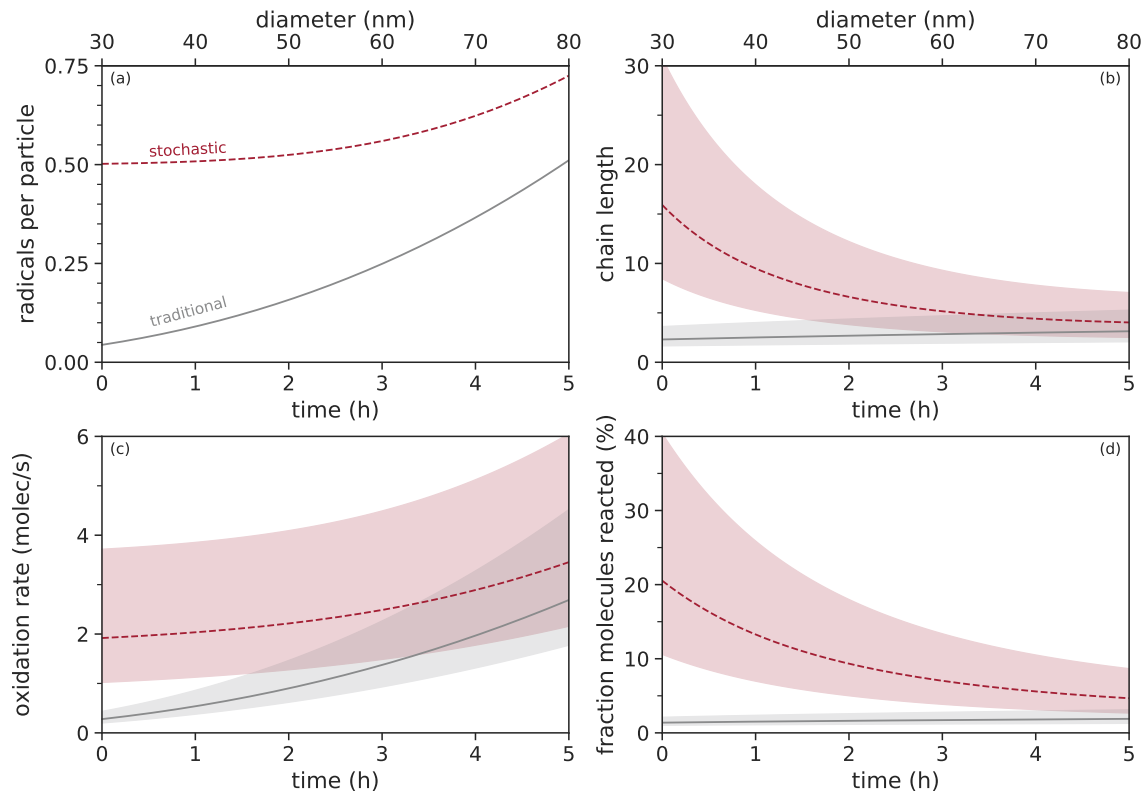


Figure 4-15: Simulated changes in particle concentrations during particle growth, using both stochastic (red, dashed) and traditional (grey, solid) kinetics.[159] Particle diameters on the top of the figure correspond to the times on the x-axis. Shaded regions show the impact of a factor of two change in the propagation rate constant. Part (a) shows the number of radicals per particle over time, part (b) shows the chain length, which is number of molecules reacted per initiation, part (c) shows the oxidation rate, and part (d) shows the fraction of molecules in the particle which have reacted due to heterogeneous processes.

what is shown in Figure 4-15d. This result more directly corresponds to changes in particle properties than the other metrics in Figure 4-15.

$$FR = \frac{\int_{-7200}^t r_i(D_p) + r_p(D_p) dt}{\left(\frac{\pi D_p^3}{6V_{molec}}\right)} \quad (4.12)$$

where  $FR$  is the fraction of molecules reacted in the particle,  $t$  is the time of the simulation in seconds,  $D_p$  is the particle diameter in nm at that given time, (equivalent to  $30+t/360$ ), and  $V_{molec}$  is the average molecular volume calculated from the density and molecular weight. This analysis ignores any effect of partitioning of reacted condensed phase molecules into the gas phase; this is a reasonable assumption for products that are lower in vapor pressure than their unreacted precursors.

Figure 4-15d shows that stochastic kinetics predicts far more heterogeneous oxidation than traditional kinetics. The larger difference in this graph, compared with Figures 4-15b and 4-15c, originates from the particle's history. Despite a decrease as size grows, the reacted fraction in the stochastic case is still over twice the value given by traditional kinetics at the end of the simulation. This could lead to measurable differences in hydroscopicity, toxicity and other properties.

The shading in Figure 4-15 shows the impact in changing the propagation rate by a factor of two; this range was chosen for illustrative purposes, and the uncertainty of the propagation rate is likely larger than a factor of two. No shading occurs in Figure 4-15a since propagation rate does not impact the number of radicals per particle. Shading in the other subplots, however, highlights that the propagation rate strongly effects many of these parameters. More work needs to be done to better determine how fast propagation occurs in complex aerosol mixtures.

## 4.5 Conclusion

For stochastic chemistry to be important in atmospheric aerosols, particles must be small, typically less than 100 nm, have a low viscosity, experience slow heterogeneous initiation from the environment, and have fast propagation chemistry. Higher tem-

peratures and humidity have potential to increase propagation and termination rates, respectively, which both enhance the impact of stochastic chemistry. The magnitude of the stochastic effect is largely dependent on the values of these parameters, with as much as a 100 times faster oxidation rate for non-viscous 40 nm particles with fast propagation rate in an environment with lower than average oxidant concentrations.

Previously published experiments dealing with heterogeneous oxidation by OH fall outside this range of conditions necessary to see stochastic effects due to larger particles, higher oxidation rates and shorter experimental times.

Analysis of remote nighttime particle growth suggests that the fraction of molecules within an 80 nm particle that underwent particle oxidation using stochastic kinetics is over twice what traditional kinetics would predict, indicating that the stochastic chemistry may be important in certain parts of the environment.

Large uncertainties remain in the model that need to be better constrained to better understand this phenomena. While many studies have looked at radical propagation in pure, model aerosols, how much propagation reactions occur in complex, secondary aerosol mixtures and its dependence on temperature and humidity is still largely unknown. Future work should also look into how much particle viscosity inhibits radical termination, and how valid the Stokes-Einstein relationship is when applied to atmospheric particle reactions.

Many experimental techniques involving the generation and measurement of particles work well when diameters are greater than 100 nm, but these techniques often struggle to generate and measure the chemical composition of smaller particles. Developing devices that adequately produce and measure the chemical composition of ultrafine particles would significantly aid in understanding the chemistry of these particles.

The model presented in the this chapter was much simpler than the complex reactions that occur for peroxy radicals. The next chapter describes this complicated chemistry, showing how peroxy behavior changes across temperature, pressures, bimolecular reactants, and structure.

# Chapter 5

## Fate of RO<sub>2</sub> in the atmosphere and combustion

### 5.1 Summary

Organic peroxy radicals (RO<sub>2</sub>) are key intermediates in the oxidation of organic compounds in both combustion systems and the atmosphere. While many studies have focused on reactions of RO<sub>2</sub> in specific applications, spanning a relatively limited range of reaction conditions, the generalized behavior of RO<sub>2</sub> radicals across the full range of possible reaction conditions has, to our knowledge, never been explored. In this work, simulations of pressure-dependent kinetics use two model RO<sub>2</sub> systems: n-propyl peroxy radical and  $\gamma$ -isobutanol peroxy radical. The fate of these radicals was studied over 250-1250 K, 0.01-100 bar, and 1 ppt-100 ppm of NO, which spans the typical range of atmospheric and combustion conditions. Showing the transitions between regimes elucidates how reactions in combustion start to impact atmospheric conditions and vice versa. Two conditions are highlighted: the suppression of the negative temperature coefficient effect by NO and the effect of functionalization on atmospheric isomerization reactions.

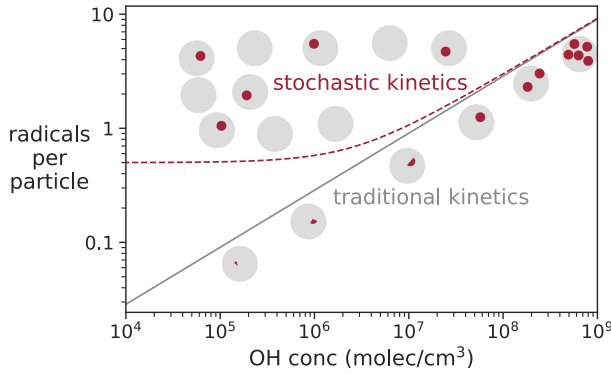


Figure 5-1: Diagram showing fate of gamma isobutanol over various temperatures and pressures.

## 5.2 Introduction

Oxidation of carbon-based molecules drives animal metabolisms, precipitates food spoilage,[168] provides for the world's electricity and transportation,[169] and produces atmospheric pollutants. Since the most abundant atmospheric oxidant, molecular oxygen, is a biradical, oxidation occurs through radical intermediates. An important and ubiquitous class of radical intermediates, the organic peroxy radicals ( $\text{RO}_2$ ), forms when a carbon-centered radical (R) combines with molecular oxygen. Due to their relative stability,  $\text{RO}_2$  radicals can accumulate to high concentrations and react in many competing degradation pathways. Macroscopic phenomena like engine performance, flame propagation, food stability, and atmospheric visibility, depend on which of the many competing reactions dominates the fate of these transient, microscopic intermediates.

Figure 5-2 shows some of the pathways which  $\text{RO}_2$  radicals undergo. Considering the bimolecular reactions (grey arrows in Fig 5-2),  $\text{RO}_2$  reacts with NO to either form an organic nitrate ( $\text{RONO}_2$ ) or an alkoxy radical (RO). When reacting with another peroxy radical,  $\text{RO}_2$  forms either two alkoxy radicals or an alcohol and carbonyl.  $\text{RO}_2$  can also react with  $\text{NO}_2$  forming  $\text{ROONO}_2$ , but the resulting peroxy nitrate isn't always stable.  $\text{RO}_2$  radicals abstract hydrogens from other hydrocarbons and  $\text{HO}_2$  to form an alkyl hydroperoxide ( $\text{ROOH}$ ), which is often a dominant path in a condensed phase or low  $\text{NO}_x$  atmosphere. Reactions with other organic groups also

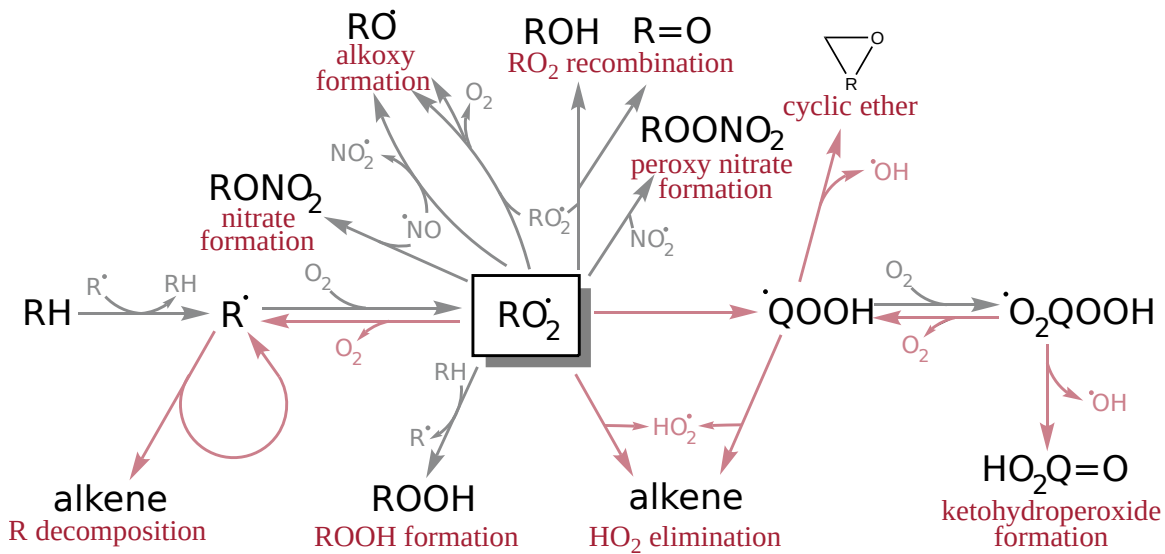


Figure 5-2: Common unimolecular (pink) and bimolecular (grey) reactions of  $\text{RO}_2$ .

occur, like the reaction with alkenes to form epoxides and an alkoxy radical.[170]

In addition to these bimolecular pathways,  $\text{RO}_2$  radicals can react unimolecularly (pink arrows in Fig 5-2). For a particular  $\text{RO}_2$ , multiple intramolecular hydrogen abstractions can result in different hydroperoxyalkyl radicals ( $\text{QOOH}$ ), each with a different fate. Other unimolecular pathways end up decomposing  $\text{RO}_2$  and its corresponding  $\text{QOOH}$  isomers into two or more products:  $\text{R}$  and  $\text{O}_2$ , an alkene and  $\text{HO}_2$ , a carbonyl and  $\text{HO}_2$ ,[143] a cyclic ether and  $\text{OH}$ ,[171] an alkoxy radical and  $\text{H}_2\text{O}$ ,[88] or two fragments each with carbonyl groups and an  $\text{OH}$ .[89]  $\text{RO}_2$  structure dictates the existence and relative importance of these unimolecular pathways. Pressure-dependent behavior at high temperatures, where a highly energetic, chemically-activated  $\text{RO}_2$  isomerizes and breaks apart before it is stabilized through collisions, further complicates the fate of this intermediate.

The lowest energy unimolecular channel, intramolecular hydrogen abstraction forming  $\text{QOOH}$ , is commonly followed by an additional  $\text{O}_2$  addition, a second intramolecular H-abstraction  $\alpha$  to the hydroperoxide group, and the decomposition of one hydroperoxide. The products are an  $\text{OH}$  radical and a molecule with carbonyl and hydroperoxide functional groups, called a ketohydroperoxide (KHP).[97] The KHP can thermally degrade producing two additional  $\text{OH}$  radicals in the process.

This important pathway allows for multiple oxidation steps and the production of the reactive OH radicals. It has domain-specific names like autooxidation in atmospheric chemistry,[172] which is distinct from the liquid phase autooxidation mechanism,[173] and the KHP pathway in the combustion literature.[40]

Traditionally, atmospheric scientists focus on bimolecular RO<sub>2</sub> reactions in the atmosphere and combustion chemists focus on its unimolecular pathways. However, recent work has shown that this clear bifurcation between regimes is not always the case.[174, 175, 176] This work discusses two such cases: ketohydroperoxide formation in the atmosphere and bimolecular reactions with NO in combustion systems.

An atmospheric KHP pathway was first postulated in 2009 to explain an unknown source of OH in forested regions.[177] This reaction sequence had been known for decades to occur in combustion and in liquid hydrocarbons exposed to O<sub>2</sub>. Further work showed that this pathway creates highly oxidized molecules which can make up a significant fraction of the mass of atmospheric particles,[39] influencing both cloud formation and human health.

Similarly, in combustion systems, the role of RO<sub>2</sub> + NO is not typically considered and has been included in a small fraction of models,[178, 176, 179, 180] despite its potential to impact ignition. Exhaust gas recycling (EGR) is a low-NO<sub>x</sub> engine technology that mixes combustion products back into the cylinder inlet and impacts RO<sub>2</sub> chemistry through high concentrations of preignition NO.[180]

Both combustion and atmospheric fields have benefited, and we conjecture will continue to benefit, from exchanging knowledge of RO<sub>2</sub> chemistry. Though most work is still domain specific, recent papers have started to bridge the gap by describing the impact of a specific RO<sub>2</sub> pathway in different applications.[181, 182, 175] Here we take an even more general approach, examining RO<sub>2</sub> branching among a large number of channels (eight in total) and across a wider range of reaction conditions than has been studied previously.

We vary temperature, pressure, and NO mixing ratio since they have significant impacts on RO<sub>2</sub> fate.[183] Temperature largely impacts the rates of unimolecular reactions which can have large activation energies. Higher pressure increases bimolecular

reaction rates by increasing the density of bimolecular reactants and decreases the time between collisions, hindering chemically activated pathways. NO competes with other reaction paths.

Structure also has a huge impact on the peroxy fate. Since the full range of chemical space cannot be examined here, we focus on two model systems which differ in their propensity to isomerize: n-propyl peroxy radical ( $\text{CH}_3\text{CH}_2\text{CH}_2\text{OO}$ ), a simple alkylperoxy radical, and  $\gamma$ -isobutanol peroxy radical ( $\text{CH}_3\text{CH}(\text{CH}_2\text{OH})\text{CH}_2\text{OO}$ ), a functionalized peroxy radical.

### 5.3 Methodology

Figure 5-3 shows the peroxy reactions for n-propyl peroxy radical and  $\gamma$ -isobutanol peroxy radical. To look at behavior of  $\text{RO}_2$  over a wide range of conditions, we combined kinetic data from a range of different sources.

All unimolecular reactions originated from published pressure-dependent reaction networks based on quantum chemical calculations. Bimolecular reactions involving peroxy radicals came from structure activity relationships derived for atmospheric studies.[184] Additional reactions that convert radical products to stable compounds for pathway characterization, like the reaction of an alkoxy product and  $\text{O}_2$  to form a ketone, were estimated using a tree-based kinetic estimation method.[28] Thermochemistry for products not obtained from the published pressure dependent networks was estimated using quantum chemical calculations or group additivity.[28].

Modeling this wide range of conditions necessitates using kinetic parameters that have not been fully validated at all conditions, leading to a decrease in accuracy. We do not expect nor aim for complete quantitative agreement. However, the trends and understanding of  $\text{RO}_2$  described here should hold true.

The model for each peroxy was simulated using Cantera.[185]. A more detailed description below describes the n-propyl peroxy radical and  $\gamma$ -isobutanol peroxy radical models and then discusses how simulations were conducted.

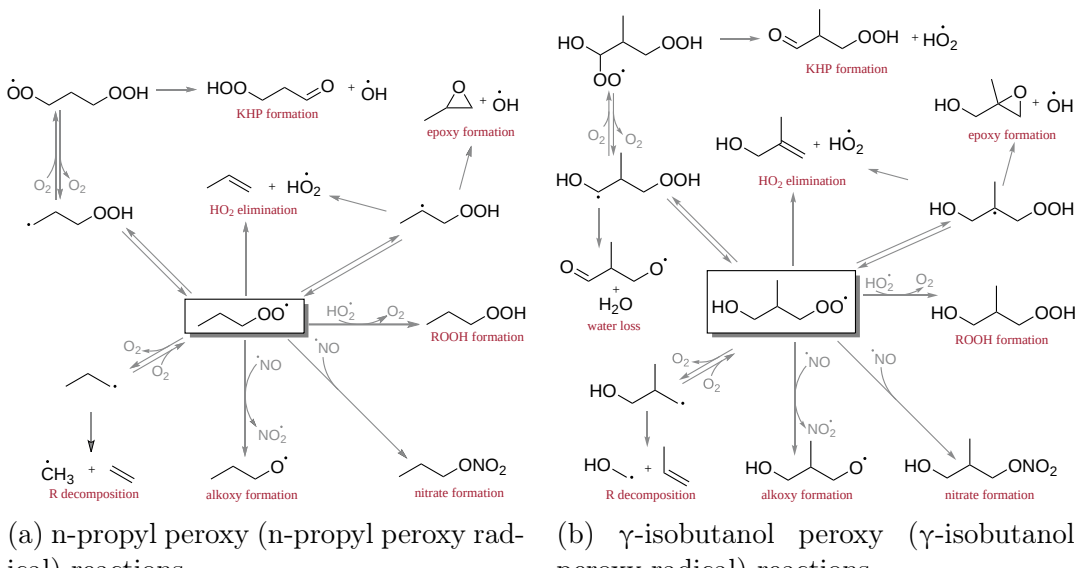


Figure 5-3: Competing pathways considered in this work.

### 5.3.1 N-propyl peroxy model

All the reactions in Figure 5-3a originated from a low temperature propane combustion model, with the exception of the reactions with NO.[40] This previously published mechanism contained oxidation pathways connecting all of its species to the final oxidation products  $\text{CO}_2$  and  $\text{H}_2\text{O}$ . For  $\text{RO}_2$  created from the first and second oxygen additions, the mechanism contained pressure-dependent rates obtained from a master equation using chemically significant eigenvalues with quantum calculations at QCISD(T) level theory with basis set extrapolation.[97] This combustion model has been validated with experiments at 800-1000 K and 30 bar.[186]

We added a combustion NO sub-mechanism to the propane combustion mechanism that has been validated with experiments from 550-1100 K, 1-60 atm, and 0-500 ppm NO.[179] Nitrate formation and four low temperature hydrogen abstraction reactions, which were not available in this submechanism, were taken from Atkinson.[134]

### 5.3.2 $\gamma$ -isobutanol peroxy model

Isobutanol was chosen to highlight the impact of functionalization because, relative to other alcohols like n-propanol, a more extensive pressure-dependent network for

the peroxy radical exists in literature.[187] The pressure-dependent rates originated from solving a master equation with the modified strong collision approximation in the Arkane software package with quantum chemical calculations done at CCSD(T)-F12a/VTZ-F12//B3LYP/CBSB7 theory.[32, 28]

To make the  $\gamma$ -isobutanol peroxy radical model complete, we added bimolecular reactions and subsequent chemistry not contained in the pressure dependent network. Kinetics of peroxy reactions with NO and HO<sub>2</sub> and subsequent hydrogen abstractions by O<sub>2</sub> were obtained from Atkinson.[134]. The oxygen addition to the QOOH radical used kinetics from Miyoshi et al. at the high pressure limit.[103] The isomerization of the second oxygen addition to form a hydroxyketohydroperoxide (not shown in Figure 5-3) came from analogous reactions in Yao et al.,[188] and the isomerization to form the ketohydroperoxide came from Goldman, both at the high pressure limit. Decomposition of  $\gamma$ -isobutanol radical came from Sarathy et al.[87]

### 5.3.3 Simulations

All simulations were conducted using the kinetic solver package Cantera.[185] Starting mixtures were simulated at constant pressure and temperature, unless otherwise noted. An initial alkyl radical mole fraction of 10<sup>-17</sup> was used which minimizes the effect of RO<sub>2</sub> + RO<sub>2</sub> reactions. The mole fraction of HO<sub>2</sub> was set as 10<sup>-12</sup>, which is realistic for the atmosphere, where RO<sub>2</sub> + HO<sub>2</sub> is more important, but is lower than HO<sub>2</sub> concentration in typical combustion systems. The remaining fraction of gas is a mixture of oxygen, 21%, and nitrogen, 79%.

The simulation is run until the concentration of the alkyl radical and its corresponding peroxide are less than 1% of the initial alkyl radical concentration. The final product concentrations are mapped to their formation pathway to determine the branching ratio of RO<sub>2</sub>. This procedure allows the branching ratio to account for the reversibility of RO<sub>2</sub>  $\rightleftharpoons$  QOOH and the well-skipping behavior of pressure-dependent reactions. The exact product to pathway mapping is described in Table 5.2. Some reactions in the n-propyl peroxy radical model were removed to allow proper tracing of radicals, which are listed in Table 5.1.

Table 5.1: Reactions removed from propane model to prevent one peroxy consumption pathway from being conflated with another.

reactions removed	conflated pathways
$\text{C}_2\text{H}_4 + \text{H} (+\text{M}) \rightleftharpoons \text{C}_2\text{H}_5 (+\text{M})$	
$2\text{C}_2\text{H}_4 \rightleftharpoons \text{C}_2\text{H}_3 + \text{C}_2\text{H}_5$	
$\text{C}_2\text{H}_5 + \text{CH}_3 \rightleftharpoons \text{C}_2\text{H}_4 + \text{CH}_4$	
$\text{C}_2\text{H}_5 + \text{H} \rightleftharpoons \text{C}_2\text{H}_4 + \text{H}_2$	
$\text{C}_2\text{H}_5 + \text{O}_2 \rightleftharpoons \text{C}_2\text{H}_4 + \text{HO}_2$	alkoxy with R decomp
$\text{C}_2\text{H}_5 + \text{O}_2 \rightleftharpoons \text{C}_2\text{H}_4 + \text{HO}_2$	
$\text{C}_2\text{H}_5 + \text{allyl} \rightleftharpoons \text{C}_2\text{H}_4 + \text{C}_3\text{H}_6$	
$\text{CH}_3\text{CH}_2\text{OO} \rightleftharpoons \text{C}_2\text{H}_4 + \text{HO}_2$	
$\text{CH}_2\text{CH}_2\text{OOH} \rightleftharpoons \text{CH}_3\text{CH}_2\text{OO}$	
$\text{C}_2\text{H}_5 + \text{O}_2 \rightleftharpoons \text{CH}_2\text{CH}_2\text{OOH}$	
$\text{npropyl} \rightleftharpoons \text{C}_3\text{H}_6 + \text{H}$	R decomp with alkene
$\text{CH}_3\text{CH}_2\text{OO} + \text{NO} \rightleftharpoons \text{NO}_2 + \text{ethoxy}$	
$\text{OH} + \text{propanal} \rightleftharpoons \text{H}_2\text{O} + \text{propionyl}$	alkoxy with isom
$\text{HO}_2 + \text{propanal} \rightleftharpoons \text{H}_2\text{O}_2 + \text{propionyl}$	

## 5.4 Results

### 5.4.1 Temperature dependence

Figure 5-4 shows the product distribution of n-propyl peroxy radical across a range of temperatures at 1 ppb NO and 1 bar. At the lower end, n-propyl peroxy radical reacts bimolecularly with abundant NO forming mostly alkoxy radicals and some alkyl nitrates. If the NO concentration was lower, a significant fraction of RO<sub>2</sub> would react with HO<sub>2</sub> or RO<sub>2</sub> instead. The role of NO concentration is discussed in detail later.

At higher temperatures, unimolecular transformations start to dominate. The dominant pathway at 600 K for propane involves an intramolecular H-abstraction (at the  $\gamma$ -carbon) which is followed by O<sub>2</sub> addition to QOOH. This KHP formation pathway allows for oxidation at multiple sites and leads to OH production, which can form more organic radicals from other organic molecules. At higher temperatures, around 750 K, n-propyl peroxy radical predominately decomposes to propene and HO<sub>2</sub>. This HO<sub>2</sub> elimination occurs either directly from RO<sub>2</sub> or through a  $\beta$ -QOOH

Table 5.2: Products used to identify specific pathways to determine branching ratios. Names use either common names or SMILES strings for representation

pathway	propane product	butanol product
hydroperoxy	n-propyl hydroperoxide	<chem>OOCC(CO)C</chem>
alkoxy	n-propoxy	<chem>[O]CC(CO)C</chem>
	n-propanal	<chem>O=CC(C)CO</chem>
	ethyl peroxy	
	ethyl hydroperoxide	
isom	<chem>O=CCCOO</chem>	<chem>OOCC(C(O[O])O)C</chem>
	carbon monoxide	<chem>O=CC(C)C(OO)O</chem>
		<chem>OOCC(CO)CO[O]</chem>
		<chem>OCC(O[O])(COO)C</chem>
		<chem>O=CC(CO)COO</chem>
		<chem>OCC(OO)(C=O)C</chem>
alkene	propene	isobutanol
water loss		<chem>O=CC(C)C[O]</chem> <chem>O=CC(C)C=O</chem>
R decom	ethene	propene 2-propen-1-ol
nitrate	1-nitro propane	$\gamma$ -nitro isobutanol
cyclic ether	propoxide	<chem>CC1C(O)OC1</chem> <chem>OCC1COC1</chem> <chem>CC(1CO1)CO</chem>

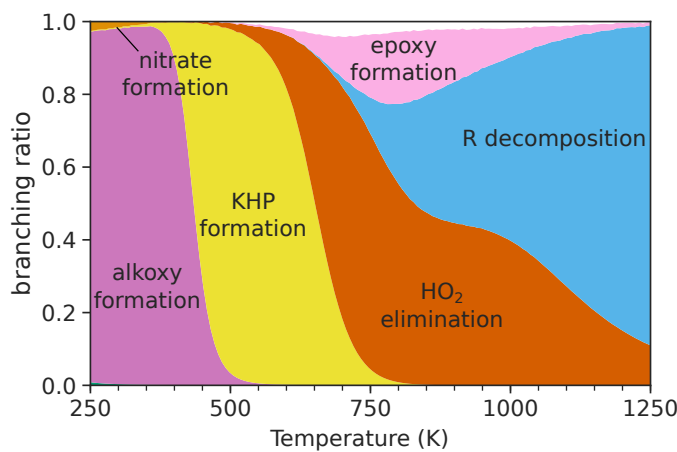


Figure 5-4: n-propyl peroxy radical branching fraction at 1 bar and 1 ppb NO over the range of temperatures relevant to atmospheric and combustion conditions.

intermediate (which is also the intermediate that forms an epoxide).

The transition between forming KHP and HO<sub>2</sub> elimination channels is a competition between two isomerizations: a six member cyclic transition state forming a  $\gamma$ -QOOH and five member transition states leading directly to HO<sub>2</sub> plus alkene or forming a  $\beta$ -QOOH. With higher temperatures, the impact of the activation energy decreases, making entropic differences more important. Since the five member ring involves less entropy loss and a higher activation energy, it more readily competes at higher temperatures. This view is complicated, in part, by the reverse reaction QOOH  $\longrightarrow$  RO<sub>2</sub>, which is also important in this system. For more discussion on the competition between these two pathways, see Merchant et al.[40]

The transition from KHP formation to HO<sub>2</sub> elimination leads to an overall decrease in reactivity with increasing temperature because the latter does not produce the oxidation-promoting OH radical. In the same temperature range as HO<sub>2</sub> elimination, epoxides also form, producing OH and increasing the system reactivity, though not to the same extent as the KHP pathway. The close competition between KHP formation, HO<sub>2</sub> elimination, and epoxide formation is sensitive to the structure of RO<sub>2</sub>.

At the highest temperatures, the n-propyl radical decomposes into ethene and methyl radical before even reacting with O<sub>2</sub> to form RO<sub>2</sub>.

#### 5.4.2 Pressure dependence

While Figure 5-4 shows how temperature variation strongly impacts product formation, it masks the interplay between temperature and other parameters, like pressure and bimolecular reactant concentrations.

Figure 5-5 highlights the impact of changing two variables on branching ratio, with the color representing a linear combination of colors used in Figure 5-4, weighted by the branching ratio of the corresponding pathway. When changing the pressure, the mixing ratio is held constant. Because of this, the concentrations of bimolecular reactants, like HO<sub>2</sub>, NO and O<sub>2</sub>, increase proportionally with pressure. Figure 5-5A focuses on temperature and pressure of n-propyl peroxy radical. The other subplots are discussed in subsequent sections.

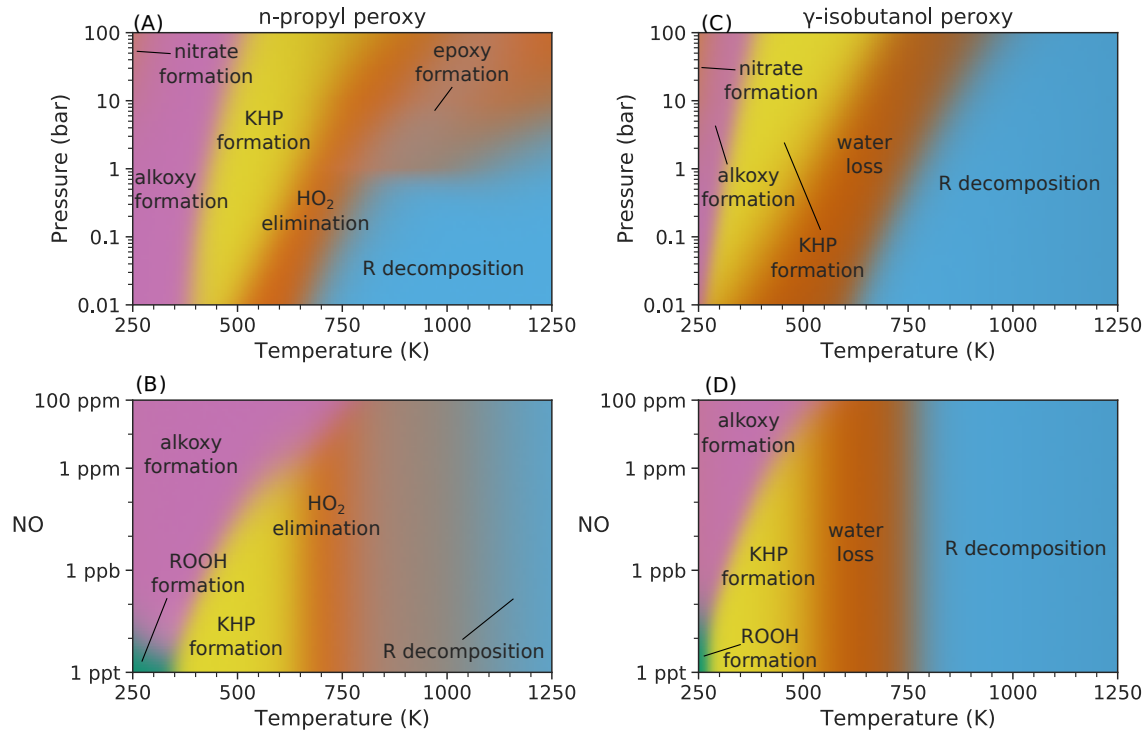


Figure 5-5: Major products from  $R \cdot + O_2$  at various temperatures, pressures and NO mixing ratios at 99% conversion. Parts (A) and (B) show n-propyl peroxy radical branching at 1 ppb NO and  $P=1$  bar, respectively. Parts (C) and (D) show  $\gamma$ -isobutanol peroxy radical branching at 1 ppb NO and  $P=1$  bar, respectively. Names correspond to reactions in Figure 5-3. Colors are linear combinations of pathway colors in Figure 5-4. Simulation details given in the Simulations Section.

For an adiabatic, constant-volume system, pressure has less effect than temperature in determining branching ratio. Looking at a system at 1 bar and 250 K and one at 4 bar at 1000 K, the quadrupling of pressures does not significantly change the products produced in Figure 5-5A. Over the same range, the temperature change passes through four different product pathways.

The pressure effect in Figure 5-5A has two causes: change in pressure-dependent rate coefficients and change in bimolecular reactant concentration. When compared to the variation of concentrations, the pressure-dependence of the rate coefficients only minimally impacts the location of transition regions in Figure 5-5A. For example, the rate coefficient for n-propyl peroxy radical to propene and HO<sub>2</sub> increases by a factor of 250 over the range 0.01-100 bar at 1000 K, which, though large, pales in comparison to the corresponding 10<sup>4</sup> increase in O<sub>2</sub> concentration.

Competition between pathways that differ in the extent of bimolecular reactions would be dominated by this concentration effect. This happens to be the case for three transitions in Figure 5-5A, corresponding to the three branching points in Figure 5-2 that involve unimolecular and bimolecular pathways. At lower temperatures, the effect of pressure is largely due to an increase in number density of bimolecular reactants, which defines the boundary between RO<sub>2</sub> bimolecular reactions and KHP formation. In the next transition, the unimolecular HO<sub>2</sub> elimination starts to compete with KHP formation, which depends on O<sub>2</sub> concentration. At the highest temperatures, the bimolecular formation of RO<sub>2</sub> competes with unimolecular decomposition of the alkyl radical, also leading to a competition depending on O<sub>2</sub> density.

From this, you might suspect that the pressure-dependent rate coefficients are inconsequential. However, they can still impact critical transition points, like the transition from KHP formation to HO<sub>2</sub> elimination in combustion. For example, applying rate constants at 100 bar to a system at 1 bar and 670 K leads to a branching ratio of 29% for KHP formation, compared to 34% from using the rates at 1 bar. Ignoring pressure-dependence can change the system behavior in a measurable way, especially at critical transitions.

There is a visual cliff in Figure 5-5A at 1 bar between 800 and 1000 K, which is an

artifact from how the phenomenological rate constants were derived.[97] This resulted from a workaround to circumvent difficulties when solving the chemically significant eigenvalues for the pressure dependent master equation since RO<sub>2</sub> and QOOH transition from distinct eigenvalues to a single one because of very fast hydrogen abstraction. This transition to indistinguishability occurs as a function of pressure and temperature. The solution involved combining RO<sub>2</sub> and QOOH in the master equation above a certain temperature, and that cutoff temperature varied based on pressure.[97] This inadvertently results in a rate coefficient that is not smooth across various pressures, making understanding the temperature and pressure dependencies in this range difficult. Figure 5-6 shows this explicitly by taking a vertical cross-section of Figure 5-5A across this cliff.

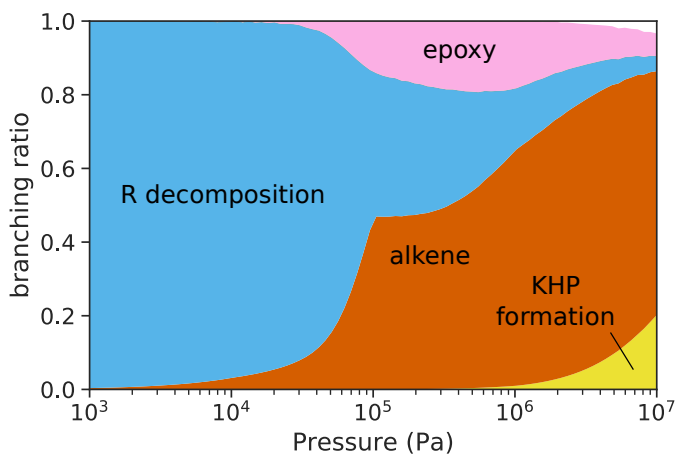


Figure 5-6: Branching ratio of Propane varying pressure at 901 K and 1 ppb NO. The discontinuity at 1 bar of pressure results from the type of pressure dependent fitting using Arrhenius parameters with logarithmic interpolation.

### 5.4.3 NO dependence

Reaction with NO, which primarily forms alkoxy radicals, can also have a significant effect on oxidative processes. The alkoxy radical has higher propensity to break C–C bonds and faster intramolecular H-abstraction than the analogous peroxy radical. The reaction with NO can also form an organic nitrate which transports NO<sub>x</sub> in the atmosphere. Figure 5-5B shows the effect of NO and temperature on the branching

of n-propyl radical + O<sub>2</sub>.

At low temperatures and NO mixing ratios, the formation of hydroperoxides, ROOH, through HO<sub>2</sub> + RO<sub>2</sub> dominates RO<sub>2</sub> fate. As NO mole fraction increases, the bimolecular reactant shifts from HO<sub>2</sub> to NO leading to formation of an alkoxy radical instead of ROOH.

Increasing NO concentration also raises the temperature necessary for ketohydroperoxide formation to compete with RO<sub>2</sub> + NO. With more than 1 ppm NO in Figure 5-5B, KHP formation ceases to dominate at any temperature, which could impact combustion engines with high initial NO concentration.[189]

Above 800 K, unimolecular reactions dominate, preventing even high concentrations of NO from significantly altering branching ratios.

#### 5.4.4 Structure dependence

The subplots for n-propyl peroxy radical and  $\gamma$ -isobutanol peroxy radical in Figure 5-5 highlights differences between the alkane and alcohol peroxy radicals. The  $\gamma$ -isobutanol peroxy radical has an additional unimolecular pathway, involving the formation of water and a ketoalkoxy radical, which represses the HO<sub>2</sub> elimination channel. In addition, the onset of unimolecular chemistry occurs at a much lower temperature due to the alcohol group. These two differences represent two impacts of functionalization: altering bond strengths and creating new potential pathways.

Weakening of the C–H bond by the nearby hydroxyl group decreases the activation energy needed to isomerize, allowing for the 6-membered isomerization to occur over a wider range of conditions forming KHP at lower temperatures.[188, 190, 191, 192] The KHP pathway is slightly different than that of n-propyl peroxy radical. After another oxygen adds to the radical, the second isomerization pulls off the hydrogen from the hydroxy group and breaks a C–O bond forming a carbonyl group and HO<sub>2</sub>, instead of abstracting the hydrogen near the –OOH group forming an OH radical. The presence of the hydroxy group in  $\gamma$ -isobutanol allows for the production of HO<sub>2</sub> instead of OH, leading to less reactive radical products. Both pathways form a hydroperoxy group which can allow chain branching chemistry to still occur.

The OH group also allows for the 6-membered isomerization to occur at higher temperatures than for alkanes. This can be followed by another hydrogen abstraction (from the alcohol) with the simultaneous breakage of the peroxy bond to form water and an ketoalkoxy radical.[88] For  $\gamma$ -isobutanol peroxy radical, this pathway is faster than  $\text{HO}_2$  elimination over all conditions examined. Since  $\text{HO}_2$  elimination has a smaller cyclic transition state, it does have less entropy loss and is more prevalent at higher temperatures, but R decomposition takes over before it is able to achieve a branching ratio of even 10%. The water loss channel, with its relatively low barrier, prevents the oxygen addition necessary for KHP formation at higher temperatures. This forces KHP formation to occur at lower temperatures, which for  $\gamma$ -isobutanol peroxy radical at 1 bar pressure only occurs significantly below 650 K.

The water formation pathway leads to more reactivity than the  $\text{HO}_2$  elimination pathway due to the production of the more reactive OH radical through subsequent decomposition of the alkoxy radical.[88] Despite the production of a more reactive radical, this pathway is not chain branching. Given that this pathway is faster than KHP formation at most relevant combustion temperatures and its lack of chain branching, no two stage ignition behavior should result from fuels forming significant quantities of  $\gamma$ -isobutanol radicals. In larger alcohols more OH production may be possible, since the product from alkoxy decomposition could undergo an additional isomerization.

In summary, the hydroxide group weakened the C–H, significantly reducing the temperature necessary for KHP formation, and added a protic hydrogen, which allowed for a water loss pathway not observed in alkyl peroxy radicals.[88]

#### 5.4.5 Application: $\text{RO}_2 + \text{NO}$ impact on engine preignition

In many low-temperature combustion scenarios, competition between unimolecular  $\text{RO}_2$  transformations, specifically the KHP formation and  $\text{HO}_2$  elimination pathways, control ignition.[40] Figure 5-5 suggests that, with enough NO, bimolecular reactions may overtake these unimolecular pathways.

At 600 K and 2 bar, a typical atmospheric concentration of NO of 1 ppb would react with n-propyl peroxy radical at one-thousandth the rate of intramolecular H-

abstraction. Thus, for NO to affect RO<sub>2</sub> branching ratio in pre-ignition chemistry, there must be an additional source of NO. Before ignition, the level of NO is typically determined by the concentration in the atmosphere. NO and NO<sub>2</sub> are typically produced during and after ignition through various high temperature pathways, with the dominant pathway requiring the thermal breakdown of O<sub>2</sub> above 2000 K.[193] If this post-combustion gas lingers in the cylinder between combustion cycles, it can significantly increase the NO concentration before ignition. If only 1% of the exhaust gas is retained between cycles, it can raise the initial NO<sub>x</sub> concentration to 100 ppb. EGR engines, which intentionally recycle post-combustion gas back into the engine, can obtain pre-ignition NO in the part per million range, which can significantly impact ignition.

However, the higher concentration of NO introduced into the engine does not necessarily shift the overall ignition properties as much as may be expected from Figure 5-5, since upon reacting, the NO cycles between NO<sub>2</sub> and HONO within the combustion system. The exact effect of NO on the branching ratio of RO<sub>2</sub> is dependent on this cycling. To show this effect, Figure 5-7 contains results from an adiabatic, constant volume simulation of propane in air, with an equivalence ratio of one and either 1 ppt or 100 ppm of initial NO. The two NO concentrations emulate non-EGR and EGR engines. For each simulation, Figure 5-7 shows pre-ignition, instantaneous values for [NO]/([NO] + [NO<sub>2</sub>] + [HONO]), the fraction propane consumed, and the peroxy branching ratio.

During ignition under both conditions, the concentration of NO plummets as it gets converted to NO<sub>2</sub>, dampening its effect on peroxy radical fate. During this process, NO increases the initial reactivity of the system, which is shown by the steeper propane consumption slope in the 100 ppm NO case. After NO is converted into NO<sub>2</sub>, the consumption of propane slows significantly. This period of inactivity from 0.15-0.4 seconds is driven by the reaction HO<sub>2</sub> + NO<sub>2</sub> → HONO + O<sub>2</sub>, which consumes radicals and slows ignition. After 0.4 s, most NO<sub>2</sub> has been consumed and the chemistry of the high-NO case resembles that of the low-NO case, with low-temperature KHP pathway initially dominating followed by HO<sub>2</sub> elimination. Overall,

Table 5.3: Reactions grouped to show branching ratios of RO<sub>2</sub> in Figure 5-7 of the main text. Names use either common names or those in Merchant et al.[40]

pathway	reaction
alkoxy from NO	$\text{NO} + \text{npropyloo} \rightleftharpoons \text{NO}_2 + \text{npropyloxy}$
KHP formation	$\text{npropyloo} \rightleftharpoons \text{QOOH}_{-1}$
HO <sub>2</sub> elimination	$\text{npropyloo} \rightleftharpoons \text{C}_3\text{H}_6 + \text{HO}_2$
alkoxy from ROO	$2 \text{npropyloo} \rightleftharpoons \text{O}_2 + 2 \text{npropyloxy}$ $\text{CH}_3\text{CH}_2\text{OO} + \text{npropyloo} \rightleftharpoons \text{O}_2 + \text{ethoxy} + \text{npropyloxy}$ $\text{CH}_3\text{OO} + \text{npropyloo} \rightleftharpoons \text{CH}_3\text{O} + \text{O}_2 + \text{npropyloxy}$ $\text{acetylperoxy} + \text{npropyloo} \rightleftharpoons \text{O}_2 + \text{acetyloxy} + \text{npropyloxy}$ $\text{ipropyl} + \text{npropyloo} \rightleftharpoons \text{O}_2 + \text{ipropyl} + \text{npropyloxy}$
ROOH formation	$\text{C}_2\text{H}_4 + \text{npropyloo} \rightleftharpoons \text{C}_2\text{H}_3 + \text{npropylooh}$ $\text{C}_2\text{H}_6 + \text{npropyloo} \rightleftharpoons \text{C}_2\text{H}_5 + \text{npropylooh}$ $\text{C}_3\text{H}_6 + \text{npropyloo} \rightleftharpoons \text{allyl} + \text{npropylooh}$ $\text{C}_3\text{H}_8 + \text{npropyloo} \rightleftharpoons \text{ipropyl} + \text{npropylooh}$ $\text{C}_3\text{H}_8 + \text{npropyloo} \rightleftharpoons \text{npropyl} + \text{npropylooh}$ $\text{CH}_2\text{O} + \text{npropyloo} \rightleftharpoons \text{HCO} + \text{npropylooh}$ $\text{CH}_3\text{OH} + \text{npropyloo} \rightleftharpoons \text{CH}_2\text{OH} + \text{npropylooh}$ $\text{CH}_4 + \text{npropyloo} \rightleftharpoons \text{CH}_3 + \text{npropylooh}$ $\text{H}_2 + \text{npropyloo} \rightleftharpoons \text{H} + \text{npropylooh}$ $\text{acetaldehyde} + \text{npropyloo} \rightleftharpoons \text{acetyl} + \text{npropylooh}$ $\text{acrolein} + \text{npropyloo} \rightleftharpoons \text{CH}_2\text{CHCO} + \text{npropylooh}$ $\text{npropyloo} + \text{propanal} \rightleftharpoons \text{npropylooh} + \text{propionyl}$ $\text{HO}_2 + \text{npropyloo} \rightleftharpoons \text{O}_2 + \text{npropylooh}$
other	$\text{npropyloo} + \text{R} \rightleftharpoons \text{npropyloxy} + \text{RO}$ $\text{npropyloo} \rightleftharpoons \text{OH} + \text{propoxide}$ $\text{npropyloo} \rightleftharpoons \text{QOOH}_{-2}$ $\text{NO} + \text{npropyloo} \rightleftharpoons \text{npropylONO}_2$

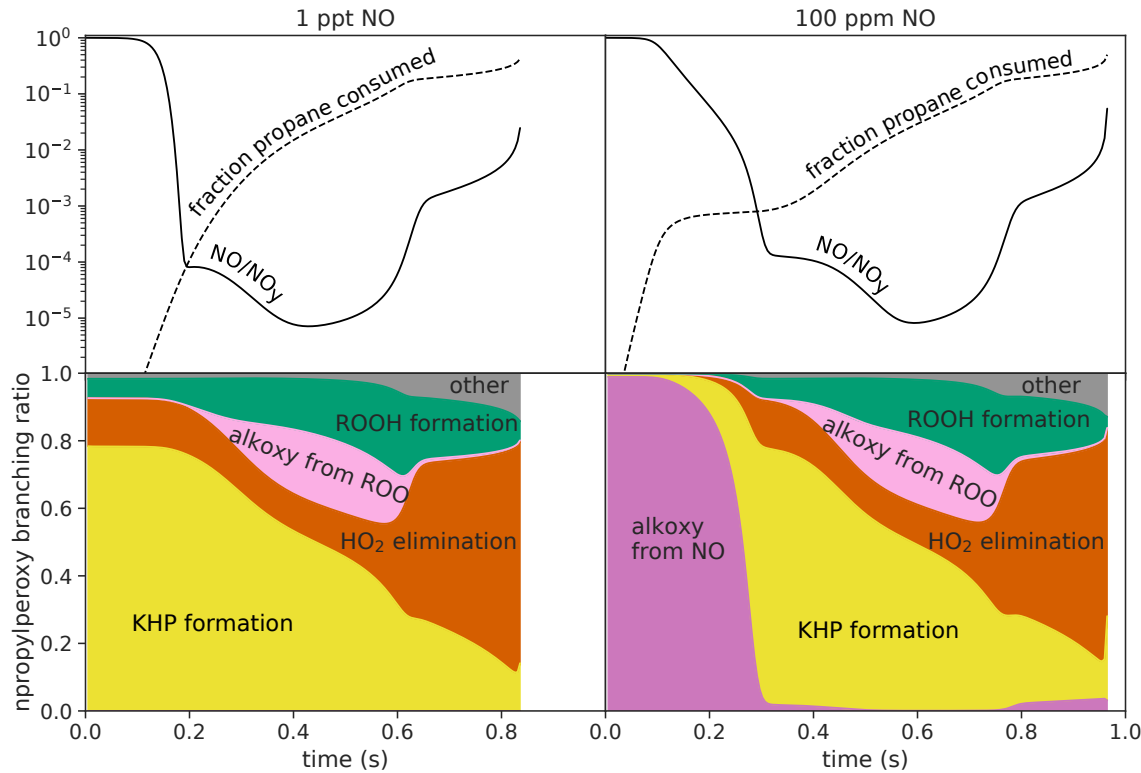


Figure 5-7: Fraction of  $\text{NO}_y = \text{NO} + \text{NO}_2 + \text{HONO}$  as NO (solid lines) and fraction propane reacted (dotted lines) for propane preignition simulation starting with 1ppt NO (left) and 100ppm NO (right). The bottom graphs show instantaneous peroxy branching ratio over the course the simulation obtained by rate of consumption of various pathways, which are listed in Table 5.3 of the Supporting Information. Simulations involved an adiabatic, constant volume system starting at 650 K and 10 bar in air with a fuel/oxygen equivalence ratio of 1.

the ignition timing of propane with 1 ppt NO and with 100 ppm NO differ less than 20% in ignition delay; this minor difference is predominantly due to the decrease in reactivity from HONO formation balancing out the highly reactive alkoxy radicals formed from  $\text{NO} + \text{RO}_2$ .

#### 5.4.6 Application: functionalization allows isomerization in atmospheric $\text{RO}_2$

Just like how bimolecular reaction with NO can impact engine ignition, in the atmosphere where  $\text{RO}_2$  primarily reacts bimolecularly, adding functional groups can enable quick unimolecular chemistry.[183] When at lower, atmospheric temperatures, rates

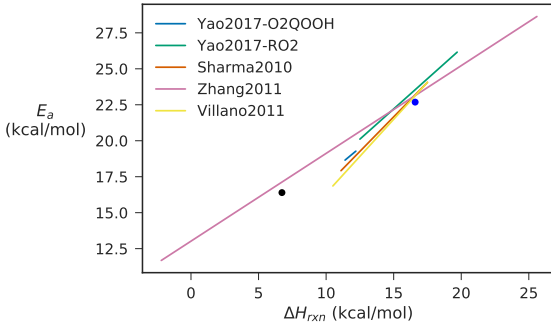


Figure 5-8: Evans-Polanyi relations in literature (lines)[188, 192, 191, 190] The values used in this work for propane (blue circle) and butanol (black circle), with activation energy approximated with enthalpy of reaction at 298 K and activation energy obtained from  $E_a + nRT$  using  $E_a$  and  $n$  from modified Arrhenius parameters and  $T = 600$  K. The high pressure rate constant for propane was obtained from Goldsmith et al.[97] and for butanol was fit using kinetics in the reverse direction and equilibrium thermo.

respond strongly to small activation energy shifts. Functional groups that lower the barrier of unimolecular reactions can help unimolecular RO<sub>2</sub> pathways compete with low-barrier collisional reactions with HO<sub>2</sub>, NO, and NO<sub>2</sub>.

The comparison of n-propyl peroxy radical and  $\gamma$ -isobutanol peroxy radical in Figure 5-5 highlights that under atmospheric conditions the peroxy must have an accessible and weakened C–H bond, typically caused by a nearby functional group, for the KHP pathway to compete. To examine this important effect, we modified our  $\gamma$ -isobutanol peroxy radical model to approximate how a change in bond strength affects the KHP formation branching ratio. This involved increasing the enthalpies of KHP pathway products of  $\gamma$ -isobutanol peroxy radical peroxy according to the change in bond strength and increasing the activation energy for RO<sub>2</sub> → QOOH by 90% of the bond energy change, based on the Evans-Polanyi relationship in Equation 5.1. This Evans-Polanyi parameter,  $\gamma$ , is within literature values (0.61-1.03) for peroxy radical intramolecular H-abstractions with six membered transition states.[192, 191, 188], as shown in Figure 5-8.

$$E_{a,modified} = E_{a,original} + \gamma \Delta E_{C-H} \quad (5.1)$$

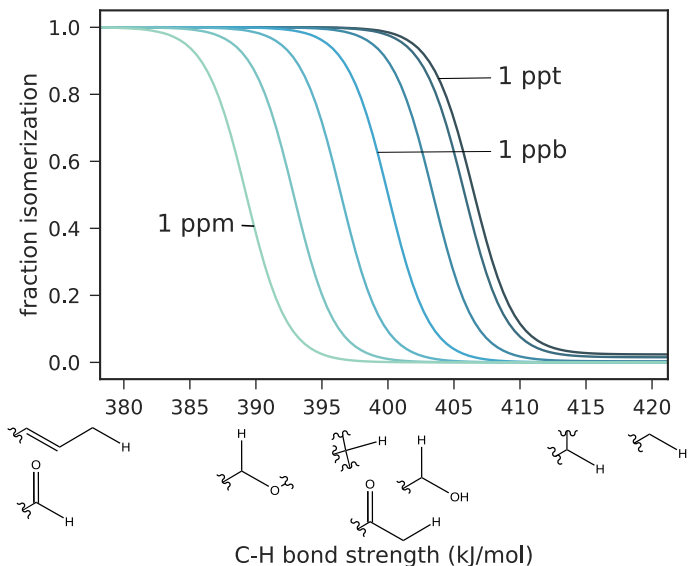


Figure 5-9: Fraction of KHP formation at 300 K, 1 bar, and 10 ppt  $\text{HO}_2$  with various C–H bond energies and mole fractions of NO. Common functional groups are shown below the bond energies to which they correspond.[194]

where  $E_{a,original}$  is the activation energy of the high pressure rate constant of  $\gamma$ -isobutanol peroxy radical H-abstraction,  $\gamma$  is the Evans-Polanyi parameter (set here to 0.9), and  $\Delta E_{\text{C}-\text{H}}$  is the change in bond strength.

These modifications to the  $\gamma$ -isobutanol peroxy radical model are shown in Figure 5-9, which relates the energies of different potential substitutions to the branching ratio forming KHP. The bond energy of the unmodified  $\gamma$ -isobutanol peroxy radical was set to 401.2 kJ/mol, the recommended bond strength of the  $\alpha$ -H in ethanol.[194] Since Figure 5-9 uses an Evans-Polanyi relationship only accounting for C–H bond strength, it ignores any differences in the contribution of ring strain due to the substitutions.

According to Figure 5-9, the primary and secondary alkane groups generally have strong bonds that hinder significant KHP formation at room temperature. They will instead react with NO or  $\text{HO}_2$  (the standard pathways in atmospheric chemical schemes). Aldehydic and allylic hydrogens, on the other hand, are typically low enough in bond strength that any atmospherically relevant concentration of NO will not prevent KHP formation. These functional groups also correspond to the hydrogen

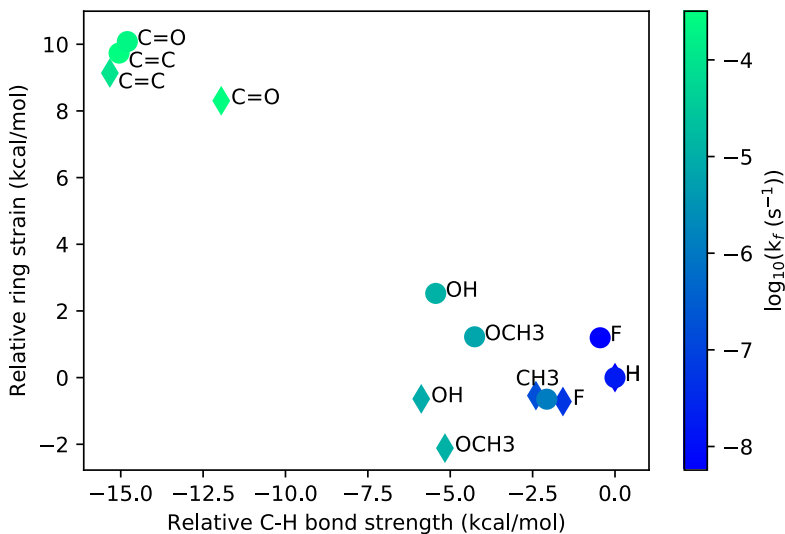


Figure 5-10: Variation in ring strain and bond strength for intramolecular hydrogen abstractions with various functional groups attached to the  $\beta$ -C with a 5-member transition state (diamonds) and attached to the  $\gamma$ -C with a 6 member transition state. Plotted values are relative to the Hydrogen substitution.[198] Relative bond strengths were estimated by the electronic energy difference of the reaction. The relative ring strain was estimated by subtracting the impact on bond strength on the barrier (using an Evans-Polanyi coefficient of 0.9) from the barrier height.

abstraction reactions most often reported in atmospheric literature.[177, 195, 196, 197, 73] Tertiary alkanes, alcohols,  $\alpha$ -ketones, and  $\alpha$ -ethers fall in a range where atmospherically relevant NO concentrations can have a strong impact on the fraction of KHP formed. While Figure 5-9 suggests that some of these pathways can occur in the atmosphere,[73] they appear less common than abstractions involving aldehydes or allylic hydrogens, possibly since slight increments in ring strain can hinder many of these reactions.

Ring strain can vary with functional group, shown by Figure 5-10. This shows a general trend of increased ring strain with lower C-H bond strength. The spread in this trend is a few kcal/mol, which can strongly impact the fate of compounds. This effect of ring strain would decrease the fraction isomerization shown in Figure 5-9.

## 5.5 Conclusions

Despite decades of study, we continue to uncover new pathways of peroxy radicals and better constrain their impacts. Some of these discoveries have involved applying knowledge in one field to another. In this piece, we took a step back from both the atmospheric and combustion applications and showed how the phenomena in both fields can be related to the same underlying principles.

$\gamma$ -isobutanol peroxy radical's hydroxide functionalization causes both the formation of highly oxidized molecules in the atmosphere (by having a weaker C–H bond) and prevents KHP formation in combustion (by allowing for well-skipping decomposition of QOOH through water formation). Looking at these two phenomena from a broader perspective, we can see how the lowering of barriers due to functionalization can help explain both observations.

Having a single framework for peroxy radicals can help expand the knowledge in every peroxy-radical-dominated application. In this work, we combined just two fields where these radicals are important. Integrating peroxy behavior from food science, astrochemistry, and biology will further help us gain a better picture of these versatile radicals.

This chapter uses a chemical mechanism that was built by hand-selecting rates and estimates. An alternative is to use machine-generated models, which is applied in the next chapter.

# Chapter 6

## Automated generation of isotope pyrolysis mechanisms

An edited version of this chapter was published by Chemical Geology.[199]

### 6.1 Summary

Position-specific isotope analysis (PSIA) can aid in understanding the origins of molecules. Destructive PSIA requires a model to track isotope substitution through reaction pathways. We present a general method based on the Reaction Mechanism Generator software to construct quantitative kinetic models with atom-specific isotope tracking and kinetic isotope effects during thermal decomposition of model compounds. A propane mechanism produced with this method is compared to experiments. Without tuning kinetic or thermodynamic parameters to experimental data, the mechanism replicated, within experimental uncertainty, the relationship between the parent molecule's position-specific values and the fragments' enrichments. These isotope-specific models can serve as an *in silico* platform to quantitatively assess secondary isotopic reactions which can scramble position-specific enrichments, design and optimize experimental conditions, and test feasibility of PSIA for new compounds. The proposed methodology creates new opportunities for applications in isotope analysis for a range of chemical compounds.

## 6.2 Introduction

Isotopic analysis helps scientists explain the origin of compounds across a wide range of disciplines.[200, 201, 202] Methods for the analysis of isotopic enrichment vary by the information they provide: bulk isotope analysis methods give information about bulk properties of mixtures; compound-specific isotope analysis methods give information about the enrichment of individual molecules in a mixture;[203] and position-specific isotope analysis (PSIA) methods give information about the enrichment at a specific position within a molecule.[43, 204] PSIA is able to obtain information about the origin of specific atoms in a given compound, but often requires more separation steps and more sample mass for similar precision.[205, 206] PSIA can involve destructive or non-destructive means. One widespread non-destructive technique for measuring intramolecular enrichment is nuclear magnetic resonance (NMR).[207] This technique requires high purity, a significant sample size if the sample is around natural abundance, and soluble compounds, somewhat limiting its scope.

Destructive PSIA typically requires conversion of the compound on which PSIA is conducted into smaller analytes, separation of the analytes, and measurement of analyte concentrations and enrichments. Once the analyte concentrations and enrichments are obtained, a model of the conversion is used to convert the analyte molecular enrichments to site preference values, which are the difference in position-specific enrichments on two sites in the original compound. Fragmentation of the parent compound has been done through enzymatic transformations, chemical reagents, electron ionization and/or high temperatures.[208, 209, 210, 211]

One particular type of destructive analysis, *on-line PSIA*, involves pyrolysis to break compounds, gas chromatography to separate products, and an isotope ratio mass spectrometer to measure analytes' bulk enrichments. This technique has been applied to acetic acid, ethanol, propane and other compounds[212, 213, 214, 215, 216] and can sometimes require only nanomoles of sample.[211]

---

Abbreviations: RMG - Reaction Mechanism Generator, RPD - reaction path degeneracy, DRG - directed relation graph with error propagation, PSIA - position-specific isotope analysis, KIE - kinetic isotope effect

One challenge for destructive PSIA is finding a model that can convert fragment enrichments into the parent compounds' position-specific enrichment.[205, 210] The model must determine *filiation*, the mapping between atoms in the parent molecule to a given product. Filiation becomes increasingly difficult to determine when secondary chemistry leads to alternative formation pathways, a process known as *atom scrambling*.[43] To develop a model of filiation, many studies modify the position-specific enrichment by doping a sample around natural abundance with the same compound highly enriched at a particular molecular position to observe changes in fragment enrichments.[215] These experiments are often done at various temperatures to determine the proper condition which obtains high parent compound conversion while minimizing atom scrambling.[43] The data from these experiments contains enough information to determine filiation.[217, 218] In addition to the time necessary to experimentally develop the model, these experiments require reagents enriched at a specific position in the molecule, which can be expensive or unavailable.

An alternative is to use kinetic models to estimate filiation. These models have potential to help experimentalists find ideal experimental conditions, understand the impact of reactive intermediates on isotope enrichments, and develop models to find position-specific enrichments without requiring specially labeled reagents. All of these could significantly improve usability of on-line PSIA for new compounds. Many pyrolysis models are available for studying small molecules that have been analyzed with on-line PSIA, but most lack the ability to track isotopic enrichment.[219] Widely applicable numerical approaches that allow models to track enrichment are very scarce.

Laurent et al. reported a computational atom-tracer approach and illustrated its application by modeling the pyrolysis of toluene into naphthalene.[219] In their approach, a set of conservation equations express the relative abundance of isotope atoms at specific positions within a molecule as a function of time. For each molecule in the reaction mechanism, the position-specific concentrations of the labeled atoms are calculated through an element balance that considers the reactions that either form or destroy the molecule. An essential component of their approach is the transfer matrix, which tracks the structural changes that reactants undergo during a reaction.

An element  $(i, j)$  in the transfer matrix is the probability that a specific labeled atom  $i$  in the reactant becomes atom  $j$  in the product and accounts for the degenerate paths that reactant atoms can follow during the course of the reaction. They developed methods for automatically detecting the most likely transfer matrix without knowledge of the actual movement of atoms. This method works for a vast majority of reactions, but can run into issues in special cases with resonance structures, reactions with significant steric effects, or when different molecules are grouped together to simplify simulations. Laurent et al. recommended manual generation of matrices when the algorithm does not work.[219]

Like Laurent et al.,[219] this paper describes a method which can create mechanisms which can track isotopic enrichment. By utilizing mechanisms created by Reaction Mechanism Generator (RMG),[28] which contains information about the movement of atoms in reactions, this work overcomes the obstacle of manually generating transfer matrices for reactions that do not fit into the methods developed by Laurent et al.[219] In addition, this method also incorporates kinetic isotope effects, has publically available source code, and produces mechanisms which can be simulated with Chemkin or Cantera.

To validate our method, we compare a propane mechanism generated with this method to experimental results. Propane is a good test case since it is the smallest hydrocarbon with multiple unique carbon positions and its position-specific enrichments have been widely studied both computationally[220, 221, 222, 223] and experimentally.[224, 210, 202, 211, 208, 225, 226] This work compares a propane mechanism produced with this method against experimental PSIA data measured by Gilbert et al.[211]

### 6.3 Calculation

The methodology to automatically construct isotope-tracking reaction mechanisms consists of consecutive steps:

1. construct the reaction mechanism without considering isotopologues.

2. reduce the mechanism, if desired
3. add all the relevant isotopologues and their corresponding reactions to the mechanism.
4. simulate the model under experimental conditions.
5. calculate  $\delta^{13}\text{C}$  values from isotopologue concentrations.

Throughout this work, the term *isotopologue* refers to the set of molecules that differ only in isotope compositions. For example, ethane exists as three distinct isotopologues when considering isotopes  $^{12}\text{C}$  and  $^{13}\text{C}$  of carbon:  $^{12}\text{C}-^{12}\text{C}$ ,  $^{12}\text{C}-^{13}\text{C}$ , and  $^{13}\text{C}-^{13}\text{C}$ .

### 6.3.1 Mechanism generation

The construction of the reaction mechanism without isotopologues is performed using RMG, an open-source software tool which enables the construction of detailed reaction mechanisms that model a wide array of radical chemistry processes such as pyrolysis, oxidation, and catalytic systems.[28, 227, 228, 229, 230, 231] Thermochemical and kinetic parameters of species and reactions in the reaction mechanism originate from structure-based estimation methods using databases of parameters known from experiments or high-level quantum chemistry calculations.

The software requires information on the system of interest: the structure of reactants, the operating conditions (temperature, pressure, final reaction time and reactant starting concentrations), and the parameters that control the complexity of produced reaction mechanism. In addition, the user can also select the databases that are used for the estimation of thermochemical and kinetic parameters. After being initialized with this information, RMG constructs the model through an iterative procedure using a rate-based enlargement scheme.[28]

RMG's iterative enlargement procedure begins with the creation of all possible reactions between the reactants, using RMG's collection of reaction templates that track

how atoms in the reactants rearrange to form products. For each of the generated reactions, RMG estimates the reaction rate constant and the thermodynamic properties of newly generated products. Next, an ordinary differential equation solver quantifies the concentrations of all species in the mechanism as a function of time and evaluates the importance of the newly generated products. The iterative procedure continues until RMG is no longer able to find new products that are kinetically important.[28]

The propane mechanism used in this work was created by RMG assuming 1 mol% propane in 99 mol% helium at a temperature of 850°C and a pressure of 2 bar with a reaction time of 0.1 seconds and a normalized flux cutoff, which is used to determine model size, of 0.1. More information about how to construct mechanisms using RMG can be found in Section 6.3.6 of the Supporting Information.

Three reduced mechanisms are derived from the mechanism output by RMG, called the ‘full model’, to assess the potential of model reduction in isotope analysis. The largest reduced model utilized directed relation graph with error propagation (DRG) in Reaction Workbench, which removes species and their corresponding reactions until a specified error is reached in target species concentrations.[232, 233] The target species in this work were the three species used in deriving site preference in Gilbert et al.[211]: ethane, ethene and methane. The tolerance in their final mole fractions was set to 25% at a temperature of 850°C, a pressure of 1.75 bar, and a residence time of 0.0846 seconds (see Section 6.3.5 of the Supporting Information).[211] The other two reduced models were reduced manually to minimize and maximize atom scrambling.

### 6.3.2 Symmetry and degeneracy improvements

As discussed in Chapter 2, incorrectly estimating the symmetry number for a reaction can have huge consequences on isotope enrichment. Since this project deals with isotopes, getting correct symmetry values for species and reactions is critical.

RMG currently uses a set of heuristics for estimating symmetry of molecules.[234] This is faster than using graph-automorphism (which also requires some heuristics), but less robust.[235]

This section goes over some of the issues and improvements in RMG with regards to symmetry, and is broken down into sections discussing the molecular symmetry input into thermodynamic calculations (which affects kinetics when the reverse rate is estimated) and the reaction path degeneracy algorithm used by RMG to calculate the reaction symmetry number.

## molecular symmetry

**resonance structure symmetry** Resonance structures can affect the symmetry of molecules, and this needed to be accounted for in RMG. To explain this, the example of allyl radical is used. RMG previously obtained a symmetry number of two for allyl radical, shown in Figure 6-1, based on the ability of the two hydrogens on the radical carbon to rotate. Because allyl has delocalized  $\pi$ -electrons, the two hydrogens are not actually able to rotate. Instead, the mixture of the two resonance structures has rotational symmetry around the central carbon, giving this molecule a symmetry of two.

Both of these give the same symmetry number for allyl radicals without isotopic variation, which makes the problem more complicated. If one of the terminal carbons is labeled with  $^{13}\text{C}$ , then the symmetry based around the central carbon would be broken. This would not be accounted for using the previous method, assuming the hydrogens could rotate. A change like this could result in enrichments around 100%, which would be unacceptable in this work.

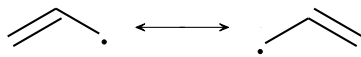


Figure 6-1: The allyl radical has two resonance forms. The molecule is symmetry about the middle carbon, which neither resonance structure is able to capture

To fix this issue, a graph of all the resonance structures is created averaging the bond number of various resonance structures, and this hybrid structure is used in determining symmetry. This change fixed the resonance-based symmetry misclassifications.

**symmetry of cyclic structures** Estimating symmetry of cyclic structures can also be tricky when using a two-dimensional graph. The previous algorithm[234] ignored the order of substituents on cyclic backbone, so a new method was written to address these issues.

This new method approximates a cyclic structure as two-dimensional, uses subgraph isomorphism to determine which groups on the ring are identical or not. It then assesses the symmetry in two ways. One is to see if flipping the ring at any atom or bond results in the same structure, which each would double the symmetry number. It then assesses whether rotating the cycle can result in the original configuration and how many times this happens.

Slight corrections are also made for chiral centers when flipping the ring because this can change the three-dimensional orientation.

These corrections allow for correct symmetry of many single cyclic structures, but still struggle with fused polycyclic rings. This method also reduced the time to find the symmetry of cyclic molecules by 50%.

**chiral effects on molecular thermodynamics** Since isotope labeling can change the number of chiral centers in a molecule, this must also be appropriately accounted for. While chirality is not symmetry, this was included in the symmetry algorithm since they both required identifying the number of different groups on each atom. The algorithm for symmetry was updated so that for each chiral center, the symmetry number was halved, since two distinct structures could exist. This assumes that all molecules consist of racemic mixtures, which is not always the case.

### reaction path degeneracy

Determining the number of ways a molecule can react, called reaction path degeneracy (RPD), is an alternative method to determine reaction symmetry numbers. In addition to fixing the symmetry for resonance structures, the RPD algorithm also had to be adjusted to properly deal with resonance structures and multiple transition states. The steps in the updated algorithm are listed below for a bimolecular reaction.

1. Label all the atoms for each reactant, so each atom can be independently identified.
2. Generate resonance structures for the reactants.
3. Determine all the product structures for every combination of resonance structures of the two reactants.
4. Eliminate duplicate product structures that are identical (including the atom labeling). This uses all product resonance structures to make the match.
5. Separate products based on the template that was matched, since they are distinct reactions.
6. Sum together all the product structures which are identical (ignoring the atom labeling). This is the reaction path degeneracy value for this reaction.

This method allows for RMG to adequately count the reaction path degeneracy for resonance structures, and identify and account for reactions with multiple pathways. This prevents the output rate from being dependent on which order the reactants and resonance structures are used when generating reactions, which previously was an issue with product branching ratio. Just like the RMG method before this, RMG does not adjust a rate coefficient for radical delocalization not contained in the rate rule tree structure.

## **limitations**

The symmetry algorithm in RMG is heuristic based, so it is likely to fail on molecular structures not considered before. A more fundamental method based on graph automorphism has been written into GENESYS, but this method also needed ample heuristics to account for discrepancies.[235] When estimating symmetry from a 2D graph, 3D structure information seems to be lost, leading to a need for heuristics even with a fundamental approach. For example, cyclohexane has a symmetry number of 6 and benzene has a symmetry number of 12. With just graph information, it is

not feasible to account for the difference between planar benzene and the 3D chair conformer of cyclohexane.

Degeneracy also can have caveats, and even when applied rigorously, it is not fundamentally accurate.[46] RMG’s degeneracy algorithm is not the most rigorously applied. Most formulations of degeneracy recommend looking at the transition state to determine duplicates,[45, 47] but RMG looks at product structures for this decision. A more fundamental approach would be to use symmetry numbers of reactants and transition states to determine symmetry’s effect on reaction rate. Though from the previous discussion about difficulties getting symmetry properly from 2D graphs, switching to symmetry will likely end up even less accurate than RMG’s implementation of degeneracy.

To help future users of RMG to ensure that their isotope model has consistent symmetry, two modules in the isotope code check for discrepancies in molecular symmetries and reaction path degeneracy, described in Section 6.3.3. These automatically run after the model generation to warn users if the models are not consistent before they are used to estimate isotopic enrichment.

### 6.3.3 Isotope generation

RMG can convert a mechanism without isotopologues into a mechanism containing isotopologues and their corresponding reactions. This is achieved by the creation of all possible isotopologues for every given molecule in the mechanism, followed by the creation of the corresponding reactions between the newly created isotopologues. Though current implementation is limited to  $^{13}\text{C}$  isotopes, the framework can be extended to other isotopes.

#### enumerating isotopologues

The creation of isotopologues is done by replacing an unlabeled atom from the original species with an atom of a different atomic mass. Graph isomorphism ensures the uniqueness of a newly generated isotopologue from other isotopologues. For example,

provided that only one  $^{13}\text{C}$  atom is allowed per isotopologue, the introduction of a  $^{13}\text{C}$  atom in propane creates two unique isotopologues: one isotopologue with  $^{13}\text{C}$  at the terminal carbon atom,  $^{13}\text{CCC}$ , and one isotopologue with  $^{13}\text{C}$  at the central carbon atom,  $\text{C}^{13}\text{CC}$ .

Though isotopologues have slight differences in enthalpy, this is not considered in the generation algorithm here, which means that no equilibrium isotope effects can be modeled. Entropy is adjusted, since a significant increase is observed with the loss of rotational symmetry in some isotopologues. Isotopically enriched compounds are given higher entropy if the substitution results in loss of molecular symmetry. For example, the implemented method gives the propane isotopologue  $^{13}\text{CCC}$  a higher entropy by  $R \ln(2)$  than the un-labeled propane isotopologue CCC, since the symmetry across the center carbon is broken with the substitution.

### enumerating reactions with isotopes

The software can generate reactions between the newly created isotopologues in two ways, which differ in speed and robustness. A species-centric method includes isotopologues when generating the reactions using the method of Section 6.3.1. The other method, which is reaction-centric, takes each reaction in the original model without isotopologues and substitutes isotopes into the reactants and products in as many ways as possible. The first method is more time consuming and robust, while the second algorithm can create smaller mechanisms, containing only the desired reactions. The second method is less robust because it would not find reactions like  $\text{CC}^{13}\text{C} \rightleftharpoons ^{13}\text{CCC}\cdot$ , since the reaction without isotopes would contain the same molecule as a reactant and product, so it would not be in the original model. Lacking these reactions can cause the second method to predict less atom scrambling.

The algorithm estimates the rate coefficients of reactions involving  $^{13}\text{C}$  isotopologues based on the structure of their unlabeled counterparts, with adjustments for reaction path degeneracy (RPD) and kinetic isotope effects (KIE). RPD is the number of ways that the same transition state structure can be obtained using different atoms and is an alternative method to deduce reaction symmetry.[48] RPD is applied

by multiplying the RPD by the preexponential factor in kinetics estimation.[47] For example, a hydrogen atom can abstract four hydrogens from a methane molecule, each with the same energy barrier, giving this reaction a RPD of four. When isotopes are present in reactions, the RPD could change, altering the rate of reaction. For example, in the reaction  $\text{CCC} + \text{H}\cdot \longrightarrow \text{CCC}\cdot + \text{H}_2$ , containing all  $^{12}\text{C}$ , the hydrogen atom can pull six different hydrogens and form the same, un-enriched, n-propyl radical. When one terminal carbon is substituted with  $^{13}\text{C}$  on propane, two distinct isotopologues of n-propyl can be formed, one with an enriched methyl group,  $^{13}\text{CCC}\cdot$ , and one with an enriched radical group,  $\text{CC}^{13}\text{C}\cdot$ . Each of these pathways can only involve the abstraction of three hydrogens, as opposed to the unsubstituted case which could abstract six hydrogens, giving these reactions half the RPD of the unsubstituted reaction. The isotope model would list these three reactions separately, with the terminally substituted reaction having approximately half the rate of the unsubstituted case, with some additional smaller changes based on KIE. The symmetry and RPD changes ensure isotopologue thermodynamics and kinetics are consistent.

### estimating kinetic isotope effects

To get more accurate enrichment values, the algorithm needs to estimate KIE in a way which only uses the information available within RMG and can be automatically applied to a wide variety of reactions. Based on these constraints, the algorithm is only able to account for classical, mass-dependent KIE, which captures the effect heavier isotopes have on the speed at which a bond breaks. Fortunately, this is often the largest contributor to the total KIE, and [236] describes in detail how it can be applied to two atom and three atom reactions. This approximation assumes only high-temperature effects (so the resulting KIE is not temperature dependent), neglects changes in zero point energy (so it does not contain any equilibrium isotope effects), accounts only for the reacting centers' atomic mass,[237] and assumes tunneling does not change between isotopologues (which is reasonable for non-hydrogen isotopes). With these assumptions, the rate constant ratio approximately equals the ratio of the imaginary vibrational frequencies of the transition state, shown in Equation 6.1.

$$\frac{k_i}{k_o} \approx \frac{\nu_i^\ddagger}{\nu_o^\ddagger} \quad (6.1)$$

where  $o$  represents a non-substituted reaction,  $i$  represents the intended reaction,  $k$  represents the rate constant, and  $\nu^\ddagger$  represents the transition state frequency.

Since it is unfeasible to calculate the imaginary frequency with quantum calculations for every transition state, the algorithm approximates the vibration frequency, using reduced masses of the atoms which either have a bond formed or broken. The exact atoms chosen depends on the type of transition state given by the reaction template. Templates for transition states centered on two atoms, which involve either one bond forming or breaking, like radical recombination reactions, are approximated with Equation 6.2. Reactions whose transition states involve three active atoms, which involve one bond forming and one bond breaking, like hydrogen abstraction reactions, are approximated with Equation 6.3, with atom 3 being transferred symmetrically between atom 1 and atom 2, as described by [236].

$$\frac{\nu_i^\ddagger}{\nu_o^\ddagger} = \left( \frac{\frac{1}{m_{i1}} + \frac{1}{m_{i2}}}{\frac{1}{m_{o1}} + \frac{1}{m_{o2}}} \right)^{1/2} \quad (6.2)$$

$$\frac{\nu_i^\ddagger}{\nu_o^\ddagger} = \left( \frac{\frac{1}{m_{i3}} + \frac{1}{m_{i1}+m_{i2}}}{\frac{1}{m_{o3}} + \frac{1}{m_{o1}+m_{o2}}} \right)^{1/2} \quad (6.3)$$

These relationships represent classical representations of isotope effects, and only use the atomic mass,  $m$ , of the atoms involved. This section discusses the assumption that the three member transition state is symmetric as opposed to asymmetric. Both of these types of transition states are given different approximations for kinetic isotope effect, so determining which function to use in RMG is important.[236] In this description,  $A$  is the left atom,  $B$  is in the center and  $C$  is on the right. In both the symmetric and asymmetric reactions, the bond between  $A$  and  $B$  is broken and the bond between  $B$  and  $C$  is formed. The framework that Melander and Saunders used to derive kinetic isotope effect assumes  $A$ ,  $B$  and  $C$  are collinear.[236]

A symmetric transition state is characterized by little change in the distance



Figure 6-2: The movement of a symmetric transition state (a) and asymmetric transition state (b) as described by Melander and Saunders.[236]

between  $A$  and  $C$  and a movement of  $B$  toward  $C$ . An asymmetric transition state involves little change in distance between  $A$  and  $B$  and a decreasing distance between  $C$  and both  $A$  and  $B$ . The movement of atoms, shown in Figure 6-2, can be determined by the motion corresponding to the imaginary frequency of the transition state.

In the reactions found in the propane model,  $B$  is always a hydrogen atom, though this is not generally necessary. To exemplify whether the reaction is symmetry or asymmetric, an example of hydrogen abstraction from methanol by  $O_2$  is used since it involves three different atoms, shown in Figure 6-3. The frequencies and geometry for the transition state were found at b3lyp/cbsb7 using Gaussian03 software package. For the single imaginary frequency, at  $-832\text{cm}^{-1}$ , the magnitude of the three atoms that involving form or break bonds is shown in Table 6.1 and visualized as green arrows in Figure 6-3.

The center atom, hydrogen, has over ten times the magnitude of either other atom. In addition, the X and Z direction have the carbon and oxygen moving in the same direction, while the hydrogen moves in the opposite direction of the other two atoms. In this example, the transition state frequency fits what we would expect from a symmetric transition state. The behavior likely results from the large mass differences between the hydrogen and either heavy atom. Since the model only has hydrogen transferring in three member transition states, this work assumes all three member transition states are more accurately described by the symmetric as opposed to asymmetric kinetic isotope effect formulation.

The values predicted by this method have systematic and random deviations from the real KIE values, shown here by comparing the estimate in this work with quantum calculations. For reactions where a linear hydrocarbon breaks to form a labeled methyl

Table 6.1: Magnitudes of vibration given by imaginary frequency of hydrogen abstraction from methanol by molecular oxygen.

atom	magnitude	X	Y	Z
carbon	0.07	-0.05	-0.02	0.04
hydrogen	0.98	0.71	-0.12	-0.66
oxygen	0.06	-0.01	0.05	0.04

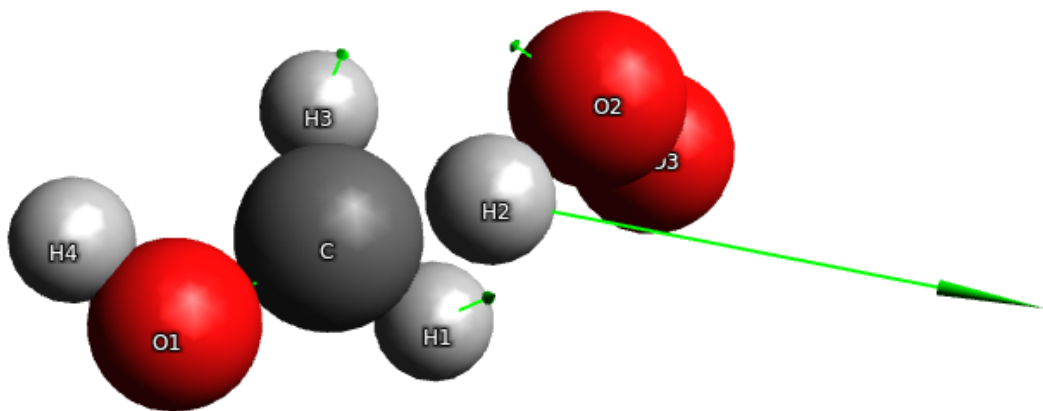


Figure 6-3: The transition state structure for hydrogen abstraction from methanol, with atom H2 being transferred between C and O2. The green arrows indicate the motion along the imaginary frequency of the transition state.

( $^{13}\text{CH}_3$ ), ethyl ( $^{13}\text{CH}_2\text{CH}_3$ ) or propyl ( $^{13}\text{CH}_2\text{CH}_2\text{CH}_3$ ) radicals as a product, [238] calculated primary fractionation factors ( $^{13}k/^{12}k$ ) between 0.951-0.958 at 300K and 0.985-0.987 at 600K using density functional theory. The approximation in this work, Equation 6.2, results in a value of 0.981 which is independent of temperature and applied to all 2-atom transition states. Since the simulation ran at 850°C (1123K), we would expect the fractionation factor should be higher than the 0.985 calculated at 600K, as the KIE generally decreases with increasing temperature. Since the algorithm in this work uses an fraction factor lower than expected (further from unity), it slightly over-predicts KIE for this type of reaction.

This generation algorithm has the major advantage that it can create a detailed kinetic model including all isotopologues, even for complicated reactive systems, within hours or days. It can generate models for the thermal chemistry of a wide range of compounds containing hydrogen, oxygen, carbon, and sulfur. The model it creates can be simulated on both commercial and open software platforms.

### minimizing model size

Generating isotopic mechanisms this way has some limitations. The enumeration of every isotopologue and their corresponding reactions causes the model size to increase exponentially with the number of carbons in the largest molecule in the model. This issue can be minimized by limiting the number of heavy atoms.

For  $^{12}\text{C}$  and  $^{13}\text{C}$  substitutions, the number of isotopologues for a compound approximately doubles for each carbon added, leading to an exponential growth in complexity with molecule size. At the same time, the fraction of a compound that has  $^{13}\text{C}$  for each carbon spot decreases approximately with the  $^{13}\text{C}$  abundance for each additional carbon. Given this information, it might be possible to ignore a large number of isotopologues with many substitutions while making only a minimal error.

In the software, the attribute `--maximumIsotopicAtoms` [integer] ignores isotopologues with more than a certain number of  $^{13}\text{C}$  spots. This section goes over what the expected error would be for a system that excludes highly enriched isotopologues.

A methane pyrolysis model was created using RMG, with a maximum carbon size to 4 carbons. From this model, four different isotope models were created: one with all isotopologues allowed, and three that limited the number of  $^{13}\text{C}$  carbons to 1, 2 or 3 per molecule. The number of isotopologues and reactions found for each model is shown in Table 6.2. In this analysis, the kinetic isotope effect was not used.

The models were simulated using methane with an enrichment fraction of 1% in 90% helium at constant temperature of 1000K and pressure of 2 bar for 1 second. The enrichments of each model were compared to the full isotopic model, which allowed four  $^{13}\text{C}$  atoms per molecule. Figure 6-4 shows the difference in enrichments for butyne between the model that allowed all isotopologues with the limited models.

Limiting the model to only one enriched  $^{13}\text{C}$  per molecule resulted in about 20‰ error in enrichment. This decreased to less than 0.4‰ when maximumIsotopicAtoms was set to 2, which is about the experimental uncertainty for some experiments.[211] Having more isotopologues led to errors way below the experimental accuracy. Each additional allowed isotopic enrichment level approximately decreases the error by the initial enrichment fraction, which for natural abundance is about 1%.

While there is some change in error with simulation time, the variability is much less than the error introduced between cases of removing isotopologues, shown by the flat lines in Figure 6-4. This indicates that there is little interaction between the dominant chemistry at a point in the simulation and the error introduced by modified maximumIsotopicAtoms.

The isotopic dynamics of different systems can vary from this example. To ensure the error introduced in a model is acceptable, we would recommend running a model altering maximumIsotopicAtoms by 1 to approximate the error that this parameter introduces.

Table 6.2: Sizes of methane pyrolysis models with various maximum in number of  $^{13}\text{C}$  per molecule.

maxIsotopicAtoms	species	reactions
0	24	179
1	78	1963
2	138	5516
3	166	7391
4	171	7603

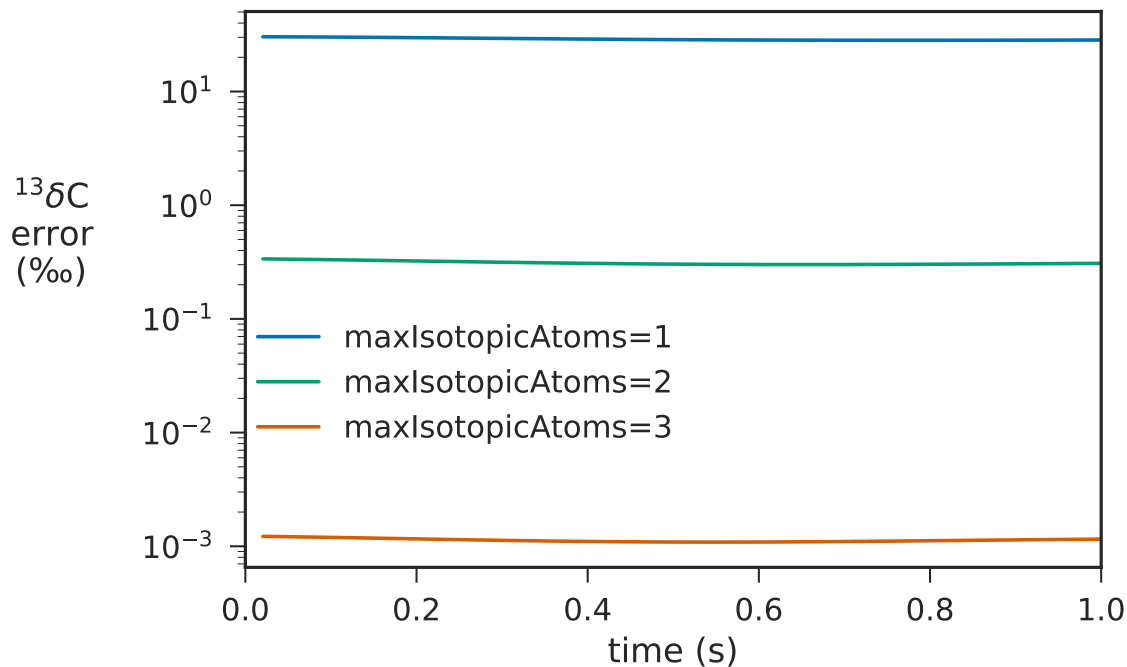


Figure 6-4: Errors in enrichments of butyne for various models created by the `maximumIsotopicAtoms` parameter.

The resulting model is also very sensitive to any mistakes in symmetry and RPD, which is discussed more in Section 6.3.3 of the Supporting Information.

### checking proper symmetry and degeneracy

Isotopic labeling of compounds can lower a molecule's rotational symmetry number, which increases the molecule's entropy, affecting equilibrium ratios and increasing

its reactivity in some reactions. If the symmetry of a labeled compound is incorrect or its corresponding reactions have incorrect RPD, it will result in non-physical enrichments. Estimating symmetry and reaction degeneracy is a constant challenge for automatic mechanism generation, so a check on the symmetry and degeneracy is conducted after model generation to give the user confidence before utilizing this model in experimental analysis.

These checks only are run after all isotopologues and their corresponding reactions are generated, but before kinetic isotope effects are applied. If `--maximumIsotopicAtoms` is used, these checks do not work since these methods require a full set of isotopologues.

**symmetry algorithm** The algorithm to check that the symmetry of isotopologues is consistent utilizes the symmetry of each isotopologue of a compound. Given a molecule with  $N$  atoms that can be labeled in the algorithm, the maximum number of isotopologues that can be created is  $2^N$ . If a molecule breaks symmetry, then that reduces the number of independent isotopologues formed. Using propane as an example, if either terminal carbon is labeled, the central symmetry of the molecule would be broken and the resulting compounds would be identical. Taking this knowledge into account, many incorrect symmetry values can be detected by counting all the isotopologues, with double counting for molecules with broken symmetry.

$$2^N = \sum_{i=1}^M \frac{\sigma_{unenriched}}{\sigma_i} \quad (6.4)$$

where  $N$  is the number of atoms that could be enriched in the system.  $M$  is the number of isotopologues for this structure,  $\sigma$  is the rotational symmetry number,  $\sigma_{unenriched}$  is the symmetry of the compound without any isotope labeling, and  $\sigma_i$  is for isotopologue  $i$ .

The symmetry number effects the entropy of the compound. Since this algorithm occurs before the addition of kinetic isotope effects, Equation 6.4 can be rewritten in terms of entropy.

$$2^N = \sum_{i=1}^M \frac{\sigma_{unenriched}}{\sigma_i} = \sum_{i=1}^M e^{\frac{S_i - S_{minimum}}{R}} \quad (6.5)$$

where  $N$  is the number of atoms that could be enriched in the system.  $M$  is the number of isotopologues for this structure,  $S_i$  is the entropy of species  $i$ ,  $S_{minimum}$  is the minimum entropy of all these isotopologues, and  $R$  is the gas constant. The term  $e^{\frac{S_i - S_{minimum}}{R}}$  is the ratio of symmetry from the unlabeled compound to the labeled compound.

With Equation 6.5, the algorithm for symmetry iterates through all isotopologues of a structure and returns whether Equation 6.5 is True given a certain tolerance. This should ensure thermodynamic consistency in most cases. If RMG predicts the same number of symmetry breaking but for the incorrect compounds, this algorithm will not catch the error.

If there is an error in symmetry estimation `rmgpy/molecule/symmetry.py` can be modified to correct for the source of the error, and the model can be rerun.

**degeneracy Algorithm** This algorithm checks that all reactions differing only by isotope labeling, called isotopologue reactions, are consistent. It is based on the notion that, in an equilibrated isotope system without any kinetic isotope effects, we would expect the fluxes of all products to be related by the equilibrium isotope ratio.

For a set of isotopologue reactions, this method sets the concentration of each reactant and product to the ratio of labeled and unlabeled symmetry numbers,  $\frac{\sigma_{unenriched}}{\sigma_i}$  used in Equation 6.4. Using the rate constant in the forward and reverse directions, it finds the fluxes produced by the reaction. If the fluxes produced by the set of reactions are proportional to their symmetry numbers (indicating thermodynamical consistancy), the algorithm returns true. This equality can be represented for a bimolecular reaction by:

$$\begin{aligned}
\frac{\sigma_{unenriched}}{\sigma_1} &= \sum_{i=1}^N \nu_{i,1} k_i \frac{\sigma_{r1i,unenriched}}{\sigma_{r1i}} \frac{\sigma_{r2i,unenriched}}{\sigma_{r2i}} \\
\frac{\sigma_{unenriched}}{\sigma_2} &\propto \sum_{i=1}^N \nu_{i,2} k_i \frac{\sigma_{r1i,unenriched}}{\sigma_{r1i}} \frac{\sigma_{r2i,unenriched}}{\sigma_{r2i}} \\
&\vdots \\
\frac{\sigma_{unenriched}}{\sigma_M} &= \sum_{i=1}^N \nu_{i,M} k_i \frac{\sigma_{r1i,unenriched}}{\sigma_{r1i}} \frac{\sigma_{r2i,unenriched}}{\sigma_{r2i}}
\end{aligned} \tag{6.6}$$

Where  $M$  is the number of isotopologues of a particular compound in the set of isotopologue reaction,  $\sigma_{unenriched}$  is the rotational symmetry number of an unlabeled version of the isotopologue,  $N$  is the total number of reactions (both forward and reverse) in the set of isotopologue reactions.  $\nu_{i,j}$  is the stoichiometric coefficient of compound  $j$  in reaction  $i$ ,  $r1_i$  is the first reactant in reaction  $i$ ,  $r2_i$  is the first reactant in reaction  $i$ , and  $r1_{i,unenriched}$  is the unenriched version of the corresponding reactant.

If Equation 6.6 is true for all different compounds in the set of isotopologue reactions, the set of reactions should be consistent thermodynamically.

### 6.3.4 Isotope mechanism simulations

Once an isotope mechanism has been created, it can be used to study the evolution of individual isotopologues by integrating a system of ordinary differential equations using simulation parameters (temperature, pressure, initial concentrations, and reactor structure) that match experimental conditions. To do this, experimental units, like  $\delta^{13}\text{C}$ , must be converted to mole fractions of isotopologues, and vice-versa.

Equation 6.7 shows the definition of  $\delta^{13}\text{C}$  used in experimental studies for a molecule or a carbon position on a molecule, denoted as  $x$ , with  $\delta^{13}\text{C}_x$  being the enrichment,  ${}^{13}R_x$  being the ratio of isotope abundance,  ${}^{13}\text{C}_x$  to  ${}^{12}\text{C}_x$ , of the sample  $x$ , and  ${}^{13}R_{std}$  being the ratio of isotope abundance of a standard.

$$\delta^{13}\text{C}_x = \left( \frac{{}^{13}R_x}{{}^{13}R_{std}} - 1 \right) \cdot 1000 \tag{6.7}$$

The model's isotopologue concentrations can be converted to position-specific ratios, shown in Equation 6.7, using the mass balance in Equation 6.8. These can be applied to an entire molecule or to a specific carbon position on a molecule.  $n_{13\text{C},j}$  is

the number of  $^{13}\text{C}$  in isotopologue  $j$  (or at a specific position within the isotopologue), and  $X_j$  is the isotopologue's mole fraction. When trying to find the intramolecular enrichment of the terminal carbons in propane, the  $^{13}\text{CCC}$  isotopologue would have values of  $n_{^{13}\text{C},j} = 1$  and  $n_{^{12}\text{C},j} = 1$ , since only the two terminal carbons are counted. By using equations 6.7 and 6.8, a list of isotopologues can be converted into position-specific enrichments.

$$^{13}\text{C}_x = \sum_{j=0}^{\text{isotopologues}} n_{^{13}\text{C},j} X_j \quad (6.8)$$

Going from enrichment values to isotopologue concentrations, the model stochastically distributes enriched isotopes, ignoring the thermodynamic effects of multiple substitutions. Using this method, about 0.02% of naturally enriched propane is expected to have two  $^{13}\text{C}$  atoms bonded to each other, also known as a  $^{13}\text{C}$ -clumped configuration. Clumped configurations are often thermodynamically favored over stochastic distributions, which has been shown for the case of  $^{13}\text{C}$ - $^{13}\text{C}$  in ethane[239, 240] and  $^{13}\text{C}$ -D in propane.[220, 221, 223] This effect, which is not properly accounted for in our model, is negligible for our analysis of position-specific isotope distributions. In addition, mixing of high and low enrichment samples can also increase the occurrence of  $^{13}\text{C}$  clumping relative to the stochastic partitioning assumed in this work.[210]

Equation 6.9 applies this assumption of stochasticity to determine the concentration of each isotopologue while ensuring mass balance is conserved.

$$X_j = \prod_{y=0}^{\text{C types}} n_{\text{C},x,y} (b_{j,y} + (-1)^{b_{j,y}} X_y) \quad (6.9)$$

where  $j$  is the isotopologue,  $X_j$  is the mole fraction of isotopologue used in the simulation,  $b_{j,y}$  is a boolean indicating that isotopologue  $j$  is  $^{12}\text{C}$  at position  $y$  (0 if substituted, 1 if not substituted), and  $X_y$  is the mole fraction of  $^{13}\text{C}$  at position  $y$ , which is determined from position-specific enrichments.

Converting from position-specific enrichments to bulk enrichments and site prefer-

ence can be done with Equations 6.10 and 6.11. Equation 6.10 relates the enrichment of each carbon atom using the isotope mass balance, with  $\delta^{13}\text{C}_x$  being the enrichment of the molecule  $x$ ,  $n_{C,y}$  being the number of indistinguishable carbons of position  $y$  in molecule  $x$ , and  $\delta^{13}\text{C}_y$  being the enrichment of a specific position  $y$  in molecule  $x$ . For example, propane has two distinct positions, a terminal (denoted  $T$ ) and central (denoted  $C$ ) carbon. Since there are two terminal ( $T$ ) carbons and one central ( $C$ ) carbon on propane,  $n_{C,T} = 2$  and  $n_{C,C} = 1$ .  $n_{C,x}$  is the total number of carbons in molecule  $x$ , which for propane is three. This relationship is only accurate at natural or low enrichments of  $^{13}\text{C}$  since  $\delta^{13}\text{C}$  values derive from ratios (not fractions).

$$\delta^{13}\text{C}_x = \frac{1}{n_{C,x}} \sum_{y=0}^{\text{C types}} n_{C,y} \delta^{13}\text{C}_y \quad (6.10)$$

Site preference can be found using equation 6.11 for a molecule with carbon types  $y$  and  $z$ .

$$SP_{y,z} = \delta^{13}\text{C}_y - \delta^{13}\text{C}_z \quad (6.11)$$

Going the other way, converting from known compound specific enrichments and site preferences to enrichments at specific positions, involves substituting the relationships between positions derived from Equation 6.11 into Equation 6.10. Overall, equations 6.7-6.11 enable complete conversion between isotopologue concentrations and enrichment values.

Since the site preference values calculated in this section come from the concentration of each isotopologue, they take into account all the KIE that are in the model and therefore represent absolute site preference values. There still can be systematic error in the site preference values if the KIE used in model generation are not accurate for the system. To obtain relative site preference values, the compound specific enrichments can be placed into the same equation used to derive relative site preference from experiments.[211]

For the propane pyrolysis example used throughout this work, the initial concentrations of reactants and the reactor operating conditions are set to match the exper-

imental conditions of Gilbert et al.[211] The calculations to derive these conditions, and their corresponding sensitivities, are shown in Section 6.3.5 of the Supporting Information. Most simulations in this work involve an initial propane bulk enrichment of -28‰ and an absolute site preference of 5.4‰ for the terminal carbon to approximate the experimental sample. In experiments that vary the site preference, the central carbon enrichment is set to -28‰ and the terminal carbon enrichment varies from -10‰ to -20‰. The reference ratio used to convert samples is Vienna Pee Dee Belemnite, which has a measured value of  $0.011115 \pm 0.000013$ .[63]

### 6.3.5 Reactor condition calculations

This section discusses the derivations for estimating pressure, residence time and initial concentration, and then it conducts sensitivity analysis to determine that the outlet mole fractions and enrichment are sensitive to neither pressure nor starting concentration and that product distribution but not enrichment is sensitive to residence time.

#### pressure

The exact pressure of the reactor is not reported.[211] The major factors that determine the pressure are the flow rate of  $2.5 \text{ cm}^3/\text{min}$  and the outlet pressure. There is some pressure drop during the 30 meters of column. The material then goes through the pyrolysis capillary before going through another 30 meter GC column, whose outlet is likely near atmospheric pressure since gas chromatograms typically operate higher than atmospheric pressure.

Inputting an outlet pressure of 1 atm, an outlet flow rate of  $2.5 \text{ cm}^3$ , temperature of  $40^\circ\text{C}$  the type of column, and the carrier gas, Agilent's Pressure Flow Calculator estimated a pressure drop of 0.75 bar.[241] of The pressure drop within the reactor, which is over 100 times shorter than the separation columns is assumed to be negligible. In this work, the pressure within the reactor is an absolute pressure of 2 bar, which is 0.24 bar higher than the estimation by Agilent's Pressure Flow Calculator.

The sensitivity of pressure on observables, in Tables 6.7 and 6.8 indicates that this difference in pressure would contribute less than 0.1% to enrichment and less than 0.01 to mole fraction of any analyte.

### residence time

The residence time of the reactor can be determined from the flow rate and size of tubing. The inner diameter of reactor is 0.025 cm and is 25 cm long, which yields a volume,  $V$ , of 0.0123 cm<sup>3</sup>. The standard flow rate through the system is 2.5 cm<sup>3</sup>/min. Since the temperature is higher through the pyrolysis chamber (700-950°C) and the pressure is higher than standard state (2 bar), the estimate of volumetric flow using the ideal gas equation of state is  $\dot{V} = \dot{V}_o \frac{T}{T_o} \frac{P_o}{P}$  where  $\dot{V}_o$  is the volumetric flow rate at  $T_o$  and  $P_o$ . In this analysis, we assume that the measured  $\dot{V}_o$  value of 2.5mL/min, which is given by Gilbert et al.,[211] is set by the outlet of the first GC column, right before the pyrolysis chamber, such that  $T_o$  would be the temperature in the first oven (323-423K), and  $P_o$  is approximately the pressure in the pyrolysis chamber. Since there is no difference in pressure between the pyrolysis chamber and the pressure used to set  $\dot{V}_o$ , the pressure term can be dropped. This leads to a volumetric flow rate dependent on the furnace temperature.

The system's residence time is then given by the volume over the volumetric flow. In this case, we would end up with:

$$\tau = \frac{V}{\dot{V}} = \frac{T_o}{T} \frac{V}{\dot{V}_o} = \frac{95\text{s-K}}{T} \quad (6.12)$$

where  $\tau$  is the reactor residence time, and using the initial temperature of the first column as 50°C. For a temperature of 850°C (1123K), this yields a reactor time of 85 milliseconds.

This analysis has some error since the mixture does not immediately heat up when entering the chamber nor does it immediately cool when exiting, and there is some uncertainty of the exact volumetric flow rate in the pyrolysis tube.

## concentration of propane

While the experimental report does not directly specify the concentration of propane in the pyrolysis chamber,[211] the concentration is important for modeling because it determines the relative importance of unimolecular and bimolecular processes. The concentration is a function of the amount of propane injected into the system and how wide the propane peak is when it reaches the pyrolysis chamber, each of which are estimated in the following two paragraphs.

There are two different conditions of injection used in experiments which lead to different total amount of propane injected into the system: one involved 0.1 mL concentrated propane with a split ratio of 40:1 and the other involved 1 mL 1% diluted propane with a split ratio of 2:1. Taking the split ratios into account, the system would have 0.0024 mL or 0.0033 mL of propane flowing through it for each system respectively. Note that these volumes are at 298K and 1 bar.

The amount of time propane passes through the pyrolysis chamber is not known from complete run of the equipment for online PSIA analysis, since detection occurs after the second GC column. The peak width can be estimated by looking at the output of propane's pyrolysis fragments from the second GC (Supplemental Figure 2 in Gilbert et al. )[211], which is approximately 20-30 seconds. Assuming that half the peak widening occurs during the second GC column (since it is made of the same column and material) this would yield an approximate time of 10-15 seconds through the pyrolysis device.

Using these two estimates, concentration of propane going through the system can be approximated by diving the total injected volume over the time. would be approximately, 0.010 to 0.020 mL/min depending on injection type and peak width estimate. The mole fraction of propane in these experiments would then be the ratio of propane going through the system to helium, which is 2.5 mL/min at 323K and 1.75 bar, with the conditions approximated in Sections 6.3.5 and 6.3.5, which is approximately 4.0 mL/min at 298K and 1 bar. The mole fraction of propane can be found from the ratio of flow rates.

$$X_{propane} = \frac{\dot{V}_{o,propane}}{\dot{V}_{o,He}} \quad (6.13)$$

where  $X_{propane}$  is the mole fraction of propane in the system,  $\dot{V}_{o,propane}$  is the flow rate of propane taken by diving the total propane injection over the peak width of propane when entering the pyrolysis chamber, and  $\dot{V}_{o,He}$  is the standard volumetric flow of helium.

From this analysis, the estimated mole fraction of propane is between 0.25% and 0.50%, depending on injection type and peak width estimate. In this work, the mole fractions used are 0.49% and 0.66% are used for the pure propane injection and natural gas injection respectively. These are at the upper limit of the concentration estimate which is still acceptable for this work since sensitivity analysis shows no significant effects of propane concentration change.

### sensitivity to reactor conditions

How much a change in the reactor condition estimates, approximated in the previous section, affect observable mole fraction and enrichment is necessary to have confidence in the estimates. To assess this dependency pressure, reactor residence time and propane concentration were varied within 20% to determine the sensitivities of condition estimates on the final mole fractions and  $\delta^{13}\text{C}$ . For the unperturbed parameters, the value described above was used. Tables 6.3-6.8 display the sensitivity results of changes in the three variables, propane initial concentration, residence time and pressure, on the two outputs,  $\delta^{13}\text{C}$  and mole fractions.

Over all the sensitivity studies, the change in  $\delta^{13}\text{C}$  by deviating 40% of the original value was less than 0.5%. Since the values of pressure, residence time, and mole fraction are within this range tested, the enrichment errors resulting from these estimates are minimal.

For mole fractions, the change in 40% of the original value minimally changes when propane concentration or pressure was modified. Increasing the propane concentration actually resulted in more conversion, indicating a positive feedback cycle, though the

Table 6.3:  $\delta^{13}\text{C}$  of various compounds after the reactor with change in starting propane concentration. The first five columns represent the fractional change in starting concentration and the last column represents the sensitivity coefficients.

Compound	0.8	0.9	1.0	1.1	1.2	$\frac{\delta\delta^{13}\text{C}}{\delta X_{o,C3H_8}} (\text{\%})$
methane	-24.16	-24.08	-24.03	-23.99	-23.96	102.99
ethyne	-31.98	-31.90	-31.83	-31.77	-31.71	134.52
methyl	-22.32	-22.31	-22.32	-22.33	-22.35	-16.05
ethane	-41.33	-41.29	-41.26	-41.24	-41.22	53.31
propene	-23.50	-23.54	-23.59	-23.63	-23.67	-87.91
propane	-24.78	-24.78	-24.78	-24.78	-24.78	-1.85
ethyl	-32.11	-32.02	-31.95	-31.88	-31.82	147.58
ethene	-32.04	-31.95	-31.88	-31.81	-31.75	148.96

Table 6.4: Fraction carbon of various compounds after the reactor with fractional change in starting propane concentration. The first five columns represent the fractional change in starting concentration and the last column represents the sensitivity coefficients.

Change in starting concentration	0.8	0.9	1.0	1.1	1.2	$\frac{\delta X_i}{\delta X_{o,C3H_8}}$
methane	0.06	0.07	0.07	0.07	0.07	3.79
ethyne	0.02	0.02	0.02	0.02	0.02	1.46
ethane	0.07	0.07	0.07	0.07	0.07	-0.09
propene	0.01	0.01	0.01	0.01	0.02	0.76
propane	0.56	0.55	0.54	0.54	0.53	-12.79
ethene	0.27	0.28	0.28	0.28	0.29	6.62

Table 6.5:  $\delta^{13}\text{C}$  of various compounds after the reactor with fractional change in residence time. The first five columns represent the fractional change in residence time and the last column represents the sensitivity coefficients.

Change in residence time	0.8	0.9	1.0	1.1	1.2	$\frac{\delta\delta^{13}\text{C}}{\delta t_{react}} (\frac{\text{\%}}{\text{s}})$
methane	-24.157	-24.091	-24.029	-23.972	-23.918	0.006
ethyne	-31.960	-31.894	-31.833	-31.775	-31.720	0.006
methyl	-22.464	-22.389	-22.320	-22.258	-22.201	0.007
ethane	-41.442	-41.348	-41.258	-41.171	-41.087	0.009
propene	-23.775	-23.676	-23.588	-23.511	-23.443	0.009
propane	-25.410	-25.093	-24.778	-24.464	-24.151	0.033
ethyl	-32.204	-32.072	-31.946	-31.827	-31.712	0.013
ethene	-32.111	-31.993	-31.879	-31.769	-31.662	0.012

Table 6.6: Fraction carbon of various compounds after the reactor with fractional change in residence time. The first five columns represent the fractional change in residence time and the last column represents the sensitivity coefficients.

Change in residence time	0.8	0.9	1.0	1.1	1.2	$\frac{\delta X_i}{\delta t_{react}} (\frac{1}{s})$
methane	0.058	0.063	0.068	0.073	0.077	0.000
ethyne	0.012	0.015	0.018	0.020	0.023	0.000
ethane	0.061	0.066	0.071	0.075	0.079	0.000
propene	0.014	0.014	0.014	0.014	0.014	-0.000
propane	0.609	0.575	0.544	0.515	0.488	-0.003
ethene	0.242	0.262	0.281	0.299	0.315	0.002

Table 6.7:  $\delta^{13}\text{C}$  of various compounds after the reactor with fractional change in pressure. The first five columns represent the fractional change in pressure and the last column represents the sensitivity coefficients.

Change in pressure	0.8	0.9	1.0	1.1	1.2	$\frac{\delta \delta^{13}\text{C}}{\delta P} (\frac{\%}{bar})$
methane	-24.16	-24.09	-24.03	-23.99	-23.96	0.25
ethyne	-31.98	-31.90	-31.83	-31.77	-31.71	0.33
methyl	-22.32	-22.31	-22.32	-22.33	-22.35	-0.04
ethane	-41.33	-41.29	-41.26	-41.24	-41.22	0.13
propene	-23.50	-23.54	-23.59	-23.63	-23.67	-0.22
propane	-24.78	-24.78	-24.78	-24.78	-24.78	-0.00
ethyl	-32.11	-32.02	-31.95	-31.88	-31.82	0.36
ethene	-32.04	-31.95	-31.88	-31.81	-31.75	0.37

Table 6.8: Fraction carbon in various compounds after the reactor with fractional change in pressure. The first five columns represent the fractional change in pressure and the last column represents the sensitivity coefficients.

Change in residence time	0.8	0.9	1.0	1.1	1.2	$\frac{\delta X_i}{\delta X_{o,C_3H_8}} (\frac{1}{bar})$
methane	0.06	0.07	0.07	0.07	0.07	0.01
ethyne	0.02	0.02	0.02	0.02	0.02	0.00
ethane	0.07	0.07	0.07	0.07	0.07	-0.00
propene	0.01	0.01	0.01	0.01	0.02	0.00
propane	0.56	0.55	0.54	0.54	0.53	-0.03
ethene	0.27	0.28	0.28	0.28	0.29	0.02

minimal change likely indicates the concentration is not critical in this study.

When the residence time was varied by 40%, the propane conversion changed by 0.12 and ethene changed by 0.8, which is the largest change found in this sensitivity analysis. Better quantifying the residence time of experiments or measuring a temperature profile in the system could help improve accuracy of modeling mole fraction distributions for online PSIA.

### 6.3.6 Code availability

Reaction Mechanism Generator (RMG) is open source and available under the MIT license. Documentation about installation and general use is available at [rmg.mit.edu](http://rmg.mit.edu). This section describes using the isotope module which is included in versions after 2.1. For up to date information on the software, see the RMG documentation at [rmg.mit.edu](http://rmg.mit.edu).

Scripts to analyze the model and reproduce figures are available in the linked data repository with DOI of [10.5281/zenodo.2567585](https://doi.org/10.5281/zenodo.2567585).

### describing isotopes in RMG

Isotopic substitution can be indicated in a molecular structure's adjacency list. The example below is methane with an isotopically labeled carbon of isotope number 13, which is indicated with i13.

```
1 C u0 p0 c0 i13 {2,S} {3,S} {4,S} {5,S}
2 H u0 p0 c0 {1,S}
3 H u0 p0 c0 {1,S}
4 H u0 p0 c0 {1,S}
5 H u0 p0 c0 {1,S}
```

Figure 6-5: The RMG adjacency of a methyl radical with a  $^{13}\text{C}$  substitution

## running the RMG isotopes algorithm

The isotopes script is located in the folder scripts. To run the algorithm, ensure the RMG packages are loaded and type

```
python /path/to/rmg/scripts/isotopes.py /path/to/input/file.py
```

The input file is identical to a standard RMG input file and should contain the conditions you want to run (unless you are inputting an already completed RMG model). Without any options, the script will run the original RMG input file to generate a model. Once the RMG job is finished, it will create new species for all isotopologues of previously generated species and then generate all reactions between the isotopologues.

Some arguments can be used to alter the behavior of the script. If you already have a model (which includes atom mapping in RMG's format) which you would like to add isotope labels to, you can use the option `--original path/to/model/directory` with the desired model files stored within with structure `chemkin/chem_annotated.inp` and `chemkin/species_dictionary.txt`. The isotope script will use the specified original model instead of running the `input.py` file. If you only desire certain reactions in the final output, you can add `--useOriginalReactions` in addition to `--original`. This will create a full set of isotopically labeled versions of the reactions you input and avoid a time-consuming generate reactions procedure.

The argument `--maximumIsotopicAtoms [integer]` limits the number of enriched atoms in any isotopologue in the model. This is beneficial for decreasing model size, runtime of model creation and runtime necessary for analysis. The estimated errors using this parameter are described in Section 6.3.3.

Adding kinetic isotope effects which are described in this paper can be obtained through the argument `--kineticIsotopeEffect simple`. Currently this is the only supported method, though other methods can be added.

If you have a desired output folder, `--output output_folder_name` can direct all output files to the specified folder. The default is to create a folder named 'iso'.

There are some limitations in what can be used in isotope models. In general,

RMG reaction libraries and other methods of kinetic estimation that do not involve atom mapping to reaction recipes are not compatible (though they can be functional if all isotopologues are included in the reaction library). The algorithm also does not function with pressure dependent mechanisms generated by RMG, and has only been tested for gas phase kinetics. This algorithm currently only works for Carbon-13 substitutions.

Following the generation, a number of diagnostics check model accuracy. Isotopologues are checked to ensure their symmetries are consistent. Then, the RPD among reactions differing only in isotope labeling is checked to ensure it is consistent with the symmetry values of reactions. More details of the algorithms behind this check are given in Section 6.3.3. If one of these checks throws a warning, the model will likely exhibit non-natural fluctuations in enrichment ten to one hundred times larger than from non-hydrogen kinetic isotope effects.

### **output from script**

The isotope generation script will output two files inside the nested folders iso/chemkin, unless --output is specified. The file species\_dictionary.txt lists the structure of all isotopologue using the RMG adjacency list structure. The other file of importance chem\_annotated.inp is a chemkin input file containing elements, species, thermo, and reactions of the entire system.

### **6.3.7 History of model development**

How a model is constructed can have a large impact on how well it can fit other systems. Changing model form and parameters to fit experimental data can easily lead to overfitting making study of any other system lead to larger errors. In this section, we present the history of model development to help any potential user of the software understand what types of errors to expect. Care was taken to minimize the potential for overfitting the data presented here, but we still think it is important to have transparency in this issue.

When the model for propane was first developed, there was no kinetic isotope effects. Significant error was observed in enrichments varying 1000‰. After detailed analysis, we noticed that this was due to errors in RMG estimating symmetry and reaction path degeneracy for reactions. These algorithms were modified to account properly with multiple resonance isomers, and a check was inserted to check for any errors in symmetry or degeneracy after the model generation is finished. Since there is not fool-proof solution to estimate 3-D structures from 2-D graph objects, we anticipate that errors may occur when this system is used for different compounds.

After a few iterations trying a reduced ethanol model, two reduced models of propane were created to simplify the model. Initially the three-reaction model was created. Based on the major reaction fluxes in the full model, three additional reactions were chosen to make the six-reaction model. The reactions placed in these models were not changed after they were chosen.

The resulting propane model was then fit to data from Gilbert et al. Similar agreement was obtained for Figures 6-9 and 6-12. Figure 6-11 had significant errors since the model did not contain kinetic isotope effects. Kinetic isotope effects were then added as described in Section 6.3.3 and were not modified after viewing the experimental comparison, though a separate scheme (using entire molecule molecular weights instead of just  $^{13}\text{C}$  or  $^{12}\text{C}$ ) was tried and abandoned. Figure 6-11 was originally plotted using the same residence time as found in Figure 6-9, but was modified to have the same conversion as experiments since that allowed for better comparison of kinetic isotope effects. The propene data from the model and reported from Gilbert et al. was then removed from Figures 6-9 and 6-11 since it was not needed in further analysis of position specific isotope assessment in Gilbert et al., led to cluttering of the figures, and was not well predicted by the model.

Finally, the starting composition enrichments were modified to match the samples used by Gilbert et al., (before this change an estimate was being used). To get more accuracy from reading the figures in Gilbert et al., Engauge Plot Digitizer was used to extract the original data from published plots. For Figure 6-9, the data was extracted three times and an average was taken. In Figure 6-9, there was a mismatch

Table 6.9: Ethyne fraction with different wall loss and pressure parameters. All experiments done at 850°C. Selectivity is carbon weighted.

Pressure (bar)	H loss rate ( $s^{-1}$ )	Selectivity ethyne
1	0	0.032
2	0	0.039
1	3e4	0.021
2	1.5e4	0.034

of about 5% between the conversion and the concentrations of products at 750°C due to amplified error in data extraction from the figure at low conversions, so each compound was scaled so that the total was 100%.

To better understand differences between experiment and the model, a hydrogen loss reaction to the wall was simulated, since wall reactions can often have a non-negligible impact in experiments.[242] The experimental setup considered here used a 0.25 mm diameter fused-silica reactor that was 250 mm long, leading to a large surface area to volume ratio. To look into the effect of wall losses on the further oxidation to ethyne radical, hydrogen radical loss rate to the walls are found using the reactor geometry and conditions as well as the wall loss rate by Moon et al.(Moon, J Appl. Phys, 2010) At 2 bar pressure, this leads to a radical loss rate of  $1.5 \times 10^4 s^{-1}$ . At 1 bar pressure, the loss rate is approximately double the rate at 2 bar. Table 6.9 looks at the how the fraction of ethyne formed varies when changing pressure with or without the presence of the hydrogen loss to walls.

Based on knowledge that some GC equipment uses the column temperature, inert gas and tube dimensions to set flow rate (instead of using flow rate at standard conditions), the conditions at which the experimental flow rate was based were modified to be the starting temperature of the 1st GC column (323K) and the same pressure of the pyrolysis tube (instead of standard conditions 298K and 1atm). This increased the estimated residence time making the model over-predict the reactivity even more, so this modification was not used, and a standard flow rate at 298K and 1atm is used as described in Section 6.3.5.

The DRG model was then created from the full model without isotopologues. DRG settings was originally set at 10% for ethene, ethane and methane, which did not converge. The tolerance was raised to 40% for the same species, and the smallest model which fit the criteria was used for all analysis.

The rate of certain reactions in the full model were not modified to fit any experimental data so that the main results are not biased by model fitting.

Ignoring symmetry and degeneracy issues, this final work does not contain any changes in the kinetic database, estimation methods, or kinetic isotope effects to better fit the data in Gilbert et al.[211]

## 6.4 Results

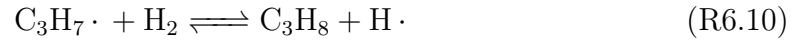
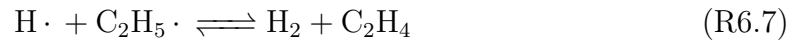
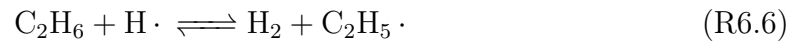
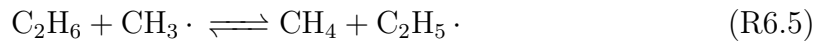
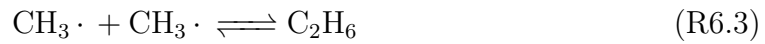
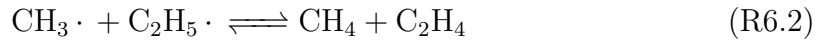
This section applies the generation algorithm to create one propane model, from which three reduced models are created, and compares all four models with experiments to understand how predictive they are.

### 6.4.1 Production of propane models

Propane contains two distinct carbon atom positions allowing for the calculation of one site preference value. Four models are used to aid in explaining the importance of full chemistry in an isotope model: a model of propane pyrolysis built using RMG from parameters described in Section 6.3.1 ('full model'), a reduced form of that model using DRG with error propagation ('DRG model'), and two manually reduced forms of the RMG model, one three-reaction model, with the minimal number of reactions to produce the three analyte compounds used to find site preference, and another six-reaction model, containing reactions that create fast atom scrambling. The three-reaction model and six-reaction model are chosen to under-emphasize and over-emphasize atom scrambling respectively and are not meant to be complete descriptions of the chemistry.

Figure 6-6 displays major reaction pathways and which models they are in, and Table 6.10 displays the sizes of the models before and after the addition of isotopo-

logues. The reactions are listed below.



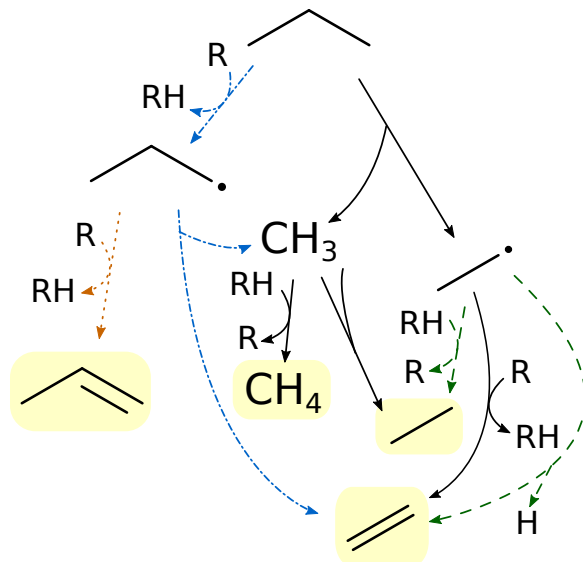
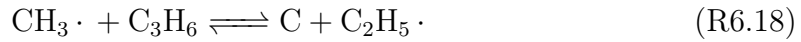
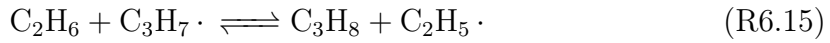
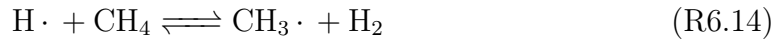


Figure 6-6: Major reactions of propane pyrolysis in the various models. Black solid lines are in all models, green dashed lines are not in the three-reaction model, blue dashed-dotted lines are only in the DRG and full models, and orange dotted lines are only in the full model. Yellow backgrounds indicate molecules which are experimentally observed.[211] All reactions are modeled as reversible.



Simulations of each model give time resolved estimates of bulk- and position-

Table 6.10: Sizes of the various propane models

model	without isotopologues		with isotopologues	
	species	reactions	species	reactions
three-reaction	6	3	24	19
six-reaction	8	6	26	35
DRG	9	18	30	167
full	31	191	343	7096

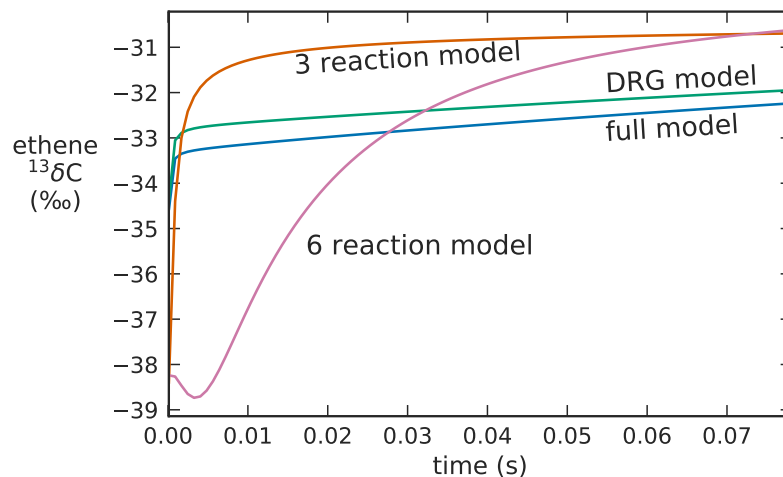


Figure 6-7: The predicted enrichment values of ethene across the course of a constant temperature and pressure reactor simulation at 850°C and 2 bar with a starting bulk enrichment of -28‰ and a terminal carbon site preference of 5.4‰.

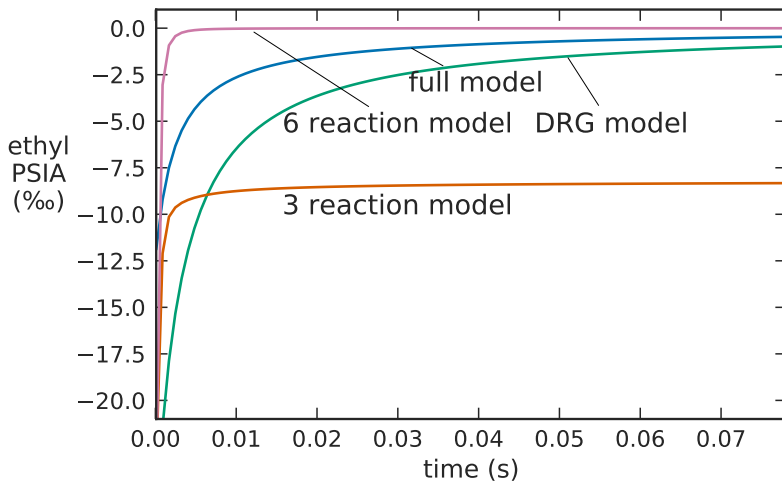


Figure 6-8: The predicted site preference of the radical carbon over the methyl carbon in ethyl radical across the course of a constant temperature and pressure reactor simulation at 850°C and 2 bar with a starting bulk enrichment of -28‰ and a terminal carbon site preference of 5.4‰.

specific enrichments. Figure 6-7 shows the predicted enrichment of ethene as a function of time. Notice that the three-reaction and six-reaction models eventually reach a higher enrichment than the other two models, with extra dynamics in the six-reaction model. Most propane in the DRG and full models undergoes hydrogen abstraction as the first decomposition step, which has a smaller KIE than the scission reaction that dominates the three- and six-reaction models. The difference in KIE of the initiation steps leads to the final difference in ethene enrichment. The full model has slightly lower enrichment than the DRG model, which is likely due to more ethane, which has low enrichment, converting to ethene.

Figure 6-8 shows the site preference values of ethyl radical as a function of time. The four models all have similar trend starting out with a large magnitude for site preference, which originates from the site preference of propane, and the magnitude decreasing over time due to secondary chemistry causing atom scrambling. The three reaction model, which lacks most secondary chemistry, approaches -8‰ while the others asymptotically approach zero at different rates based on the magnitude of secondary chemistry in each model.

Obtaining the data shown in either Figure 6-7 or 6-8 would be difficult or impos-

sible with on-line PSIA equipment since it typically only measures stable products after they leave the pyrolysis chamber. In this regard, detailed isotopic models can provide the ability to understand dynamic phenomena inside on-line PSIA systems.

#### 6.4.2 Experimental comparison

In this section, we compare the models with experimental data to gauge model accuracy.[211] To accurately test the ability of this new procedure at predicting filiation, no kinetic values were altered to fit the experimental data. Section 6.3.7 of the Supporting Information reports a detailed history of the development of the isotope methodology and the models tested to help elucidate any bias toward experimental results.

The predictions of the isotope model are only expected to be accurate if the underlying chemistry found through mechanism generation is itself valid. Figure 6-9 compares the predicted product distribution with experiments. The mole fractions of this plot are weighted per carbon atom. For this simulation, a batch reactor is modeled for the amount of time corresponding to the residence time estimated from the reactor dimensions and operating conditions (see Supporting Information Section 6.3.5 for more information). The product distribution shows adequate production of ethane and methane while over-predicting ethene and ethyne and under-predicting propene. Higher propane conversion is predicted than observed in experiments (see Figure 6-10).

Figure 6-11 compares the enrichments found in experiments to the estimated values from both the full and DRG models. The exit time chosen for this simulation corresponds to the same conversion as experiments to give a more representative comparison of KIE, since enrichment highly depends on conversion.

Figure 6-12 compares the full model estimates to the experiment that was used to determine filiation. The slope in these plots represent filiation values, which show good agreement between experiments and the model. To better understand the slope accuracy, a total of sixteen experimental slopes are compared with the model predictions. Table 6.11 shows the difference in model and experimental slopes, scaled by

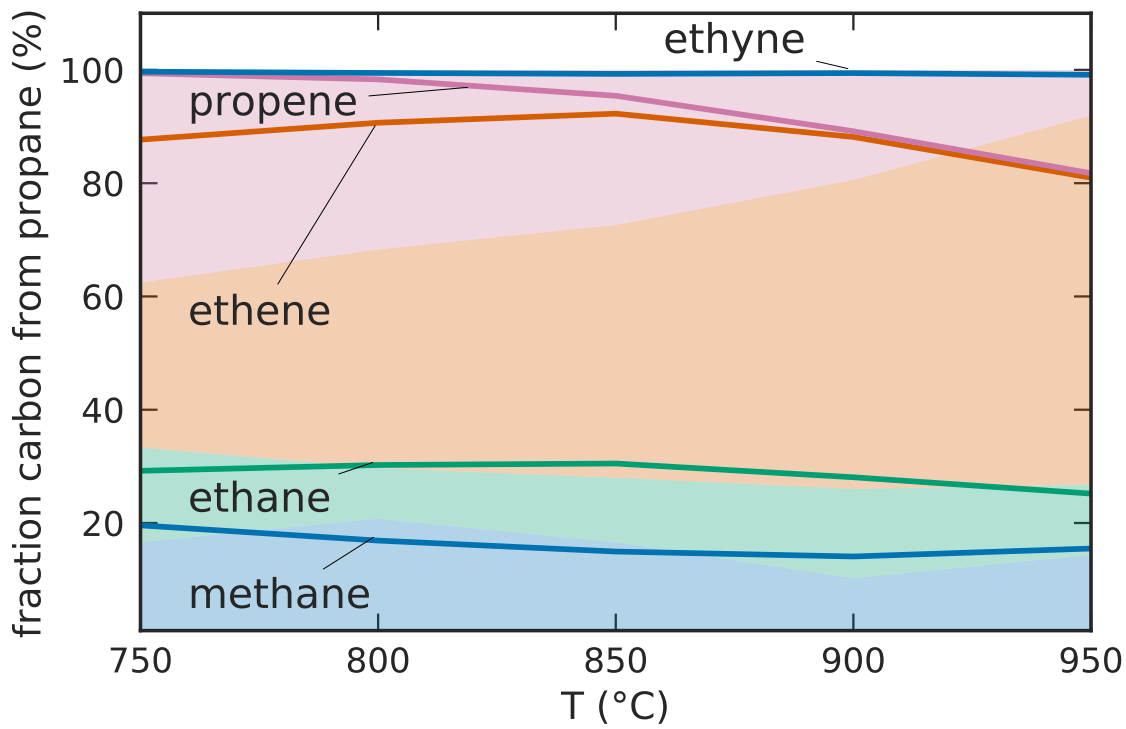


Figure 6-9: Experimental values are shaded areas and the full model results are shown as lines. All values are stacked. Ethyne is not reported in experiments but is predicted by the model. Experimental values were inferred from Figure 1a of [211].

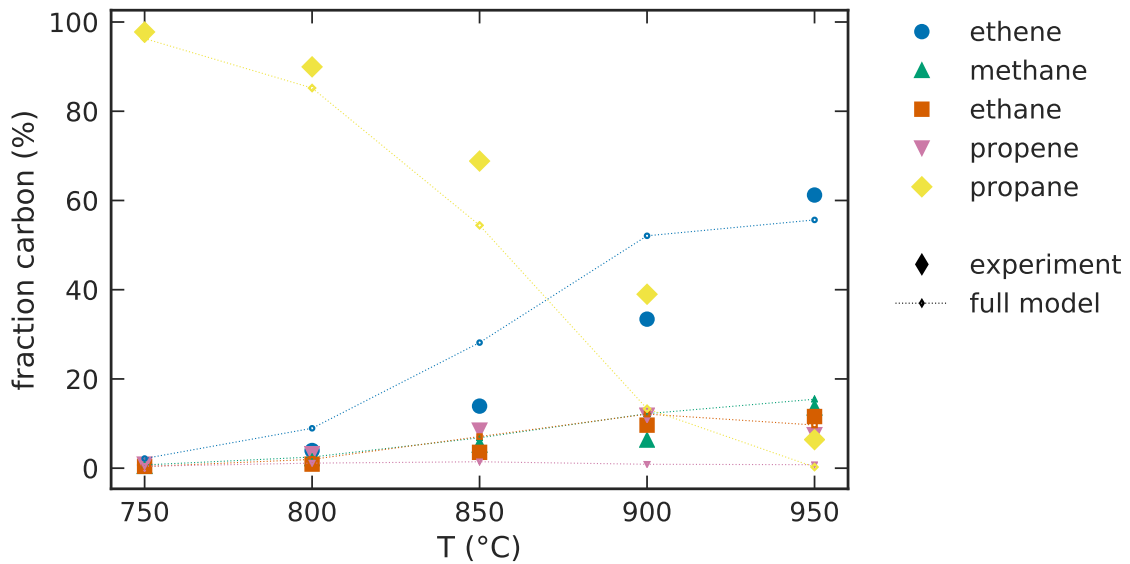


Figure 6-10: Comparison between simulation and experiment of carbon-weighted yields of five analytes.

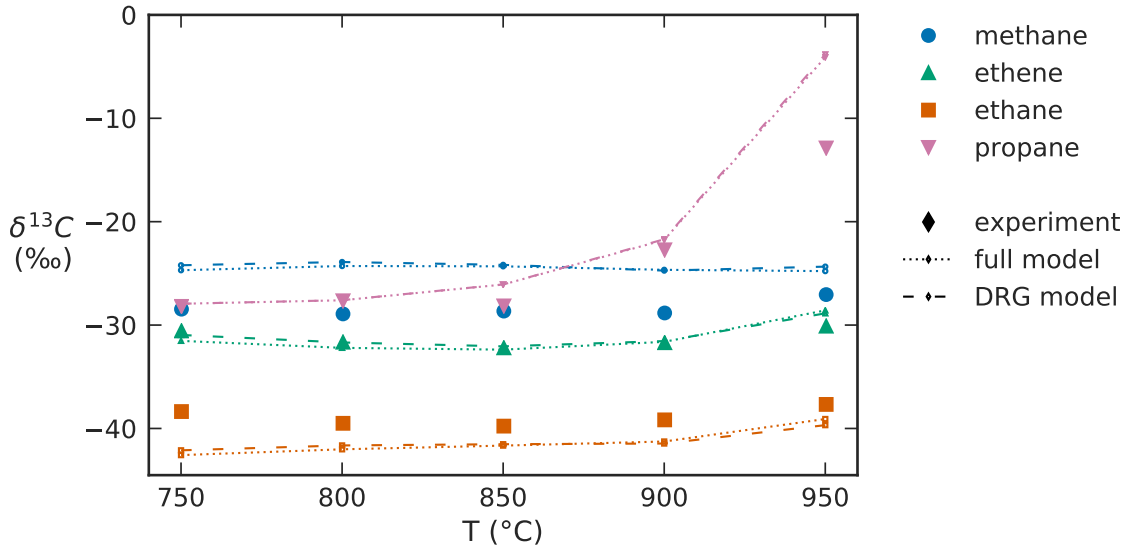


Figure 6-11: The enrichments predicted by the full model (dotted lines) and DRG model (dashed lines) enrichment predictions are compared to experimental data (large symbols) from Figure 1b in [211].

the experimental uncertainty.

## 6.5 Discussion

### 6.5.1 Automatic generation capabilities

The algorithm for creating isotopically labeled reaction networks can convert a wide variety of combustion, pyrolysis and other processes modeled by RMG into a system that can trace isotopic enrichments. Potential compounds can contain hydrogen, carbon, oxygen, and sulfur. This functionality is enabled by the usage of reaction recipes that identify reaction types and track reacting atoms between those types.

The isotope model creation algorithm corrects for different properties of isotopologues by modifying entropy for changes in symmetry numbers and kinetics due to KIE and RPD. All three of these modifications are widely applicable and can be used on reactions of new compounds.

The time necessary to obtain an isotopic model varies with processor capabilities, what you are modeling, any constraints placed on the model and the size of the model

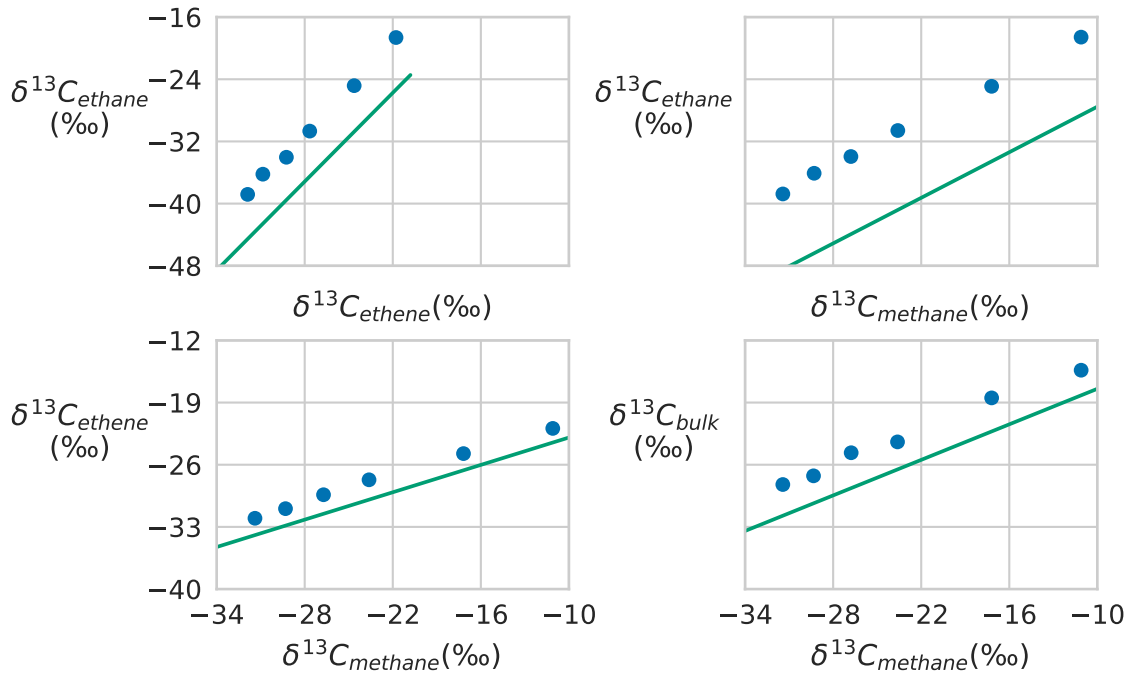


Figure 6-12: The full model (lines) reproduces the slopes from [211] at 850°C. These slopes are the critical filiation values needed to interpret PSIA data. The offsets between the example data and the lines are due in part to imperfect estimates of KIE.

Table 6.11: Variance of model errors on atom filiation

temperature (°C)	full model	DRG model	6 reaction model	3 reaction model
all	0.5	0.6	6.5	1.7
800	0.9	0.9	2.0	1.0
850	0.6	0.5	3.5	0.5
900	0.5	0.2	8.6	1.0
950	0.4	0.9	10.6	3.2

Model error is the difference of the model slope and experimental slope scaled by the uncertainty of the experimental slope,  $\frac{m_{model} - m_{exp}}{\sigma_{exp}}$ . The variance of model errors gives an indication of accuracy. Model errors with a variance near one indicate that the model uncertainty is about the same as the experimental uncertainty. Variances significantly greater than one indicate that the model does not match experiments. Variances less than one either originate from coincidence or a conservative estimate of experimental error.

desired. For reference, the full propane model with isotopes described in this paper, with 323 species and 7096 reactions, took a single core 44 hours.

Since the number of isotopologues scales exponentially with number of carbons in a molecule, we implemented a parameter which limits the number of enriched carbons in a molecule, which is described in Section 6.3.3. This option can reduce final model size and model generation time, with less than 1% deviation from the full model when allowing for two enriched carbons per molecule at natural abundances (<sup>13</sup>C natural abundance is about 1%, so doubly substituted isotopologues would occur with frequency around 0.01%). In addition to limiting model generation size, usage of reduction techniques on the model without isotopologues added, like DRG, can also decrease the model size. These options allow for the wider applicability of the methodology described here encompassing larger starting molecules while obtaining good computational scaling.

### 6.5.2 Prediction accuracy

When using this algorithm to develop models for isotopic reactions, the accuracy of the resulting model is critical. In Section 6.4.2, we compared our model with experimental results to assess the accuracy of the simulation.

#### product distribution

Figures 6-9 show fair agreement between the model and data, especially since no kinetic or thermodynamic parameters were adjusted to fit the data. The DRG model, which lacked propene, also overestimated the ethene, but to a greater extent (shown in Figure 6-13). The full model parameters can be tuned to obtain better agreement, though no rate modifications were used in the main body of this paper. Some other sources of uncertainty leading to deviations in Figure 6-9 involve the estimation of the actual experimental reactor conditions (described more in Section 6.3.5 of the Supporting Information) and kinetic and thermo parameter estimation.

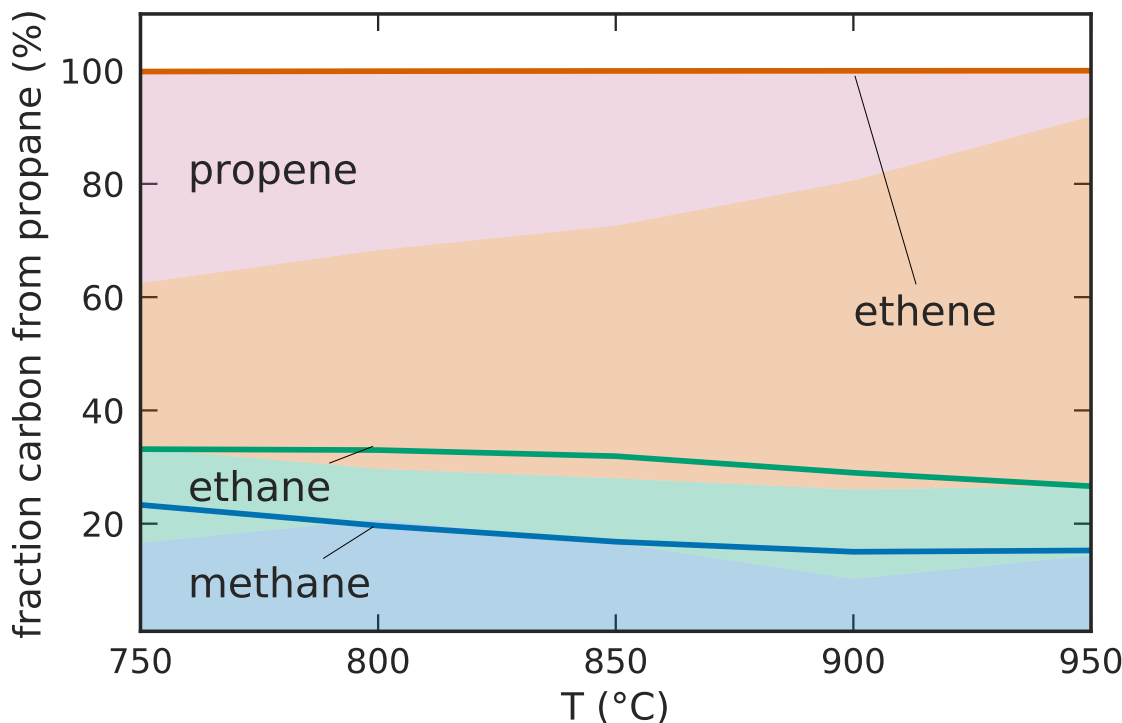


Figure 6-13: Comparison of product distributions of the DRG model (lines) against experiments (areas). Propene is not a product in the DRG model, but is shown in pink from experiments.

Though both model and experiments show a trend of decreasing propene product mixing ratio with temperature, less propene is estimated by the model than is found in experiments. The model also predicts significant production of a compound not reported experimentally, ethyne, which originates from a radical abstracting a hydrogen from ethene. These two factors, along with the higher conversion obtained in the simulations, indicate that the model is predicting faster reactions than those observed in experiments. This apparent higher reactivity can be due to many possible errors. One explanation involves incorrectly estimating experimental conditions like the temperature distribution in the reactor. Another source could come from uncertainties in the kinetic estimation methods. The model also lacked reactions with walls, which could be significant since the reactor is narrow, giving it a high surface area. These wall reactions would reduce free radical reactions and overall reactivity of the system. A model was created of the fastest moving radical, hydrogen atom, reacting

with the walls, which resulted in a decrease in ethyne production. Another possible source of error is that the RMG model is generated using high pressure limit kinetic values, whereas much of propane pyrolysis should be pressure dependent, leading to other potential deviations.[93] These factors can all contribute to the apparent higher reactivity of the model.

Even with deviation in the product distributions shown in Figure 6-9, the error in the full and DRG models for enrichments (Figure 6-11) and filiation (Table 6.11) are much lower, indicating that enrichment and filiation could be less sensitive to overall reactivity than product distribution.

## enrichments

The model seems to over-predict KIE and atom scrambling. The larger KIE in the model can be seen in Figure 6-11 by the difference in enrichment of methane and ethane, which form from the same methyl radical. The gap between the two analytes shows the strength of KIE. The larger gap between methane and ethane enrichment in the model indicates higher KIE is modeled for those reactions. In addition, both models show higher propane  $^{13}\text{C}$  enrichments than experiments, indicating that the model is reacting away less enriched propane than actually happens. The larger KIE results from a simplified representation in Equations 6.2 and 6.3. Creating methods that estimate KIE from experimental values for more specific types of reaction could reduce this error, though this could result in over-fitting if not done properly.

Figure 6-11 shows slightly more atom scrambling in the model than in experiments, which is shown by the change in enrichment of methane, ethane and ethene towards the bulk enrichment of -28‰ at the higher temperature conditions. This overestimate of atom scrambling likely resulted from the higher predicted overall reactivity of the model, as discussed in Section 6.5.2, which causes greater conversion between various products than actually occurred in the experiments.

In Figures 6-7 and 6-8, enrichments between the full and DRG models converged within 1‰ towards the end of a simulation. In Figure 6-11, the minor differences between full and DRG model is dwarfed by comparison to the experimental values.

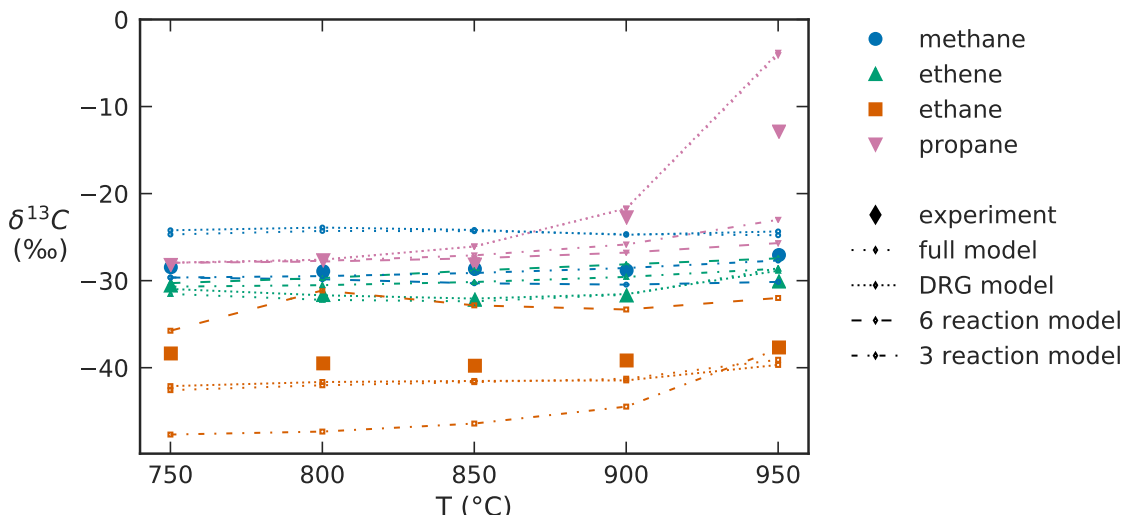


Figure 6-14: Comparison of enrichments between the four models and experiments for four compounds. The same propane conversion is reached for each model.

These both suggest that negligible loss of information occurred from model reduction, despite allowing for product concentrations to change by 25% in the reduction procedure. Emphasis should be placed on the accuracy of KIE and atom scrambling when developing an isotopic model, since they result in more error than model reduction. There is potential for using DRG when creating isotopic models, despite the reduction algorithm not explicitly accounting for enrichment.

The enrichments of the three and six reaction models are shown in Figure 6-14 and show more significant deviation than the full or DRG model, due to missing chemical data.

## filiation

The full and DRG models' slopes at various enrichments, shown in Figure 6-12, are very similar to experimental data. In Table 6.11, the full and DRG models' filiation values are within experimental uncertainty. The full model error also decreases at higher temperatures which could result from the kinetics estimations in RMG increasing in accuracy at higher temperatures or from the potential cancellation of error between the exaggerated KIE and atom scrambling.

In contrast, the errors of the 3 and 6 reaction models in Table 6.11 are significant.

Simply minimizing or maximizing the amount of atom scrambling pathways does not lead to accurate depiction of the real phenomena.

From the four models analyzed, reactions forming compounds not used in the analysis, like propene or ethyne, are not needed for filiation or enrichment estimations, but these major pathways must be included for determining product distribution.

### 6.5.3 Applications

Though propane was used as an example to illustrate the accuracy and caveats of the algorithm here, this isotope modeling package can describe many different compounds and chemistries. Using RMG with conditions similar to work published using RMG's rate rules should give reasonable results. The most common application used for RMG is oxidation and pyrolysis of hydrocarbons and oxygenated hydrocarbons in the gas phase, though condensed phase applications, heterogenous mechanisms, and reactions involving nitrogen and sulfur have been published.[28, 227]

A detailed model can elucidate phenomena difficult to perceive in experiments, like concentrations of highly reactive intermediates or the exact atom pathways that cause certain enrichment profiles. Time dependent plots of compound-specific and site preference enrichments can be extracted from the resulting model, as shown in Figures 6-7 and 6-8. Detailed flux analysis generated in the simulation can help better understand complexities in the reacting system, see Figures 6-15 and 6-16.

If data can be obtained from the model with near-experimental accuracy, as done for filiation with the full and DRG models, this approach has the potential to partially replace experimental measurements. The accurate slopes found from the model can be applied to create a relationship between fragments' compound specific enrichments and the parent compound's site preference values, avoiding the numerous experiments and enriched reagent necessary to find these relationships experimentally.[43] We are currently investigating applying this approach to more complex models built with RMG.

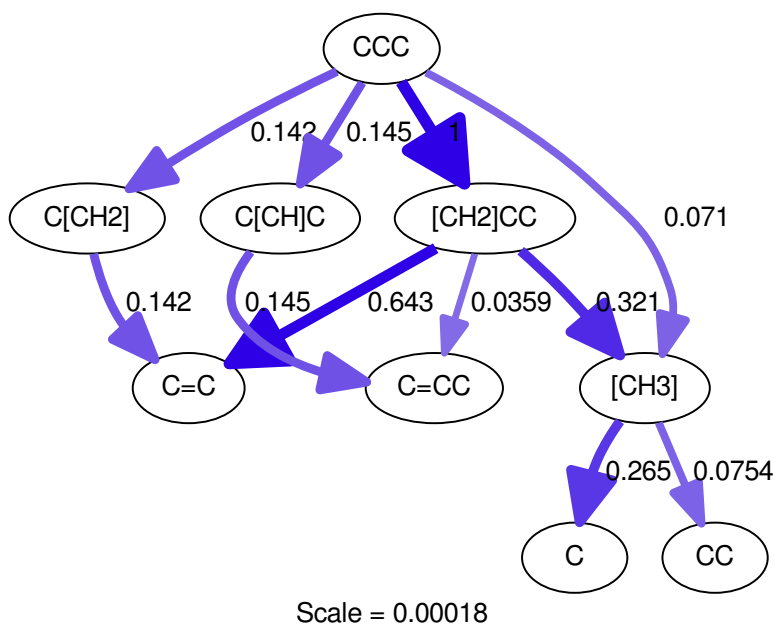


Figure 6-15: A reaction flux diagram of the full model showing carbon pathways during a simulation of 1% propane at 750°C and 2 bar at 1 ms. The arrow size and color represents relative magnitude of carbon flux, scaled by the scale factor in kmol/m<sup>3</sup>-s. The numbers are the relative flux scaled to the propane to n-propyl radical reaction.

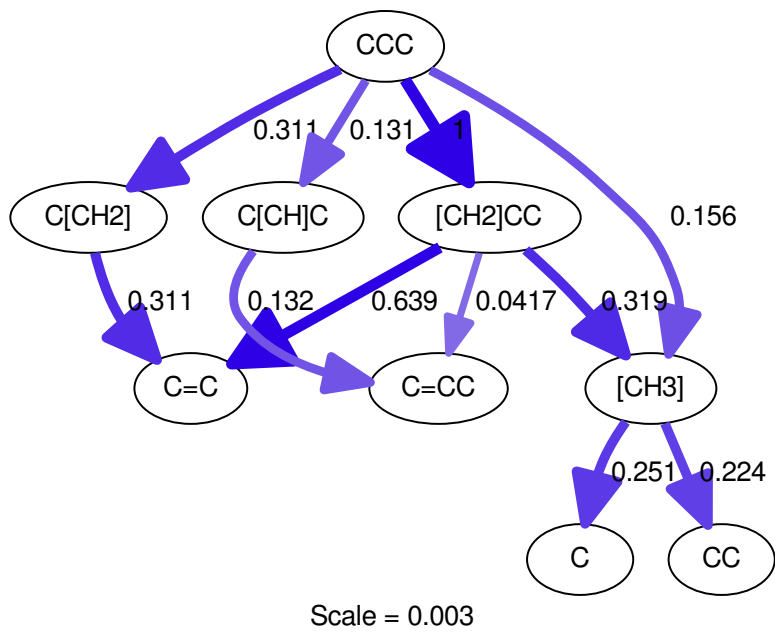


Figure 6-16: A reaction flux diagram of the full model showing carbon pathways during a simulation of 1% propane at 850°C and 2 bar at 1 ms. The arrow size and color represents relative magnitude of carbon flux, scaled by the scale factor in kmol/m<sup>3</sup>-s. The numbers are the relative flux scaled to the propane to n-propyl radical reaction.

## 6.6 Conclusion

RMG-isotope algorithm is able to rapidly produce a detailed mechanisms that can trace isotopes without manual modification. This program is open-source under the MIT X/11 license. The algorithm adjusts for molecular symmetry, reaction path degeneracy and first order KIE in all isotopologues.

A model of propane pyrolysis created with this method, which includes atom scrambling, predicts the transfer of isotopes within experimental uncertainties over a 200°C range without any fitting to experimental data. The model obtains qualitative agreement with experiments in product distribution and enrichment measurements.

A propane model reduced by the DRG method achieved similar accuracy as the full model for enrichment and the transfer of isotopes, despite having 92% fewer species and 97% fewer reactions. Smaller models failed to reproduce the data. The model shows more atom scrambling, stronger kinetic isotope effects, higher conversion of propane, and less formation of propene than observed in experiments. Ethyne was also produced in the model, though it was not reported in experiments.

Discrepancies between the model and experiment, could have occurred due to differences in temperature profile; incorrect kinetic, thermo or KIE parameters in the model; or loss of radicals to the wall in experiments. These can be improved with better measurements and fitting of data to experiments.

Overall, RMG-isotope algorithm can easily create models to help design and optimize experiments for PSIA studies, facilitating examining the sources of complex fuels, which could become a mechanism and of detecting and enforcing unpermitted usage of fossil fuel usage.



# Chapter 7

## Conclusion and Future Directions

### 7.1 Main Findings

Much of the work in this thesis helps connect disciplines, applying knowledge from one field to that of another. Chapter 4 applies stochastic kinetics, which has not before achieved significant attention in the atmospheric community, to the study of heterogeneous aerosol oxidation. It shows a scenario where stochastic effects could be important and provides guidelines for when stochastic kinetics can be safely neglected. This has potential to better study ultrafine atmospheric aerosols.

Chapter 5 shows the connection between the autoxidation chemistry that occurs in the atmosphere to the ignition phenomena that happens in combustion, using both alkane and oxygenated fuels. By looking at oxidation chemistry across these conditions, this work is able to show how one type of RO<sub>2</sub> pathway that matters in one field can start to impact another field, with a change in the molecular structure.

In Chapter 6, the tools used in computer-based mechanism generation were applied to the analysis of isotopic samples. The generated model showed good agreement when tracking isotopic reactions. Furthermore, the tool generated by this work has potential to improve our ability to test for intramolecular isotopic enrichment of new compounds.

To bridge these disciplines, challenges arose that led to the advancement of fundamental kinetics and biofuel ignition. Chapter 2 clarifies a longstanding contradiction

within academic literature about how to obtain the correct reaction rate when two reactants are identical. This knowledge is essential in Chapter 6, but can also be applied to any field where theory is used to predict the reaction rate of reactions with identical reactants. Chapter 3 develops better rate constants for isobutanol peroxy radicals, which is used in Chapter 5. In addition, this work helps to explain why no two stage ignition occurs for this fuel. The data from this work, when put in detailed models, can help get a truer representation of isobutanol oxidation.

By connecting information between disciplines, this thesis places the groundwork to better model and understand ultrafine atmospheric aerosols, generate a more wholistic view of biofuel degradation (in both our atmosphere and combustion), and improve diagnostics to determine molecular origins. These are all small advances in the greater challenge of developing technology for a zero-carbon future.

## 7.2 Future Directions

The work in this thesis are just pieces in a larger puzzle. Much more work is necessary in order to understand the kinetic challenges of various emerging technologies. This section discusses some of the next steps needed to better model the chemistry of emerging fuels and improve atmospheric experimental techniques.

### 7.2.1 Obtaining better phenomenological rate coefficients

In the course of this thesis, multiple issues have come up that hindered a full, accurate determination of pressure dependent rates, specifically the approximation methods used to convert the master equation, which is a function of energy, to rates that are functions of temperature and pressure. Allen et al. provides a good overview of three of these methods, all of which were used in this thesis.[32] The modified strong collision and reservoir state approximations were used for isobutanol in Chapter 3, and the chemically significant eigenvalue approximation from Goldsmith et al. was used to obtain the propane pressure dependent kinetics applied in Chapter 5.[97]

The chemically significant eigenvalue method is generally more accurate than the

other two methods.[32] Though as discussed in Chapter 5 and in previous studies,[97, 32] the significant eigenvalue value does not work when the number of eigenvalues is less than the number of isomers, which occurs more at lower pressures and higher temperatures. Different techniques exist to try to fix this issue, like the one implemented in Goldsmith et al., which have their own issues, like non-smooth behavior in the resulting reaction rates, seen in Chapter 5.

Developing a better solution to allow chemically significant eigenvalues to work when the number of distinct eigenvalues is less than the number of isomers can help improve the accuracy of pressure dependent results, allowing for models to better predict fuel properties. Implementing this into Arkane, which is part of the Reaction Mechanism Generator suite, can allow the wider combustion community to benefit from this innovation.

### 7.2.2 Intuitive automation of rate constant determination

In Chapter 3, comparing quantum rates from those estimated in detailed kinetic mechanisms showed significant variation. For new molecules of interest, estimates frequently come from extrapolating a structure activity relationship to functional groups where it was not intended. These estimates occur in current state-of-the-art mechanisms, as shown in Figure 3-17.

As computers have gotten faster, the fraction of time taken by humans, as opposed to the computer, to obtain reaction rates from quantum calculations has increased. This has caused human effort to become the bottleneck to obtaining the volume of rates necessary to reduce the prevalence of sensitive rate coefficients that have been inaccurately estimated or manually tuned.

Many programs have been created to automate the quantum calculations and rate constant determination. These significantly speed up the rate of obtaining rate constants, but do not specify which reactions should be calculated. This currently requires a subject expert to run a simulation and determine the important reactions. A system for integrating these components is enumerated below:

1. Generate a mechanism that contains approximate uncertainty values.
2. Run a simulation for the system of interest that finds the parameters that lead to the largest uncertainty.
3. For each parameter where quantum calculations can reduce the uncertainty, calculate quantum values.
4. Update the model with new values and use it in either step (1) to find new reactions or in step (2) to reestimate the sensitivities using the new rates.

For the first three tasks, separate programs exists that can accomplish each goal. For step (1) there is Reaction Mechanism Generator. For step (2) there is Cantera. For step (3) there is Automated Reaction Calculator (ARC). The main challenge is integrating these pieces.

If this were to be implemented, it would still be limited by some of the underlying software. To expand functionality, ARC would likely benefit significantly from expanding into doing variational transition state theory, multi-reference calculations, and multi-conformer transition state theory, which can allow for the calculation of barrierless reactions and for obtaining more accurate rates for systems at low temperature or with multiple low-energy electronic states.

### 7.2.3 Data requirements for rate constant estimation

Even if the all sensitive reaction rates could be automated and inserted into the model, as discussed in the previous section, there would still be a need for estimating rates without quantum calculations, due to time and budget constraints when calculating potential reactions which are not included in the model. If these estimates can be improved, then less quantum calculations may be required to get similar accuracy.

Current databases of reaction rate coefficients and thermodynamic properties typically report what is needed for detailed kinetic models, namely thermodynamic parameters available as NASA polynomials and reaction rate coefficients in modified

Arrhenius form. While this is useful for adding the reactions to a detailed mechanism, it does not provide all the information to estimate rate constants for other reactions. Better data is needed for better estimates.

When trying to fit data to models using just the original structure and the final output in a machine learning model, too many degrees of freedom can prevent effective extrapolation. Fixing this issue will likely require leveraging underlying data which might be useful in making the model, like geometries, frequencies, energies, etc.

There is a need to develop a database which contains quantum outputs which to serve as useful model training parameters for reaction rate estimation. If a large enough database of relevant intermediary data exists, more fundamental understanding of the system can be leveraged to generate better estimates of kinetic and thermodynamic parameters, preventing machines from incorrectly learning on the dataset.

#### 7.2.4 Computer assisted on-line position specific isotope assessment (PSIA)

Chapter 6 shows that RMG is able to effectively predict molecular products in PSIA, with potential to replace the experimentally intensive step of mapping products to the spot on the original reactants. To make this a reality, a simpler and more robust method of determining mapping can be employed on RMG data.

This better method would involve running a simulation for each unique isotope spot, without kinetic isotope effects, where that spot is 100% labeled isotopically and the others have 0% labeling. The fraction of products that are labeled indicates the fraction coming from that carbon. This information, combined with relative product distributions from experiments can be used to find the precursor-product atom mapping using a linear algebra approach similar to Wolyniak et al.[217]

Once this simpler method has been tested, the next step would be to lower the barrier for experimentalists to use the software, which could involve partnering with them to improve usability, so that all they have to do is put in the input molecule, experimental conditions, and relative proportions of observed compounds, and the

software returns the filiation values and some measure of confidence in the result.

### 7.2.5 Measuring stochastic oxidation in aerosols

Chapter 4 shows that stochastic kinetics may matter at some atmospheric conditions, and that experiments have yet to be run under conditions where they would see stochastic effects. Appendix A discusses experimental efforts conducted in an attempt to measure a stochastic effect. The difficulty to measure stochastic effects comes from a few sources:

1. Creating aerosols with average volume-weighted diameter distributions of around 50 nm.
2. Measuring chemical properties of aerosol particles with diameters from 40-80 nm.
3. Choosing an initial aerosol composition that is liquid, has fast propagation chemistry, and does not oxidize upon exposure to light

Appendix A discusses the causes of these three challenges and potential next steps to overcome them.

## 7.3 Path forward

While this thesis presents some improvements towards better understanding alternative fuels and atmospheric chemistry, the problem of halting anthropogenic emissions related to climate change still looms large. Solving this larger problem will require finding innovative strategies to not only reduce emissions, but also moving societies better consider sustainability in decision making. Technology development and improvements in scientific understanding will need to work in tandem to experts in policy, economics, and human behavior. With a deep desire to adapt our lifestyle to a carbon-free reality, both personally and at a societal level, this global problem can be managed.

# Chapter 8

## Bibliography

- [1] Intergovernmental Panel on Climate Change. Global Warming of 1.5C. Special Report 15, IPCC, Incheon, Republic of Korea, October 2018.
- [2] Dahmus, J.B. Can Efficiency Improvements Reduce Resource Consumption? *J. Ind. Ecol.*, 18(6):883–897, December 2014. ISSN 1530-9290. doi: 10.1111/jiec.12110.
- [3] Freeman, R., Yearworth, M. and Preist, C. Revisiting Jevons' Paradox with System Dynamics: Systemic Causes and Potential Cures. *Journal of Industrial Ecology*, 20(2):341–353, June 2015. ISSN 1088-1980. doi: 10.1111/jiec.12285.
- [4] Godin-Beekmann, S., Newman, P.A. and Petropavlovskikh, I. 30th anniversary of the Montreal Protocol: From the safeguard of the ozone layer to the protection of the Earth's climate. *Comptes Rendus Geoscience*, 350(7):331–333, November 2018. ISSN 1631-0713. doi: 10.1016/j.crte.2018.11.001.
- [5] Abbasi, S.A. and Abbasi, T. Monitoring Ozone Loss and Its Consequences: Past, Present, and Future. *Ozone Hole*, pages 121–131, 2017. doi: 10.1007/978-1-4939-6710-0\_7.
- [6] Fouquet, R. Path dependence in energy systems and economic development. *Nat. Energy*, 1:16098, July 2016. ISSN 2058-7546. doi: 10.1038/nenergy.2016.98.

- [7] Robert-Jan Bartunek and David Goodman. EU carbon emissions rose in 2017: Eurostat. *Reuters*, May 2018.
- [8] Covert, T., Greenstone, M. and Knittel, C.R. Will We Ever Stop Using Fossil Fuels? *J. Econ. Perspect.*, 30(1):117–138, February 2016. ISSN 0895-3309. doi: 10.1257/jep.30.1.117.
- [9] Zhang, H., Baeyens, J., Cáceres, G., Degrève, J. and Lv, Y. Thermal energy storage: Recent developments and practical aspects. *Progress in Energy and Combustion Science*, 53:1–40, March 2016. ISSN 0360-1285. doi: 10.1016/j.jpecs.2015.10.003.
- [10] Cho, J., Jeong, S. and Kim, Y. Commercial and research battery technologies for electrical energy storage applications. *Progress in Energy and Combustion Science*, 48:84–101, June 2015. ISSN 0360-1285. doi: 10.1016/j.jpecs.2015.01.002.
- [11] Kumar, R., Sahoo, S., Joanni, E., Singh, R.K., Tan, W.K., Kar, K.K. and Matsuda, A. Recent progress in the synthesis of graphene and derived materials for next generation electrodes of high performance lithium ion batteries. *Progress in Energy and Combustion Science*, 75:100786, November 2019. ISSN 0360-1285. doi: 10.1016/j.jpecs.2019.100786.
- [12] Bains, P., Psarras, P. and Wilcox, J. CO<sub>2</sub> capture from the industry sector. *Progress in Energy and Combustion Science*, 63:146–172, November 2017. ISSN 0360-1285. doi: 10.1016/j.jpecs.2017.07.001.
- [13] Koornneef, J., Ramírez, A., Turkenburg, W. and Faaij, A. The environmental impact and risk assessment of CO<sub>2</sub> capture, transport and storage – An evaluation of the knowledge base. *Progress in Energy and Combustion Science*, 38 (1):62–86, February 2012. ISSN 0360-1285. doi: 10.1016/j.jpecs.2011.05.002.
- [14] Sprecher, B., Xiao, Y., Walton, A., Speight, J., Harris, R., Kleijn, R., Visser, G. and Kramer, G.J. Life Cycle Inventory of the Production of Rare Earths

and the Subsequent Production of NdFeB Rare Earth Permanent Magnets. *Environ. Sci. Technol.*, 48(7):3951–3958, April 2014. ISSN 0013-936X. doi: 10.1021/es404596q.

- [15] Bandara, H.M.D., Darcy, J.W., Apelian, D. and Emmert, M.H. Value Analysis of Neodymium Content in Shredder Feed: Toward Enabling the Feasibility of Rare Earth Magnet Recycling. *Environ. Sci. Technol.*, 48(12):6553–6560, June 2014. ISSN 0013-936X. doi: 10.1021/es405104k.
- [16] vom Lehn, F., Cai, L. and Pitsch, H. Sensitivity analysis, uncertainty quantification, and optimization for thermochemical properties in chemical kinetic combustion models. *Proceedings of the Combustion Institute*, July 2018. ISSN 1540-7489. doi: 10.1016/j.proci.2018.06.188.
- [17] Karwat, D.M., Wagnon, S.W., Teini, P.D. and Wooldridge, M.S. On the chemical kinetics of n-Butanol: Ignition and speciation studies. *J. Phys. Chem. A*, 115(19):4909–4921, 2011. ISSN 1089-5639. doi: 10.1021/jp200905n.
- [18] Chang, Y., Jia, M., Niu, B., Zhang, Y., Xie, M. and Li, Y. Construction and assessment of reduced oxidation mechanisms using global sensitivity analysis and uncertainty analysis. *Proceedings of the Combustion Institute*, July 2018. ISSN 1540-7489. doi: 10.1016/j.proci.2018.07.006.
- [19] Merchant, S.S., Zanoelo, E.F., Speth, R.L., Harper, M.R., Van Geem, K.M. and Green, W.H. Combustion and pyrolysis of iso-butanol: Experimental and chemical kinetic modeling study. *Combust. Flame*, 160(10):1907–1929, 2013. doi: 10.1016/j.combustflame.2013.04.023.
- [20] Bykov, V., Yu, C., Gol'dshtein, V. and Maas, U. Model reduction and mechanism comparison of hydrogen/oxygen auto-ignition. *Proceedings of the Combustion Institute*, August 2018. ISSN 1540-7489. doi: 10.1016/j.proci.2018.06.189.
- [21] Hughes, K.J., Fairweather, M., Griffiths, J.F., Porter, R. and Tomlin, A.S. The application of the QSSA via reaction lumping for the reduction of complex

- hydrocarbon oxidation mechanisms. *Proceedings of the Combustion Institute*, 32(1):543–551, 2009. ISSN 1540-7489. doi: 10.1016/j.proci.2008.06.064. 3.
- [22] Kooshkbaghi, M., Frouzakis, C.E., Boulouchos, K. and Karlin, I.V. Spectral Quasi-Equilibrium Manifold for Chemical Kinetics. *J. Phys. Chem. A*, April 2016. ISSN 1089-5639. doi: 10.1021/acs.jpca.6b01709.
- [23] Saunders, S.M., Jenkin, M.E., Derwent, R.G. and Pilling, M.J. Protocol for the development of the Master Chemical Mechanism, MCM v3 (Part A): Tropospheric degradation of non-aromatic volatile organic compounds. *Atmos. Chem. Phys.*, 3(1):161–180, 2003.
- [24] Curran, H.J. AramcoMech. NUI Galway, 2017.
- [25] Burke, S.M., Burke, U., Mc Donagh, R., Mathieu, O., Osorio, I., Keesee, C., Morones, A., Petersen, E.L., Wang, W., DeVerter, T.A. et al. An experimental and modeling study of propene oxidation. Part 2: Ignition delay time and flame speed measurements. *Combust. Flame*, 162(2):296–314, February 2015. ISSN 00102180. doi: 10.1016/j.combustflame.2014.07.032.
- [26] Sarathy, S.M., Oßwald, P., Hansen, N. and Kohse-Höinghaus, K. Alcohol combustion chemistry. *Prog. Energy Combust. Sci.*, 44:40–102, 2014. doi: 10.1016/j.pecs.2014.04.003.
- [27] Aumont, B., Szopa, S. and Madronich, S. Modelling the evolution of organic carbon during its gas-phase tropospheric oxidation: Development of an explicit model based on a self generating approach. *Atmospheric Chem. Phys. Discuss.*, 5(1):703–754, 2005. ISSN 1680-7324. doi: 10.5194/acpd-5-703-2005.
- [28] Gao, C.W., Allen, J.W., Green, W.H. and West, R.H. Reaction mechanism generator: Automatic construction of chemical kinetic mechanisms. *Comput. Phys. Commun.*, 203:212–225, June 2016. ISSN 0010-4655. doi: 10.1016/j.cpc.2016.02.013.

- [29] Coley, C.W., Green, W.H. and Jensen, K.F. Machine Learning in Computer-Aided Synthesis Planning. *Acc. Chem. Res.*, 51(5):1281–1289, May 2018. ISSN 0001-4842. doi: 10.1021/acs.accounts.8b00087.
- [30] Pechukas, P. Transition state theory. *Annu. Rev. Phys. Chem.*, 32(1):159–177, 1981.
- [31] Truhlar, D.G., Garrett, B.C. and Klippenstein, S.J. Current Status of Transition-State Theory. *J. Phys. Chem.*, 100(31):12771–12800, 1996.
- [32] Allen, J.W., Goldsmith, C.F. and Green, W.H. Automatic estimation of pressure-dependent rate coefficients. *Phys. Chem. Chem. Phys.*, 14(3):1131–1131, 2012. ISSN 6172534580. doi: 10.1039/c1cp22765c.
- [33] Deutschmann, O., Schmidt, R., Behrendt, F. and Warnat, J. Numerical modeling of catalytic ignition. *Symposium (International) on Combustion*, 26(1): 1747–1754, January 1996. ISSN 0082-0784. doi: 10.1016/S0082-0784(96)80400-0.
- [34] Gillespie, D.T. Stochastic Simulation of Chemical Kinetics. *Annu. Rev. Phys. Chem.*, 58(1):35–55, April 2007. ISSN 0066-426X. doi: 10.1146/annurev.physchem.58.032806.104637.
- [35] Vanzani, P., Rigo, A., Zennaro, L., Di Paolo, M.L., Scarpa, M. and Rossetto, M. Reaction rates of  $\alpha$ -tocopheroxyl radicals confined in micelles and in human plasma lipoproteins. *Biophys. Chem.*, 192:20–26, August 2014. ISSN 0301-4622. doi: 10.1016/j.bpc.2014.06.002.
- [36] Székely, T. and Burrage, K. Stochastic simulation in systems biology. *Comput. Struct. Biotechnol. J.*, 12(20-21):14–25, October 2014. ISSN 2001-0370. doi: 10.1016/j.csbj.2014.10.003.
- [37] Bartholomay, A.F. A Stochastic Approach to Statistical Kinetics with Application to Enzyme Kinetics. *Biochemistry-US*, 1(2):223–230, March 1962. ISSN 0006-2960. doi: 10.1021/bi00908a005.

- [38] Ingold, K.U. Autoxidation of lipids and antioxidation by  $\alpha$ -tocopherol and ubiquinol in homogeneous solution and in aqueous dispersions of lipids: Unrecognized consequences of lipid particle size as exemplified by oxidation of human low density lipoprotein. *Proc. Natl. Acad. Sci. USA*, page 5, 1993.
- [39] Ehn, M., Thornton, J., Kleist, E., Sipilä, M., Junninen, H., Pullinen, I., Springer, M., Rubach, F., Tillmann, R., Lee, B. et al. A large source of low-volatility secondary organic aerosol. *Nature*, 506:476–9, 2014. ISSN 0028-0836. doi: 10.1038/nature13032.
- [40] Merchant, S.S., Goldsmith, C.F., Vandeputte, A.G., Burke, M.P., Klippenstein, S. and Green, W.H. Understanding low-temperature first stage ignition delay : Propane. *Combust. Flame*, 162:3658–3673, 2015. doi: 10.1016/j.combustflame. 2015.07.005.
- [41] Collard, F.X. and Blin, J. A review on pyrolysis of biomass constituents: Mechanisms and composition of the products obtained from the conversion of cellulose, hemicelluloses and lignin. *Renew. Sustain. Energy Rev.*, 38:594–608, 2014. ISSN 1364-0321. doi: 10.1016/j.rser.2014.06.013.
- [42] Ţerbănescu, C. Kinetic analysis of cellulose pyrolysis: A short review. *Chem. Pap.*, 68(7):847–860, 2014. doi: 10.2478/s11696-013-0529-z.
- [43] Gauchotte-Lindsay, C. and Turnbull, S.M. On-line high-precision carbon position-specific stable isotope analysis: A review. *TrAC-Trend. Anal. Chem.*, 76:115–125, February 2016. ISSN 01659936. doi: 10.1016/j.trac.2015.07.010.
- [44] Goldman, M.J., Ono, S. and Green, W.H. Correct Symmetry Treatment for X + X Reactions Prevents Large Errors in Predicted Isotope Enrichment. *J. Phys. Chem. A*, 123(12):2320–2324, March 2019. ISSN 1089-5639. doi: 10.1021/acs.jPCA.8b09024.
- [45] Karas, A.J., Gilbert, R.G. and Collins, M.A. Rigorous derivation of reaction

- path degeneracy in transition state theory. *Chem. Phys. Lett.*, 193(1-3):181–184, 1992.
- [46] Pollak, E.L.I. and Pechukas, P. Symmetry numbers, not statistical factors, should be used in absolute rate theory and in Brøsted relations. *J. Am. Chem. Soc.*, 100(10):2984–2991, 1978. doi: 10.1021/ja00478a009.
- [47] Bishop, D.M. and Laidler, K.J. Symmetry numbers and statistical factors in rate theory. *J. Chem. Phys.*, 42(5):1688–1691, March 1965. ISSN 0021-9606, 1089-7690. doi: 10.1063/1.1696178.
- [48] Fernández-Ramos, A., Ellingson, B.A., Meana-Pañeda, R., Marques, J.M.C. and Truhlar, D.G. Symmetry numbers and chemical reaction rates. *Theor. Chem. Acc.*, 118(4):813–826, October 2007. ISSN 1432-881X, 1432-2234. doi: 10.1007/s00214-007-0328-0.
- [49] McIntosh, G.J. A theoretical kinetic model of the temperature and pH dependent dimerization of orthosilicic acid in aqueous solution. *Phys. Chem. Chem. Phys.*, 14(2):996–1013, 2012. ISSN 1463-9076, 1463-9084. doi: 10.1039/C1CP22273B.
- [50] Vandeputte, A.G., Reyniers, M.F. and Marin, G.B. Theoretical study of the thermal decomposition of dimethyl disulfide. *J. Phys. Chem. A*, 114(39):10531–10549, October 2010. ISSN 1089-5639, 1520-5215. doi: 10.1021/jp103357z.
- [51] Tranter, R.S., Klippenstein, S.J., Harding, L.B., Giri, B.R., Yang, X. and Kiefer, J.H. Experimental and theoretical investigation of the self-reaction of phenyl radicals. *J. Phys. Chem. A*, 114(32):8240–8261, August 2010. ISSN 1089-5639, 1520-5215. doi: 10.1021/jp1031064.
- [52] Miller, J.A. and Klippenstein, S.J. The recombination of propargyl radicals and other reactions on a C<sub>6</sub>H<sub>6</sub> potential. *J. Phys. Chem. A*, 107(39):7783–7799, October 2003. ISSN 1089-5639, 1520-5215. doi: 10.1021/jp030375h.

- [53] Babikov, D., Semenov, A. and Teplukhin, A. One possible source of mass-independent fractionation of sulfur isotopes in the Archean atmosphere of Earth. *Geochim. Cosmochim. Ac.*, 204:388–406, May 2017. ISSN 0016-7037. doi: 10.1016/j.gca.2017.01.029.
- [54] Dauphas, N. and Schauble, E.A. Mass fractionation laws, mass-independent effects, and isotopic anomalies. *Annu. Rev. Earth Planet. Sci.*, 44(1):709–783, June 2016. ISSN 0084-6597, 1545-4495. doi: 10.1146/annurev-earth-060115-012157.
- [55] Truhlar, D.G. and Garrett, B.C. Variational transition-state theory. *Acc. Chem. Res.*, 13(12):440–448, December 1980. ISSN 0001-4842. doi: 10.1021/ar50156a002.
- [56] Teplukhin, A. and Babikov, D. Several Levels of Theory for Description of Isotope Effects in Ozone: Symmetry Effect and Mass Effect. *J. Phys. Chem. A*, 122(47):9177–9190, November 2018. ISSN 1089-5639. doi: 10.1021/acs.jpca.8b09025.
- [57] Gilson, M.K. and Irikura, K.K. Symmetry numbers for rigid, flexible, and fluxional molecules: Theory and applications. *J. Phys. Chem. B*, 114(49):16304–16317, December 2010. doi: 10.1021/jp110434s.
- [58] McQuarrie, D.A. and Simon, J.D. 26-8 We can calculate equilibrium constants in terms of partition coefficients. In *Physical Chemistry: A Molecular Approach*. University Science Books, 1997.
- [59] Velivetskaya, T.A., Ignatiev, A.V., Yakovenko, V.V. and Vysotskiy, S.V. Experimental studies of the oxygen isotope anomalies ( $\Delta^{17}\text{O}$ ) of  $\text{H}_2\text{O}_2$  and their relation to radical recombination reactions. *Chem. Phys. Lett.*, 693:107–113, February 2018. ISSN 0009-2614. doi: 10.1016/j.cplett.2018.01.012.
- [60] Mauersberger, K., Erbacher, B., Krankowsky, D., Gunther, J. and Nickel, R.

Ozone isotope enrichment: Isotopomer-specific rate coefficients. *Science*, 283 (5400):370–372, 1999.

- [61] Bigeleisen, J. and Mayer, M.G. Calculation of equilibrium constants for isotopic exchange reactions. *J. Chem. Phys.*, 15(5):261–267, May 1947. ISSN 0021-9606, 1089-7690. doi: 10.1063/1.1746492.
- [62] Ivanov, M.V. and Babikov, D. On molecular origin of mass-independent fractionation of oxygen isotopes in the ozone forming recombination reaction. *Proc. Natl. Acad. Sci. U. S. A.*, 110(44):17708–17713, October 2013. ISSN 0027-8424, 1091-6490. doi: 10.1073/pnas.1215464110.
- [63] Dunn, P.J.H., Malinovsky, D. and Goenaga-Infante, H. Calibration strategies for the determination of stable carbon absolute isotope ratios in a glycine candidate reference material by elemental analyser-isotope ratio mass spectrometry. *Anal. Bioanal. Chem.*, 407(11):3169–3180, April 2015. ISSN 1618-2642, 1618-2650. doi: 10.1007/s00216-014-7926-1.
- [64] Junk, G.A. and Svec, H.J. Nitrogen isotope abundance measurements. Chemistry-Radiochemistry ISC-1138, United States Atomic Energy Commission, Ames, Iowa, 1958.
- [65] Attendorn, H.G. and Bowen, R.N.C. *Radioactive and Stable Isotope Geology*. Chapman & Hall, London, 1997. ISBN 0 412 75280 8.
- [66] Babikov, D. Recombination reactions as a possible mechanism of mass-independent fractionation of sulfur isotopes in the Archean atmosphere of Earth. *Proc. Natl. Acad. Sci. U. S. A.*, 114(12):3062–3067, March 2017. ISSN 0027-8424, 1091-6490. doi: 10.1073/pnas.1620977114.
- [67] Gillespie, D.T. A general method for numerically simulating the stochastic time evolution of coupled chemical reactions. *J. Comput. Phys.*, 22(4):403–434, 1976. ISSN 0021-9991. doi: 10.1016/0021-9991(76)90041-3.

- [68] Gillespie, D.T. Exact stochastic simulation of coupled chemical reactions. *J. Phys. Chem.*, 81(25):2340–2361, December 1977. ISSN 0022-3654. doi: 10.1021/j100540a008.
- [69] Goss, P.J.E. and Peccoud, J. Quantitative modeling of stochastic systems in molecular biology by using stochastic Petri nets. *Proc. Natl. Acad. Sci. U. S. A.*, 95(12):6750–6755, June 1998. ISSN 0027-8424, 1091-6490. doi: 10.1073/pnas.95.12.6750.
- [70] Pavlov, A. and Kasting, J. Mass-Independent Fractionation of Sulfur Isotopes in Archean Sediments: Strong Evidence for an Anoxic Archean Atmosphere. *Astrobiology*, 2(1):27–41, March 2002. ISSN 1531-1074. doi: 10.1089/153110702753621321.
- [71] Bunker, P.R. and Jensen, P. *Molecular Symmetry and Spectroscopy*. NRC Research Press, Ottawa, 2 edition, 2006. ISBN 978-0-660-19628-2.
- [72] Mayer, R. Elemental sulfur and its reactions. In Oae, S., editor, *Organic Chemistry of Sulfur*, pages 33–69. Springer US, Boston, MA, 1977. ISBN 978-1-4684-2051-7 978-1-4684-2049-4. doi: 10.1007/978-1-4684-2049-4\_2.
- [73] Mentel, T.F., Springer, M., Ehn, M., Kleist, E., Pullinen, I., Kurtén, T., Rissanen, M., Wahner, A. and Wildt, J. Formation of highly oxidized multifunctional compounds: Autoxidation of peroxy radicals formed in the ozonolysis of alkenes – deduced from structure–product relationships. *Atmos. Chem. Phys.*, 15(12): 6745–6765, 2015. doi: 10.5194/acp-15-6745-2015.
- [74] Zhang, X., McVay, R.C., Huang, D.D., Dalleska, N.F., Aumont, B., Flagan, R.C. and Seinfeld, J.H. Formation and evolution of molecular products in  $\alpha$ -pinene secondary organic aerosol. *Proc. Natl. Acad. Sci. U. S. A.*, 112(46): 14168–14173, November 2015. ISSN 0027-8424, 1091-6490. doi: 10.1073/pnas.1517742112.

- [75] Agency, U.E.P. Registration of Isobutanol as a Gasoline Additive: Opportunity for Public Comment. *Fed. Regist.*, 83(61):13460–13463, March 2018.
- [76] Pruitt, S.E. Letter of approval of isobutanol fuel additive to Butamax Advanced Biofuels, LLC., June 2018.
- [77] Rodríguez-Antón, L.M., Gutierrez-Martín, F. and Doce, Y. Physical properties of gasoline, isobutanol and ETBE binary blends in comparison with gasoline ethanol blends. *Fuel*, 166:73–78, February 2016. ISSN 0016-2361. doi: 10.1016/j.fuel.2015.10.106.
- [78] Koninckx, J. *Comment Submitted by Jan Koninckx, Chief Executive Officer, Butamax Advanced Biofuels, LLC.* Clean Air Act Registration of Isobutanol as a Gasoline Additive (40 CFR 79). U.S. eRulemaking Management Office, May 2018. tracking number: 1k2-92vq-kyka.
- [79] Mack, J.H., Schuler, D., Butt, R.H. and Dibble, R.W. Experimental investigation of butanol isomer combustion in Homogeneous Charge Compression Ignition (HCCI) engines. *Applied Energy*, 165:612–626, March 2016. ISSN 0306-2619. doi: 10.1016/j.apenergy.2015.12.105.
- [80] Rajesh Kumar, B., Saravanan, S., Rana, D. and Nagendran, A. A comparative analysis on combustion and emissions of some next generation higher-alcohol/diesel blends in a direct-injection diesel engine. *Energ. Convers. Manage.*, 119:246–256, July 2016. ISSN 0196-8904. doi: 10.1016/j.enconman.2016.04.053.
- [81] Hui, X., Niemeyer, K.E., Brady, K.B. and Sung, C.J. Reduced Chemistry for Butanol Isomers at Engine-Relevant Conditions. *Energy Fuels*, 31(1):867–881, January 2017. ISSN 0887-0624. doi: 10.1021/acs.energyfuels.6b01857.
- [82] Weber, B.W. and Sung, C.J. Comparative Autoignition Trends in Butanol Isomers at Elevated Pressure. *Energy Fuels*, 27(3):1688–1698, March 2013. ISSN 0887-0624. doi: 10.1021/ef302195c.

- [83] Shahsavan, M. and Mack, J.H. Numerical study of a boosted HCCI engine fueled with n-butanol and isobutanol. *Energ. Convers. Manage.*, 157:28–40, February 2018. ISSN 0196-8904. doi: 10.1016/j.enconman.2017.11.063.
- [84] Pan, L., Zhang, Y., Tian, Z., Yang, F. and Huang, Z. Experimental and Kinetic Study on Ignition Delay Times of iso-Butanol. *Energy Fuels*, 28(3):2160–2169, March 2014. ISSN 0887-0624. doi: 10.1021/ef4021069.
- [85] Zheng, J., Meana-Pañeda, R. and Truhlar, D.G. Prediction of Experimentally Unavailable Product Branching Ratios for Biofuel Combustion: The Role of Anharmonicity in the Reaction of Isobutanol with OH. *J. Am. Chem. Soc.*, 136(13):5150–5160, April 2014. ISSN 0002-7863. doi: 10.1021/ja5011288.
- [86] Smith, G.P., Golden, D.M., Frenklach, M., Moriarty, N.W., Eiteneer, B., Goldenberg, M., Bowman, C.T., Hanson, R.K., Song, S., Gardiner, W.C. et al. GRI-MECH 3.0. [http://www.me.berkeley.edu/gri\\_mech/](http://www.me.berkeley.edu/gri_mech/).
- [87] Sarathy, S.M., Vranckx, S., Yasunaga, K., Mehl, M., Oswald, P., Metcalf, W.K., Westbrook, C.K., Pitz, W.J., Kohse-Höinghaus, K., Fernandes, R.X. et al. A comprehensive chemical kinetic combustion model for the four butanol isomers. *Combust. Flame*, 159(6):2028–2055, June 2012. ISSN 00102180. doi: 10.1016/j.combustflame.2011.12.017.
- [88] Welz, O., Klippenstein, S.J., Harding, L.B., Taatjes, C.A. and Zádor, J. Unconventional Peroxy Chemistry in Alcohol Oxidation: The Water Elimination Pathway. *J. Phys. Chem. Lett.*, 4(3):350–354, February 2013. ISSN 1948-7185. doi: 10.1021/jz302004w.
- [89] Ray, D.J.M., Redfearn, A. and Waddington, D.J. Gas-phase oxidation of alkenes: Decomposition of hydroxy-substituted peroxy radicals. *J. Chem. Soc., Perkin Trans. 2*, 0(5):540–543, January 1973. ISSN 1364-5471. doi: 10.1039/P29730000540.

- [90] Sun, H., Bozzelli, J.W. and Law, C.K. Thermochemical and Kinetic Analysis on the Reactions of O<sub>2</sub> with Products from OH Addition to Isobutene, 2-Hydroxy-1,1-dimethylethyl, and 2-Hydroxy-2-methylpropyl Radicals: HO<sub>2</sub> Formation from Oxidation of Neopentane, Part II. *J. Phys. Chem. A*, 111(23):4974–4986, June 2007. ISSN 1089-5639. doi: 10.1021/jp070072d.
- [91] Lizardo-Huerta, J.C., Sirjean, B., Bounaceur, R. and Fournet, R. Intramolecular effects on the kinetics of unimolecular reactions of  $\beta$ -HOROO· and HOQ·OOH radicals. *Phys. Chem. Chem. Phys.*, 18(17):12231–12251, April 2016. ISSN 1463-9084. doi: 10.1039/C6CP00111D.
- [92] Zádor, J., Fernandes, R.X., Georgievskii, Y., Meloni, G., Taatjes, C.A. and Miller, J.A. The reaction of hydroxyethyl radicals with O<sub>2</sub>: A theoretical analysis and experimental product study. *Proc. Combust. Inst.*, 32(1):271–277, January 2009. ISSN 1540-7489. doi: 10.1016/j.proci.2008.05.020.
- [93] Wong, B.M., Matheu, D.M. and Green, W.H. Temperature and molecular size dependence of the high-pressure limit. *J. Phys. Chem. A*, 107(32):6206–6211, August 2003. ISSN 1089-5639, 1520-5215. doi: 10.1021/jp034165g.
- [94] Frisch, M.J., Trucks, G.W., Schlegel, H.B., Scuseria, G.E., Robb, M.A., Cheeseman, J.R., Montgomery, J.A., Vreven, T., Kudin, K.N., Burant, J.C. et al. Gaussian 03, Revision D.01. Gaussian, Inc., 2004.
- [95] Werner, H.J., Knowles, P.J., Knizia, G., Manby, F.R. and Schütz, M. Molpro: A general-purpose quantum chemistry program package. *WIREs Comput Mol Sci*, 2:242–253, 2012.
- [96] Fogueri, U.R., Kozuch, S., Karton, A. and Martin, J.M.L. A simple DFT-based diagnostic for nondynamical correlation. *Theor. Chem. Acc.*, 132(1), January 2013. ISSN 1432-881X, 1432-2234. doi: 10.1007/s00214-012-1291-y.
- [97] Goldsmith, C.F., Green, W.H. and Klippenstein, S.J. Role of O<sub>2</sub> + QOOH in low-temperature ignition of propane. 1. temperature and pressure dependent

- rate coefficients. *J. Phys. Chem. A*, 116(13):3325–3346, 2012. ISSN 1089-5639. doi: 10.1021/jp210722w.
- [98] Johnson III, R.D. *NIST Computational Chemistry Comparison and Benchmark Database*. Number 101 in NIST Standard Reference Database. National Institute of Standards and Technology, August 2019.
- [99] Alecu, I.M., Zheng, J., Zhao, Y. and Truhlar, D.G. Computational Thermochemistry: Scale Factor Databases and Scale Factors for Vibrational Frequencies Obtained from Electronic Model Chemistries. *J. Chem. Theory Comput.*, 6(9):2872–2887, September 2010. ISSN 1549-9618. doi: 10.1021/ct100326h.
- [100] Green, N.J.B. and Bhatti, Z.A. Steady-state master equation methods. *Phys. Chem. Chem. Phys.*, 9(31):4275–4290, August 2007. ISSN 1463-9084. doi: 10.1039/B704519K.
- [101] Jasper, A.W. and Miller, J.A. Lennard-Jones parameters for combustion and chemical kinetics modeling from full-dimensional intermolecular potentials. *Combust. Flame*, 161(1):101–110, January 2014. ISSN 0010-2180. doi: 10.1016/j.combustflame.2013.08.004.
- [102] Antonov, I.O., Kwok, J., Zádor, J. and Sheps, L. A Combined Experimental and Theoretical Study of the Reaction OH + 2-Butene in the 400–800 K Temperature Range. *J. Phys. Chem. A*, 119(28):7742–7752, July 2015. ISSN 1089-5639, 1520-5215. doi: 10.1021/acs.jpca.5b01012.
- [103] Miyoshi, A. Systematic computational study on the unimolecular reactions of alkylperoxy (RO<sub>2</sub>), hydroperoxyalkyl (QOOH), and hydroperoxyalkylperoxy (O<sub>2</sub>QOOH) radicals. *J. Phys. Chem. A*, 115(15):3301–3325, April 2011. ISSN 1089-5639. doi: 10.1021/jp112152n.
- [104] Luo, Y.R. and Cheng, J.p. Bond disassociation energies. In *CRC Handbook of Chemistry and Physics*. CRC Press/Taylor & Francis, Boca Raton, FL, 100 edition, June 2019.

- [105] Chen, D., Wang, K. and Wang, H. Violation of collision limit in recently published reaction models. *Combust. Flame*, 186:208–210, December 2017. ISSN 0010-2180. doi: 10.1016/j.combustflame.2017.08.005.
- [106] Welz, O., Savee, J.D., Eskola, A.J., Sheps, L., Osborn, D.L. and Taatjes, C.A. Low-temperature combustion chemistry of biofuels: Pathways in the low-temperature (550–700K) oxidation chemistry of isobutanol and tert-butanol. *Proc. Combust. Inst.*, 34(1):493–500, January 2013. ISSN 1540-7489. doi: 10.1016/j.proci.2012.05.058.
- [107] Welz, O., Zádor, J., Savee, J.D., Ng, M.Y., Meloni, G., Fernandes, R.X., Sheps, L., Simmons, B.A., Lee, T.S., Osborn, D.L. et al. Low-temperature combustion chemistry of biofuels: Pathways in the initial low-temperature (550 K–750 K) oxidation chemistry of isopentanol. *Phys. Chem. Chem. Phys.*, 14(9):3112–3127, February 2012. ISSN 1463-9084. doi: 10.1039/C2CP23248K.
- [108] Curran, H.J., Gaffuri, P., Pitz, W.J. and Westbrook, C.K. A comprehensive modeling study of iso-octane oxidation. *Combust. Flame*, 129(3):253–280, May 2002. ISSN 0010-2180. doi: 10.1016/S0010-2180(01)00373-X.
- [109] Oakley, L.H., Casadio, F., Shull, K.R. and Broadbelt, L.J. Theoretical Study of Epoxidation Reactions Relevant to Hydrocarbon Oxidation. *Ind. Eng. Chem. Res.*, 56(26):7454–7461, July 2017. ISSN 0888-5885. doi: 10.1021/acs.iecr.7b01443.
- [110] Bugler, J., Power, J. and Curran, H.J. A theoretical study of cyclic ether formation reactions. *Proceedings of the Combustion Institute*, 36(1):161–167, January 2017. ISSN 1540-7489. doi: 10.1016/j.proci.2016.05.006.
- [111] Fan, J., Rosenfeld, D., Zhang, Y., Giangrande, S.E., Li, Z., Machado, L.A.T., Martin, S.T., Yang, Y., Wang, J., Artaxo, P. et al. Substantial convection and precipitation enhancements by ultrafine aerosol particles. *Science*, 359(6374): 411–418, January 2018. ISSN 0036-8075, 1095-9203. doi: 10.1126/science.aaan8461.

- [112] Rychlik, K.A., Secrest, J.R., Lau, C., Pulczinski, J., Zamora, M.L., Leal, J., Langley, R., Myatt, L.G., Raju, M., Chang, R.C.A. et al. In utero ultrafine particulate matter exposure causes offspring pulmonary immunosuppression. *Proc. Natl. Acad. Sci. USA*, 116(9):3443–3448, February 2019. ISSN 0027-8424, 1091-6490. doi: 10.1073/pnas.1816103116.
- [113] Nie, L., Yang, W., Zhang, H. and Fu, S. Monte Carlo simulation of microemulsion polymerization. *Polymer*, 46(9):3175–3184, April 2005. ISSN 0032-3861. doi: 10.1016/j.polymer.2005.01.085.
- [114] Gentry, S.T., Kendra, S.F. and Bezpalko, M.W. Ostwald Ripening in Metallic Nanoparticles: Stochastic Kinetics. *J. Phys. Chem. C*, 115(26):12736–12741, July 2011. ISSN 1932-7447. doi: 10.1021/jp2009786.
- [115] Mozurkewich, M. Effect of statistics of small numbers on the chemistry of trace species in atmospheric particles. *Geophys. Res. Lett.*, 24(24):3209–3212, 1997.
- [116] Lushnikov, A.A., Bhatt, J.S. and Ford, I.J. Stochastic approach to chemical kinetics in ultrafine aerosols. *J. Aerosol Sci.*, 34(9):1117–1133, September 2003. ISSN 0021-8502. doi: 10.1016/S0021-8502(03)00082-X.
- [117] Lakey, P.S.J., Berkemeier, T., Krapf, M., Dommen, J., Steimer, S.S., Whalley, L.K., Ingham, T., Baeza-Romero, M.T., Pöschl, U., Shiraiwa, M. et al. The effect of viscosity and diffusion on the HO<sub>2</sub> uptake by sucrose and secondary organic aerosol particles. *Atmos. Chem. Phys.*, 16(20):13035–13047, October 2016. ISSN 1680-7324. doi: 10.5194/acp-16-13035-2016.
- [118] Shiraiwa, M., Garland, R.M. and Pöschl, U. Kinetic double-layer model of aerosol surface chemistry and gas-particle interactions (K2-SURF): Degradation of polycyclic aromatic hydrocarbons exposed to O<sub>3</sub>, NO<sub>2</sub>, H<sub>2</sub>O, OH and NO<sub>3</sub>. *Atmos. Chem. Phys.*, 9(24):9571–9586, December 2009. ISSN 1680-7324. doi: 10.5194/acp-9-9571-2009.

- [119] Apsokardu, M.J. and Johnston, M.V. Nanoparticle growth by particle-phase chemistry. *Atmos. Chem. Phys.*, 18(3):1895–1907, February 2018. ISSN 1680-7316. doi: <https://doi.org/10.5194/acp-18-1895-2018>.
- [120] Wiegel, A.A., Wilson, K.R., Hinsberg, W.D. and Houle, F.A. Stochastic methods for aerosol chemistry: A compact molecular description of functionalization and fragmentation in the heterogeneous oxidation of squalane aerosol by OH radicals. *Phys. Chem. Chem. Phys.*, 17(6):4398–4411, January 2015. ISSN 1463-9084. doi: 10.1039/C4CP04927F.
- [121] Wiegel, A.A., Liu, M.J., Hinsberg, W.D., Wilson, K.R. and Houle, F.A. Diffusive confinement of free radical intermediates in the OH radical oxidation of semisolid aerosols. *Phys. Chem. Chem. Phys.*, 19(9):6814–6830, March 2017. ISSN 1463-9084. doi: 10.1039/C7CP00696A.
- [122] Richards-Henderson, N.K., Goldstein, A.H. and Wilson, K.R. Large Enhancement in the Heterogeneous Oxidation Rate of Organic Aerosols by Hydroxyl Radicals in the Presence of Nitric Oxide. *J. Phys. Chem. Lett.*, 6(22):4451–4455, November 2015. ISSN 1948-7185. doi: 10.1021/acs.jpclett.5b02121.
- [123] Kaiser, J.C., Riemer, N. and Knopf, D.A. Detailed heterogeneous oxidation of soot surfaces in a particle-resolved aerosol model. *Atmos. Chem. Phys.*, 11(9):4505–4520, 2011. ISSN 1680-7316. doi: 10.5194/acp-11-4505-2011. WOS:000290618600031.
- [124] Nah, T., Kessler, S.H., Daumit, K.E., Kroll, J.H., Leone, S.R. and Wilson, K.R. OH-initiated oxidation of sub-micron unsaturated fatty acid particles. *Phys. Chem. Chem. Phys.*, 15(42):18649–18663, October 2013. ISSN 1463-9084. doi: 10.1039/C3CP52655K.
- [125] Nah, T., Kessler, S.H., Daumit, K.E., Kroll, J.H., Leone, S.R. and Wilson, K.R. Influence of molecular structure and chemical functionality on the heterogeneous OH-initiated oxidation of unsaturated organic particles. *J. Phys. Chem. A*, 118(23):4106–4119, 2014. ISSN 1089-5639. doi: 10.1021/jp502666g.

- [126] George, I.J., Vlasenko, A., Slowik, J.G., Broekhuizen, K. and Abbatt, J.P.D. Heterogeneous oxidation of saturated organic aerosols by hydroxyl radicals: Uptake kinetics, condensed-phase products, and particle size change. *Atmos. Chem. Phys.*, 7(16):4187–4201, August 2007. ISSN 1680-7316. doi: <https://doi.org/10.5194/acp-7-4187-2007>.
- [127] Hearn, J.D. and Smith, G.D. A mixed-phase relative rates technique for measuring aerosol reaction kinetics. *Geophys. Res. Lett.*, 33(17):L17805, September 2006. ISSN 1944-8007. doi: 10.1029/2006GL026963.
- [128] Heine, N. and Wilson, K. Rapid autoxidation of squalene particles forms multi-functional hydroxyperoxides. *Abstr. Pap. Am. Chem. S.*, 251:373, March 2016.
- [129] Smith, J.D., Kroll, J.H., Cappa, C.D., Che, D.L., Liu, C.L., Ahmed, M., Leone, S.R., Worsnop, D.R. and Wilson, K.R. The heterogeneous reaction of hydroxyl radicals with sub-micron squalane particles: A model system for understanding the oxidative aging of ambient aerosols. *Atmos. Chem. Phys.*, 9(9):3209–3222, May 2009. ISSN 1680-7324. doi: 10.5194/acp-9-3209-2009.
- [130] Denisov, E. and Afanas'ev, I. *Oxidation and Antioxidants in Organic Chemistry and Biology*. Taylor & Francis, Boca Raton, FL, 1st edition, March 2005. ISBN 978-0-8247-5356-6 978-1-4200-3085-3. doi: 10.1201/9781420030853.
- [131] Kim, P. and Lee, C.H. Fast Probability Generating Function Method for Stochastic Chemical Reaction Networks. *Commun. Math. Comp. Chem.*, 71: 57–69, 2014.
- [132] Gillespie, D.T., Petzold, L.R. and Seitaridou, E. Validity conditions for stochastic chemical kinetics in diffusion-limited systems. *J. Chem. Phys.*, 140(5): 054111, February 2014. ISSN 0021-9606. doi: 10.1063/1.4863990.
- [133] Bielski, B.H., Arudi, R.L. and Sutherland, M.W. A study of the reactivity of HO<sub>2</sub>/O<sub>2</sub> with unsaturated fatty acids. *J. Biol. Chem.*, 258(8):4759–4761, April 1983. ISSN 0021-9258, 1083-351X.

- [134] Atkinson, R. Gas-Phase Tropospheric Chemistry of Volatile Organic Compounds: 1. Alkanes and Alkenes. *J. Phys. Chem. Ref. Data*, 26(2):215–290, 1997. ISSN 0047-2689. doi: 10.1063/1.556012.
- [135] Renbaum-Wolff, L., Grayson, J.W., Bateman, A.P., Kuwata, M., Sellier, M., Murray, B.J., Shilling, J.E., Martin, S.T. and Bertram, A.K. Viscosity of  $\alpha$ -pinene secondary organic material and implications for particle growth and reactivity. *Proc. Natl. Acad. Sci. USA*, 110(20):8014–8019, May 2013. ISSN 0027-8424, 1091-6490. doi: 10.1073/pnas.1219548110.
- [136] Che, D.L., Smith, J.D., Leone, S.R., Ahmed, M. and Wilson, K.R. Quantifying the reactive uptake of OH by organic aerosols in a continuous flow stirred tank reactor. *Phys. Chem. Chem. Phys.*, 11(36):7885–7895, September 2009. ISSN 1463-9084. doi: 10.1039/B904418C.
- [137] Ruehl, C.R., Nah, T., Isaacman, G., Worton, D.R., Chan, A.W.H., Kolesar, K.R., Cappa, C.D., Goldstein, A.H. and Wilson, K.R. The Influence of Molecular Structure and Aerosol Phase on the Heterogeneous Oxidation of Normal and Branched Alkanes by OH. *J. Phys. Chem. A*, 117(19):3990–4000, May 2013. ISSN 1089-5639. doi: 10.1021/jp401888q.
- [138] Lim, C.Y., Browne, E.C., Sugrue, R.A. and Kroll, J.H. Rapid heterogeneous oxidation of organic coatings on submicron aerosols. *Geophys. Res. Lett.*, 44(6): 2949–2957, March 2017. ISSN 0094-8276. doi: 10.1002/2017GL072585.
- [139] Lambe, A.T., Zhang, J., Sage, A.M. and Donahue, N.M. Controlled OH Radical Production via Ozone-Alkene Reactions for Use in Aerosol Aging Studies. *Environ. Sci. Technol.*, 41(7):2357–2363, April 2007. ISSN 0013-936X. doi: 10.1021/es061878e.
- [140] McNeill, V.F., Yatavelli, R.L.N., Thornton, J.A., Stipe, C.B. and Landgrebe, O. Heterogeneous OH oxidation of palmitic acid in single component and internally mixed aerosol particles: Vaporization and the role of particle phase. *Atmos.*

*Chem. Phys.*, 8(17):5465–5476, September 2008. ISSN 1680-7316. doi: <https://doi.org/10.5194/acp-8-5465-2008>.

- [141] Kolesar, K.R., Buffaloe, G., Wilson, K.R. and Cappa, C.D. OH-Initiated Heterogeneous Oxidation of Internally-Mixed Squalane and Secondary Organic Aerosol. *Environ. Sci. Technol.*, 48(6):3196–3202, March 2014. ISSN 0013-936X. doi: 10.1021/es405177d.
- [142] Arangio, A.M., Slade, J.H., Berkemeier, T., Pöschl, U., Knopf, D.A. and Shiraiwa, M. Multiphase Chemical Kinetics of OH Radical Uptake by Molecular Organic Markers of Biomass Burning Aerosols: Humidity and Temperature Dependence, Surface Reaction, and Bulk Diffusion. *J. Phys. Chem. A*, 119(19): 4533–4544, May 2015. ISSN 1089-5639, 1520-5215. doi: 10.1021/jp510489z.
- [143] Cheng, C.T., Chan, M.N. and Wilson, K.R. Importance of Unimolecular HO<sub>2</sub> Elimination in the Heterogeneous OH Reaction of Highly Oxygenated Tartaric Acid Aerosol. *J. Phys. Chem. A*, July 2016. ISSN 1089-5639. doi: 10.1021/acs.jpca.6b05289. 3.
- [144] Richards-Henderson, N.K., Goldstein, A.H. and Wilson, K.R. Sulfur Dioxide Accelerates the Heterogeneous Oxidation Rate of Organic Aerosol by Hydroxyl Radicals. *Environ. Sci. Technol.*, 50(7):3554–3561, April 2016. ISSN 0013-936X. doi: 10.1021/acs.est.5b05369.
- [145] Chim, M.M., Chow, C.Y., Davies, J.F. and Chan, M.N. Effects of Relative Humidity and Particle Phase Water on the Heterogeneous OH Oxidation of 2-Methylglutaric Acid Aqueous Droplets. *J. Phys. Chem. A*, 121(8):1666–1674, March 2017. ISSN 1089-5639. doi: 10.1021/acs.jpca.6b11606.
- [146] Chim, M.M., Lim, C.Y., Kroll, J.H. and Chan, M.N. Evolution in the Reactivity of Citric Acid toward Heterogeneous Oxidation by Gas-Phase OH Radicals. *ACS Earth Space Chem.*, 2(12):1323–1329, December 2018. doi: 10.1021/acsearthspacechem.8b00118.

- [147] Kwong, K.C., Chim, M.M., Hoffmann, E.H., Tilgner, A., Herrmann, H., Davies, J.F., Wilson, K.R. and Chan, M.N. Chemical Transformation of Methanesulfonic Acid and Sodium Methanesulfonate through Heterogeneous OH Oxidation. *ACS Earth Space Chem.*, 2(9):895–903, September 2018. doi: 10.1021/acsearthspacechem.8b00072.
- [148] Jacobs, M.I., Xu, B., Kostko, O., Wiegel, A.A., Houle, F.A., Ahmed, M. and Wilson, K.R. Using Nanoparticle X-ray Spectroscopy to Probe the Formation of Reactive Chemical Gradients in Diffusion-Limited Aerosols. *J. Phys. Chem. A*, 123(28):6034–6044, July 2019. ISSN 1089-5639. doi: 10.1021/acs.jpca.9b04507.
- [149] Lam, H.K., Shum, S.M., Davies, J.F., Song, M., Zuend, A. and Chan, M.N. Effects of inorganic salts on the heterogeneous OH oxidation of organic compounds: Insights from methylglutaric acid–ammonium sulfate. *Atmospheric Chem. Phys.*, 19(14):9581–9593, July 2019. ISSN 1680-7324. doi: 10.5194/acp-19-9581-2019.
- [150] DeCarlo, P.F., Kimmel, J.R., Trimborn, A., Northway, M.J., Jayne, J.T., Aiken, A.C., Gonin, M., Fuhrer, K., Horvath, T., Docherty, K.S. et al. Field-Deployable, High-Resolution, Time-of-Flight Aerosol Mass Spectrometer. *Anal. Chem.*, 78(24):8281–8289, December 2006. ISSN 0003-2700, 1520-6882. doi: 10.1021/ac061249n.
- [151] Gong, Z., Pan, Y.L., Videen, G. and Wang, C. Optical trapping and manipulation of single particles in air: Principles, technical details, and applications. *J. Quant. Spectrosc. Ra.*, 214:94–119, July 2018. ISSN 00224073. doi: 10.1016/j.jqsrt.2018.04.027.
- [152] Järvinen, E., Virkkula, A., Nieminen, T., Aalto, P.P., Asmi, E., Lanconelli, C., Busetto, M., Lupi, A., Schioppo, R., Vitale, V. et al. Seasonal cycle and modal structure of particle number size distribution at Dome C, Antarctica. *Atmos. Chem. Phys.*, 13(15):7473–7487, August 2013. ISSN 1680-7324. doi: 10.5194/acp-13-7473-2013.

- [153] Kontkanen, J., Lehtipalo, K., Ahonen, L., Kangasluoma, J., Manninen, H.E., Hakala, J., Rose, C., Sellegrí, K., Xiao, S., Wang, L. et al. Measurements of sub-3 {nm} particles using a particle size magnifier in different environments: From clean mountain top to polluted megacities. *Atmos. Chem. Phys.*, 17(3): 2163–2187, February 2017. ISSN 1680-7324. doi: 10.5194/acp-17-2163-2017.
- [154] Lee, A.K.Y., Abbatt, J.P.D., Leaitch, W.R., Li, S.M., Sjostedt, S.J., Wentzell, J.J.B., Liggio, J. and Macdonald, A.M. Substantial secondary organic aerosol formation in a coniferous forest: Observations of both day- and nighttime chemistry. *Atmos. Chem. Phys.*, 16(11):6721–6733, June 2016. ISSN 1680-7324. doi: 10.5194/acp-16-6721-2016.
- [155] Lee, S.H., Young, L.H., Benson, D.R., Suni, T., Kulmala, M., Junninen, H., Campos, T.L., Rogers, D.C. and Jensen, J. Observations of nighttime new particle formation in the troposphere. *J. Geophys. Res. Atmos.*, 113(D10), May 2008. ISSN 2156-2202. doi: 10.1029/2007JD009351.
- [156] Man, H., Zhu, Y., Ji, F., Yao, X., Lau, N.T., Li, Y., Lee, B.P. and Chan, C.K. Comparison of Daytime and Nighttime New Particle Growth at the HKUST Supersite in Hong Kong. *Environ. Sci. Technol.*, 49(12):7170–7178, June 2015. ISSN 0013-936X. doi: 10.1021/acs.est.5b02143.
- [157] Salimi, F., Rahman, M.M., Clifford, S., Ristovski, Z. and Morawska, L. Nocturnal new particle formation events in urban environments. *Atmos. Chem. Phys.*, 17(1):521–530, January 2017. ISSN 1680-7324. doi: 10.5194/acp-17-521-2017.
- [158] Ortega, I.K., Suni, T., Boy, M., Grönholm, T., Manninen, H.E., Nieminen, T., Ehn, M., Junninen, H., Hakola, H., Hellén, H. et al. New insights into nocturnal nucleation. *Atmos. Chem. Phys.*, 12(9):4297–4312, May 2012. ISSN 1680-7324. doi: 10.5194/acp-12-4297-2012.
- [159] Kammer, J., Perraudin, E., Flaud, P.M., Lamaud, E., Bonnefond, J.M. and Villenave, E. Observation of nighttime new particle formation over the French

- Landes forest. *Sci. Total Environ.*, 621:1084–1092, April 2018. ISSN 0048-9697. doi: 10.1016/j.scitotenv.2017.10.118.
- [160] Brown, S.S. and Stutz, J. Nighttime radical observations and chemistry. *Chem. Soc. Rev.*, 41(19):6405–6447, September 2012. ISSN 1460-4744. doi: 10.1039/C2CS35181A.
- [161] Knopf, D.A., Forrester, S.M. and Slade, J.H. Heterogeneous oxidation kinetics of organic biomass burning aerosol surrogates by O<sub>3</sub>, NO<sub>2</sub>, N<sub>2</sub>O<sub>5</sub>, and NO<sub>3</sub>. *Phys. Chem. Chem. Phys.*, 13(47):21050–21062, November 2011. ISSN 1463-9084. doi: 10.1039/C1CP22478F.
- [162] Martinez, M. OH and HO<sub>2</sub> concentrations, sources, and loss rates during the Southern Oxidants Study in Nashville, Tennessee, summer 1999. *J. Geophys. Res.*, 108(D19), 2003. ISSN 0148-0227. doi: 10.1029/2003JD003551.
- [163] Hites, R.A. Correcting for Censored Environmental Measurements. *Environ. Sci. Technol.*, 53(19):11059–11060, October 2019. ISSN 0013-936X. doi: 10.1021/acs.est.9b05042.
- [164] Bianchini, R.H., Tesa-Serrate, M.A., Costen, M.L. and McKendrick, K.G. Collision-Energy Dependence of the Uptake of Hydroxyl Radicals at Atmospherically Relevant Liquid Surfaces. *J. Phys. Chem. C*, 122(12):6648–6660, March 2018. ISSN 1932-7447. doi: 10.1021/acs.jpcc.7b12574.
- [165] Bahreini, R., Keywood, M.D., Ng, N.L., Varutbangkul, V., Gao, S., Flanagan, R.C., Seinfeld, J.H., Worsnop, D.R. and Jimenez, J.L. Measurements of Secondary Organic Aerosol from Oxidation of Cycloalkenes, Terpenes, and *m*-Xylene Using an Aerodyne Aerosol Mass Spectrometer. *Environ. Sci. Tech.*, 39(15):5674–5688, August 2005. ISSN 0013-936X, 1520-5851. doi: 10.1021/es048061a.
- [166] Fernández-Ramos, A., Miller, J.A., Klippenstein, S.J. and Truhlar, D.G. Mod-

- eling the kinetics of bimolecular reactions. *Chem. Rev.*, 106(11):4518–4584, November 2006. ISSN 0009-2665, 1520-6890. doi: 10.1021/cr050205w.
- [167] Howard, J.A. 9.2. Alkylperoxyl radicals. In *Peroxyl and Related Radicals*, volume 13 of *Landolt-Börnstein - Group II Molecules and Radicals*, pages 34–67. Springer, Berlin, 1997.
- [168] Ahmed, M., Pickova, J., Ahmad, T., Liaquat, M., Farid, A. and Jahangir, M. Oxidation of Lipids in Foods. *Sarhad J. Agric.*, 32(3):230–238, August 2016. ISSN 10164383. doi: 10.17582/journal.sja/2016.32.3.230.238.
- [169] Agency, I.E. Key World Energy Statistics 2017. Technical report, International Energy Agency, Paris, 2017.
- [170] Stark, M.S. Epoxidation of Alkenes by Peroxyl Radicals in the Gas Phase: Structure-Activity Relationships. *J. Phys. Chem. A*, 101(44):8296–8301, 1997. doi: 10.1021/jp972054\%2B.
- [171] Wijaya, C.D., Sumathi, R. and Green, W.H. Thermodynamic properties and kinetic parameters for cyclic ether formation from hydroperoxyalkyl radicals. *J. Phys. Chem. A*, 107:4908–4920, 2003. ISSN 1089-5639. doi: 10.1021/jp027471n.
- [172] Crounse, J.D., Nielsen, L.B., Jørgensen, S., Kjaergaard, H.G. and Wennberg, P.O. Autoxidation of organic compounds in the atmosphere. *J. Phys. Chem. Lett.*, 4:3513–3520, 2013. ISSN 1948-7185. doi: 10.1021/jz4019207.
- [173] Ingold, K.U. Peroxy radicals. *Acc. Chem. Res.*, 2(1):1–9, January 1969. ISSN 0001-4842. doi: 10.1021/ar50013a001.
- [174] Crounse, J.D., Paulot, F., Kjaergaard, H.G. and Wennberg, P.O. Peroxy radical isomerization in the oxidation of isoprene. *Phys. Chem. Chem. Phys.*, 13(30): 13607–13613, July 2011. ISSN 1463-9084. doi: 10.1039/C1CP21330J.
- [175] Hyttinen, N., Knap, H.C., Rissanen, M.P., Jørgensen, S., Kjaergaard, H.G. and Kurtén, T. Unimolecular HO<sub>2</sub> Loss from Peroxy Radicals Formed in Autoxida-

tion is Unlikely under Atmospheric Conditions. *J. Phys. Chem. A*, May 2016. ISSN 1089-5639. doi: 10.1021/acs.jpca.6b02281.

- [176] Glaude, P.A., Marinov, N., Koshiishi, Y., Matsunaga, N. and Hori, M. Kinetic Modeling of the Mutual Oxidation of NO and Larger Alkanes at Low Temperature. *Energ. Fuel*, 19(5):1839–1849, September 2005. ISSN 0887-0624, 1520-5029. doi: 10.1021/ef050047b.
- [177] Peeters, J., Nguyen, T.L. and Vereecken, L. HO<sub>x</sub> radical regeneration in the oxidation of isoprene. *Phys. Chem. Chem. Phys.*, 11(28):5935–5939, July 2009. ISSN 1463-9084. doi: 10.1039/B908511D.
- [178] Alzueta, M.U., Muro, J., Bilbao, R. and Glarborg, P. Oxidation of dimethyl ether and its interaction with nitrogen oxides. *Isr. J. Chem.*, 39(1):73–86, 1999.
- [179] Anderlohr, J., Bounaceur, R., Piresdacruz, A. and Battinleclerc, F. Modeling of autoignition and NO sensitization for the oxidation of IC engine surrogate fuels. *Combust. Flame*, 156(2):505–521, February 2009. ISSN 00102180. doi: 10.1016/j.combustflame.2008.09.009.
- [180] Andrae, J.C.G. Kinetic Modeling of the Influence of NO on the Combustion Phasing of Gasoline Surrogate Fuels in an HCCI Engine. *Energ. Fuel*, 27(11):7098–7107, November 2013. ISSN 0887-0624, 1520-5029. doi: 10.1021/ef401666c.
- [181] Møller, K.H., Otkjær, R.V., Hyttinen, N., Kurtén, T. and Kjaergaard, H.G. Cost-Effective Implementation of Multiconformer Transition State Theory for Peroxy Radical Hydrogen Shift Reactions. *J. Phys. Chem. A*, 120(51):10072–10087, December 2016. ISSN 1089-5639, 1520-5215. doi: 10.1021/acs.jpca.6b09370.
- [182] Anglada, J.M., Martins-Costa, M., Francisco, J.S. and Ruiz-López, M.F. Interconnection of Reactive Oxygen Species Chemistry across the Interfaces of

Atmospheric, Environmental, and Biological Processes. *Acc. Chem. Res.*, 48 (3):575–583, March 2015. ISSN 0001-4842. doi: 10.1021/ar500412p.

- [183] Ehn, M., Berndt, T., Wildt, J. and Mentel, T. Highly Oxygenated Molecules from Atmospheric Autoxidation of Hydrocarbons: A Prominent Challenge for Chemical Kinetics Studies. *Int. J. Chem. Kinet.*, 49(11):821–831, November 2017. ISSN 1097-4601. doi: 10.1002/kin.21130.
- [184] Atkinson, R. Atmospheric reactions of alkoxy and  $\beta$ -hydroxyalkoxy radicals. *Int. J. Chem. Kinet.*, 29(2):99–111, January 1997. ISSN 1097-4601. doi: 10.1002/(SICI)1097-4601(1997)29:2<99::AID-KIN3>3.0.CO;2-F. 00296.
- [185] Goodwin, D.G., Moffat, H.K. and Speth, R.L. An object-oriented software toolkit for chemical kinetics, thermodynamics, and transport processes, 2016.
- [186] Gallagher, S.M., Curran, H.J., Metcalfe, W.K., Healy, D., Simmie, J.M. and Bourque, G. A rapid compression machine study of the oxidation of propane in the negative temperature coefficient regime. *Combustion and Flame*, 153(1): 316–333, April 2008. ISSN 0010-2180. doi: 10.1016/j.combustflame.2007.09.004.
- [187] Goldman, M.J. Pressure-dependent kinetics of isobutanol peroxy radicals. *TBD*, 2019.
- [188] Yao, Q., Sun, X.H., Li, Z.R., Chen, F.F. and Li, X.Y. Pressure-Dependent Rate Rules for Intramolecular H-Migration Reactions of Hydroperoxyalkylperoxy Radicals in Low Temperature. *J. Phys. Chem. A*, April 2017. ISSN 1089-5639, 1520-5215. doi: 10.1021/acs.jpca.6b10818.
- [189] Zhao, H., Wu, L., Patrick, C., Zhang, Z., Rezgui, Y., Yang, X., Wysocki, G. and Ju, Y. Studies of low temperature oxidation of n-pentane with nitric oxide addition in a jet stirred reactor. *Combust. Flame*, 197:78–87, November 2018. ISSN 0010-2180. doi: 10.1016/j.combustflame.2018.07.014.
- [190] Sharma, S., Raman, S. and Green, W.H. Intramolecular Hydrogen Migration in Alkylperoxy and Hydroperoxyalkylperoxy Radicals: Accurate Treatment of

Hindered Rotors. *J. Phys. Chem. A*, 114(18):5689–5701, May 2010. ISSN 1089-5639, 1520-5215. doi: 10.1021/jp9098792.

- [191] Zhang, F. and Dibble, T.S. Effects of Olefin Group and Its Position on the Kinetics for Intramolecular H-Shift and HO<sub>2</sub> Elimination of Alkenyl Peroxy Radicals. *J. Phys. Chem. A*, 115(5):655–663, February 2011. ISSN 1089-5639, 1520-5215. doi: 10.1021/jp1111839.
- [192] Villano, S.M., Huynh, L.K., Carstensen, H.H. and Dean, A.M. High-pressure rate rules for Alkyl + O<sub>2</sub> reactions. 1. the dissociation, concerted elimination, and isomerization channels of the alkyl peroxy radical. *J. Phys. Chem. A*, 115(46):13425–13442, 2011. ISSN 1089-5639. doi: 10.1021/jp2079204.
- [193] Hebbar, G.S. NOx from diesel engine emission and control strategies: A review. *Int. J. Mech. Eng. Rob. Res.*, 3(4):471, 2014.
- [194] Luo, Y.R. *Comprehensive Handbook of Chemical Bond Energies*. CRC Press, Boca Raton, FL, 1 edition, 2007.
- [195] Peeters, J. and Nguyen, T.L. Unusually fast 1,6-H shifts of enolic hydrogens in peroxy radicals: Formation of the first-generation C 2 and C 3 carbonyls in the oxidation of isoprene. *J. Phys. Chem. A*, 116(24):6134–6141, 2012. ISSN 1089-5639. doi: 10.1021/jp211447q.
- [196] Crounse, J.D., Knap, H.C., Ørnsø, K.B., Jørgensen, S., Paulot, F., Kjaergaard, H.G. and Wennberg, P.O. Atmospheric Fate of Methacrolein. 1. Peroxy Radical Isomerization Following Addition of OH and O<sub>2</sub>. *J. Phys. Chem. A*, 116(24): 5756–5762, June 2012. ISSN 1089-5639, 1520-5215. doi: 10.1021/jp211560u. 4.
- [197] Eddingsaas, N.C., Loza, C.L., Yee, L.D., Seinfeld, J.H. and Wennberg, P.O.  $\alpha$ -pinene photooxidation under controlled chemical conditions – Part 1: Gas-phase composition in low- and high-NO<sub>x</sub> environments. *Atmos. Chem. Phys.*, 12(14):6489–6504, July 2012. ISSN 1680-7324. doi: 10.5194/acp-12-6489-2012. 3.

- [198] Otkjær, R.V., Jakobsen, H.H., Tram, C.M. and Kjaergaard, H.G. Calculated Hydrogen Shift Rate Constants in Substituted Alkyl Peroxy Radicals. *J. Phys. Chem. A*, 122(43):8665–8673, November 2018. ISSN 1089-5639. doi: 10.1021/acs.jpca.8b06223.
- [199] Goldman, M.J., Vandewiele, N.M., Ono, S. and Green, W.H. Computer-generated isotope model achieves experimental accuracy of filiation for position-specific isotope analysis. *Chemical Geology*, 514:1–9, June 2019. ISSN 0009-2541. doi: 10.1016/j.chemgeo.2019.02.036.
- [200] Gentile, N., Siegwolf, R.T., Esseiva, P., Doyle, S., Zollinger, K. and Delémont, O. Isotope ratio mass spectrometry as a tool for source inference in forensic science: A critical review. *Forensic Sci. Int.*, 251:139–158, June 2015. ISSN 03790738. doi: 10.1016/j.forsciint.2015.03.031.
- [201] Marcus, R.A. Mass-independent isotope effect in the earliest processed solids in the solar system: A possible chemical mechanism. *J. Chem. Phys.*, 121(17):8201, 2004. ISSN 00219606. doi: 10.1063/1.1803507.
- [202] Piasecki, A., Sessions, A., Lawson, M., Ferreira, A.A., Santos Neto, E.V., Ellis, G.S., Lewan, M.D. and Eiler, J.M. Position-specific  $^{13}\text{C}$  distributions within propane from experiments and natural gas samples. *Geochim. Cosmochim. Ac.*, 220:110–124, January 2018. ISSN 0016-7037. doi: 10.1016/j.gca.2017.09.042.
- [203] Elsner, M., Jochmann, M.A., Hofstetter, T.B., Hunkeler, D., Bernstein, A., Schmidt, T.C. and Schimmelmann, A. Current challenges in compound-specific stable isotope analysis of environmental organic contaminants. *Anal. Bioanal. Chem.*, 403(9):2471–2491, July 2012. ISSN 1618-2642, 1618-2650. doi: 10.1007/s00216-011-5683-y.
- [204] Eiler, J.M. The Isotopic Anatomies of Molecules and Minerals. *Annu. Rev. Earth Pl. Sci.*, 41(1):411–441, 2013. doi: 10.1146/annurev-earth-042711-105348.

- [205] Schmidt, T.C., Zwank, L., Elsner, M., Berg, M., Meckenstock, R.U. and Haderlein, S.B. Compound-specific stable isotope analysis of organic contaminants in natural environments: A critical review of the state of the art, prospects, and future challenges. *Anal. Bioanal. Chem.*, 378(2):283–300, January 2004. ISSN 1618-2642, 1618-2650. doi: 10.1007/s00216-003-2350-y.
- [206] Romek, K.M., Nun, P., Remaud, G.S., Silvestre, V., Taiwe, G.S., Lecerf-Schmidt, F., Boumendjel, A., De Waard, M. and Robins, R.J. A retrosynthetic approach to the prediction of biosynthetic pathways from position-specific isotope analysis as shown for tramadol. *P. Natl. Acad. Sci. USA*, 112(27):8296–8301, July 2015. ISSN 0027-8424, 1091-6490. doi: 10.1073/pnas.1506011112.
- [207] Diomande, D.G., Martineau, E., Gilbert, A., Nun, P., Murata, A., Yamada, K., Watanabe, N., Tea, I., Robins, R.J., Yoshida, N. et al. Position-specific isotope analysis of xanthines: A  $^{13}\text{C}$  nuclear magnetic resonance method to determine the  $^{13}\text{C}$  intramolecular composition at natural abundance. *Anal. Chem.*, 87(13): 6600–6606, July 2015. ISSN 0003-2700, 1520-6882. doi: 10.1021/acs.analchem.5b00559.
- [208] Gao, L., He, P., Jin, Y., Zhang, Y., Wang, X., Zhang, S. and Tang, Y. Determination of position-specific carbon isotope ratios in propane from hydrocarbon gas mixtures. *Chem. Geol.*, 435:1–9, October 2016. ISSN 00092541. doi: 10.1016/j.chemgeo.2016.04.019.
- [209] Dias, R.F., Freeman, K.H. and Franks, S.G. Gas chromatography-pyrolysis-isotope ratio mass spectrometry: A new method for investigating intramolecular isotopic variation in low molecular weight organic acids. *Org. Geochem.*, 33(2): 161–168, 2002. doi: 10.1016/S0146-6380(01)00141-3.
- [210] Piasecki, A., Sessions, A., Lawson, M., Ferreira, A.A., Neto, E.V.S. and Eiler, J.M. Analysis of the site-specific carbon isotope composition of propane by gas

source isotope ratio mass spectrometer. *Geochim. Cosmochim. Ac.*, 188:58–72, September 2016. ISSN 0016-7037. doi: 10.1016/j.gca.2016.04.048.

- [211] Gilbert, A., Yamada, K., Suda, K., Ueno, Y. and Yoshida, N. Measurement of position-specific  $^{13}\text{C}$  isotopic composition of propane at the nanomole level. *Geochim. Cosmochim. Ac.*, 177:205–216, March 2016. ISSN 00167037. doi: 10.1016/j.gca.2016.01.017.
- [212] Nimmanwudipong, T., Gilbert, A., Yamada, K. and Yoshida, N. Analytical method for simultaneous determination of bulk and intramolecular  $^{13}\text{C}$ -isotope compositions of acetic acid: Determination of intramolecular isotope composition of acetic acid. *Rapid Commun. Mass Sp.*, 29(24):2337–2340, December 2015. ISSN 09514198. doi: 10.1002/rcm.7398.
- [213] Gilbert, A., Yamada, K. and Yoshida, N. Accurate method for the determination of intramolecular  $^{13}\text{C}$  isotope composition of ethanol from aqueous solutions. *Anal. Chem.*, 85(14):6566–6570, July 2013. ISSN 0003-2700, 1520-6882. doi: 10.1021/ac401021p.
- [214] Corso, T.N. and Brenna, J.T. High-precision position-specific isotope analysis. *P. Natl. Acad. Sci. USA*, 94(4):1049–1053, 1997. doi: 10.1073/pnas.94.4.1049.
- [215] Wolyniak, C.J., Sacks, G.L., Pan, B.S. and Brenna, J.T. Carbon position-specific isotope analysis of alanine and phenylalanine analogues exhibiting non-ideal pyrolytic fragmentation. *Anal. Chem.*, 77(6):1746–1752, March 2005. ISSN 0003-2700, 1520-6882. doi: 10.1021/ac048524v.
- [216] Yamada, K., Tanaka, M., Nakagawa, F. and Yoshida, N. On-line measurement of intramolecular carbon isotope distribution of acetic acid by continuous-flow isotope ratio mass spectrometry. *Rapid Commun. Mass Sp.*, 16(11):1059–1064, June 2002. ISSN 0951-4198, 1097-0231. doi: 10.1002/rcm.678.
- [217] Wolyniak, C.J., Sacks, G.L., Metzger, S.K. and Brenna, J.T. Determination of intramolecular  $\Delta^{13}\text{C}$  from incomplete pyrolysis fragments. Evaluation

- of pyrolysis-induced isotopic fractionation in fragments from the lactic acid analogue propylene glycol. *Anal. Chem.*, 78(8):2752–2757, April 2006. ISSN 0003-2700, 1520-6882. doi: 10.1021/ac0522198.
- [218] Gilbert, A., Yamada, K. and Yoshida, N. Evaluation of on-line pyrolysis coupled to isotope ratio mass spectrometry for the determination of position-specific  $^{13}\text{C}$  isotope composition of short chain n-alkanes (C6-C12). *Talanta*, 153:158–162, June 2016. ISSN 00399140. doi: 10.1016/j.talanta.2016.03.014.
- [219] Laurent, C., Frewin, C.J. and Pepiot, P. A novel atom tracking algorithm for the analysis of complex chemical kinetic networks. *Combust. Flame*, 173 (Supplement C):387–401, November 2016. ISSN 0010-2180. doi: 10.1016/j.combustflame.2016.08.016.
- [220] Piasecki, A., Sessions, A., Peterson, B. and Eiler, J. Prediction of equilibrium distributions of isotopologues for methane, ethane and propane using density functional theory. *Geochim. Cosmochim. Ac.*, 190:1–12, October 2016. ISSN 0016-7037. doi: 10.1016/j.gca.2016.06.003.
- [221] Webb, M.A. and Miller, T.F. Position-specific and clumped stable isotope studies: Comparison of the Urey and path-integral approaches for carbon dioxide, nitrous oxide, methane, and propane. *J. Phys. Chem. A*, 118(2):467–474, January 2014. ISSN 1089-5639. doi: 10.1021/jp411134v.
- [222] Ni, Y., Ma, Q., Ellis, G.S., Dai, J., Katz, B., Zhang, S. and Tang, Y. Fundamental studies on kinetic isotope effect (KIE) of hydrogen isotope fractionation in natural gas systems. *Geochim. Cosmochim. Ac.*, 75(10):2696–2707, May 2011. ISSN 0016-7037. doi: 10.1016/j.gca.2011.02.016.
- [223] Cheng, B. and Ceriotti, M. Direct path integral estimators for isotope fractionation ratios. *J. Chem. Phys.*, 141(24):244112, December 2014. ISSN 0021-9606. doi: 10.1063/1.4904293.

- [224] Xie, H., Ponton, C., Formolo, M.J., Lawson, M., Peterson, B.K., Lloyd, M.K., Sessions, A.L. and Eiler, J.M. Position-specific hydrogen isotope equilibrium in propane. *Geochim. Cosmochim. Ac.*, 238:193–207, October 2018. ISSN 00167037. doi: 10.1016/j.gca.2018.06.025.
- [225] Li, Y., Zhang, L., Xiong, Y., Gao, S., Yu, Z. and Peng, P. Determination of position-specific carbon isotope ratios of propane from natural gas. *Org. Geochem.*, 119:11–21, May 2018. ISSN 0146-6380. doi: 10.1016/j.orggeochem.2018.02.007.
- [226] Liu, C., McGovern, G.P., Liu, P., Zhao, H. and Horita, J. Position-specific carbon and hydrogen isotopic compositions of propane from natural gases with quantitative NMR. *Chem. Geol.*, 491:14–26, July 2018. ISSN 0009-2541. doi: 10.1016/j.chemgeo.2018.05.011.
- [227] Goldsmith, C.F. and West, R.H. Automatic generation of microkinetic mechanisms for heterogeneous catalysis. *J. Phys. Chem. C*, 121(18):9970–9981, May 2017. ISSN 1932-7447, 1932-7455. doi: 10.1021/acs.jpcc.7b02133.
- [228] Allen, J.W., Scheer, A.M., Gao, C.W., Merchant, S.S., Vasu, S.S., Welz, O., Savee, J.D., Osborn, D.L., Lee, C., Vranckx, S. et al. A coordinated investigation of the combustion chemistry of diisopropyl ketone, a prototype for biofuels produced by endophytic fungi. *Combust. Flame*, 161(3):711–724, 2014. doi: 10.1016/j.combustflame.2013.10.019.
- [229] Dames, E.E., Rosen, A.S., Weber, B.W., Gao, C.W., Sung, C.J. and Green, W.H. A detailed combined experimental and theoretical study on dimethyl ether/propane blended oxidation. *Combust. Flame*, 168:310–330, June 2016. ISSN 0010-2180. doi: 10.1016/j.combustflame.2016.02.021.
- [230] Class, C.A., Liu, M., Vandeputte, A.G. and Green, W.H. Automatic mechanism generation for pyrolysis of di-tert-butyl sulfide. *Phys. Chem. Chem. Phys.*, 18(31):21651–21658, 2016. ISSN 1463-9076, 1463-9084. doi: 10.1039/C6CP02202B.

- [231] Gao, C.W., Vandeputte, A.G., Yee, N.W., Green, W.H., Bonomi, R.E., Magooon, G.R., Wong, H.W., Oluwole, O.O., Lewis, D.K., Vandewiele, N.M. et al. JP-10 combustion studied with shock tube experiments and modeled with automatic reaction mechanism generation. *Combust. Flame*, 162(8):3115–3129, August 2015. ISSN 00102180. doi: 10.1016/j.combustflame.2015.02.010.
- [232] Pepiot-Desjardins, P. and Pitsch, H. An efficient error-propagation-based reduction method for large chemical kinetic mechanisms. *Combust. Flame*, 154(1-2): 67–81, July 2008. ISSN 00102180. doi: 10.1016/j.combustflame.2007.10.020.
- [233] ReactionDesign. CHEMKIN Reaction Workbench. Reaction Design, January 2017.
- [234] Yu, J. *Estimation Method for the Thermochemical Properties of Polycyclic Aromatic Molecules*. PhD thesis, Massachusetts Institute of Technology, Cambridge, MA, USA, 2005.
- [235] Vandewiele, N.M., Van de Vijver, R., Van Geem, K.M., Reyniers, M.F. and Marin, G.B. Symmetry calculation for molecules and transition states. *J. Comput. Chem.*, 36(3):181–192, January 2015. ISSN 01928651. doi: 10.1002/jcc.23788.
- [236] Melander, L. and Saunders, W.H. *Reaction Rates of Isotopic Molecules*. Wiley, New York, 1980. ISBN 0-471-04396-6.
- [237] Skaron, S.A. and Wolfsberg, M. The calculation of isotopic partition functions ratios by a perturbation theory technique: Dissection of the isotope effect. *J. Am. Chem. Soc.*, 99(16):5253–5261, 1977. doi: 10.1021/ja00458a005.
- [238] Tang, Y., Perry, J.K., Jenden, P.D. and Schoell, M. Mathematical modeling of stable carbon isotope ratios in natural gases. *Geochim. Cosmochim. Ac.*, 64 (15):2673–2687, 2000. doi: 10.1016/S0016-7037(00)00377-X.
- [239] Clog, M., Lawson, M., Peterson, B., Ferreira, A.A., Santos Neto, E.V. and Eiler, J.M. A reconnaissance study of  $^{13}\text{C}$ - $^{13}\text{C}$  clumping in ethane from natural gas.

*Geochim. Cosmochim. Ac.*, 223:229–244, February 2018. ISSN 0016-7037. doi: 10.1016/j.gca.2017.12.004.

- [240] Webb, M.A., Wang, Y., Braams, B.J., Bowman, J.M. and Miller, T.F. Equilibrium clumped-isotope effects in doubly substituted isotopologues of ethane. *Geochim. Cosmochim. Ac.*, 197:14–26, January 2017. ISSN 0016-7037. doi: 10.1016/j.gca.2016.10.001.
- [241] Agilent. Pressure flow calculator. Agilent, June 2013.
- [242] Howard, C.J. Kinetic measurements using flow tubes. *J. Phys. Chem.*, 83(1): 3–9, 1979.
- [243] Sheehy, P.M., Volkamer, R., Molina, L.T. and Molina, M.J. Oxidative capacity of the Mexico City atmosphere-Part 2: A ROx radical cycling perspective. *Atmos. Chem. Phys.*, 10(14):6993–7008, 2010. ISSN 1680-7316. doi: 10.5194/acp-10-6993-2010.
- [244] Carrasquillo, A.J., Hunter, J.F., Daumit, K.E. and Kroll, J.H. Secondary Organic Aerosol Formation via the Isolation of Individual Reactive Intermediates: Role of Alkoxy Radical Structure. *J. Phys. Chem. A*, page DOI: 10.1021/jp506562r, September 2014. ISSN 1089-5639, 1520-5215. doi: 10.1021/jp506562r.
- [245] Incorporated, T. Condensation monodisperse aerosol generator. Model 3475 Spec Sheet, 2019.
- [246] Weber, E.J. Variation in corn (*Zea mays L.*) for fatty acid compositions of triglycerides and phospholipids. *Biochem. Genet.*, 21(1-2):1–13, February 1983. ISSN 0006-2928, 1573-4927. doi: 10.1007/BF02395387.
- [247] Rekdal, K. and Mel, T.B. UV-initiated autoxidation of methyl linoleate in micelles studied by optical absorption. *Chem. Phys. Lipids*, 75(2):127–136, February 1995. ISSN 0009-3084. doi: 10.1016/0009-3084(94)02413-Y.

- [248] Arudi, R.L., Sutherland, M.W. and Bielski, B.H. Purification of oleic acid and linoleic acid. *J. Lipid Res.*, 24:485–489, 1983.
- [249] DeCarlo, P.F., Slowik, J.G., Worsnop, D.R., Davidovits, P. and Jimenez, J.L. Particle Morphology and Density Characterization by Combined Mobility and Aerodynamic Diameter Measurements. Part 1: Theory. *Aerosol Sci. Technol.*, 38(12):1185–1205, January 2004. ISSN 0278-6826, 1521-7388. doi: 10.1080/027868290903907.
- [250] Noureddini, H., Teoh, B.C. and Davis Clements, L. Densities of vegetable oils and fatty acids. *J. Am. Oil Chem. Soc.*, 69(12):1184–1188, December 1992. ISSN 0003021X. doi: 10.1007/BF02637677.



# Appendix A

## Atmospheric Aerosol Experiments

Chapter 4 shows that stochastic kinetics might effect small, liquid particles with a fast propagation reaction rate. It also mentions that experiments are typically outside the range to be affected by it. This section discusses the experimental efforts as a part of this thesis which have advanced the measurement of stochasticity. Unfortunately, the results are not conclusive, and they are written here to provide guidance on future efforts to measure stochastic chemistry in atmospheric aerosols.

### A.1 Experimental requirements

The findings in chapter 4 place numerous constraints on the properties of aerosols and their environment for stochastic chemistry to happen. While these conditions are all interrelated, general guidelines can help constrain the experimental space. Table A.1 shows desired values for the experiments.

Particles should be small, generally less than 80 nm, with a lower bound de-

Table A.1: Recommended values for seeing stochastic effects

property	target value
particle diameter	40-80 nm
propagation rate coefficient	high (at least $10^{-21}$ cm <sup>3</sup> /molec-s)
viscosity	< 1.4 Pa-s
OH concentration	low (no more than $5 \times 10^5$ molec/cm <sup>3</sup> )

terminated to ensure good mixing,[132] estimated in Chapter 4 to be around 30 nm. Equipment is needed that can produce and measure the chemical properties of particles in this size range.

The particles also need to have low viscosity, ideally low enough so that the termination reaction is not diffusion limited. Given a termination rate of  $2 \times 10^{-15}$  cm<sup>3</sup>/molec-s at 300 K with a density of 1 g/cm<sup>3</sup> using Stokes-Einstein equation, a viscosity of 1.4 Pa-s results in a diffusion rate equal to termination rate, so ideally the viscosity should be less than 1.4 Pa-s.

Propagation chemistry needs to be fast enough to see an effect. Since the higher the propagation rate coefficient the larger the effect (with some diminishing returns), there is no clear cutoff. Though looking at Figure 4-13, having propagation at least  $10^{-21}$  cm<sup>3</sup>/molec-s would get close to the maximal effect.

Like the propagation rate coefficient, lower initiation rates also lead to a higher stochastic effect. Given a propagation rate of  $10^{-21}$  cm<sup>3</sup>/molec-s and 40 nm particle, having a surface area weighted initiation rate below 100 molec/s-μm<sup>2</sup>, which for OH at 300 K and 1 atm with all collisions being reactive corresponds to a concentration of approximately  $5 \times 10^5$  molec/cm<sup>3</sup>, would result in a factor of 5 faster oxidation by applying stochastic kinetics. This is less than general OH concentration during the daytime,[243] indicating that during the daytime, traditional kinetics might be acceptable to model aerosol oxidation.

## A.2 Producing aerosols

The first step in an aerosol experiment is to produce aerosols. Multiple methods exist to obtain aerosols of the appropriate size. One method, described here as the atomizing method, involves dissolving the aerosol component into a volatile solvent and atomizing it with a TSI Constant Output Atomizer. The solution is then passed through an absorbent column to strip the remaining solvent off of the particles.[244] To tune the size of particles, the concentration of starting solution is changed.

Another method, described here as the nucleation method, involves heating a bulk

solution of the aerosol component while flowing gas by, and having the component homogeneously nucleate to form the desired particles.[125] To tune the particle properties, the heating temperature and flow rate can be modified. The benefit of this method is that pure organic particles can be produced, though it is hard to tune the particle sizes, and if a mixture is used, the composition depends on the relative volatilities.

The third method, described here as the coating method, combines strategies from the previous two methods. First, seed particles are generated from the atomizing method, and these are either blown over or bubbled through a solution of the aerosol component, which coats onto the seed particles. The temperature of heating and the concentration of the initial atomized solution can tune the ratio of the two components. This method is used in the Continuous Monodisperse Aerosol Generator (CMAG) produced by TSI Incorporated.[245]

These methods each have advantages and disadvantages. The CMAG, for instance, can get narrowly sized particles with a geometric standard deviation less than 1.10 when the particles are larger than 500 nm, though for smaller particles the distribution widens. Its specifications also only go down to 100 nm,[245] which is larger than the desired range of sizes mentioned in Table A.1.

In these experiments, only the coating method and the atomizing method were employed, primarily because it is easier to tune particle sizes. The nucleation method is still worth looking into if the other two methods do not produce the desired small sizes.

### A.2.1 coating method

The first method employed was the coating method using a CMAG, which has the advantage of producing narrower sizes, which for this work typically had a geometric standard deviation of 1.3.

A really dilute solution, with a conductance around 50-200  $\mu\text{S}/\text{cm}$  of NaCl was used for seed, which created particles on the order of a few nanometers. About 120 mL of liquid is necessary to coat the particles, since the seed aerosol bubbles through

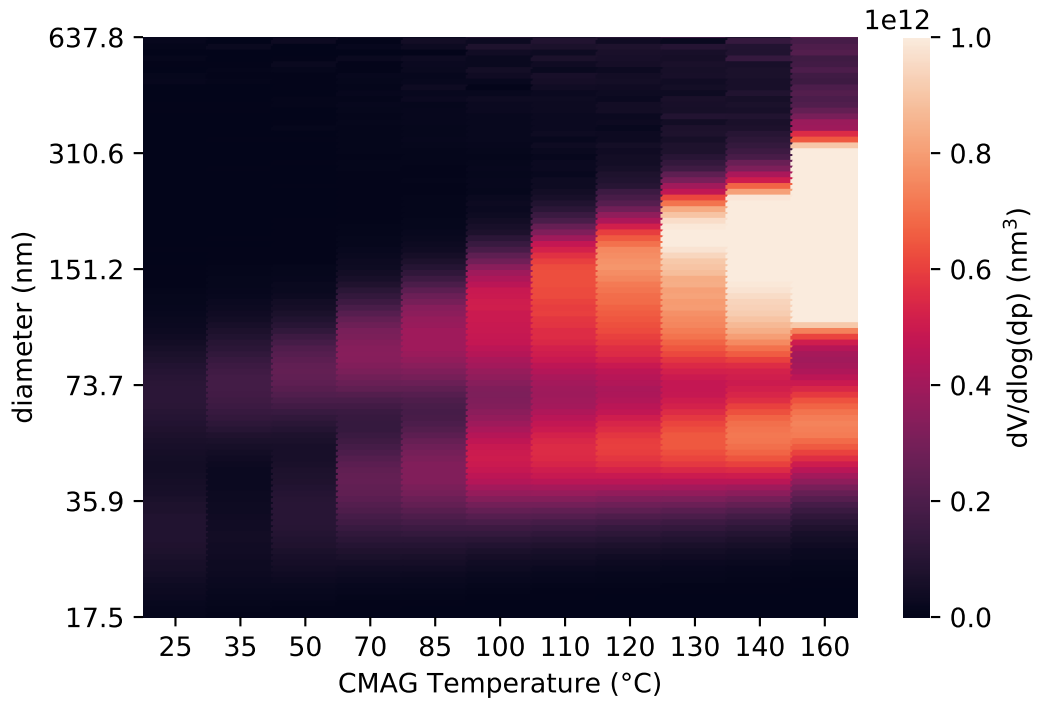


Figure A-1: Size distributions of CMAG-generated particles at various corn oil temperatures. The conductance of this NaCl seed solution was  $50 \mu\text{S}/\text{cm}$ . Data was obtained on February 2nd, 2019.

the oil.

The average size and total mass was heavily controlled by the temperature of the heated liquid. Figure A-1 shows how the size distribution changes with different heating temperatures.

One central trade off in this method is that smaller particles require lower oil temperatures, which has multiple downsides. Lower temperatures produce less mass, requiring more time to fill the chamber. This allows particles to agglomerate within the chamber, reducing the benefit to generating small particles to begin with.

Another impact of using low temperatures is that there may be more bias in what compounds in an oil mixture gets vaporized and what does not. This can make it hard to know exactly what constitutes the particles. For example, corn oil contains around 86% triglycerides,[246] though after partitioning at  $60^\circ\text{C}$ , the fraction triglycerides might be lower in the vapor phase, requiring additional analytical tests

Table A.2: Comparison of CMAG at 60°C to two atomizer runs. Atomizer experiments conducted with corn oil in hexane on July 16 2019.

volume weighted statistic	CMAG	Atomizer 0.05% oil	Atomizer 0.002% oil
geo. mean diameter (nm)	116	260	130
geo. standard dev	1.6	1.6	1.8
mode (nm)	120	230	110
production rate ( $\mu\text{g}/\text{min}$ )	10	47	18

to fully understand the particle composition.

A third limitation of using the CMAG is the amount of reagent necessary. For specialty chemicals, like purified polyunsaturated triglycerides, obtaining 120 mL can be expensive, and due to their short shelf life, may not last long.

Over many experiments, the typical volume-weighted size distribution when starting oxidation has a median around 120 nm and geometric standard deviation of 1.4, when using corn oil as the starting compound with the CMAG at 60°C and waiting till aerosol loadings of 50 to 100  $\mu\text{g}/\text{m}^3$ ,

### A.2.2 atomizing method

Due to potential issues using corn oil (see Section A.3 for more details) and due to the cost of large quantities of purified triglycerides, the atomizing method seemed appealing. Nitrogen gas was used to atomize the liquid to prevent oxidation of before entering the chamber. To get small particles, very small amounts of the aerosol component (around 10  $\mu\text{L}$ ) were dissolved in dimethyl chloride (DCM) (around 100 mL). After atomizing, the resulting mixture was put through an activated charcoal tube to adsorb the DCM, and then put into the chamber.

Table A.2 shows key aerosol properties for two concentrations in the atomizer and properties from the CMAG running at 60°C. The overall rate of particle formation was not significantly different than for the CMAG, indicating that this method has a similar drawback of increased filling time when generating smaller particles.

The benefits of using the atomizing method involves using only small quantities of the aerosol component, and being independent of vapor pressure differences.

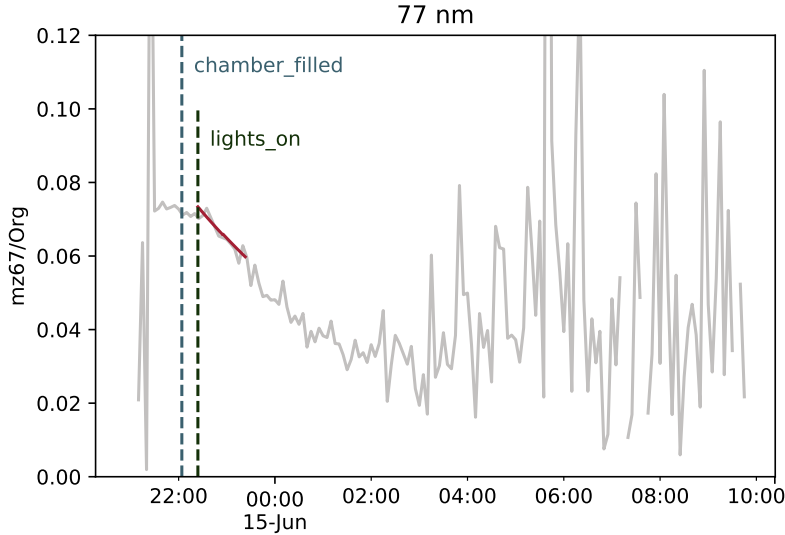


Figure A-2: Ratio of m/z 67 over all organic for the 77 nm ptof size bin of the AMS, showing noisy signal appear 3-4 hours into the experiment. Data from June 14, 2019. Grey line shows 5 minute data averages, and red line shows the exponential fit to derive a rate constant. Particles were produced using corn oil in CMAG. See Section A.6.2 and A.8 for more details.

Some issues arose with this method. The gas chromatography instrument, which was used for determining OH concentration and the dilution rate, was no longer usable due to the overbearing presence of DCM, having peak area a thousand times higher than any injected 2-methyl-2-butene or hexafluorobenzene. There is also possibility that DCM and 2-methyl-2-butene (which is an impurity in the DCM), impacts the observed chemistry, though this has not yet been examined.

Overall, both methods produced aerosols at sizes larger than desired, with a significant fraction of mass being above 100 nm. The lack of particles in the proper range would make measurements more difficult because particles agglomerated and grew over the course of the experiment, causing the mass spectrum of sub-100 nm aerosols to turn very noisy a few hours into an experiment, shown in Figure A-2.

### A.3 Aerosol composition

The composition of aerosols can have a large impact on not just whether stochastic effects dominate, but also how many gas phase reactions impact the oxidation rate.

In this thesis, three different compounds were tried for the aerosol composition, each of which is discussed below. Table A.4 shows the chemicals used in these experiments.

### A.3.1 squalene

Squalene was initially chosen because it is a liquid, has numerous double bonds which would speed up propagation, and has previous been used in heterogeneous oxidation studies.[125] After loading squalene particles to  $25 \mu\text{g}/\text{m}^3$ , adding  $\text{H}_2\text{O}_2$  and turning on the lights, nucleation occurred, as shown in Figure A-3. After nucleation, the particle loading rose to around  $1000 \mu\text{g}/\text{m}^3$ . This nucleation indicated that gas-phase chemistry was rapidly occurring. In this experiment, the only major constituents were squalene and  $\text{H}_2\text{O}_2$  with trace amounts of 1,2,4-trimethyl benzene and hexafluorobenzene. By switching to corn oil, discussed in the next section, the nucleation no longer occurred, indicating that the squalene was having substantial gas-phase reactions, causing nucleation.

Other groups that use squalene run at much higher aerosol concentration, at or above  $1 \text{ mg}/\text{m}^3$ , which reduces the fraction of squalene in the vapor phase and the fraction of gas phase reactions involving squalene.[125] These high concentration would hinder sharing equipment with other group members and was not pursued.

### A.3.2 corn oil

Since squalene was too volatile in this system. A less volatile, but equally reactive liquid was needed for experiments. Polyunsaturated fatty acids, which have been previously used for heterogeneous oxidation experiments,[124] had similar estimated volatility to squalene, and likely would not work either. The triglyceride forms were not available in large enough quantities to use the CMAG, so they were not initially used. Corn oil was chosen due to its high fraction of double-unsaturated fatty acids in triglyceride form,[246] so this was used for the rest of the experiments with the CMAG.

With corn oil, some other problems arose. The first issue was a delay in oxidation

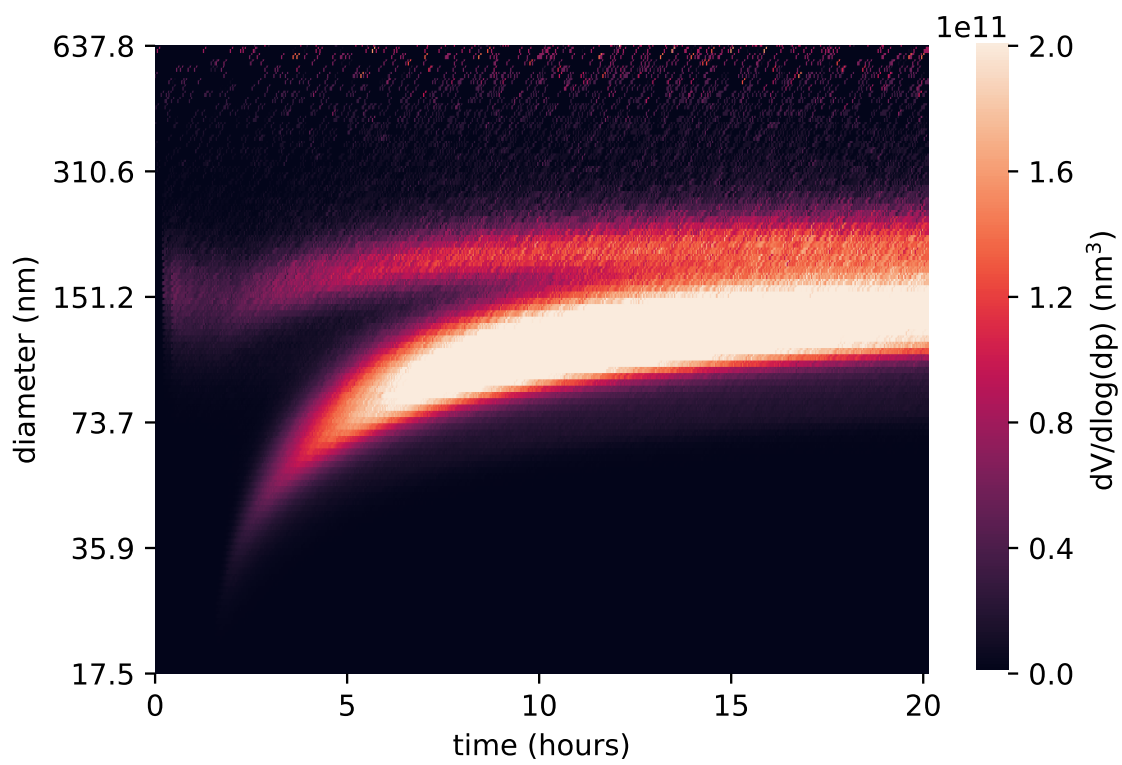


Figure A-3: Graph shows volume weighted particle density over the course of the experiment on January 22, 2019. Lights were turned on at 50 minutes.

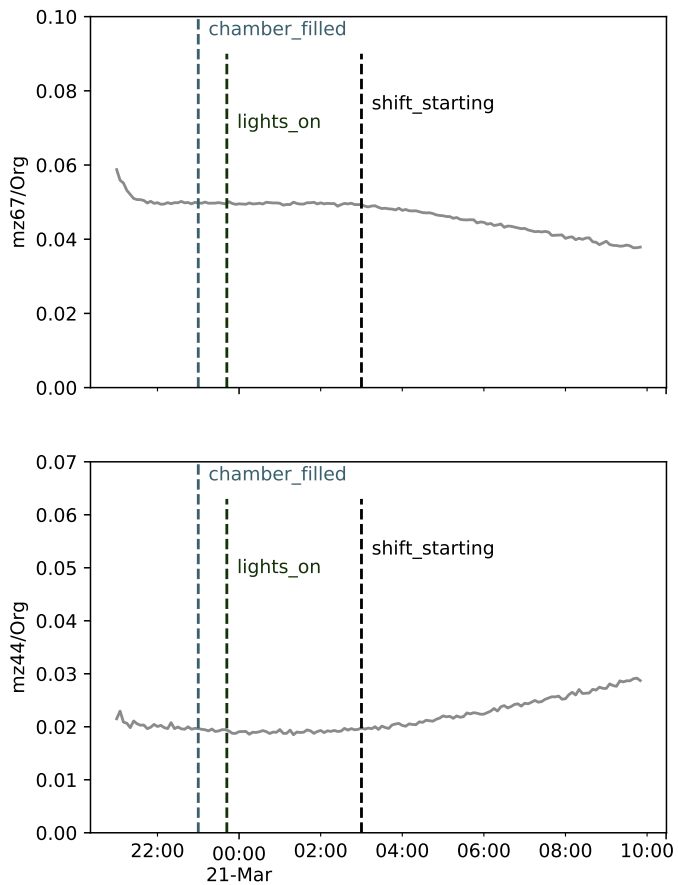


Figure A-4: Shows normalized mz67 (unreacted linoleic acid trace) and mz44 (oxidized trace) over course of experiment with corn oil particles. This data was taken on March 20th 2019 using only 25% of the lights in the chamber.

from when the lights were turned on. With full lights and oxidant, the delay appears around 5-25 minutes. With lower lights, however, this delay time can increase much longer, with Figure A-4 showing a delay of 3 hours. This time delay allows smaller particles to agglomerate and disappear before useful data is obtained. The extra free variable of time delay makes fitting more prone to bias or overfitting. A probable cause of this delay might be the presence of antioxidants that prevent propagation chemistry, inhibiting us from seeing oxidation before the antioxidants have been consumed.

Another issue encountered with corn oil was that oxidation would occur with lights on even in the absence of  $\text{H}_2\text{O}_2$ . This was thought initially to be due to chromophore impurities absorbing light and possibly initiating photolysis. When similar rates were discovered with purified trilinolein particles without light (discussed in the next

Table A.3: Selected experiments with various amounts of H<sub>2</sub>O<sub>2</sub> and lights.

date	lights on	30% H <sub>2</sub> O <sub>2</sub> added	oil temp (°C)	degradation rate (s <sup>-1</sup> ) <sup>a</sup>
March 20 2019 <sup>b</sup>	25%	0.3 mL	120	$1.2 \pm 0.3 \times 10^{-5}$
April 1 2019	100%	0.46 mL	70	$8.6 \pm 0.5 \times 10^{-5}$
April 2 2019	75%	0.31 mL	70	$4.0 \pm 0.4 \times 10^{-5}$
July 5 2019	50%	0.025 mL	60	$3.6 \pm 0.7 \times 10^{-5}$
July 16 2019	100%	0 mL	60	$2.6 \pm 0.4 \times 10^{-5}$

<sup>a</sup> from the 100 nm pToF size bin of mz67 normalized to Org.

<sup>b</sup> used the 125 nm size bin for analysis.

section), this hypothesis was ruled out.

Given these limitations, it was worthwhile to try a different type of particle.

### A.3.3 trilinolein

Purified trilinolein, whose fatty acids make up about 46% of the fatty acids in corn oil,[246] was used to try to overcome the shortcomings of corn oil. Due to the cost of purified trilinolein, experiments with trilinolein used the atomizing method of particle production.

No time delay was observed with trilinolein, shown in Figure A-5, indicating that it was likely an impurity in corn oil that had caused this effect.

Figure A-6 compares experiments without oxidant, showing the decay rates of two repeated experiments as a function of size of particles. While one experiment showed approximately a flat trend of oxidation rate with size, which would be consistent with a volumetric-based oxidation process, the second run had large deviations with size, and in a way not expected from stochastic chemistry. This change between experiments indicates a lack of repeatability in the measurement, and it is unclear why this happened. The activated charcoal may have stopped adsorbing DCM, leading more to flow into the GC. Possibly there was contamination from another source, like high NO<sub>x</sub> from the AADCO. Another alternative might be that the triglyceride, dissolved in DCM, got oxidized between the two experiments, even though it was stored in an aluminum wrapped vial in the fume hood.

One hypothesis is that the triglycerides themselves are photolyzing. This could

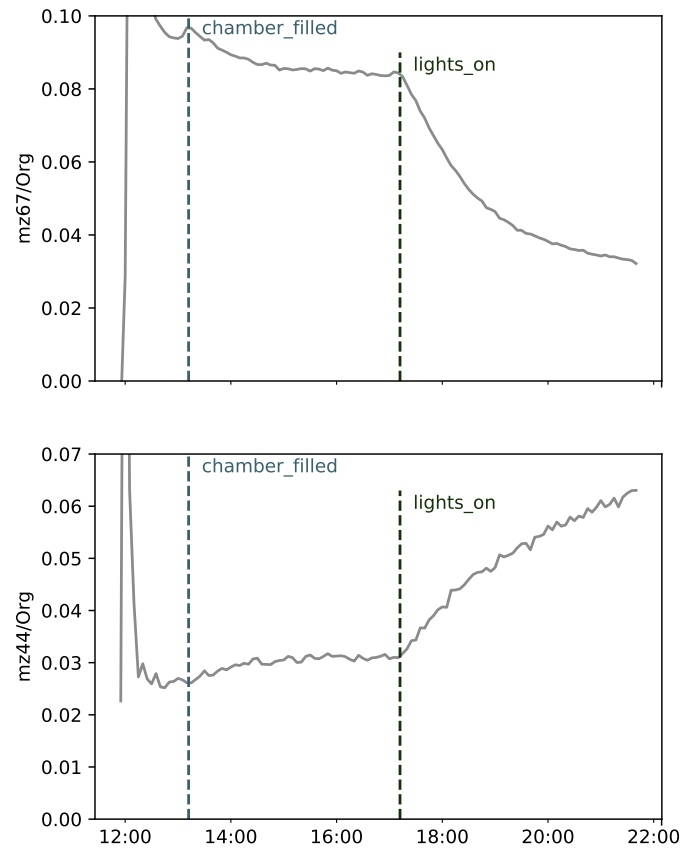


Figure A-5: Shows normalized  $mz67$  (unreacted linoleic acid trace) and  $mz44$  (oxidized trace) over course of experiment with trilinolein particles. This data was taken on July 19th 2019 using full light intensity of the chamber and no added oxidants.

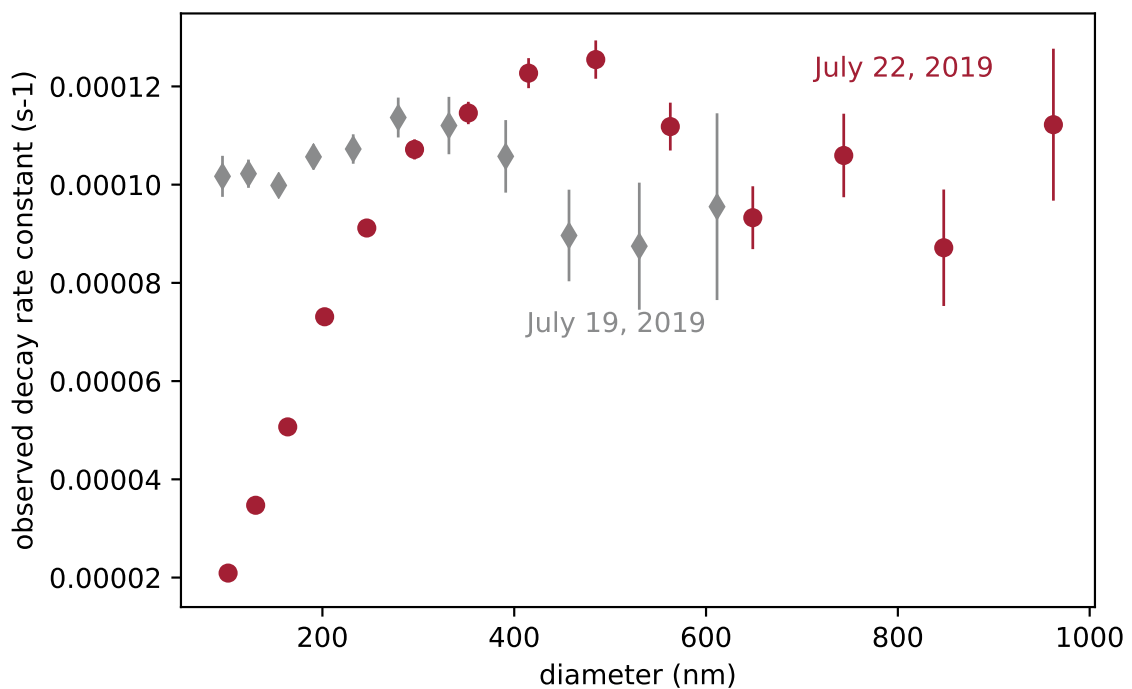


Figure A-6: Shows how oxidation rate changed with volume over two experiments without added oxidant, using full lights with trilinolein particles. The experiment with grey diamonds occurred on July 19 2019, and the experiment with red circles occurred on July 22 2019.

be the case if there are hydroperoxide groups present on the triglycerides. A previous heterogenous oxidation study with the fatty acid version of trilinolein, linoleic acid, did not mention any oxidation without lights, though the manuscript does not mention that they conducted an experiment without lights either.[124]

Previous analysis of UV-absorption of polyunsaturated fatty acids shows that their may be photolysis occurring if hydroperoxide gorups are present. An absorption peak around 232 nm is characteristic of the hydroperoxide groups in fatty acids.[247] Peak broadening also occurs in micells, where the highest observed wavelength with absorption was 320 nm, relative to bulk solution, with no measured absorption above 300 nm.[247] Purification to remove the hydroperoxide groups dramatically decreased bulk absorption, such that no absorption occurred above 260 nm.[248] The lights in the experimental chamber have a peak value of 340 nm with no measured flux below 290 nm. This has less energy than what pure fatty acid photolysis requires, but the higher energy photons could still cause photolysis of hydroperoxide groups, which may be present in both the corn oil and the purified triglyceride. Given other results showing that micells altered absorption patterns,[247] it is also possible that the ultrafine aerosols are able to absorb at different ranges than the bulk solution. Given this knowledge, studying size dependent absorption of ultrafine brown carbon might present another research opportunity.

Photolysis presents a few problems. The presence of photolysis increases the initiation rate, making it more difficult to see stochastic effects. Since the initiation rate was constrained in previous analysis using the OH concentration and Equation 4.1, it no longer holds when photolysis is present and the concept of an uptake coefficient breaks down. The presence of photolysis might make it more difficult to prove that the an observation is stochastic, since it could originate from variations in unknown absorption cross sections and quantum yields. If photolysis is the driver, more oxidation will result in more photolysis, which would not give the first-order decay used to analyze this work. Previous studies have looked at this oxidation pattern,[247] which could be adapted to the chemistry here.

Over all the three compounds studied, each one has problems that significantly

Table A.4: Materials used in experiments

Material	Purity	Amount	Source
squalene	> 98%	100 mL	Sigma
corn oil	N/A	20 L	Manzola <sup>1</sup>
linoleic acid	>98%	50 mL	Sigma
dichloro methane	>99.8% (w/ 40-150 ppm 2m2b)	1 L	Sigma
H <sub>2</sub> O <sub>2</sub>	30% (contains inhibitor)	100 mL	Sigma
2-methyl-2-butene (2m2b)	> 99%	100 mL	Sigma
1,2,4-trimethyl benzene	98%	25 mL	Sigma
hexafluoro benzene	99%	25 g	Sigma

<sup>1</sup> expiration date: Jan 13, 2020

complicate analysis.

## A.4 Oxidation chamber

In these experiments, there needs to be a place where oxidation occurs. In the lab, there are a few options. There is a large 7.5 m<sup>3</sup> bag ('the large chamber'), a 0.1 m<sup>3</sup> bag ('the small chamber'), and a flow tube. When designing experiments, the residence time of particles in the chamber is of major concern, and for these three instruments the residence times with a 5 L/min flow rate are approximately 1 day, 20 minutes, and one minute, respectfully. Since this experiment requires lower than atmospheric oxidation rates, the large chamber is ideal, and has been used for all these experiments.

## A.5 Oxidation source

For stochastic effect to be most noticeable, it is ideal to have a low and constant oxidation rate. For a constant rate, either the oxidant source must be frequently injected or the rate constant of oxidant formation from precursors needs to be lower than the inverse of the length of time of an experiment.

Various oxidants exist that could initiate oxidation. Common ones used in lab include HONO and O<sub>3</sub>. The photolysis rate with full lights for HONO is less than

an hour, which could be done in this experiment but would require constant injection. This would also add  $\text{NO}_x$  to the chamber which can create ozone, complicating analysis if the particles contained alkene groups.

Ozone could also work. Its reaction rate would depend largely on the surface area of aerosols and the uptake coefficient, both of which change over the course of the experiment. If the reaction rate is sufficiently slow that ozone concentrations do not change significantly over the course of the experiment, then multiple injections would not be necessary. Applying Equation 4.1 to a system with  $50 \mu\text{g}/\text{m}^3$  of 100 nm particles and an uptake coefficient of  $10^{-5}$ , the consumption rate of ozone lifetime would be about 80 hours, which is longer than the experimental timescale, so it could be added only at the start of the experiment.

Ozone has an additional complication in that initiation forms two radicals in the same particle, which unless one radical is easily expelled from the system, could make the stochastic effect different than what was discussed in Chapter 4. Simulating a system with both single radical and double radical initiation, with a constant total oxidation, shows relatively little dependence on the type of oxidation (see Figure A-7). The largest change occurs when there is little stochastic effect, which decreased for the 100 nm particle in Figure A-7 from a difference of 21% (at single radical initiation) to that of 12% (98% double radical initiation). In order to confidently show stochasticity, an increase in rate of at least 200% would be necessary, which at that point the impact from double initiation should not matter.

Ozone also breaks C–C bonds, leading to fragments that might cause unexpected gas phase chemistry. The impacts of this have not been explored.

### A.5.1 $\text{H}_2\text{O}_2$ photolysis

Since the photolysis rate of  $\text{H}_2\text{O}_2$  with all the lights on is around  $1.4 \times 10^{-6} \text{ s}^{-1}$ , the lifetime of  $\text{H}_2\text{O}_2$  is longer than that of the experiments, so one injection at the start of experiments is all that is necessary. An additional benefit of  $\text{H}_2\text{O}_2$  is that if there is enough of it, it can form a buffered system with the following reactions:

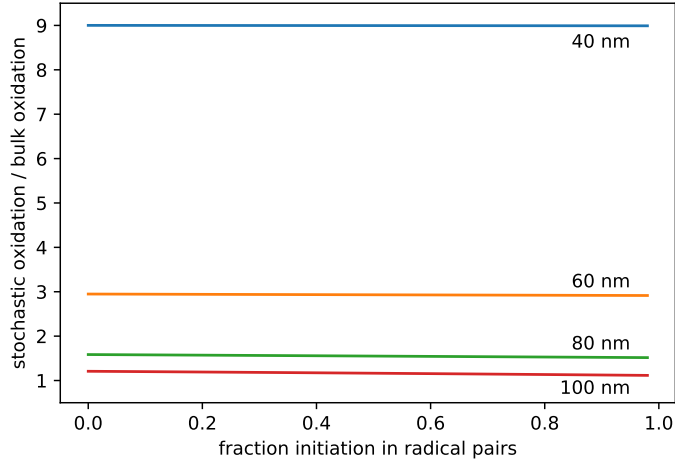
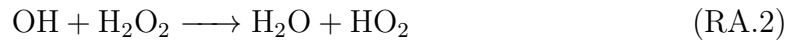


Figure A-7: Simulation showing impact of two radical initiation using the model discussed in Chapter 4. Simulation used a total first-order initiation rate per molecule of  $6 \times 10^{-5} \text{ s}^{-1}$ , density of  $0.9188 \text{ g/cm}^3$ , molecular weight of  $280 \text{ g/mol}$ , propagation rate coefficient of  $3.5 \times 10^{-20} \text{ cm}^3/\text{molec-s}$  and a termination rate of  $10^{-14} \text{ cm}^3/\text{molec-s}$ .



The equilibrium concentration of OH in this system with full chamber lights at 293 K was theoretically evaluated to be  $1.5 \times 10^5 \text{ molec/cm}^3\text{-s}$ .

If the system is buffered, there might be a substantial  $\text{HO}_2$  concentration, which might need to be included in analysis. The model with  $\text{HO}_2$  is discussed in Section 4.3.2.

Given the need for only one injection and the stable and relatively low concentration of OH, this was chosen as the best oxidant source.

### A.5.2 OH concentration measurement

The OH concentration can be measured indirectly by either gas chromatography (GC) or chemical ionization mass spectrometry (CIMS). Gas chromatography records data about every 20 minutes, where CIMS can record every second. Both of these measure the decay of an OH tracer, which in these experiments was either 2-methyl-2-butene or trimethyl benzene, and compare that to a dilution tracer, which for the GC was hexafluorobenzene.

In these experiments, only the GC was used due to its ease of data analysis and less reliance on outside research groups, since the equipment was maintained by Harvard. The lower time resolution did not impact the results significantly due to the long experiment times. In the cases of full chamber lights at 293 K with approximately 50-100  $\mu\text{g}/\text{m}^3$  of particles, the OH concentration deduced from the GC was 1.0 to  $1.5 \times 10^5$  molec/ $\text{cm}^3\text{-s}$ , which was in excellent agreement with theory.

Using an OH tracer requires that the tracer not be a major sink for OH, which is true when there is excess  $\text{H}_2\text{O}_2$  that buffers the OH concentration. However, if lower OH concentrations are desired than can be done by dimming the lights, and OH is no longer buffered, the presence of the OH tracer will significantly impact OH concentration. At the extreme, the tracer may display a zero'th order dependence making deducing the OH concentration both dependent on time and to the initial  $\text{H}_2\text{O}_2$  concentration and OH tracer measurements. In the cases without a buffered OH concentration, having an OH tracer would cause the OH concentration to increase as the tracer is consumed, making the analysis more complicated. Due to this the OH tracer was only used when OH concentration was buffered, and estimates of the OH concentration were made combining Reactions RA.1-RA.3 with the OH uptake on particles.

When using the GC, separating the peaks of hexafluorobenzene and 2-methyl-2-butene was difficult. Below are the scripts indicating the temperature ramp and valve directions that led to good separation. Five minutes was spaced between each cycle to allow the furnace to fully cool before the next set. Note that even though the

Table A.5: Temperature settings for the gas chromatography runs using 2-methyl-2-butene and hexafluorobenzene. Hold indicates how long the temperature is kept constant. Ramp rate indicates how fast a ramp will occur (following the hold). This ramp occurs until the final temperature is reached

Initial temp (°C)	Hold (min)	Ramp rate (K/min)	Final temp (°C)
-10	0	7.142	40
40	1	150	190
190	1.5	0	190

Table A.6: The valve settings for the gas chromatography runs with 2-methyl-2-butene and hexafluorobenzene.

Time (min)	Event
0.1	Vacuum Pump On
3	Vacuum Pump Off
3.1	Heat Trap 2 On
4.1	Inject Sample On
7	Heat Trap 2 Off
8.9	Inject Sample Off

temperature ramp in Table A.5 goes to -10°C, the furnace will not typically go below 40°C because there is no cooling mechanism. With these settings, the 2-methyl-2-butene peak occurs between 5.5-6.3 minutes, and the hexafluorobenzene peak occurs between 7-7.9 minutes.

## A.6 Measuring aerosols

### A.6.1 size

One critical part of these experiments is measuring the aerosol properties. This can be done with a scanning mobility particle sizer (SMPS), which provides narrow particle distribution data over the full range of sizes in this experiment. This is typically considered to be an excellent standard for obtaining size distributions. This, however, gives no information about the particle composition, and therefore, the oxidation rate.

## A.6.2 composition

A second instrument is needed to get particle chemical properties. The device used in this study was the Aerodyne Aerosol Mass Spectrometer (AMS).[150] Another option is to use a optical levitating particle trap, which can measure the oxidation of single particles. The levitating particle trap uses optics to center a particle. While levitated, various instruments can measure particle properties. The smaller particles are harder to stabilize, and studies struggle to measure particles smaller than 200 nm.[151] This device has not been studied in this work, but might be worth looking into. The rest of this section focuses on the AMS.

Due the ionization method of the mass spectrometer and the high temperature of the aerosol vaporizer, the molecules are highly fragmented before being measured by the mass spectrometer. For trilinolein, the fragment that appears to best correspond to unoxidized triglyceride occurs at mass to charge ratio 67 (mz67), with a formula of C<sub>5</sub>H<sub>7</sub>. This corresponds to the last five carbons on the fatty acid chain. Oxidizing the double bond on the fatty acid likely decreases the fractionation factor of this radical substantially. When this is normalized to another signal which is roughly independent of oxidation, like total organic mass, this gives a measure of how much of the particle is oxidized.

What particles the AMS detects is due to a few factors, discussed previously.[150] In general, potential variation of these parameters with composition was not explored and may introduce some error in the analysis. One of the most important issues was a drop off in measurement rates for particles below 70 nm. At the AMS inlet, they diffuse more like gasses and do not make it to the heated impactor (and into the mass spectrometer). This inhibits seeing the smallest particles that likely have the highest degree of stochastic effect.

## A.6.3 size and composition

The AMS has a size-selecting feature that gives different mass spec signals with size, abbreviated as pToF. This reduces the signal amount by approximately 98%, but

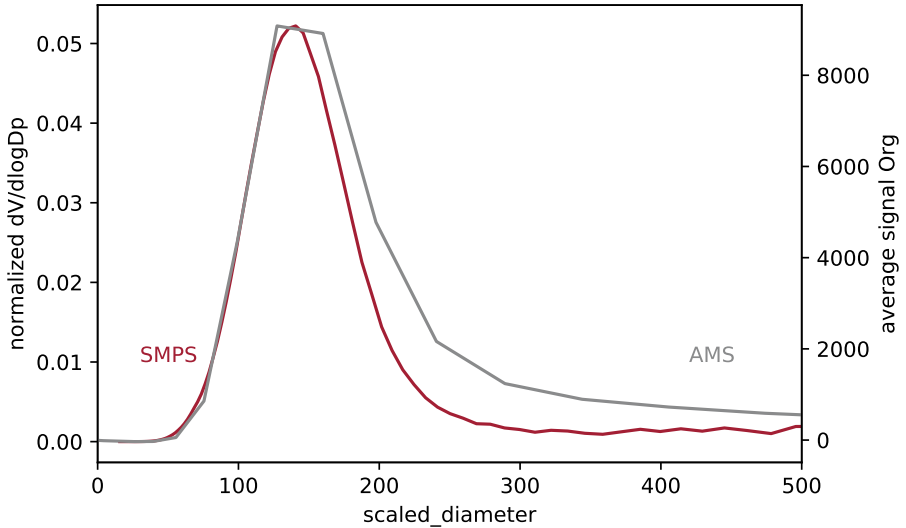


Figure A-8: Fitting of the AMS size bins to SMPS data using a calibration factor of 0.85. Data is from July 16, 2019.

allows for size specific data to be captured. The size bins are much more spread out than the SMPS and represent the aerodynamic diameter (instead of the mobility diameter), which are not identical but are interrelated.[249] In this work, the AMS size distribution graph is fit to the SMPS graph as a calibration over the time range of data fitting using the total organic trace from the AMS data. Figure A-8 shows this fitting for one run. A longer tail in the AMS occurs at higher sizes from particles bouncing on the vaporizer. Increasing vaporizer temperature did not impact this behavior.

With this calibration, the three most interesting size bins occur around 75 nm, 100 nm, and 130 nm. As shown in Figure 4-11, a change in 30 nm can lead to a noticeable shift in particle properties. The sparsity of bin sizes in the pToF is a limitation of this method. However, being able to collect both size and composition for each time point throughout an experiment is still immensely helpful.

When pToF was used, the recording frequency of data was set to 1 minute, consisting of 50 seconds of pToF data, and 10 seconds of non-size dependent data. Compared to the typical value of 20 seconds of pToF data collection per minute, this change increased the signal by 2.5 times, improving data quality.

## A.7 typical experimental steps

This section shows steps done during a typical experiment using corn oil with the CMAG to produce particles, an OH tracer, and the AMS pToF settings. Times for each experiment and experimental data are available in the Kroll group datastore, along with scripts to run the analysis. Standard procedures for instruments are listed on the Kroll group Notion site.

1. Ensure AMS, SMPS, and CMAG are connected to chamber.
2. Make sure the ozone and NO<sub>x</sub> monitors are reading low values, so that previous experiments do not contaminate this experiment.
3. Reduce the temperature in the chamber to 20°C and the flowrate to 5 L/min.  
Turn off chamber lights.
4. Start the SMPS, modifying the density to 0.9188,[250] and ensure there are fewer than 1 µg/m<sup>3</sup> in chamber.
5. Inject 0.6 µL hexafluorobenzene, 1 µL 2-methyl-2-butene, and 200 µL of 30% H<sub>2</sub>O<sub>2</sub> into chamber.
6. Start the GC using the correct protocol method, and ensure that it sees the 2-methyl-2-butene and hexafluorobenzene peaks.
7. Start the AMS, increasing the pToF collection time to 50 s.
8. Turn on the CMAG, flow air through it, venting the products for the first 5 minutes after temperatures have stabilized. Then send the aerosol to the chamber.
9. When the AMS reads approximately 100 µg/m<sup>3</sup>, turn off the CMAG.
10. Turn on the lights.
11. After 5+ hours, turn off the AMS, SMPS, and GC. Increase the temperature set point to 40°C and increase the flowrate to 30 L/min.

## A.8 AMS pToF analysis methods

The following steps were performed when analyzing the AMS data:

1. Extract the pToF data in Igor following the lab standard analysis procedure described in the Kroll lab Notion site.
2. Calibrate the AMS pToF size bins with the SMPS data from the same run.
3. For the pToF data, divide mz67 data by total organic.
4. Fit an exponential decay starting around the time the lights were turned on. The baseline value can be set to zero, a non-zero value, or allowed to be fit. The chosen method should be consistent across all datasets.
5. The effective update coefficient,  $\gamma_{eff}$  can be found with Equation 4.1, replacing  $r_i/[X]$  with the first order exponential decay value and  $\gamma$  with  $\gamma_{eff}$ .

## A.9 Conclusions and gaps

Despite no conclusive results, much was learned in these experiments. Oxidation rate was able to be quantified for corn oil and trilinolein using the peak at mz67 normalized to total organic mass. Size resolved values were also able to be obtained with the pToF setting. The time delay effect of corn oil was overcome by using pure trilinolein. These effects occurred regardless of whether the coating method or atomizing method was used to generate aerosols.

Unfortunately, gaps remain in determining the effect of stochasticity in experimental aerosols. The unexpected oxidation caused by lights without any H<sub>2</sub>O<sub>2</sub> is still not completely understood. Factors causing variation between experiments has also not been explained. Using external oxidants with the atomizing method (where there can be high levels of DCM and 2-methyl-2-butene), has not been studied.

If someone wants to measure this effect in the future, possible improvements to the experiments exist, enumerated below.

1. It might be worthwhile to switch to a more unsaturated compound, like glyceryl trilinolenate, which would have faster propagation chemistry, so the stochastic effect could more easily be seen. This would change the ideal peak from  $m/z$  67 to something smaller, since the end has two less carbons, which may also improve the signal. Using oxygenated compounds instead of alkenes, as long as they have a low enough viscosity, might be another option since they would be less sensitive to ozone.
2. Another way to improve the propagation reaction rate would be to increase the temperature in the chamber from 20°C to 40°C, which might increase the propagation reaction rate coefficient by a factor of 2-5.
3. It might be worthwhile to try to see a stochastic effect with the current equipment by obtaining repeatable pToF measurements using the atomizing method at various light intensities without any external oxidant. Hopefully, a significant stochastic effect can be seen in the experiment with the lowest lights.
4. If this is not the case, it may be necessary to improve the production and measurement of 40-60 nm particles, which would likely require instrument development. Either modifying the AMS to allow smaller particles through or switching to a different measuring method would can be pursued.

Though the stochastic effect has been proven in enough systems that it is highly likely to occur in aerosols at atmospheric temperature and pressure, going to extremes, with very rapid propagation rates, low oxidation rates, etc., might indicate that this effect only occurs in very special situations that rarely happen in the actual atmosphere. It is useful to keep this piece of information in mind when studying this effect.